Investigation of the conversion of fuels in the presence of solid oxygen carriers and the development of a plasma-assisted chemical looping system for H_2 production

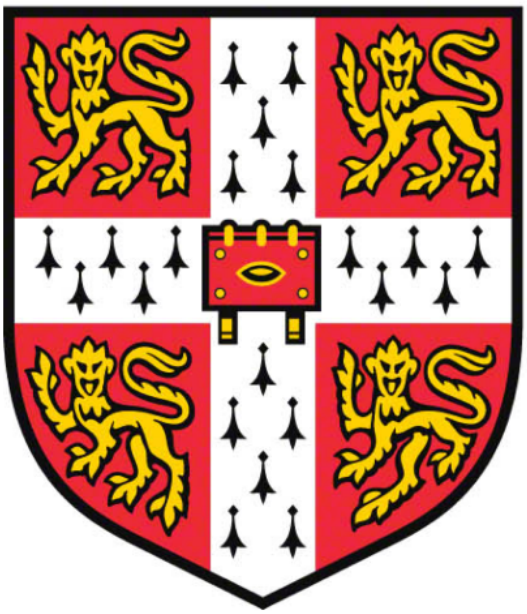

Yaoyao Zheng
Queens' College

A dissertation submitted for the degree of

Doctor of Philosophy

Department of Engineering

University of Cambridge

December 2018

Preface

This dissertation is a result of my own work that has been carried out in the Department of Engineering, University of Cambridge between October 2014 and March 2018. It includes nothing which is the outcome of work done in collaboration, except where specifically acknowledged in the text. It is not substantially the same as any that I have submitted, or, is being concurrently submitted for a degree or diploma or other qualification at the University of Cambridge or any other University or similar institution except as declared in the Preface and specified in the text. I further state that no substantial part of my dissertation has already been submitted, or, is being concurrently submitted for any such degree, diploma or other qualification at the University of Cambridge or any other University or similar institution except as declared in the Preface and specified in the text.

This dissertation contains approximately 64749 words, 95 figures and 26 tables.

Yaoyao Zheng
Department of Engineering
University of Cambridge

December 2018

Acknowledgements

First, I would like to sincerely thank my supervisor Dr Stuart A. Scott, for his unhesitating support, guidance and encouragement throughout my PhD. I would also like to express great gratitude to my advisor Prof. John Dennis, from the Department of Chemical Engineering and Biotechnology, for his precious advice on this work. I am extremely grateful to Dr Rob Grant, from Gas Recovery and Recycle limited, for his generous provision of many equipment and devices, without which I would not be able to carry out the plasma-based topics. I would also like to thank Rob for many helpful discussions with him. It has been my great pleasure to work with Drs Ewa Marek and Wenting Hu, from who I have learnt immensely in research. Sincere gratitude to Ewa and Wenting's continuous encouragement through my research is also acknowledged.

It would not have been possible to accomplish a PhD without the help of many support staff. Hereby I would like to thank Roy Slater, Robert Leroy, Jack Graham, Juan Dickerson and John Harvey from the Department of Engineering, as well as Zlatko Saracevic from the Department of Chemical Engineering and Biotechnology. They are always with great patience to help in every possible way.

I would like to thank my colleagues: Drs Mohammad Ismal, Felix Donat, Ruinan Mao, Peng Dai; Richard Goerke, Martin Chan, Matthias Schnellmann, Paul Hodgeson, Zach Bond, Samual Gabra. I will always keep the treasurable memories of the time together at Cambridge. Thank you for bringing me joy in times of difficulty.

My studentship was kindly funded by China Scholarship Council and Cambridge Trust. Research studentship to support the writing-up stage of my PhD was also provided by Cambridge Philosophical Society. I am sincerely grateful to these funding bodies.

I thank friends from the college, the department and in Cambridge, for bringing so much enjoyment to my life here. I wish to give my deepest gratitude to my families: mum, dad, and brother, for their understanding and support for all the decisions I have made. Last but not least, I must thank my beloved boyfriend Qifeng, for his being supportive, inspiring and encouraging as always, especially in my hard times.

List of Publications & Conference Presentations

The outcome of the work described in this dissertation has been submitted to peer reviewed journals for publication, and presented or to be presented in international conferences. These include:

Publications:

1. Y. Zheng, R. Grant, W. Hu, E. Marek, S.A. Scott, H_2 production from partial oxidation of CH_4 by Fe_2O_3-supported Ni-based catalysts in a plasma-assisted packed bed reactor, Proceedings of the Combustion Institute. (2018). doi:10.1016/j.proci.2018.05.101. (This work was included in Chapter 8.0).

2. Y. Zheng, R. Grant, W. Hu, S.A. Scott, Pyrolysis of wood pellets in the presence of oxygen carriers in a fluidised bed coupled with a DBD reactor for tar quantification, Chemical Engineering Journal. 355 (2019) 858–870. doi:10.1016/J.CEJ.2018.08.090. (This work was included in Chapter 5.0).

3. E.J. Marek, Y. Zheng, S.A. Scott, Enhancement of char gasification in CO_2 during chemical looping combustion, Chemical Engineering Journal. 354 (2018) 137–148. doi:10.1016/J.CEJ.2018.07.215. (Part of this work was included in Chapter 3.0).

Conferences:

1. July 2018 ***H_2 production from partial oxidation of CH_4 by Fe_2O_3-supported Ni-based catalyst in a plasma-assisted packed bed reactor.*** 37th International Symposium on Combustion, Dublin Ireland. Oral presentation.
2. Sept 2017 ***Combustion of biomass using Fe- and Cu-based oxides in a fluidised bed reactor coupled with a plasma reactor for online tar measurement.*** 23rd International Symposium On Combustion Processes, Rynia Poland. Oral presentation.
3. Dec 2015 ***In situ gasification of a Polish char by CO_2 in the presence of Fe_2O_3 in a fluidised bed for chemical looping combustion.*** UK-Sino Forum on Clean

Energy and Environmental Engineering Technology, Ningbo China. Oral presentation.

4. Sept 2015 ***In situ Gasification of a Polish Char in CO_2 in the presence of Fe-based oxygen carriers in FB for chemical looping combustion.*** 6th IEAGHG High Temperature Solid Looping Cycles Network Meeting, Milan Italy. Oral presentation.
5. July 2015 ***Chemical Looping Combustion (CLC) of Solid Fuels in the presence of Fe-based Oxygen Carriers.*** 4th Cambridge University Fluids Energy Turbo Expo (FETE) Conference. Poster presentation.

Abstract

Chemical looping combustion (CLC) is an alternative technique that was originally developed for the purpose of carbon capture and storage (CCS). It employs oxygen carriers (usually transition metal oxides) to provide oxygen for the combustion of fuels in a fuel reactor. The reduced oxygen carriers can be regenerated in an air reactor. The redox property of the oxygen carriers exhibits promising capability for converting fuels for other chemical processes such as reforming, partial oxidation, and *etc*. This dissertation is concerned with understanding the effect of adopting typical oxygen carriers on various conversion techniques, suited for different fuels.

Combustion of a solid fuel, a Polish coal-derived char was first carried out in a fluidised bed reactor in the presence of Fe-based oxygen carriers: Fe_2O_3 and ZrO_2-supported Fe_2O_3. To avoid inefficient combustion arising from direct solid-solid reaction between the char and the oxygen carriers, CO_2 was introduced to the fluidised bed, to allow the char to be gasified *in situ*, prior to the reaction with the oxygen carriers. The focus of this study was to understand how the oxygen carriers affect the *in situ* gasification step. The results of *in situ* gasification in oxygen carriers were compared with those in an inert bed. Fe_2O_3 was found not to alter the gasification step, given that the gasification of the char was free of external mass transfer limitation. A numerical model, was developed to describe the gasification behaviour, as well as predicting the effect of CO on gasification. The inhibition effect of CO on char gasification seems more significant than expected.

Combustion of biomass, a type of wood pellets, by Fe_2O_3 or mayenite-supported CuO was studied in a fluidised bed, respectively. The aim was to understand how efficient the wood pellets were combusted by the oxygen carriers, as well as the distribution of the products. The products from direct thermal processing of biomass usually contain condensable volatiles, which was defined as tar here. Therefore, in addition to commercial analysers for gaseous products, a tar measurement system, based on a plasma reactor, was developed. With the developed measuring system, it was found that both Fe_2O_3 and mayenite-supported CuO were efficient for combusting biomass, particularly the latter one. The chemical looping oxygen uncoupling (CLOU) nature of CuO makes mayenite-supported CuO a promising candidate for the direct combustion of biomass, without introducing any reactive gaseous oxidant.

The final part (Chapters 6, 7 and 8) of the dissertation was focused on developing and investigating a plasma-assisted chemical looping system for H_2 production from CH_4 at mild temperatures (~ 673 K). The active oxygen carriers investigated include $SrFeO_{3-\delta}$, Fe_2O_3, and Ni-doped $SrFeO_{3-\delta}$ and Fe_2O_3. $SrFeO_{3-\delta}$ was over-reactive in such system, leading to total combustion of CH_4 to CO_2 and H_2O. The addition of Ni onto $SrFeO_{3-\delta}$, however, significantly improved the selectivity towards H_2; whilst the high reactivity was only active in the fresh cycle. Fe_2O_3 was found inert for converting CH_4 to H_2; on the other hand, doping Ni onto Fe_2O_3 to form NiO/Fe_2O_3 dramatically improved H_2 production and the reactivity maintained high for three redox cycles. The energy cost of H_2 production from the plasma-assisted chemical looping system was found comparable to that for water electrolysis.

Table of Contents

1.0 Introduction

1.1. Chemical looping combustion

1.1.1 Carbon capture and storage (CCS)

Fossil fuels are the primary energy resource worldwide [1], despite promising renewable sources of energy such as solar energy, wind energy and hydropower, which in total account for about 7% [2]. According to the report from International Energy Agency (IEA) [3], in 2015, there is still around 82% of the world energy supply derived from fossil fuels, and there has been no significant change of their share in the total energy supply in the past several decades, *i.e.* from 1971 to 2015. The combustion of fossil fuels, as the main approach to supply energy, however, generates a substantial amount of CO_2, which is a greenhouse gas (GHG). IPCC [4] is over 95% certain that global warming is a consequence of GHG emissions. According to IEA's report published in 2017 [3], since the 1870s, the amount of CO_2 emitted from the burning of fossil fuels has increased dramatically and in 2015, it reached to over 35 Gt. It has been realised that in the 20th century, the global average temperature increased by 1 K [2]. The European Union has set a target of reducing GHG emission by at least 20% by 2020, based on the baseline of 1990 [3]. As one of the main greenhouse gases, CO_2 emissions should be controlled. Because of the abundance and low cost of fossil fuels, they are likely to remain an important part of the energy system for many decades to come. To continue to tap this convenient energy source without incurring the downsides, techniques to capture CO_2 produced from fossil fuel combustion processes and store it underground have been proposed. These techniques are called carbon capture and storage (CCS). Currently CCS for power plants is mainly sub-classified into three categories: pre-combustion, post-combustion, oxy-fuel combustion.

Pre-combustion

Pre-combustion capture is a technique that separates the carbon and hydrogen in the fuel prior to combustion [5]. The fuel is firstly converted into a mixed stream of gas products, known as 'syngas', mainly consisting of CO, H_2 and CO_2. The process is called reforming for gaseous and liquid fuels, and gasification for solid fuels. Steam is then introduced to the mixture to generate a mixed stream of CO_2 and H_2, followed by the separation of CO_2.

This finally gives a H_2-rich product stream, which can be used in many applications such as electricity generation [6]. One of its limitations is the high capital cost of the gasifier. In addition, if the gasification or reforming is by O_2, a considerable amount of energy is used to drive the air separation unit to provide O_2. The energy penalty for pre-combustion is about 8% - 12% [7,8], where the energy penalty is defined as follows.

Energy penalty = $1- \frac{\eta_{with\ capture}}{\eta_{without\ capture}}$.

$\eta_{with\ capture}$ and $\eta_{without\ capture}$ stand for power plants energy efficiency with and without carbon capture installed, respectively. The value of the energy penalty varies with the types of power plant, with pulverised coal (PC) power plants normally showing the highest energy penalty, and natural gas combined cycle (NGCC) the least [9].

Post-combustion

Post-combustion carbon capture separates CO_2 from the exhaust gas of a conventional combustion process. CO_2 is normally absorbed by a solvent (typically amine-based), and then released from the solvent to be further compressed and stored. There are also other approaches to the separation of CO_2, such as membrane filtration and cryogenic separation [10]. One significant advantage of post-combustion is its suitability for retrofit in current operating power plants without causing dramatic change and affecting the conventional operations. However, this also incurs an energy penalty due to the regeneration of the solvent and gas compression, causing about an 11% decrease in the overall efficiency (from ~39% to ~28%) of the power plant [9,11].

Oxy-fuel combustion

In oxy-fuel combustion processes, the fuel is burned in a mixture of O_2 and CO_2 rather than in air. The presence of CO_2 in the mixture is simply to lower the temperature in the flame. This burning atmosphere results in a flue gas stream containing mainly CO_2 and steam, which simplifies the capture of CO_2 [12] (as the gas is free of N_2). CO_2 can be captured from the mixed stream by the condensation of H_2O. The major cost and energy penalty arises from O_2 production in the air separation unit. The thermal efficiency of coal-steam cycle plant decreases from ~ 44% without capture to ~ 36% with capture [7].

Chemical looping combustion (CLC)

Chemical looping combustion is an alternative to conventional combustion. The term 'chemical looping' is used to describe cyclic processes which employ oxygen carriers to provide oxygen for the conversion of fuels [13]. Oxygen carriers are typically transition metal oxides that are able to give up oxygen through reduction whilst oxidising a fuel. The reduced oxides are regenerated in air in order to be used in the next combustion cycle. A mixed flue gas stream containing CO_2 and steam is obtained and CO_2 is captured by condensation. In this system, air is only used to oxidise the reduced oxygen carriers, and would never mix with CO_2 produced from the reaction of the fuel and oxygen carrier. Thus, unlike conventional combustion where a substantial amount of energy is used for separating CO_2 and N_2, the CO_2 is not diluted with a large amount of N_2 in this case. A diagram of the CLC process is presented in Fig. 1-1. It involves two interconnected fluidised bed reactors, a fuel reactor and an air reactor.

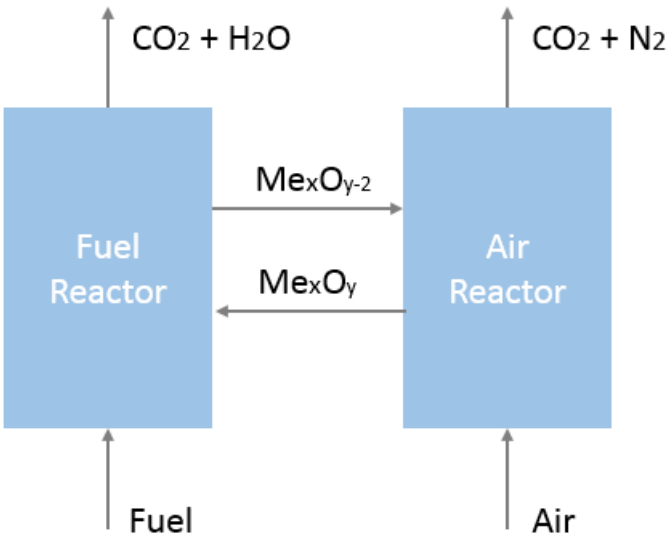

Figure 1-1 Systematic Diagram of CLC

Fuel reactor: $(n+\frac{m}{2})\ Me_xO_y + C_nH_{2m} \rightarrow (n+\frac{m}{2})\ Me_xO_{y-2} + nCO_2 + mH_2O$ R. 1-1

Air reactor: $Me_xO_{y-2} + O_2 \rightarrow Me_xO_y$ R. 1-2

Reaction R. 1-2 in the air reactor is always exothermic [14]. When two fluidised bed reactors are interconnected, the inter-transport of the solid oxygen carriers can provide

heat for the reaction in the fuel reactor. The heated air (N_2 and O_2), leaving the air reactor at high temperature (~ 1223 K), can be used to generate steam, or when the operation is pressurised, to drive a gas turbine. CLC has attracted great research interest in the past two decades, with work mainly focused on reactor design [15–17], oxygen carriers [18–20] and thermodynamic efficiency [21,22] , mostly on gaseous fuels. Chemical looping combustion of solid fuels is investigated in this dissertation (coal-derived char in Chapter 3, and biomass in Chapter 5). The combustion of solid fuels accounts for a major portion of the world's electricity supply. For instance, coal makes up to over 40% [23]. Solid fuel is also less expensive than oil and natural gas due to its large amount available [24]. Hence, solid fuels are expected to remain its role as a primary energy source in future decades.

1.1.2 Chemical looping combustion

CLC started with the conversion of gaseous fuels [25–28], followed by the interest in solid fuels at a later stage [14,29–31]. Leion *et al*. [32] carried out work on the reactivity of several types of coals and a petroleum coke using natural mineral ilmenite, in addition to a synthetic material composed of $Fe_2O_3/MgAl_2O_4$ in a fluidised bed reactor. The results demonstrated the viability of the application of CLC to various types of solid fuels. Both ilmenite and $Fe_2O_3/MgAl_2O_4$ increased the gasification rate of the fuels, and they exhibited similar reactivity. Linderholm *et al*. [33] published a study of CLC with solid fuel in a continuous 10 kW combustor comparing different natural minerals (ilmenite, ilmenite and lime, manganese ore, and manganese ore and lime). Manganese ore as an oxygen carrier showed a faster rate of gasification than ilmenite, and the addition of lime particles into the manganese ore improved the rate further. On the other hand, compared to CLC with gaseous fuels, the use of solid fuels is more complicated since the solid particles of fuel and oxygen carriers are difficult to separate [14]. The solid fuel inventory may follow the recycled stream of the oxygen carrier and enter the air reactor, where it can burn to produce CO_2 that contaminates the air stream. Therefore, in terms of solid feed, one option is to adopt an initial gasification step prior to combustion.

1.1.3 Oxygen carriers for CLC

Suitable materials for oxygen carriers should have the ability to release and capture oxygen at a temperature range of interest from ~ 1073 - 1473 K [24]. Hence, materials

suitable as oxygen carriers are usually transition metals oxides, and promising candidates ideally should have high oxygen capacity, high reactivity for redox, good resistance to mechanical force, and less likely to agglomerate. They should also be thermodynamically favoring fuel conversion to CO_2 and H_2O. Additionally, materials that are environmentally friendly and with low cost, are preferred. There are few pure oxygen carriers that meet all the criteria. Practically, other materials such as Al_2O_3 are used to support the active oxygen carriers. This helps to increase the mechanical strength of oxygen carriers [13]. Besides, due to the dilution of the oxygen carriers on the supports, side effect of sintering/agglomeration can be minimised and the overall reactivity would improve owing to the increased surface area.

Fe_2O_3, CuO, NiO and MnO_2- based oxygen carriers are the mostly investigated looping agents in CLC. Fe_2O_3 is abundant, cheap, shows high reactivity. It can be reduced to different states (Fe_3O_4, FeO, or Fe). In a sulphur-containing environment, using Fe-based oxygen carriers is advantageous [34]. For solid fuels like char, sulphur-containing gases such as H_2S and SO_2 are products in gasification. Sulphur-containing gases can react with oxygen carriers to form sulphates and sulphites. Depending on the oxygen carriers used, this can lead to the deactivation of the oxygen carriers. For Fe_2O_3/Fe_3O_4 systems, due to the thermodynamic property of the pair, iron cannot form sulphates and sulphides [34] so that deactivation caused by sulphur is not an issue for Fe_2O_3. On the other hand, there are some limitations of Fe-based materials. Usually, the reduction of Fe_2O_3 to Fe_3O_4 is more favored, as it is the fastest step; further phase reduction reactions are slow, especially the phase change from FeO to Fe [26]. However, limiting reduction to $Fe_2O_3 \rightarrow Fe_3O_4$ would limit the oxygen transport capacity. In terms of supporting materials for Fe_2O_3, Al_2O_3, TiO_2 and ZrO_2 are commonly used. The direct use of Al_2O_3 with Fe_2O_3 causes the formation of $FeAl_2O_4$, leading to decreased rate of reduction from Fe_2O_3 to phases beyond Fe_3O_4 [35]. To avoid the formation of $FeAl_2O_4$, when exploiting Al_2O_3 as the support material, one solution is to add some additional materials, such as MgO to form $MgAl_2O_4$. Some researchers used $Fe_2O_3/MgAl_2O_4$ as the oxygen carrier for CLC, and they found good reactivity of Fe_2O_3 and inertness of the support, $MgAl_2O_4$ [34,36]. Alternatively, ZrO_2 is promising as a support due to its inertness [37].

Copper-based oxygen carriers show very high reactivity (*e.g.* higher than Fe-based ones) in CLC. CuO has the ability to release gaseous oxygen, and this is known as chemical looping oxygen uncoupling (CLOU). At temperatures above 1073 K, CuO starts to decompose to Cu_2O and gaseous O_2. Chuang *et al.* [38] tested the performance of reduction and oxidation of Cu-based oxygen carriers over multiple cycles for CLC at elevated temperatures from 1073 to 1173 K. The results show that the yield of CO_2 at 1173 K was lower than that at 1073 K. This is because between reduction and oxidation, the reactor was purged with N_2. At higher temperatures, CuO decomposed to Cu_2O and gaseous O_2during the N_2 purging. For this reason, some of the oxygen was lost from CuO. On the other hand, the main concerns of using CuO are the agglomeration of particles and the need for low operating temperature. Cu has a melting temperature of 1358 K. For this reason, use of CuO/Cu is normally limited to below 1173 K (~ sintering temperature of Cu). To overcome this issue, support material is always necessary for CuO, when operated at high temperatures. Various methods for preparing CuO have been studied in order to minimise this phenomenon. Chuang *et al.* [38] compared samples of CuO supported on Al_2O_3, prepared from mechanical mixing, wet impregnation and co-precipitation methods, among which only the co-precipitated one gave no agglomeration.

Ni-based materials are another branch of materials used due to its excellent reactivity, however they are more expensive than Fe_2O_3 and CuO. Besides, environmental and health issues limit their use in the fluidised beds. Another concern is their easy deactivation by H_2S. Mn-based oxygen carriers are also of interest. Mn-based oxygen carriers have a lower cost and higher oxygen transport capacity than iron. Similar to CuO/Cu, Mn_2O_3 is able to release gaseous oxygen to become Mn_3O_4 [24]. However, at temperatures above 1173 K, for $Mn_2O_3 \rightarrow Mn_3O_4 + O_2(g)$, the equilibrium $O_{2(g)}$is above 21.4%, higher than the amount in air (~ 20.8%). This brings difficulty for the regeneration of the material. Normally, active Mn-based oxides are mixed with other active materials to form spinels, resulting in better properties than pure Mn-based oxides [25].

Perovskites, which can easily donate oxygen, are another group of materials suitable as oxygen carriers. They can be expressed as ABO_3, which can gradually lose oxygen whilst maintaining the perovskite structure: $ABO_3 \leftrightarrow ABO_{3-\delta} + \delta/2\ O_2$. $SrFeO_{3-\delta}$is one of the most studied perovskites due to its relatively low cost and high potential for losing oxygen.

The non-stoichiometry of the material, 3-δ, has been shown to be a function of temperature and pO_2 [39]. Moreover, $SrFeO_{3-\delta}$ starts releasing gaseous oxygen at temperatures as low as ~ 400°C in air [40,41], and the process is characterised by fast kinetics and good resistance to carbonation over multiple redox cycles [42].

Other materials of interest are natural minerals [43] due to their low price [33], [44]. However, the cost of preparation of the materials from raw materials and lifetime of materials should also be considered when evaluating their feasibility. The most promising natural mineral is ilmenite ($FeTiO_3$). The issue with ilmenite is that an activation step is needed [44]. Initial redox reactions of ilmenite show low reactivity. After several cycles of redox (normally over 10 cycles), both the porosity and reactivity of the material increases. Activated ilmenite exhibits high mechanical strength and reactivity, as well as a low tendency to agglomerate. Table 1-1 summarised the properties of the main oxygen carriers that have been discussed as above.

Table 1-1 Summarised properties of the main oxygen carriers.

Oxygen carriers	Reactivity	Cost	Oxygen capacity	Recyclability /stability	Health and Safety level
Fe_2O_3/Fe_3O_4	Medium	Low	Low	High	High
CuO/Cu	High	Medium	High	Low	High
NiO/Ni	High	Medium	High	Medium	Low (*i.e.* carcinogenic)
Mn_2O_3/Mn_3O_4	Medium high	Medium	Low	Low	Medium
$SrFeO_{3-\delta}$ (in perovskite phase)	High	High	Low	High	Medium
Ilmenite	Medium (requires activation)	Low to medium (need to include processing cost)	Medium	High	Medium to high

Oxygen carriers can be prepared *via* several methods, typically mechanical mixing, wet impregnation and co-precipitation. The properties of the oxygen carriers can significantly vary as a result of different preparation methods used. For mechanical mixing, metal

oxides and the support material powders are simply mixed, then the particles are calcined at high temperatures (*e.g.* 1273 K). Impregnation methods use metal oxide precursors, usually in the form of nitrate-solution, to be deposited on a solid support material. The co-precipitation method is more complex, and it uses solutions of both the active metal and the support material, by adjusting the pH of the solution to form co-precipitates of insoluble oxide precursors. A final calcination step to convert the precursors to the oxides is also needed here. Oxygen carriers prepared by co-precipitation often exhibit better performance. Chuang *et al.* [38] examined the performance of Al_2O_3 supported Cu-based oxygen carriers prepared from the three methods. Only co-precipitation method produced particles with a high loading of copper, and they did not agglomerate at 1073 - 1173 K.

1.1.4 **Reaction between solid fuels and oxygen carriers**

For the conversion of solid fuels in the chemical looping scheme, owing to the slow or negligible solid-solid reaction rate between oxygen carriers and the fuels, either an initial gasification step or a CLOU materials is required. For the first approach, the gasification step converts the solid fuels into gases (either *in situ* or *ex situ*), followed by the oxidation of the products by the oxygen carriers. Fe-based oxygen carriers for the *in situ* gasification of chars for CLC have been studied by Saucedo *et al.* [14]. They found that heterogeneous reaction took place between the produced CO (from gasification) and Fe_2O_3. The overall gasification rate increased, owing to the removal of CO from the char surface and the enhanced surface CO_2 concentration. This conclusion was believed to apply to the situation where the gasification step is limited by mass transfer. No catalytic effect of the oxygen carriers on the rate of gasification was observed. For the second approach, *i.e.* CLOU, Mattisson *et al.* [24] first described the phenomenon of combusting solid fuels by gaseous oxygen that released from oxygen carriers. They tested CuO/Cu_2O, Mn_2O_3/Mn_3O_4 and Co_3O_4/CoO for combustion of a petroleum coke, and found promising performance of CuO/Cu_2O and Mn_2O_3/Mn_3O_4 due to their high CLOU nature. Compared to the reaction rate in a CLC material scheme, *i.e.* with Fe_2O_3/Fe_3O_4, the rate with CuO/Cu_2O was found to be 50 times higher.

1.2 Gasification

1.2.1 Introduction to gasification

Gasification is the thermal conversion of carbonaceous matter into gaseous products containing CO, CO_2 and H_2. Gasification of solid fuels such as coal consists of two stages, starting with pyrolysis (discussed in 1.3), where moisture and volatiles leave the solid fuel under thermal effect. This is followed by the gasification of char. Pyrolysis is a fast reaction, compared to the gasification of char [45]. Therefore, char gasification is usually the rate-determining step in the overall gasification. Direct coal gasification would generate a large variety of products, mainly due to a huge number of volatiles produced under heating. This brings more uncertainty to the process. Alternatively, gasification of solid fuel derived char (from devolatisation in inert gas) significantly simplifies the process. This is particularly suitable for solid fuels such as coal, in which char usually makes up a large fraction of the fuel.

1.2.2 Gasification of char with CO_2

Gasification of char can either be conducted in steam or CO_2. In this dissertation, CO_2 is the gasification agent used. The gasification performance is dependent on multiple factors including char type, how the char is prepared (which affects the pore structure and surface area), particle size, gasification temperature, and gasification agent. Liu *et al.* [46] carried out of gasification of three chars, using CO_2 as the gasification agent, with temperatures ranging from 1273 to 1573 K. The three chars, which were prepared by different methods from the same parent coal, were denoted as A, B and C respectively. Char A was prepared from the pyrolysis of the parent coal with a slow heating rate (10 K/min) in a fixed bed reactor at 1173 K for 30 min. Char B was prepared by feeding the coal through in a drop tube furnace at 1373 K. Char C was prepared by firstly being demineralised with HF and HCl, followed by the same procedures as char B. Generally, the carbon conversion increased with increasing temperature. The gasification rate versus conversion varied among the three chars, as seen in Fig. 1-2. For char A, the rate decreased with increasing conversion; for char B, at 1573 K, it had a maximum rate at a conversion of ~ 0.27; for char C, at 1373 K, it had a minimum rate at a conversion of ~ 0.42, followed by an increase, whilst at a conversion of ~ 0.8, it dropped again. At higher temperatures, the rate curves always reached a maximum value (parabolic trend).

Figure 1-2 Comparison of the gasification rate (*i.e.* rate of conversion) for the three types of chars (a). char A, (b). char B, and (c). char C. Note that the figure was reproduced from [46]. For copyright issue, the figure is removed here.

The difference in the rates was caused by variation in the structure and surface area of the char due to the preparation methods, as well as the minerals present. The coal type also has a strong influence on the reactivity of the char. Beamish *et al*. [47] examined the reactivity of 18 types of chars with particle size of ~ 220 μm, produced from lignite to high volatile bituminous coals in a Thermogravimetric Analyser (TGA) with CO_2 as the gasification agent. The high volatile bituminous coal derived chars showed 20 - 30 times higher reactivity than most subbituminous coal-derived chars. The reactivity difference

between lignite coal char and subbituminous coal chars was small, despite a difference in volatile matter of ~ 10 wt.% (~ 60 wt.% for lignite coal and ~ 50 wt.% for subbituminous coal), which indicates an insignificant effect of volatile matter on the reactivity. Char reactivity was also found to show a strong correlation with the calcium content: higher calcium content (than other metal elements including Mn, Fe, Na and P) results in higher reactivity. Additionally, the form of calcium also matters.

Amongst the several factors, the most important one affecting the gasification rate is the operating temperature. A change in temperatures can alter the rate-limiting factor in the overall reaction. The gasification process can be controlled by the reaction rate (kinetically controlled), intra-particle mass-transfer, or external mass-transfer, described as regimes I, II, and III, as follows [45].

Regime I: this is normally a low-temperature regime, where the chemical reaction rate is the rate-controlling step and the experimentally observed activation energy is the intrinsic activation energy of the reaction.

Regime II: a medium-temperature regime, where the chemical reaction is limited by intra-particle mass transfer of gas from the particle surface into the particle. The activation energy observed experimentally is about half the intrinsic activation energy.

Regime III: a high-temperature regime, where the chemical reaction is limited by external mass transfer of gas from bulk phase to the surface of the particle. In this situation, the overall gasification rate is dominated by the external mass transfer, and the experimentally obtained activation energy would be close to zero.

The effectiveness factor is introduced to take into account the effect of internal mass transfer resistance. The effectiveness factor η is defined as:

$$\eta = \frac{the\ observed\ reaction\ rate\ \boldsymbol{r_{obs}}}{the\ rate\ without\ mass\ transfer\ restriction\ \boldsymbol{r_s}}, \qquad \text{Equation 1-1}$$

when $\eta = 1$, this means the overall reaction rate is not affected by diffusion. Thiele modulus, ϕ, is another dimensionless number, which was developed by Ernest Thiele

(paper: relation between catalytic activity and size of particle, 1939) to describe the relationship between diffusion and reaction rate in a porous catalyst pellet without mass transfer limitation, *i.e.* $\phi^2 = \frac{reaction\ rate}{diffusion\ rate}$. For a spherical particle and first order reaction, the following relationship between the effectiveness factor [48] and the Thiele modulus [49] can be obtained:

$$\eta = \frac{3}{\phi}\left[\frac{1}{\tanh(\phi)} - \frac{1}{\phi}\right], \qquad \text{Equation 1-2}$$

where

$$\phi = R\sqrt{\frac{k}{D}}. \qquad \text{Equation 1-3}$$

R is the sphere radius, k is the volumetric rate constant and D is the diffusion coefficient. When ϕ is very small (<0.1), η is around 1, resulting $r_{obs} = r_s$. When ϕ is much larger than 0.1, $\eta \approx \frac{3}{\phi}$, in which case the diffusion limitation is significant, and the particle is in regime II.

Equation 1-2 should only really be applied to the case where the solid is not itself consumed by the reaction (*i.e.* catalytic). For non-catalytic reactions, in the limiting cases of ϕ< 0.1 and for the case where the reaction rate is independent of the state of the solid, it is correct to apply Eq. 1-2. For high ϕ, the reactant does not reach the centre of the particle and the reaction is confined to a thin surface front which burns inwards, with material consumed at a rate of $\frac{3}{\phi}$ times that, if the reaction was uniform throughout. Shrinking core is proposed to describe the reaction in regime II, where instead of general rate constant, an effective shrinking core rate constant

$$k' = \eta \cdot k = \frac{3}{R}\sqrt{kD}$$

is used, and it is only approximately correct. The reaction rate constant is a strong function of temperature. An increase in temperature increases the reaction rate constant. As a consequence, the Thiele module can increase with temperature and the effectiveness

factor decreases. Increasing particle size can also lead to a lower effectiveness factor. Therefore, changes in operating temperature and particle size can alter the controlling regime. Usually, the temperature effect is more significant. Hodge *et al*. [50] measured char gasification rates under CO_2 from 1273 to 1673 K. Observed activation energies of 78 to 156 kJ/mol at higher temperatures, and 242 to 281 kJ/mol at lower temperatures were observed, indicating internal diffusion limitations at higher temperatures. The change in the gasification rate when in different fuel sizes is often used to experimentally examine the presence of mass transfer limitation. Saucedo *et al*. [14] investigated different regimes of the gasification of a lignite char. At a temperature of 1173 K, changing the char particle size from 800 to 2130 μm led to a noticeable change in the rate of gasification, suggesting the effect of mass transfer limitation. While at 1073 K, it was found that the gasification rate was not a function of fuel size, implying little mass transfer effect.

1.3 Pyrolysis

1.3.1 Introduction to pyrolysis

Pyrolysis is the first step of thermal treatment of solid fuels. It is the processing of fuels in the absence of oxygen or air, and is usually used to produce char, condensable liquid fuels and gaseous products such as CO, H_2, CH_4, CO_2 [51]. Pyrolysis can be classified into conventional, fast and flash pyrolysis, depending on parameters mainly including operating temperature, heating rate and particle size, as indicated in Table 1-2. In pyrolysis, moisture is the first product to leave the fuel, and this happens when the temperature is above 373 K (chemisorbed water needs higher temperature). When the temperature increases further, falling in the range of 395 to 475 K, internal bond breakage and rearrangements occur and free radicals are formed [51,52]. The predominant functional groups in the products are carboxyl, carbonyl and hydro-peroxide. Carbon-rich char is a main product of pyrolysis in conventional pyrolysis. If the purpose is to obtain mainly liquid and gaseous products, fast pyrolysis would be suitable; flash pyrolysis is operated to achieve primarily gas-based products [52].

Biomass (studied in Chapter 5), as a relative clean solid fuel when compared to coal, mainly consists of hemicellulose, cellulose, and lignin. The overall performance of pyrolysis is determined by the combined effect of each component's behavior under

thermal treatment [51–53]. Hemicellulose and cellulose decompose at relatively low temperatures, compared to lignin. Hemicellulose starts to decompose at 470 K, and the process is normally completed by 530 K. The decomposition temperature of cellulose is in the range of 510 to 620 K, and that of lignin is between 550 and 770 K [51].

Table 1-2 Range of operating parameters of main types of pyrolysis

Parameters	Conventional pyrolysis	Fast pyrolysis	Flash pyrolysis
Pyrolysis temperature (K)	550 - 950	850 - 1250	1050 - 1300
Heating rate (K/s)	0.1 - 1.0	10 - 200	> 1000
Particle size (mm)	5 - 50	< 1	< 0.240
Solid residence time (s)	450 - 550	0.5 - 10	< 0.5

Pyrolysis is not a single reaction but a complicated process involving multiple physical and chemical transformations. A large variety of product species are formed during pyrolysis, and secondary reactions make the process even more complex. Pyrolysis was initially considered to consist of primary and secondary reactions [54]. For instance, biomass is firstly pyrolysed into non-condensable gases, volatiles and char, through the primary reactions. Some of the produced volatiles can further decompose into gaseous products and char through secondary reactions. Typically, primary reactions are endothermic, and secondary reactions are normally exothermic. Koufopanos *et al*. [55] proposed a mechanism in which biomass firstly decomposes into a mixture of gases and volatiles, and char. This is then followed by reactions between gaseous products (non-condensable gases and tar) and solid char**.** This approach attempts to hide the complexity of pyrolysis by grouping components into loose categories.

Miller and Bellan [56], on the other hand, suggested that different fractions of biomass (cellulose, hemicellulose and lignin) firstly produce some intermediates, which then decompose into char, gas and tar. The tar generated can further decompose to gases. Other mechanisms have been proposed to explain the effect of process conditions on both the kinetics of pyrolysis and the yields of the products [51,57], but pyrolysis is still not fully understood.

1.3.2 Pyrolysis products

The main products obtained from pyrolysis are char, non-condensable gases, and condensable volatiles (which usually become viscous tar below 473 K). Tar consists of more than 300 compounds, containing functional groups such as carboxyls, carbonyls and phenolics [58]. Due to its complicated composition, it is always a challenge to fully understand its properties because of interactions between each individual compound. The relationship between tar yield and operating conditions, however, can be determined from experimental results. Maximum tar yield occurs in a temperature range between 623 and 773 K [51,52]. When temperature increases further, heavy molecules present in the char and liquid can be further broken down, causing an increase in the overall amount of gaseous product [52]. Therefore, as temperature rises, the yield of tar is always a combined effect of more heavy carbon-based material going to tar, and certain fractions of the tar being decomposed into gaseous products. The yield of char can be maximised using a relatively low temperature and a slow heating rate. A study of the effect of temperature on bio-char yield was carried out by Rocha *et al*. [59]. In the low temperature range of 723 to 773 K, the gravimetric yield of char was between 12 wt.% to 14 wt.%. When the temperature increased to above 923 K, the yield dropped significantly to < 7 wt.%. To maximise the gaseous products, it is widely accepted that high temperatures and high heating rates would help [57,60,61]. For each individual gaseous species, the yields with temperature differ. Normally, an increase in temperature favours the production of syngas. Kantarelis and Zabaniotou [62] studied fast pyrolysis of cotton stalks in a fixed bed reactor between 673 and 1033 K. Their results showed that the overall gas yield increased with temperature; the H_2 content increased significantly from 18 vol% to 39 vol% of the total gaseous products as the temperature increased from 673 to 1033 K, whilst CO_2 dropped sharply. CH_4 showed a maximum yield at 773 K.

1.3.3 Removal of biomass tar

The formation of unwanted condensable products (when it is not the target product of the process, such as bio-oil), *i.e*. tar, is one of the main issues in the pyrolysis and gasification of biomass. Considerable efforts have been put into the reduction and removal of tar [51,63–66]. Tar removal approaches can be categorised into primary and secondary methods [67]. Primary approaches refer to those treatments inside the gasifier and aim to

reduce the formation of the produced tar from the gasification process *in situ*. Secondary approaches are methods to remove the tar formed after gasification. Tar can be removed either physically or chemically. In primary approaches, since less tar is formed, it reduces the load on downstream processes. Secondary approaches are often reported to be more effective in tar removal but they normally require extra units for specific treatment [65].

- **Primary tar removal methods**

Inside a gasifier, the formation of tar can be minimised by adjusting the operating conditions, selection of proper catalysts, or modification of the gasifier design [65]. High temperatures and pressures are preferred to achieve a high conversion of biomass carbon and low tar content in the off-gas. Operating temperatures above 1073 K are usually required for gasification for a clean gaseous product stream, and higher temperatures also lead to fewer species of tar formed [68–70]. Knight [71] studied pressurised gasification of wood chips up to 21.4 bar. High pressures significantly decreased the amount of tar, and at 21.4 bar, there was nearly no phenol (which was found at lower pressures) detected. The presence of the gasification agent itself is also able to decrease the tar yield due to reforming reactions, *e.g.* CO_2 reforming to give CH_4 and CO as the primary reforming products [72,73]. In the absence of catalysts, CO_2 normally starts to reform tar at temperatures higher than 823 K [74]. The nature of the gasification agent (*e.g.* H_2O and O_2) can also affect the compositions and quantity of the gaseous products [65].

Adopting catalysts inside the gasifier is an effective way of affecting the reactions, and thus the products. The presence of catalysts can promote the gasification of char, change the compositions of gaseous products and reduce tar formation [65]. Commonly-used catalysts for tar reduction are zeolites, olivine, iron or Ni-based catalysts and dolomite [67]. Corella *et al*. [75] reported a reduction of tar yield from 6.5 wt.% to 1.3 wt.% in the presence of dolomite. Corella *et al*. [76] further found that dolomite did not significantly alter the amounts of the CH_4 and C_2H_n produced, but increased the amount of H_2 and decreased the amount of CO. However, dolomite is friable, and thus not suitable for fluidised systems [65]. Olivine was shown to be more resistant, and has comparable catalytic performance to dolomite [77]. Ni-based catalysts are also reported to have good performance in tar abatement and the improving the yield of hydrogen, whilst a negative side of Ni is its easy deactivation [78]. Deactivation can be reduced by adjusting the

operating conditions, *e.g.* increasing the temperature, or regenerating the catalyst through burn-off if possible. In general, the catalyst to be used inside the primary reactor should meet following criteria: 1) high tar reduction efficiency; 2) high resistance to deactivation at operating temperatures (> 1073 K); 3) high mechanical strength in fluidised system. Ideally, the catalyst should also be inexpensive, less likely to sinter at the operating temperature and be easily regenerated. Nickel is attractive, in some respects, but is expensive and is a carcinogen, meaning its use in fluidised system could be problematic (owing to its loss in the fines elutriated from the bed).

- **Secondary approaches to tar removal**

Physical or mechanical removal of tar after gasifiers employs extra units to capture the tar in the downstream. These units can be a filter, cyclone, electrostatic precipitator, or scrubber *etc*. [67]. Physical methods normally operate at low temperatures at which the tar condenses (*e.g.* 473 – 573 K). Chemical approaches are aimed at completing the conversion of tar formed from the upstream into more desirable components, and they normally take place in a second reactor. Cracking techniques are more frequently used and the commonly-studied approaches include thermal cracking, catalytic cracking, plasma cracking or a combination thereof. Thermal cracking, by definition, uses a high temperature (usually above 1273 K) to crack the tar into lighter gaseous products. The catalysts used in the primary reactor for tar reduction can also be employed in the downstream to decrease the temperature needed for thermal cracking. The desired properties for catalysts in a downstream tar conversion unit are similar to those in the primary reactor, except that high mechanical strength might not be required as the catalyst bed inside the secondary tar removal reactor is normally fixed [67]. Plasma cracking, which is essentially using plasma to breakdown the tar, is usually achieved by thermal, or arc plasma (refer to 1.4 for the new terminology). It has comparable tar destruction efficiency to incineration process, making it highly attractive [79]. In addition to direct plasma cracking, other processes such as reforming of tar in waste air stream by plasma reactors to reduce the tar have also been widely studied recently, and more description regarding this is presented in 1.4.

1.4 Plasma

In recent decades, plasma has attracted intensive interest in the field of chemical engineering, due to its excellent capability of stimulating chemical reactions [80]. Plasma, known as the fourth state of matter (other states are solid, liquid and gas), is an ionised gas, where free electrons are formed as a result of ionisation. The ions and electrons coexist, with the overall plasma being neutral. The energy required for creating plasma can be from thermal heating, electric discharge, or electromagnetic fields. Plasmas are subdivided into thermal and non-thermal plasma. The latter refers to a condition where the temperature of the heavy particles, ions and electrons are the same, *i.e.* they are in thermal equilibrium. An electric arc is an example of thermal plasma [80]. In a non-thermal plasma the temperature of electrons is much higher than that of the heavy particles and ions, resulting in a non-equilibrium system. Practically, non-thermal plasma is more frequently used because [81]: 1) electromagnetic fields naturally transport charged species, resulting in their concentrations and energies varying in space. This means that it would be difficult to have a system in perfect thermal equilibrium; 2) it is more energy-efficient to feed the energy only to the extent that could effectively create the desired products for a particular reaction, rather than bringing the whole system to the equilibrium.

Plasma was initially mainly used for ozone generation, and it has been studied since the 19th century. In the late 1990s, researchers started to apply this technology, mainly non-thermal plasma, in the destruction of harmful compounds in air (*i.e.* mainly NOx) [82,83] and synthesis of products from hydrocarbons [84,85], which otherwise would require high temperature or pressure. Prieto *et al.* [86,87] carried out work to understand the possibility of converting heavy oils to light hydrocarbons in a plate-plate type plasma reactor using argon as a carrier gas. The heavy oil was converted into product species including CH_4, C_2H_4, C_2H_6, C_3H_6, and C_4H_{10}. Their study, for the first time, demonstrated the possibility of using a plasma reactor to crack heavy oils at ambient temperature and pressure, and showed significant selectivity towards ethylene. Plasma reactors were later studied for the destruction of volatile organic compounds (VOCs), or tar as unwanted product, based on toluene, xylene and benzene as model compounds [88,89]. The group at University College London has studied a coupled fluidised bed-plasma system for gasification of waste [90–92], including the removal of tar. A plasma converter, operated at ~ 1473 K, was positioned after the gasifier to convert the products primarily to syngas.

Tar measurement was carried out off-line. The tar removal efficiency was obtained by taking the difference in the tar level before, and after the plasma converter. The system processed a continuous feed flow rate of up to 100 kg/h of waste, and showed very effective removal of tar compounds in the presence of thermal plasma. Voltage supply, fuel concentrations, carrier flow rate, distance between the two electrodes and frequency are the main factors influencing the removal efficiency. Other aspects of recent interest for employing plasma include reforming of fuels (*e.g.* H_2 production from CH_4 reforming in plasma reactors), surface treatment of materials, sterilisation, and *etc.* [80]. The application of plasma for H_2 production is described in 1.5.3. Other applications are beyond the interest of this dissertation, and thus not reviewed. Here, the operating temperatures of interest are rather low, compared to those for thermal plasma, as the focus is on non-thermal plasma. The application of such plasma to the conversion and removal of VOCs, or tar, is reviewed below.

1.4.1 Dielectric barrier discharge (DBD) and its application on tar removal

The most common configurations of non-thermal plasma used are corona discharge and dielectric barrier discharge [80]. In a corona discharge, the discharge expands from the pinpoint of the high voltage electrode to the outer space, as shown in Fig. 1-3. A corona region is a pattern of bright sparks near the pinpoint. This is also where ionisation occurs. Outside this ionisation region, the electric field is low, and current is only carried by electron drift. Only dark discharge is seen in the drift region. The plasma formed in corona discharge, therefore, has poor uniformity and contains sparks. Sparks can lead to local over-heating and noises, and thus need to be avoided in many applications.

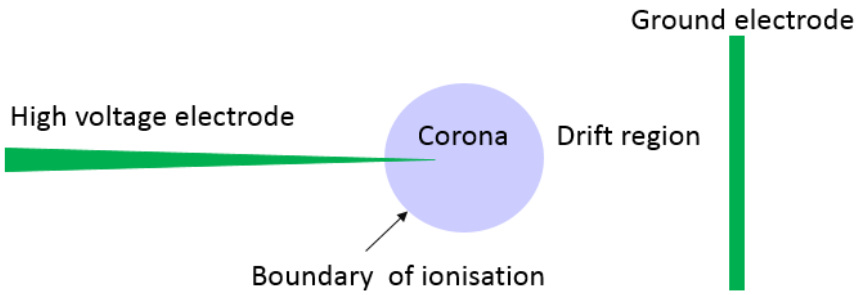

Figure 1-3 Illustration of corona discharge.

In a DBD, at least one barrier material is employed between the two electrodes. Figure 1-4 shows several typical configurations of DBD reactors including planar and cylindrical types. Typical potential change of a plate type DBD reactor is presented in Fig. 1-5. The discharge builds up on the surface of the barrier, which creates a reverse electric field. As a result, in order to have a strong enough electric field to break down the gases passing through the gap, a higher voltage is needed [93]. However, a DBD can create a more homogenous discharge by spreading micro-discharges over the electrode surface, and arcing can also be avoided by selecting proper dielectric materials. In general, DBD has two advantages over corona discharge [94]: 1) the formation of arc is avoided or lessened; 2) higher probability of collision between electron, ions and molecules due to more homogenous distribution of plasma. Popular materials used for the dielectric barrier are glass, quartz, alumina and ceramics [94].

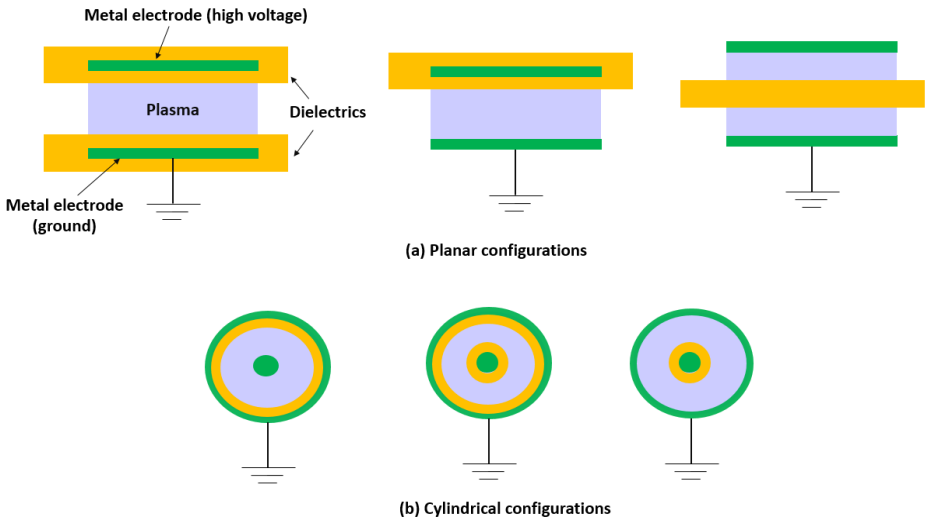

Figure 1-4 Typical configurations of DBD reactors.

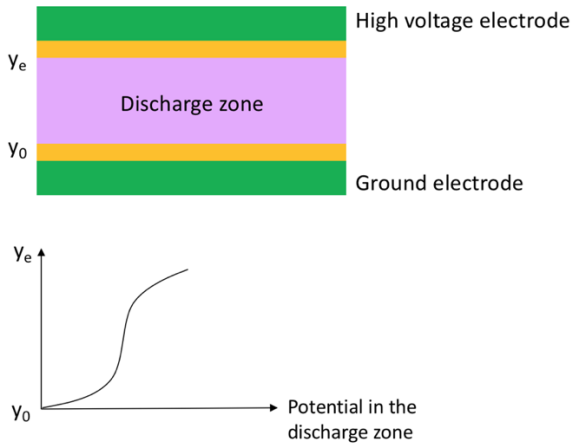

Figure 1-5 Typical potential change in the plasma discharge zone of a plate type DBD reactor [95].

DBD technology was originally developed by Siemens in 1857 [93]. It involved a double-walled cylindrical glass tube, with gas flowing though the gap between the inner and outer walls. The two electrodes were positioned inside the inner tube and outside the outer tube. The purpose of this reactor was to generate ozone from atmospheric air. The Siemens tube was quickly found to be an ideal reactor for decomposing gases without excess heat. It has now become a promising technology for abatement of VOCs from waste air [88]. To improve the removal efficiency, catalysts (mostly Ag, Mn, Ce, Cu, Mn, Fe, Ni, Zn based) have been loaded within a DBD reactor [88,96–100]. Most of the experimental studies of the removal of VOCs, or tar, using DBD employ toluene, benzene, xylene, or a mixture of the three as a model compound. On the other hand, because tar consists of a wide range of compounds, besides the three above, it would be interesting to investigate the tar removal efficiency of a product stream containing actual tar compounds from thermal treatment (*e.g.* combustor, fluidised reactor *etc.*). This has been actively studied in the field of waste-to-energy [67], though more by thermal plasma approach [90–92].

1.4.2 Plasma chemistry

As an ionised gas, ionisation is always the first reaction to consider in plasma. Due to the low mass and high mobility of electrons, they are always the first to get energy from electric fields. The energy can then be transferred to all other plasma components to support ionisation, excitation, dissociation and other plasma-chemical processes. The rate

of such processes depends on the number of electrons available to transfer the energy. There are mainly five mechanisms for ionisation [101]: direct ionisation by electron impact (DIEI), stepwise ionisation by electron impact (SIEI), ionisation by collision of heavy particles (ICHP), photo-ionisation (PI) and surface ionisation (SI). DIEI is considered an important process in non-thermal discharge, where electric fields and electron energies are quite high, but the excitation level of neutral species is relatively moderate. DIEI is the ionisation of neutral and previously unexcited species (*i.e.* atoms, radicals, or molecules) by an electron, whose energy is high enough to stimulate the ionisation act in one collision. The ionisation occurs when the energy ΔE transferred by an incident electron with a high energy of E, to the valence electron exceeds the ionisation potential.

When the concentration of excited neutrals is high enough, the energy required for ionisation can also be directly transferred to the preliminary electronically excited neutrals by colliding with electrons, and this is known as SIEI. When the level of electronic excitation is high enough, the probability of obtaining ionisation energy for free electron is much lower than that for excited neutrals. Compared to direct electron ionisation, SIEI is composed of more than one step. Initially, neutrals need to obtain energy from an electron-neutral collision so as to become excited; and this is followed by a collision with a relatively low-energy electron to cause the actual ionisation. For the direct collision of the heavy particles (ions and neutrals), acquiring energy that is high enough for ionisation does not guarantee an effective ionisation event. This is mainly due to their low velocities. Regardless of having enough energy, it is very difficult for a heavy particle to transfer this energy to an electron (which is moving very fast) inside an atom. This suggests that heavy particles must have a high kinetic energy for ICHP.

Beside electron collision, the energy for ionisation can also be supplied by a photon. The wavelength of such photons is usually less than 100 nm (ultraviolet radiation). However, the contribution of photo-ionisation process is usually not significant in plasma systems due to low concentrations of high-energy photons. Surface ionisation is when collisions happen between electrons, ions, and photons with surfaces. The surface-related ionisation is very different from the aforementioned four mechanisms, and beyond the scope of the interest here.

1.5 Production of hydrogen

Hydrogen, is a clean energy source in the sense that it does not generate CO or CO_2 when being consumed. Its high heating value (on a mass basis) also makes it advantageous than other fuels in some applications. At 298 K and 1 atm, the heating value (lower to higher heating values) of H_2 is 120 - 142 MJ/kg, compared to 50 - 55.5 MJ/kg for CH_4, and ~ 45 MJ/kg for diesel fuel (data from Ref. [102]). There are multiple ways of producing H_2, including steam reforming of methane or other hydrocarbons, chemical looping reforming, gasification of solid fuels, reforming of oil, water splitting/dissociation through electrolysis, chemical approach or high temperature, plasma (-assisted) decomposition *etc*. [103]. Introduction of the main techniques relevant to this work are presented as follow.

1.5.1 Steam reforming of methane (SRM)

Steam reforming of natural gas, mainly methane, is the most common and cheapest (with an energy cost of below 160 MJ/kg of hydrogen produced [104]) industrial process used for the production of H_2. It makes up about 50% of the total H_2 production [103]. The operating temperatures of the reformer, where the main reaction ($CH_4 + H_2O \rightarrow H_2 + CO$) takes place, is usually above 1073 K [105]. Catalysts can be employed in the reformer to lower the processing temperature or/and increase the yield of H_2.

The research on SRM dates back to 19th century, when SRM over Ni-based catalyst was first reported and patented [106]. Later on, in the early 20th century, other catalysts, including iron, cobalt, promoted nickel, alkali, and alkaline earths were found effective in reducing the operating temperature of SRM [106]. Owing to the good performance of Ni-based catalysts, SRM over Ni for H_2 production has been widely investigated and utilised. Some catalysts such as rhodium and ruthenium, have been reported more catalytically active for SRM [107]; while their applications are limited by the high cost. For these reasons, Ni-based catalysts are more practically used. However, deactivation of Ni, is often an issue in the reforming of hydrocarbons. The deactivation mainly results from oxidation of Ni to NiO, poisoning of the surface active sites, or coking over the Ni-based materials [108]. A significant amount of work has been carried out to eliminate the deactivation of Ni. Alkali was found helpful for suppressing the formation of coke, as it could neutralise the acidic sites active for cracking on the support, and promote the

reaction between coke and steam [108]. Other methods for eliminating the coking include selection of appropriate supports, and modification of the characteristics of the material such as particle size, surface area, and *etc*. [109]. In terms of the oxidation of Ni for deactivation, Matsumura and Nakamori [110] studied SRM over Ni catalyst on various supports (*i.e*. silica, γ-alumina, and zirconia) at 773 K, much lower than the temperature for conventional SRM. Metallic phase Ni on the silica and zirconia were obtained by reducing the calcined (prepared at 973 K) materials in H_2 at 773 K; whilst Ni/γ-alumina was only obtained by reduction at a higher temperature, 973 K. When reforming by steam at 773 K, the activity of Ni/silica was found to decrease due to the oxidation of nickel, similarly, Ni/γ-alumina particles were also partially oxidised; Ni/ZrO_2 was found the most effective in H_2 production, and no significant deactivation was observed. The accumulated hydroxyl groups on the surface of the ZrO_2 support was believed to be responsible for the high yield of H_2. From the perspective of the processing parameters, to improve the purity of H_2 in the product stream and eliminate carbon from SRM, a high steam to CH_4 ratio can be adopted. For this reason, the ratio of H_2O to CH_4 as feedstock is usually controlled at 2.5 to 3 [111].

In addition to the participation of catalysts, a water-gas shift step ($H_2O + CO \rightarrow H_2 + CO_2$) is usually employed downstream for SRM plants to increase the yield of H_2. Due to the exothermic nature of the water-gas shift reaction (WGSR), it is usually operated at temperatures of around 673 K. As a whole, H_2 production from CH_4 steam reforming plants often requires multiple stages, making the process more appropriate for large scale H_2 production and not requiring high H_2 purity.

1.5.2 Chemical looping reforming of CH_4

Chemical looping reforming techniques have been studied, following the rise of research interest in CLC. Similar to CLC, the reforming techniques under the chemical looping concept normally requires two inter-connected reactors, with an operating temperature usually above 973 K [112,113]. There are two schemes for employing chemical looping technology for the reforming of methane, or other hydrocarbons [13]. The first is to integrate reforming (*e.g*. with steam) process with chemical looping combustion (SR-CLC), as first proposed by Ryden and Lyngfelt [114]. In this process, SR of hydrocarbons to H_2-rich gas would take place in a tubular reactor through conventional catalytic

processes. It differs from conventional reforming by employing a CLC system to provide heat for the reformer (positioned inside a fluidised bed) externally. The reduced oxygen carriers were sent to an air reactor for re-oxidation, similar to conventional CLC. The second scheme is auto-thermal chemical looping reforming (a-CLR). The generation of H_2 from CH_4 by oxygen carriers takes place in the fuel reactor; and re-oxidation of the reduced oxygen carriers happens in a separate regeneration reactor. Instead of regeneration of the materials in air for CLC, CO_2 or steam is usually used for the re-oxidation as this helps improve the yield of H_2. Another advantage of using steam is that it allows high purity H_2 to be produced.

Compared to SR-CLC, a-CLR has the advantage of avoiding the need for a complex or extra unit to supply heat for the reforming process. However, it has high requirements for the oxygen carriers to be used. A good selectivity of oxygen carrier for the generation of H_2-rich gas is a crucial criterion for material screening. The commonly used oxygen carriers are not much different from those for CLC, mainly including Fe-, Cu-, Ni-, Mn-based metal oxides, and mixed oxides [115]. Ni-based oxygen carriers showed very high selectivity towards H_2-rich gas [116], which is similar to conventional SRM; whereas direct use of Fe-, Cu- and Mn- based oxygen carriers resulted in total combustion, giving mostly CO_2 and H_2O. It was found that the addition of a small portion of NiO (*i.e.* 1%) into Fe_2O_3 can significantly improve the yield of H_2 and CO [117]. Other than conventional oxygen carriers, some perovskites were also found to show promising results for the partial oxidation of CH_4, for H_2 and syngas production. Such perovskites include $La_xSr_{1-x}Fe_yCo_{1-y}O_{3-\delta}$, $La_xSr_{1-x}FeO_{3-\delta}$, $LaFeO_{3-\delta}$ and *etc*. [112]. As found in the study [112], the addition of a small amount of NiO (~ 5%) onto the perovskite structure was found significantly improved H_2 yield, similar to the synergistic effect of adding NiO to Fe_2O_3. On the other hand, the preparation of such perovskite structures is costly and time-consuming. The non-stoichiometry in the obtained samples is also very hard to control, which brings the difficulty in maintaining high homogeneity of bed materials from different batches.

In general, the production of H_2 from chemical looping reforming currently is under research stage, though intensive work on this has been ongoing. The application of this technology at an industrial scale still requires more effort. Most of the current research has been focused on material selection and preparation. Whilst, holistic understanding of the actual energy and financial cost for the application of such technology is important for determining the feasibility of the technology.

1.5.3 Plasma-involved processes for H_2 production from CH_4

Conventional thermo-catalytic technologies for H_2 production from CH_4 are more suited for large scale production due to the need of large equipment size or complex operating systems, and usually high metal/metal oxides capacity. For small and medium-scale H_2 production, other approaches could be more advantageous. In such a scenario, the concept of using plasma for hydrogen production becomes increasingly attractive. The application of plasma for H_2-rich gas production from CH_4 can be mainly classified into three categories: 1). direct cracking of CH_4; 2). reforming of CH_4; 3). partial oxidation of CH_4 [101]. For the first approach, plasma is used to directly dissociate CH_4 into H_2 and carbon black (soot). The H_2 can be collected, whereas the carbon in solid phase usually remains inside the reactor. This process results in CO_2-free gas products, and ideally the carbon black should be collected as a useful product.

Practically, complete collection of the solid carbon is difficult, especially when catalysts are employed to assist the cracking, leading to energy loss (in carbon) and deactivation of the catalyst. The accumulation of solid carbon inside the plasma reactor, depending on the form of carbon, can also be problematic. The accumulated carbon can potentially affect the electric field and consequently affect the formation of plasma. Furthermore, the highly endothermic nature of the cracking reaction, which requires a substantial amount of energy input, also limits the use of such scheme for H_2 production [118].

Compared to the direct decomposition of CH_4, the other two approaches, reforming and partial oxidation of CH_4 by plasma, have been studied to a wider extent, particularly in non-thermal plasma reactors, *e.g.* DBD reactors [101,119–122]. For the reforming process in plasma, it is essentially putting the conventional reforming of CH_4, either in CO_2 or steam, in a plasma-assisted reactor. The advantage of such process is that it allows the reforming process to happen at low temperature, where the selectivity towards H_2-rich gas is favored, but the reaction rate can be speeded up by plasma. The adoption of catalysts, usually solid particles, not only improves the conversion and H_2 production, but also helps easier formation and stabilisation of plasma. Tu *et al.* [123] studied dry reforming of methane (DRM) over a Ni/Al_2O_3 catalyst in a DBD reactor. The bed material fully packed the plasma discharge zone. It was found that by adding the catalyst pellets, the discharge mode switched from filamentary micro-discharge to predominant surface discharge on the catalyst surface (and a small zone of micro-discharges between the catalyst and the quartz wall). This change in the discharge mode should be beneficial as

it increases the chances of chemical interaction between the gas phase and solid surface. The breakdown voltage, which is the minimum voltage required for a system/substance to become conductive, also decreased significantly when the bed was fully packed. Besides, the use of Ni-based catalyst significantly improved the yield of H_2, giving an increased H_2/CO mole ratio from 0.84 to 2.53. Additionally, the presence of Ni was found to widen the distribution of discharge across the bed, suggesting the conductive Ni active sites help the spread and expand the discharge over the catalyst surface. When introducing the catalysts, the position of packed catalytic zone is also important. Wang *et al*. [124] at Tsinghua University studied the effect of three packing modes of the commercial catalyst Ni/Al_2O_3 in a DBD system for DRM from 573 to 773 K. The three contact modes were a): catalyst (fixed by quartz wool on the two sides) positioned in the downstream of the plasma discharge zone in the reactor, where the plasma discharge was not externally heated; b) catalyst positioned just next to the plasma discharge zone, where both the plasma discharge zone and the catalyst were externally heated; c) the catalyst zone and discharge zone fully overlapped each other and externally heated. The results showed that mode c) exhibited the best conversion of CH_4, as well as the selectivity to CO and H_2. Similar to conventional reforming approaches, carbon deposition was commonly found in reforming in DBD reactors. The group at Tsinghua University [119] further studied the effect of introducing steam into the CO_2 reforming of CH_4 in the DBD reactor, and found that the addition of steam helped reduce the degree of carbon deposition. They considered the removing effect due to the steam gasification of the solid carbon. On the other hand, the endothermic nature of the reforming process means that it also requires external energy input. The other drawback is that the use of a reforming gas (CO_2, or H_2O) causes burden on later separation process, and reduces the purity of H_2.

For the partial oxidation of CH_4 in similar non-thermal plasma reactors, where typically a gaseous oxygen stream is fed to the reactor, it exhibits the advantage of its exothermic nature of the oxidation process [101]. The need of a pure oxygen stream requires some oxygen-making process, and this increases the energy penalty. However, if the oxygen can be supplied for the oxidation of CH_4 from a solid, and the solids can be regenerated for the continuous or cycling production of H_2, this would be very promising for H_2 production. This is essentially a chemical looping system. Such a concept of a plasma-assisted chemical looping system for H_2 production is therefore proposed and demonstrated in Chapters 6, 7 and 8.

1.5.4 Hydrogen production techniques based on the splitting of water

H_2 production from fossil fuels, such as the SRM and chemical looping reforming of methane, always generates environmental emissions, such as CO_2. This leads to the need of looking for H_2 production from a clean and abundant resource, and this concept is known as 'green hydrogen production' [103]. Water, as a rich resource on the earth, can be a promising candidate. In the past several decades, there has been a large body of work on H_2 production from water splitting. The most mature technique that has been used is the water electrolysis. ~ 3.9% of the total H_2 production worldwide is from water electrolysis [125], and it is currently the most common industrial process for generating pure hydrogen [103]. Water is decomposed to H_2 and O_2 by an external circuit. Typical electrolysers for water electrolysis are solid oxide (SOE), alkaline (AE), and polymer electrolyte membrane electrolysers (PEME), where AE is the most mature technique and usually produces hydrogen with a purity over 99.8%. Catalyst such as platinum, are often adopted to improve the rate of electrolysis. The main limitation for expanding the application of this technology is its high cost. This not only comes from the electricity (which has probably come from a fossil fuel, and thus greener than expected) and the expensive catalyst, but also some pre-treatment process. The electrolysers are sensitive to the purity of water used, otherwise, side reactions would dominate in electrolysis. For this reason, purification prior to the actual electrolysis is required, leading to a significant increase in the operating cost of this technology [126].

Thermal decomposition of water, which uses heat to split water into H_2 and O_2, has also been studied for H_2 production. This approach requires extremely high temperature, which is normally above 2500 K, and only at above 3000 K is the decomposition significant (> 50% conversion of water) [127]. This brings technical difficulty for the separation of H_2 and O_2. The membranes for the separation cannot stand such high temperature, thus the mixed H_2 and O_2requires cooling before being separated. Materials, therefore, become the main constraint limiting the application of this technology. Another technique for water splitting for H_2 production is the S-I cycle, a thermochemical way for obtaining H_2 from water. The cycle requires following steps of R. 1-3 to R.1-6 [103].

$$H_2SO_4(aq) \xrightarrow{(573 \text{ to } 773 \text{ K})} H_2O(g) + SO_3(g) \qquad \text{R. 1-3}$$

$$SO_3(g) \xrightarrow{(1073 \text{ to } 1173 \text{ K})} O_2(g) + SO_2(g) \quad \text{R. 1-4}$$

$$SO_2(g) + I_2(g) + H_2O(l) \rightarrow HI(g) + H_2SO_4(aq) \quad \text{R. 1-5}$$

$$HI(g) \xrightarrow{\sim 700 \text{ K}} H_2(g) + I_2(g) \quad \text{R. 1-6}$$

A big advantage of S-I cycle it that it avoids the need for catalysts and separation membranes. It is operated at reasonable temperature range and requires low energy input. However, the technical and commercial viability needs further confirmation. There are many other water splitting techniques such as photocatalytic approach, high-temperature electrolysis, dark fermentation and *etc*. [103], where most of them are currently under R&D stage, with their practical application limited by the extremely high cost or low energy efficiency.

1.6 Objectives and structure of the dissertation

The aim of the dissertation was to investigate the conversion of various fuels in the presence of oxygen carries, so as to understand how the oxygen carriers would affect the conversion of fuels *in situ*. Depending on the type of fuels, the conversion techniques and so as the operating conditions could vary. For the solid fuels like coal char, as direct solid-solid reaction between the oxygen carriers and the fuel is impossible, a gasification step, or CLOU material is needed. Here, CO_2 gasification of a Polish coal-derived char was carried out prior to the reaction with the oxygen carriers. The focus of this study was on the influence of the oxygen carriers on the gasification rate. For biomass, as under thermal treatment (*i.e*. pyrolysis), multiple phases of products can be generated, and these include non-condensable gases (*e.g*. CO, CO_2, CH_4 *etc*.), condensable volatiles, and char. The non-condensable and condensable products usually react with the oxygen carriers directly. For biomass, as the composition of char is usually low and under such scenario, it is possible to employ oxygen carriers such as Fe_2O_3 to achieve good conversion of the pyrolysis products. For purely gaseous fuels such as CH_4, chemical looping combustion of CH_4 at operating temperatures at above 800°C have been studied to a wide extent including total combustion and chemical looping for H_2 production from CH_4 can be obtained. Lowering the operating temperature for the conversion of gaseous fuels by oxygen carriers becomes attractive in this case, particularly for H_2-rich gas production, where the forward water-gas shift reaction is favored, leading to more production of H_2.

This initiated the idea of using plasma-assisted system for the purpose of decreasing the operating temperature but still allows the chemical reactions to take place. This constitutes the second part (*i.e.* chemical looping conversion of fuels at mild temperatures, as presented in chapters 6, 7, and 8) of the dissertation. A plasma-assisted chemical looping system at mild temperatures for H_2 production from CH_4 was proposed and investigated. The aim was to have a system which

(1) could be operated at milder temperature (*e.g.* ≤ 773 K) than those for conventional H_2 production techniques,
(2) could achieve H_2 production in a single step,
(3) would run comparable energy penalty in reference to other existing H_2 production techniques (*e.g.* 320 to 510 MJ/kg for water electrolysis).

The structure of this dissertation is as follows. Chapter 2 illustrates the experimental set-up used in this work, and describes the methodologies of material preparation, experimental procedures and sample characterisation. Chapter 3 presents *in situ* CO_2 gasification of a Polish coal-derived char in the presence of Fe-based oxygen carriers. A kinetic model to describe the CO_2 gasification of the char was developed in Chapter 4. In addition to understanding the rate of char gasification by CO_2, Chapter 4 further investigated the inhibition effect of CO on CO_2 gasification. Chapter 5 focuses on understanding the effect of oxygen carriers (Fe_2O_3 and mayenite-supported CuO) on the distribution of products from biomass pyrolysis, and the effect of CO_2 on product distribution. For this work a new method of measuring tars was developed, making use of a plasma reactor in the sample line for tar conversion. Chapters 6 to 8 presents the investigation on the development of a plasma-assisted packed bed chemical looping system for H_2 production, wherein Chapter 6 focuses on understanding of the electrical signal of the developed plasma-assisted reactor, Chapter 7 focused on testing H_2 production with the developed system packed with $SrFeO_{3-\delta}$, a highly active chemical looping agent. Based on the preliminary results on Chapter 7, Chapter 8 further investigated H_2 production with the system packed with Fe-based and Ni-doped oxygen carriers. Finally, conclusions from the current work as well as recommendations for future work are drawn in Chapter 9.

2.0 Experimental methods

2.1 Introduction

The source of chemicals and gases used for experiments, methods for the preparation and characterisation of the materials, the apparatus employed for the research and typical experimental procedures are described in this chapter. Due to the wide range of experimental conditions used in this study, more detailed descriptions about individual experimental conditions and investigations are presented in corresponding chapters.

2.2 Preparation of materials

2.2.1 Sources and specifications of chemicals and gases

Lists of chemicals and gases with specifications are presented in Tables 2-1 and 2-2 respectively. The gases used were supplied by BOC.

Table 2-1 List of chemicals used with specifications from suppliers.

Molecular Formula	Specifications	Supplier
γ-Al_2O_3	3 mm pellets	Sigma-Aldrich
$Al(OH)_3$	Reagent grade, < 5 μm	Sigma-Aldrich
$CaCl_2$	≥ 97.0%, granulated	Sigma-Aldrich
$Ca(OH)_2$	≥ 98%, < 5 μm	Fisher Scientific
CuO	≥ 98%, < 10 μm	Sigma-Aldrich
C_2H_5OH	≥ 99.8%	Fisher Scientific
Fe_2O_3	> 95 wt%, < 10 μm	Fisher Scientific
$Fe(NO_3)_3 \cdot 9H_2O$	ACS reagent, ≥ 98 wt%	Sigma-Aldrich
HNO_3	≥ 99.5%	Sigma-Aldrich
H_2O (de-ionised)	< 1μs/cm	Using Pure Lab Prime purifier (ELGA Lab water)
NaOH	Pellets, extra pure	Sigma-Aldrich
$Ni(NO_3)_2 \cdot 6H_2O$	≥ 98.5%	Sigma-Aldrich
$SrCO_3$	≥ 98%	Sigma-Aldrich
$Zr(OH)_4$	> 97 wt%	Sigma-Aldrich

Table 2-2 List of gases used with grade information from BOC.

Gas species	Specification
Air	≥ 99.995%
N_2	≥ 99.998%
Ar	≥ 99.998%
CH_4	≥ 99.5%
5 vol% H_2 in N_2	≥ 99.999%
CO_2	≥ 99.90%
10 vol% CO in N_2	≥ 99.99%

2.2.2 Preparation of materials

- **Chemicals and sand**

Information regarding the materials used in this work including oxygen carriers, fuels and various sand is described in this section. Synthesis of oxygen carriers used methods including mixing, dry-impregnation and co-precipitation.

Fe_2O_3

Fe_2O_3 particles were prepared by solid mixing. It started from the granulation of Fe_2O_3 powders using de-ionised (DI) water as a binder, with a mass ratio of 10:1 for Fe_2O_3 powder to DI water. After mixing in a commercial mixer, the resulting granules were sieved to appropriate size and calcined in air at 1273 K for 6 h in air. Information on the exact fraction size is presented in appropriate sections.

Mayenite-supported CuO

Wet mixing approach was employed to prepare mayenite-supported CuO, following the protocol described by Hu *et al*. [128]. Typically, 5.61 g of $Ca(OH)_2$ and 8.85 g of $Al(OH)_3$ powders were mixed with 200 ml of DI water in a 1 L beaker. The resulting slurry was stirred on a hotplate at 313 K for 2 h. 15.00 g of CuO powder was then added to the mixture. Further mixing for 20 h was performed, and the obtained mixture was dried in ventilated air at 353 K for 48 h. The dried cake was then crushed and calcined in air at 1273 K for 6 h. The obtained granules were finally sieved to 355 - 425 μm. The resulting mayenite-supported CuO particles contain 60 wt% CuO, 23 wt% Al_2O_3, and 17 wt% CaO.

ZrO_2

ZrO_2 particle was prepared from zirconium (IV) hydroxide $Zr(OH)_4$. $Zr(OH)_4$ powder was firstly wetted and bound by DI water. The mass ratio of $Zr(OH)_4$ to DI water was about 1:4 (*i.e*. 20 g $Zr(OH)_4$ requires around 80 ml DI water). The mixture was agitated with a magnetic stirrer at 353 K for 30 minutes, until a relative homogenous state was observed. The temperature was then increased to 393 K for 4 h to remove the water. Simultaneously, agitation was maintained to avoid phase separation. The resulting $Zr(OH)_4$ was dried (without agitation) at 393 K for another 5 h, followed by calcination in air at 1273 K for 6 h. $Zr(OH)_4$ would decompose into H_2O and ZrO_2 at temperatures above 773 K [129].

Therefore, ZrO_2 particles were obtained and finally sieved to a size fraction of 180 μm - 355 μm.

NiO/Fe_2O_3 and $NiFe_2O_4/Fe_2O_3$

Dry-impregnation method was used to prepare NiO/Fe_2O_3 and $NiFe_2O_4/Fe_2O_3$. Nickel nitrate hexahydrate, $Ni(NO_3)_2 \cdot 6H_2O$, was mixed with Fe_2O_3 (prepared from solid mixing, with particle size of 600 - 850 μm), followed by the addition of DI water to just dissolve the nitrate. The resulting mixture was stirred at 313 K for 20 min, followed by drying at 398 K for 12 h. The dried mixture was then calcined in air at 823 K for 5 h to form NiO/Fe_2O_3, or at 1123 K for 5 h to produce $NiFe_2O_4/ Fe_2O_3$. In both cases, the molar ratio of Ni to the total metal (*i.e.* Ni + Fe) was about 1: 10.

Al_2O_3, Ni/Al_2O_3 and NiO/Al_2O_3

The preparation of Al_2O_3 started with γ-Al_2O_3 pellets being crushed to a size fraction of 600 - 850 μm. The resulting particles were then calcined in air at 1273 K for 6 h. The preparation of NiO/Al_2O_3 followed the same protocol (*i.e.* dry-impregnation) as that for NiO/Fe_2O_3. The prepared NiO/Al_2O_3 was divided into two equal portions. One portion was used as prepared, *i.e.* NiO/Al_2O_3. The other portion was reduced in 5 % H_2 at 1073 K for 30 min to obtain Ni/Al_2O_3. Similarly, the resulting Al_2O_3-supported Ni-based particles had a sieve size of 600 - 850 μm, with a Ni to total metal molar ratio of 1: 10.

$SrFeO_{3-\delta}$ and $NiO/SrFeO_{3-\delta}$

$SrFeO_{3-\delta}$ was prepared *via* solid mixing. Stoichiometric amounts of $SrCO_3$ and Fe_2O_3 (0.72 mol and 0.36 mol respectively, molar ratio of 2:1) were mixed, and followed by the addition of ethanol, C_2H_5OH, as a binder to improve mixing. The resulting mixture was then ball milled for 3 h at 25 Hz, followed by drying in air at 323 K for 24 h. The resulting particles were calcined in air at 1273 K for 19 h. The preparation of $NiO/SrFeO_{3-\delta}$ followed the dry-impregnation method as for NiO/Fe_2O_3 and NiO/Al_2O_3. The obtained particles were sieved to 600 – 850 μm with a Ni to total metal molar ratio of 1:10.

ZrO_2-supported Fe_2O_3

ZrO_2-supported Fe_2O_3 containing 65 wt% Fe_2O_3 and 35 wt% ZrO_2, was prepared by co-precipitation method. Zirconium (IV) hydroxide power, $Zr(OH)_4$, was firstly 'dissolved' in deionised water at 343 K for about 10 minutes to form 0.1 M $Zr(OH)_4$ solution/dispersion. Around same volumetric amount of 0.5 M nitric acid was slowly added into $Zr(OH)_4$ dispersion. The dispersion was agitated at 343 K for 2 h. $Fe(NO_3)_3 \cdot 9H_2O$ was then added into the acidic solution (pH = 0.5). NaOH was later added to the solution of nitrates, resulting in precipitates formed in a pH environment of 9.8 $\pm$ 0.2. The precipitate was stirred for a further 10 minutes, before aging at room temperature without stirring for another 2 h. Afterwards, the precipitate was washed with DI water until its ionic conductivity fell below 100 μScm^{-1}, and pH to around 7 to eliminate the presence of free Na^+. Then the precipitates were dried in air at 383 K for 40 h. The dried cake was calcined at 1273 K for 6 h, followed by crushing and sieving to the desired particle size fraction (180 - 355 μm).

Silica and alumina sand

Both the received silica sand and alumina sand were washed with DI water, followed by drying at 353 K for 24 h. The particles size fraction for use were 250 - 350 μm for silica sand, and 355 – 425 μm and 600 – 850 μm for alumina sand (for appropriate use).

The material and bulk densities of each material were measured. The bulk density was determined from the weight of a known volume of material. To obtain the material density, the voidage was measured by slowly adding water to a packed bed of sample just to the surface and recording the volume of water added.

- **Solid fuels**

Polish coal-derived char

The coal char was derived from a Polish coal, a brown lignite coal, kindly provided by Institution for Chemical Processing of Coal. Proximate and ultimate analysis data are provided by the institution, as presented in Tables 2-3 and 2-4.

Table 2-3 Proximate analysis of the coal.

	ad (air-dry) wt%	daf (dry ash free) wt%
Moisture	14.0 + 0.1	-
Volatile	38.09 + 0.17	53.35 + 0.25
Fixed carbon (balanced)	43.31	-
Ash	14.6 + 0.2	-
Higher heating value (HHV)	18466 ± 83 kJ/kg	
Lower heating value (LHV)	17471 ± 101 kJ/kg	

Table 2-4 Elemental analysis.

Element	wt%
Carbon	48.4 ± 0.6
Hydrogen	2.99 ± 0.27
Nitrogen	0.56 ± 0.15
Oxygen	19.9 ± 0.69
Sulphur	0.9 ± 0.04

The received Polish coal was air dried for 48 h, followed by mechanical size reduction and sieving to size fraction of 1000 - 2240 μm. Then, the char-making process was carried out in a stainless-steel reactor (illustrated in Fig. 2-1.), fed with 1 L alumina sand (350 - 425 μm, with a material density of 3950 ± 70 kg/m^3) as the fluidising bed. N_2 was used to fluidise the bed at a flow rate of around 300 ml/s (all the flow rates in this thesis are expressed at 293 K and 1 atm). The superficial gas velocity was ~ 0.27 m/s, with a ratio of superficial velocity to minimum fluidising velocity, U/U_{mf}, of ~ 4.8 (refer to 2.3.1 for the determination of U_{mf}). The bed was operated at 1173 K, and the sieved coal was continuously fed into the reactor at a feeding rate of 200 mg/s. The produced volatiles from the reactor were burned in ambient air by a burner, which was positioned above the top of the reactor, as shown in Fig. 2-1. The whole feeding process took about one hour, and the reactor was maintained at 1173 K for another hour to keep relative homogeneity of the solid product. The reactor was then cooled down to ambient temperature in flowing N_2. The obtained coal char was sieved into desired size fractions including 300 – 425 μm, 425 - 600 μm, 600 - 850 μm, and 850 - 1180 μm. They are stored in sealed bottles and chances of contact with air before use were minimised.

Wood pellets

The received wood pellets were crushed and sieved to a size fraction of 4.0 - 4.2 mm. They were air dried at ambient environment for 24 h prior to use. The elemental analysis results of the wood sample are presented in Table 2-5.

Table 2-5 Elemental analysis.

Element	wt%
Carbon	46.33
Hydrogen	6.12
Nitrogen	0.00
Oxygen (balanced)	47.55

2.3 Apparatus

Experimental set-ups employed and developed include a stainless-steel fluidised bed reactor, a quartz tube fluidised bed reactor, a quartz tube fluidised bed coupled with plasma reactor in the downstream, and a plasma-assisted packed bed reactor. The configurations, and experimental procedures for running each set-up, are described below.

2.3.1 Stainless steel fluidised bed reactor

An electrically-heated, stainless-steel (316) fluidised bed reactor was used for the preparation of the coal-derived char at 1173 K. Figure 2-1 is a schematic diagram of the set-up. The stainless-steel tube (i.d. 78 mm, 1130 mm in height), loaded with 1 L alumina sand, was surrounded by electrical heating coils, which were PID controlled *via* a K-type thermocouple immersed in the fluidised bed. N_2 for fluidisation passed through a windbox, a distributor with 37 evenly distributed identical holes (diameter of 0.4 mm), and then to the main body of the bed. An electrical feeder was housed to the top of the tube to feed the coal continuously. A slotted lid with two holes (*i.e.* one allowing products, and the other for thermocouple to go through), sited on the top of the reactor. A burner was positioned above the top of the reactor to burn off any volatiles, before their entering the extraction system.

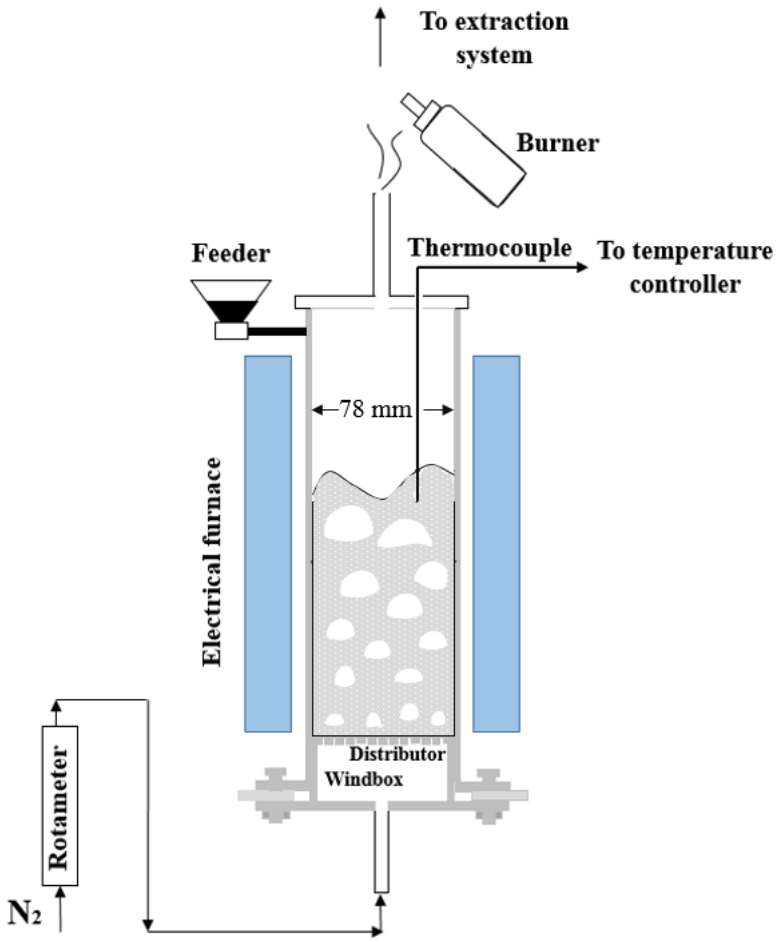

Figure 2-1 Set-up of the stainless steel fluidised bed reactor.

2.3.2 Quartz tube fluidised bed reactor

An open-ended quartz tube fluidised bed reactor was used for the investigation of the gasification of the Polish coal-derived char in various bed materials, as well as the study of the CO inhibition effect on the char gasification. A diagram describing the set-up is shown in Fig. 2-2. The quartz tube (i.d. 29 mm), with a porous distributor, was loaded with appropriate solid materials (silica sand, Fe_2O_3 or ZrO_2-supported Fe_2O_3) and externally heated by an electrical furnace. The temperature of the bed was measured by a K-type thermocouple, operated by a PID controller. Flows of gases (N_2, Air, CO or/and CO_2) were controlled by rotameters and solenoid valves (allow for an easy switching of the gases) controlled to enter the quartz reactor. Char sample was introduced from the top of the reactor in batch. The gas at the reactor outlet was sampled and dried by $CaCl_2$ before entering the gas analyser, Fourier transform infrared (FTIR, Perkin Elmer 100) analyser.

For a typical gasification experiment, 20 ml solid particles (silica sand, Fe_2O_3 or ZrO_2-supported Fe_2O_3) were fed into the reactor in cold. The reactor was then heated up to the desired operating temperature (from 1123 to 1248 K). The bed in the heating up stage was fluidised by air at 50 ml/s. As the operating temperature was reached, the fluidising gas switched from air to N_2 at the same flow rate for 5 min to remove potential oxygen. This was followed by gas switching to the gasification agent, CO_2, at a volumetric concentration from 20% to 100% (balance N_2), at a total flow rate of 50 ml/s. For the investigation of the effect of CO on the gasification of Polish char, the fluidising gas changed from N_2 to a mixed gas stream of 20% CO_2 and various CO concentrations (balance N_2), with other conditions being the same. The fluidised bed was expected to operate in a bubbling regime. The minimum fluidisation velocity of the bed, U_{mf}, was estimated from the correlation provided by Wen and Yu [130]:

$$Re_{mf} = \sqrt{1135.7 + 0.0408\, N_{Ga}}\text{-}33.7.$$

Where the Reynolds number, Re_{mf} is a function of the minimum fluidisation velocity, U_{mf}, the particle diameter, d_p, the dynamic viscosity, μ, and the density of the fluidising gas, ρ_f:

$$Re_{mf} = \frac{\rho_f U_{mf} d_p}{\mu}$$

and the Galileo number, N_{Ga}, is obtained by

$$N_{Ga} = \frac{{d_p}^3 \rho_f (\rho_s - \rho_f) g}{\mu^2},$$

where the ρ_s represents the density of the solid particles and g is the acceleration due to gravity. The particles used here were 250 – 355 μm for silica sand, 180 – 250 μm for Fe_2O_3 and ZrO_2-supported Fe_2O_3, with corresponding particle densities of 2600 $\pm$ 50 kg/m^3, 2800 $\pm$ 60 kg/m^3, and 2160 $\pm$ 80 kg/m^3. The diameter of the particles, d_p, used for obtaining U_{mf} was taken as the mean average of the upper and lower limit of the sieve size. The resulting ratios of the superficial velocity to the minimum fluidisation velocity, U/U_{mf}, were between 6.6 - 9.0, for different materials under various operating temperatures. The dynamic viscosity and density of the fluidising gas at temperatures up to 1248 K were extrapolated from NIST Chemistry WebBook [131].

Typically, 0.04 g Polish char, with a particle size fraction of 600 - 850 μm, was dropped to the fluidised bed from the top. This much larger char size (than those for the fluidising

bed particles) allowed easy separation of bed materials from remaining char ash. [CO] and [CO_2] were measured by FTIR. The whole gasification time allowed for completion under various conditions was between around 900 s to over 3000 s, depending on the gasification temperature and the type of the solid particles in bed. The response time of the sampling system and the analyser, defined as the time taken to respond from 5% to 95% of a full step change, was 3 s, negligible when compared to the gasification time needed here.

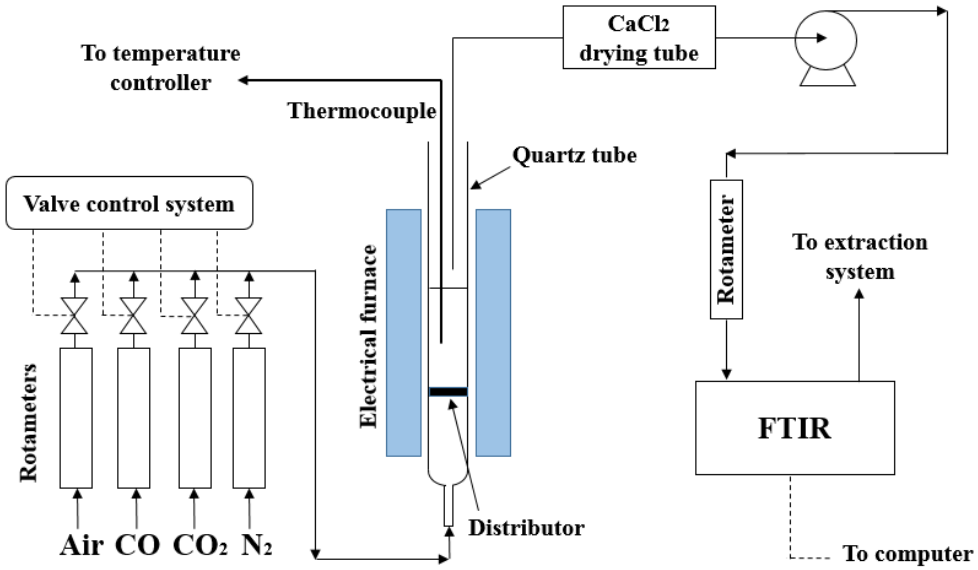

Figure 2-2 Set-up of the quartz tube fluidised bed reactor.

2.3.3 Quartz tube fluidised bed reactor coupled with a plasma reactor

The investigation of the processing of biomass (wood pellets) in the presence of alumina sand and oxygen carriers of 355 - 425 μm, was carried out in a fluidised bed reactor, coupled with a dielectric barrier discharge (DBD) reactor in the downstream for online quantification of tar produced from the upstream. The material density values were 3950 ± 70 kg/m_3 for alumina sand, 2900 ± 100 kg/m^3 for Fe_2O_3, and 2000 ± 80 kg/m^3 for mayenite-supported CuO. The effect of CO_2, *i.e.* 18% CO_2 (balance N_2), on the product distribution from thermal treatment, which is essentially the gasification of the wood, was also investigated in the same set-up. Figure 2-3 presents a schematic diagram of the set-up. The fluidised bed is the quartz tube reactor as described in 2.3.2. The gaseous product from the fluidised bed was sampled to the DBD reactor. The sampling line from the fluidised bed to the DBD reactor, together with the DBD reactor, was externally heated by heating tapes (Omega, STH051) to prevent any tar condensation. A trap, immersed in

ice water and consisting of a tube packed with $CaCl_2$ and ceramic beads, and plugged with glass wool at each end (not shown in Fig. 2-3), was placed after the DBD reactor, before the pump to trap tar and water. The gas was then analysed by a FTIR (ThermoFisher Scientific, NICOLET iS10) and a paramagnetic oxygen analyser (ABB, EL3020).

The configuration of the DBD reactor (cross sectional view) is shown in Fig. 2-4. It consisted of two metal electrodes, with the high voltage electrode being a stainless-steel rod (diameter of 25.0 mm, length of 80 mm) and the ground electrode being a stainless-steel tube (i.d. 36.0 mm), and a dielectric quartz tube (i.d. 26.0 mm, o.d. 30.0 mm). The quartz tube just covered the inside high voltage electrode, resulting a gap (3.0 mm) between the outer surface of the quartz tube and the inner surface of the ground electrode, to allow the sampled gas to flow through. The 80 mm long, and 3.0 mm gap regime was where plasma was regenerated. The DBD reactor was sealed by two Teflon end-caps, which also provided electrical insulation and support for the electrodes. Alternating voltage ranging from 13.2 to 15.2 kV (peak to peak) at a frequency of ~ 22 kHz was supplied to generate plasma *via* a plasma generator (PVM500-2500, Information Unlimited). The determination of the dissipated plasma power in the DBD reactor was described below.

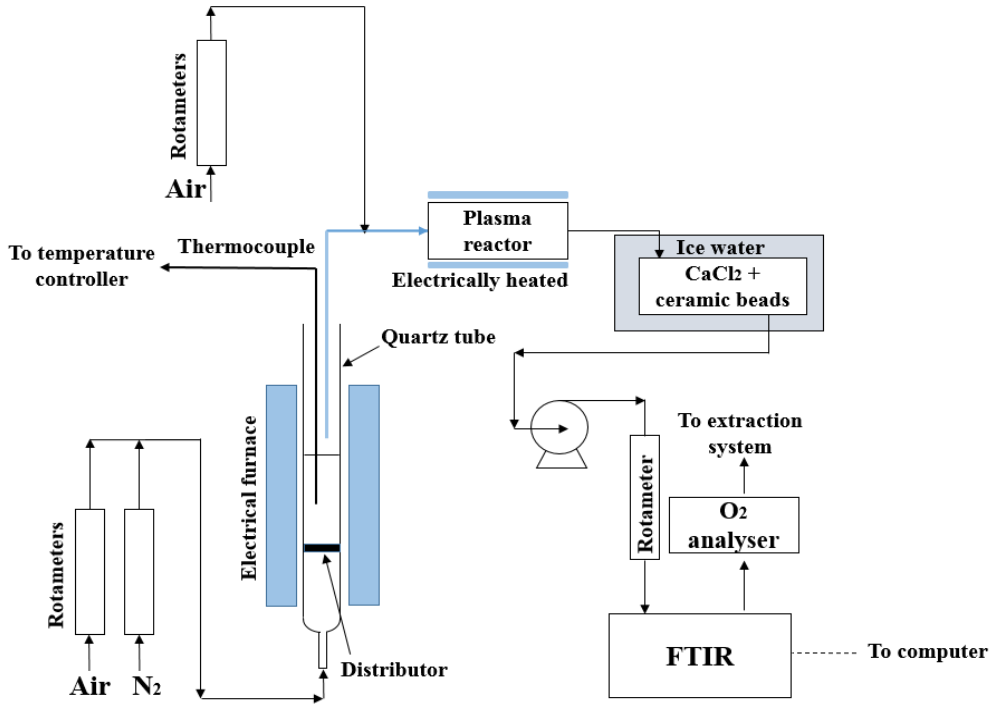

Figure 2-3 Set-up of a quartz tube fluidised bed reactor coupled with a plasma reactor in the downstream for the quantification of tar from upstream.

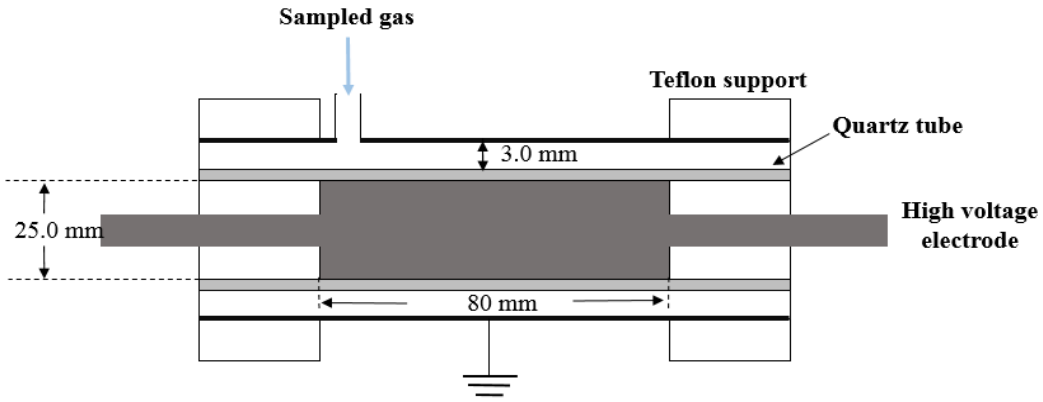

Figure 2-4 Configuration of the plasma reactor for the quantification of tar from upstream.

Specific energy density (SED) was used to characterise the density of plasma energy within the reactor and is given by

$$SED = \frac{P}{Q},$$

where P is the power input (W), Q is the gas flow rate (L/s) passed through the reactor. The power input is related to the frequency f of the ac supply by

$$P = E \times f.$$

The energy input per cycle E is [93]

$$E = \int_0^t V(t)\, I(t)dt = \int_0^t V(t)dq,$$

where $V(t)$ is the voltage and $I(t)$ is the current. Thus, the power can be determined from the V-q Lissajous diagram. The voltage was measured using a high voltage probe (TESTEC, 1000:1, 30 kV, 50 MHz) with the sensing head connected to the high voltage electrode. The charge was obtained from the voltage (Tektronix probe, P6015A, 1:1) across a 1 μF capacitor, connected in series between the reactor ground electrode and earth. Both the voltage and charge signals were collected simultaneously using an oscilloscope (Tektronix, TDS 3012) in X-Y mode. Figure 2-5 is a typical V-q Lissajous curve from one experiment. The energy input was obtained by taking the area enclosed by the curve.

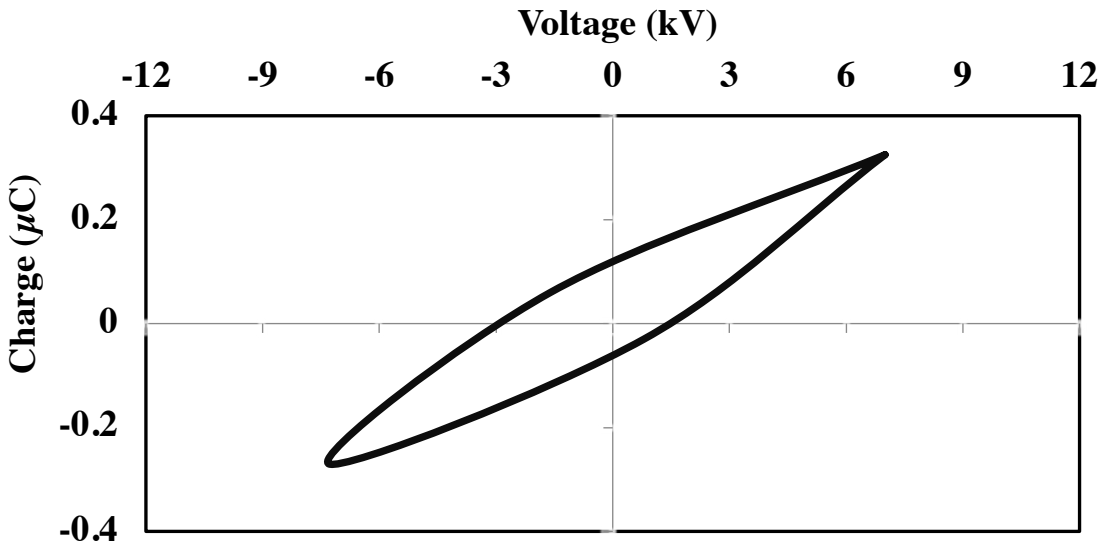

Figure 2-5 *V-q* Lissajous plot from a typical experiment, with frequency of 22 kHz, and voltage 14.4 kV with the DBD reactor described in Fig. 2-4. This typical plot was obtained with the fluidised bed operated at 873 K, with mayenite-supported CuO as the bed and N_2 as the fluidising agent. The sampled stream was diluted by air before entering the DBD reactor.

For a typical experiment, the fluidised bed was loaded with 20 ml of bed material (*i.e.* alumina sand, Fe_2O_3, or mayenite-supported CuO), and fluidised by pure N_2 at a flow rate of ~ 3 L/min. The temperature of the bed varied from 773 to 1173 K, giving a U/U_{mf} of 1.7 to 3.4 in alumina sand, 3.0 to 5.8 in mayenite-supported CuO, and 2.2 to 4.3 in Fe_2O_3. The air stream entering the sampling line was set at 0.45 L/min, and the total flow rate of the sampling line was set at 0.90 L/min. The temperatures of the sampling line and the DBD reactor were kept at 573 K and 523 K, respectively. After each experiment, the fluidising gas was switched from N_2 to air to burn off the char (produced from in N_2). Any produced CO and CO_2 from the burn-off was measured to quantify the char. For every experiment, 0.0538 $\pm$ 0.0004 g of wood was fed. Sufficient bed material was provided in each batch experiment to allow full conversion of the carbon content in wood to CO_2, assuming Fe_2O_3 was reduced to Fe_3O_4, or CuO to Cu_2O. The duration of the experiment was set to be equal to the pyrolysis time for the fuel, assuming that this can be determined by noting when CH_4 was no longer detected. Each experiment was repeated three times. For the experiments using 18% CO_2 as the fluidising agent, alumina sand was used as the bed material, whilst all other conditions were kept identical.

The quantification of the tar produced from the fluidised bed, was carried out by taking the difference in the signals from the FTIR between two runs: with the plasma on, and off, meaning that two separate experiments were performed with other conditions being the same. Here, tar was defined as any carbon-containing gaseous species except CO, CO_2 and CH_4. The aim was to develop a method to allow the total quantification of tar; whilst the composition of the tar can be of interest, it was not a focus of the current study. The difference in signals of CH_4, CO and CO_2 with plasma either on or off was used to account for the carbon content in the tar being burned in the plasma. To obtain a real-time signal would require two sampling lines in parallel, one with plasma and one without. Here, for the sake of proof of principle, only one sampling line was used and the experiment repeated to allow the difference to be determined. Assuming that tar can be converted to CO, CH_4 and CO_2 completely, the amount of carbon in the tar entering the sampling system is given by:

$$m_{\mathrm{C,tar}} = \sum_{i=\mathrm{CO,CO_2\ or\ CH_4}} m_i^{on} - \sum_{i=\mathrm{CO,CO_2\ or\ CH_4}} m_i^{off},$$

where m_i^{on} and m_i^{off} are respectively the mass of carbon in the carbon-containing species *i* (CO, CO_2 or CH_4) that enters the sampling system with the plasma being on or off, respectively. Here, m_i^{on} and m_i^{off} were determined by taking the integral of the rate of species *i* that enters the sampling system and detected by FTIR, with plasma running $R_i(t)$ over pyrolysis time from t_0 to t_a:

$$m_i = \int_{t_0}^{t_a} R_i(t)\, dt.$$

The above equation gives the mass of carbon entering the sampling system over the duration of an experiment. To obtain the total amount of carbon in each species, for instance in tar, the ratio of the total gas flow rate in the fluidised bed, F_{FB}, to the flow rate into to the sampling line F_{sampling} was used:

$$M_{\mathrm{C,tar}} = m_{\mathrm{C,tar}} \times \frac{F_{\mathrm{FB}}}{F_{\mathrm{sampling}}},$$

where $M_{\mathrm{C,tar}}$ is the total amount carbon in the tar produced in the fluidised bed.

Following each experiment, the residual amount of carbon remaining in the bed was measured by burning off in air. The carbon balance was calculated by:

$$m\,\% = \frac{(\sum_i m_i^{off} + m_{\mathrm{C,burn-off}} + m_{\mathrm{C,tar}}) \times \frac{F_{\mathrm{FB}}}{F_{\mathrm{sampling}}}}{M_{\mathrm{C,total}}} \times 100\%$$

$$M_{\mathrm{C,total}} = M_{\mathrm{wood,total}} \times x_{\mathrm{C}},$$

where $M_{\mathrm{wood,total}}$ is the total mass of wood fed into the FB, and x_{C} is the weight fraction of elemental carbon in the wood. $M_{\mathrm{C,total}}$ is the total carbon content in the wood fed. $m_{\mathrm{C,burn-off}}$ is the amount of carbon in the char determined from air burn-off, after pyrolysis time t_a:

$$m_{\mathrm{C,burn-off}} = \int_{t_a}^{t_b} R_{\mathrm{co,burn-off}} + R_{\mathrm{co_2,burn-off}}\, dt,$$

where $R_{\mathrm{co,burn-off}}$and $R_{\mathrm{co_2,burn-off}}$ are the rates of production of CO and CO_2 (expressed as equivalent mass of carbon and corrected for dilution in the sampling system) during burn-off from $t_a$to t_b.

The yield of gaseous species i, Y_i, of tar, Y_{tar}, of char, Y_{char} can be calculated respectively from:

$$Y_i = \frac{m_{(\mathrm{i,off})} \times \frac{F_{\mathrm{FB}}}{F_{\mathrm{sampling}}}}{M_{\mathrm{C,total}}}$$

$$Y_{\mathrm{tar}} = \frac{M_{\mathrm{C,tar}}}{M_{\mathrm{C,total}}}$$

$$Y_{\mathrm{char}} = \frac{m_{(\mathrm{C,burn-off})\times\frac{F_{\mathrm{FB}}}{F_{\mathrm{sampling}}}}}{M_{\mathrm{C,total}}}.$$

2.3.4 Plasma-assisted packed bed reactor

A DBD-plasma-assisted packed bed reactor was developed and used for the investigation of H_2 production from CH_4 in a plasma-assisted chemical looping system. Figure 2-6 illustrates the designed set-up, where a quartz tube (i.d. 25.0 mm, o.d. 28.0 mm) acted as the reactor as well as a part of the dielectric material between the two electrodes. A co-axial stainless-steel rod (diameter of 12.0 mm) within the quartz tube formed the high voltage electrode (supported by a cap and the distributor of the quartz tube). A stainless-steel mesh wrapped around the outer surface of the quartz tube, formed the ground electrode, enclosing a height of 20 mm. The gap between the quartz tube and the high voltage rod surface (6.5 mm) was the plasma discharge zone, packed with the oxygen carriers (a volume of 7.5 ml), where the packing is also part of the dielectric material. The system was operated at atmospheric pressure, and externally heated. Ac power was supplied to the DBD reactor and the applied voltage, frequency and plasma power can be

obtained *via* an oscilloscope, as described in 2.3.2. The gas (pure CH_4, pure Ar, mixed stream of CH_4 and Ar, or air depending on specific experiment) inflow entered the bed from the bottom of the reactor at an appropriate flow rate (refer corresponding chapters for the exact values), low enough to prevent fluidisation. In some experiments, the emitted ultraviolet and visible (UV-Vis, 200 to 800 nm) light from excited species was measured by an UV-Vis spectrometer (HAMAMATSU, TM-UV/VIS: C10082CA). An optical fibre was positioned inside the quartz tube reactor above the plasma region, where the UV-Vis light can be captured, but not too close to affect the plasma activity. The signal transferred through the fibre to the spectrometer. The sampled gas from the DBD reactor was dried before entering the analysers. For the experiment with pure CH_4 as the gas inflow, an extra N_2 dilution stream was mixed with sampled gas, resulting a stream of ~ 20% CH_4 in N_2 (refer to Fig. 2-6 and Chapter 6, 6.2.2). H_2 and O_2 were measured by a thermal conductivity analyser (ABB, Caldos27) and a paramagnetic oxygen analyser (ABB, magnos206), respectively. Other carbon-containing gas species were measured by a FTIR (MKS Instruments - MultiGas™) analyser. To minimise the flammability of the flue gas from the set-up, it was burned in Bunsen burner before entering the extraction system.

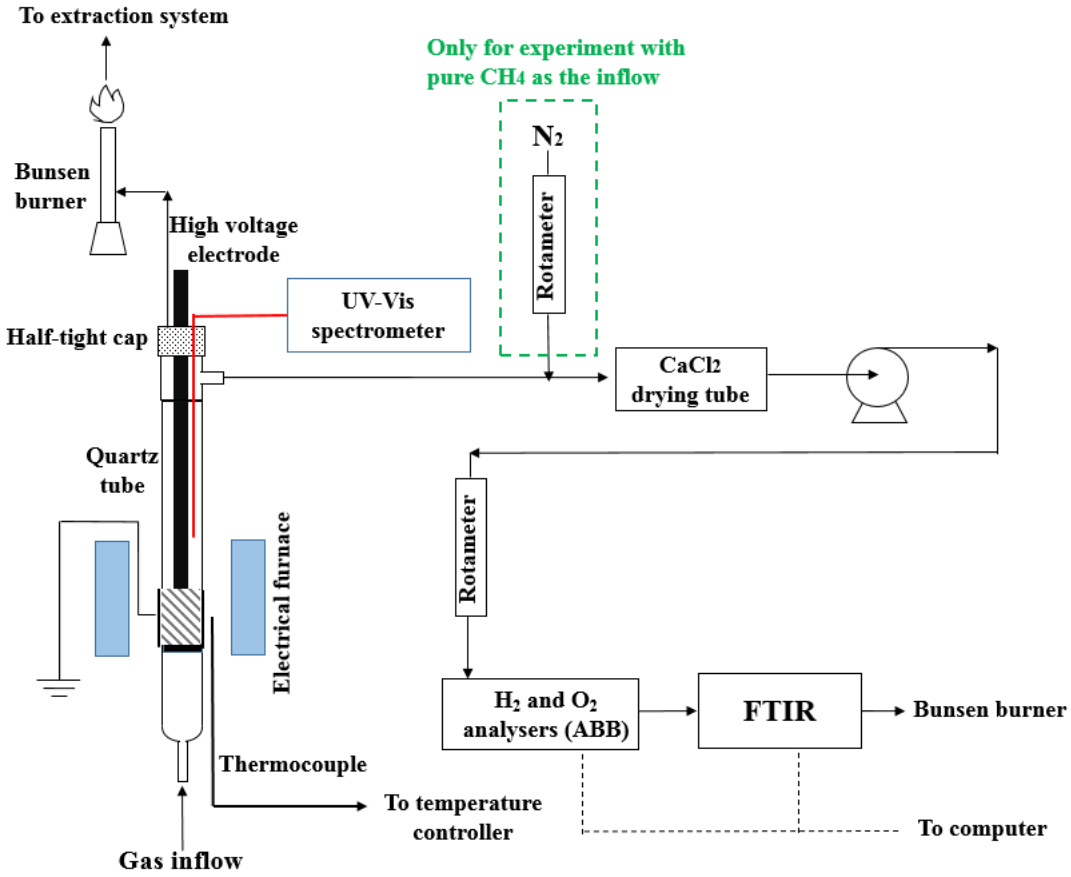

Figure 2-6 Set-up of the plasma-assisted oxygen carrier-packed bed reactor for H_2 production.

2.4 Characterisation of the materials

2.4.1 Analysis by X-Ray Powder Diffraction (XRD)

XRD analysis was performed using an Empyrean PANalytical diffractometer. A typical diffractogram was collected in the range of 2θ, which is defined as the angle between the incident beam and the detector, from 5° to 80° using Cu K_α radiation with a voltage of 40 kV and current of 40 mA, providing X-rays with characteristic wavelengths at 1.5406 Å and 1.5444 Å with an intensity ratio of 2:1. In a typical scan, the size of the samples were reduced to below 50 μm by manual grinding with a mortar and pestle. The powder was carefully packed into and filled full a sample holder disc to produce a flat surface, before being loaded into the diffractometer. The diffractometer was set up in a Brag-Brentano geometry where the sample was fixed, whilst both the source and the detector rotated along the goniometer circle simultaneously. The scan step size was 0.0167°, with a continuous scan speed of 0.0278 °/s. The spectra obtained were manually compared with those from Inorganic Crystal Structure Database (ICSD) as a primary approach for

phase identification, together with the use of the software Material Analysis Using Diffraction (MAUD) as an auxiliary method (for confirmation).

2.4.2 SEM-EDX

The surface and internal morphologies, together with the determination of chemical elements of samples, were studied using scanning electron microscope with energy dispersive X-ray spectroscopy (SEM/EDX). The analysis was performed with TESCAN MIRA3 FEG-SEM combined with Oxford Instruments Aztec Energy X-maxN 80 EDS system at an accelerating voltage of 15 kV, working distance of 14 mm and 1000x magnification.

2.4.3 Brunauer-Emmett-Teller (BET) and mercury intrusion porosimetry (MIP)

The surface area and pore size distribution of the samples were measured by a TriStar 3000 (Micrometrics, Series No. 1001) gas adsorption analyser. In a typical analysis, sample particles were firstly degassed in vacuum at room temperature. This was followed by N_2 purging into the sampling chamber isothermally at 77 K, with the absolute pressure increasing from 0.01 to 1 bar. Then the gas was withdrawn to a pressure of 0.14 bar. The amount of N_2 adsorbed and desorbed was recorded as a function of pressure. The specific surface area of the particles was then estimated using the Brunauer-Emmett-Teller (BET) theory [132]. The pore size distribution and volume (for pore size smaller than 200 nm) were calculated from the Barrett-Joyner-Halenda (BJH) model [133]. Alternatively, the pore-related parameters including pore size and volume are also measured by MIP. Characterisation of the porosity by this method is achieved by applying a pressure to a sample that is immersed in mercury. The measurement was performed in an AutoPore IV 9500 Automated Mercury Porosimeter. In a typical test, the injection pressure was raised from 0.10 to 60000.00 psia (0.007 to 4136.854 bar). The contact angle, surface tension, and density for Hg in these tests were 130°, 0.485 N/m and 13.54 g/mL, respectively.

3.0 *In situ* CO_2 gasification of a Polish coal-derived char in the presence of Fe_2O_3-based oxygen carriers

3.1 Introduction

As outlined in Chapter 1, CLC of solid fuels requires either (1) CLOU oxygen carriers, or (2) a separate gasification step prior to the combustion of the gasification products by conventional CLC oxygen carriers. The latter approach can be carried out *in situ* or *ex situ*. *In situ* CO_2 gasification of a Polish coal-derived char in a fluidised bed reactor in the presence of typical Fe_2O_3-based oxygen carriers is studied in this chapter. The presence of oxygen carriers on CO_2 gasification of a Polish char is to be understood. Saucedo *et al*. [14] carried out an experimental and numerical modelling study on the effect of Fe_2O_3 on the gasification of a German lignite char. Their results showed a much-improved rate of CO_2 gasification in the presence of Fe_2O_3, compared to the gasification in inert sand, as shown in Fig. 3-1. The gasification of the lignite char itself was found to be limited by external mass transfer. The improved gasification rate was explained by assuming that the Fe_2O_3 removed the inhibition effect of CO on gasification by removing the accumulated CO on the char particle surface *via* combustion. The re-generated reagent (from combustion of CO by Fe_2O_3), CO_2, improved the surface CO_2 concentration, and thus positively influenced the gasification. The current research investigates the effect of oxygen carries on another type of char, and hopefully free of external mass transfer limitation. Extrapolating the results by Saucedo *et al*., for a solid fuel free of external transfer limitation, the oxygen carriers should not influence the char gasification step, given that catalytic effect of the oxygen carriers is insignificant. The aim of this research is to verify the mechanism for the fuels without mass transfer limitation.

Figure 3-1 Gasification of Hambach lignite coal, m_{batch} ~ 0.15 g, d_p= + 710, -1000 μm in 12.5 mol% CO_2, balance N_2, at 1073, 1123 and 1173 K in a of silica sand or Fe_2O_3. The figure was reproduced from Ref. [14]. For copyright issue, the figure is removed here.

The work starts by studying CO_2 gasification of a Polish char (lignite char) in silica sand for the identification of the controlling regime of the gasification, and to provide a baseline. Then, the replacement of silica sand by Fe-based oxygen carriers allows the investigation of the effect of oxygen carriers on gasification.

3.1.1 Fe_2O_3 reduction as source of oxygen

Fe_2O_3, as a cheap and abundant metal oxide with good reactivity, has a great potential for industrial applications of CLC. Research on the kinetics of Fe_2O_3 reduction has progressively developed from a single-step reduction mechanism [134] where Fe_2O_3 is directly reduced to Fe, to the complex mechanism that has taken into account all the four phases (haematite, magnetite, wustite and metallic iron) [135]. A list of the reduction reactions of Fe-O system by CO is presented below.

$3\ Fe_2O_3 + CO \rightarrow 2\ Fe_3O_4 + CO_2$ R-3.1

$Fe_3O_4 + CO \rightarrow 3\ FeO + CO_2$ R-3.2

$FeO + CO \rightarrow Fe + CO_2$ R-3.3

In a CO-rich reducing environment, haematite (Fe_2O_3) is subsequently reduced to magnetite (Fe_3O_4), wustite (FeO), and finally iron (Fe). The final state of hematite in the reduction process depends on the ratio of CO/CO_2 in the gases surrounding the material and the temperature. The thermodynamic phase equilibrium of the Fe-O system at temperatures of interest for gasification (~ 1000 - 1400 K) is presented in Fig. 3-2. For temperatures above 1000 K, a phase transition of $Fe_2O_3 \rightarrow Fe_3O_4$ has a partial pressure ratio of CO_2 to CO, $\frac{P_{CO_2}}{P_{CO}}$, at equilibrium of higher than 10^4, meaning that the presence of Fe_2O_3 will permit nearly full combustion of CO. $FeO \rightarrow Fe$ is believed to be the slowest step [48], [136,137] and usually avoided in CLC of solid fuels.

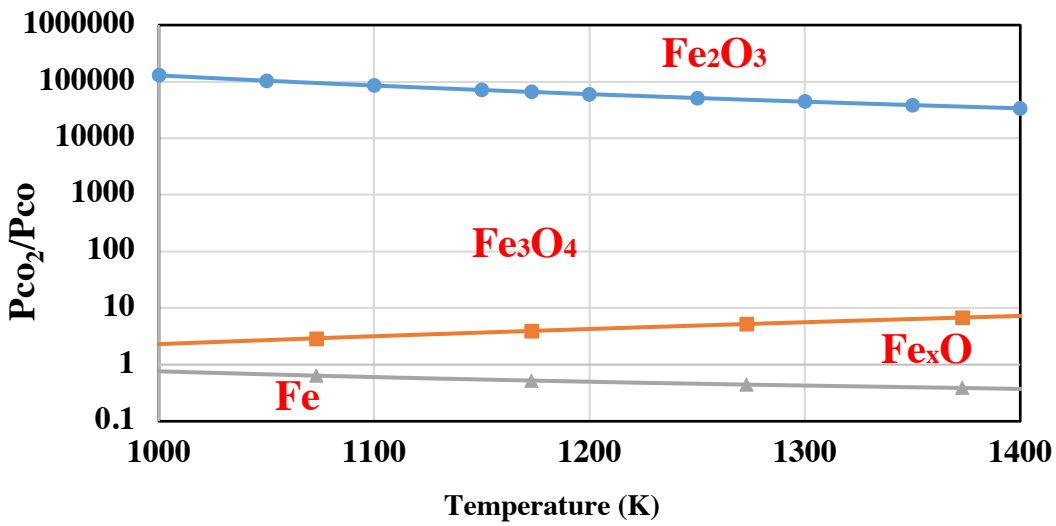

Figure 3-2 Phase diagram of Fe_2O_3 to Fe from 1000 to 1400 K. Giddings and Gordon [138] data source for the partial pressure of oxygen was used for the phase boundaries containing wustite (Fe_xO), then a conversion from oxygen partial pressure to the ratio of CO_2 to CO was made by using the Gibbs free energy of CO combustion ($CO + ½ O_2 = CO_2$) computed from MTDATA software [139] using SGTE database. For the phase boundary of Fe_2O_3 to Fe_3O_4, data from NASA database was used.

3.1.2 Support material- ZrO_2

Support materials, such as the most commonly used Al_2O_3, tend to interact with Fe_2O_3 (to form *e.g.* $FeAl_2O_4$ for Fe_2O_3 and Al_2O_3). $FeAl_2O_4$ is unreactive, resulting a negative impact on the overall performance of the material [37]. Usually, an inert support that helps improve the mechanical strength and only dilutes the active metal oxides is desirable.

ZrO_2, is selected as a support material for Fe_2O_3 due to its inertness to Fe_2O_3. Liu *et al*. [37] carried out chemical looping H_2 production using Fe_2O_3/ZrO_2, and found no evidence of ZrO_2 altering the thermodynamics of Fe-O system. It is initially expected that ZrO_2 should also be inert in ZrO_2-supported Fe_2O_3 for gasification; whilst its actual performance is investigated in this chapter.

3.2 Experimental methods

3.2.1 Preparation of the materials

The fuel, Polish char (with a particle size fraction of 600 – 850 μm), was derived from the devolatilisation of a Polish coal, as described in 2.2.2. CO_2 gasification of the char in silica sand was first studied to provide fundamental understanding of CO_2 gasification of the fuel. Then the bed material was switched to two active oxygen carries respectively: Fe_2O_3 and ZrO_2-supported Fe_2O_3 (65 wt.% Fe_2O_3). The particle size fractions used for each bed material were 180 – 250 μm for Fe_2O_3, 180 – 355 μm for ZrO_2-supported Fe_2O_3, and 250 – 355 μm for silica sand. Fe_2O_3 was prepared from the granulation of the commercial Fe_2O_3 powder with DI water, and ZrO_2-supported Fe_2O_3 was prepared by co-precipitation. Detailed procedures for the preparation of the two oxygen carriers as well as the silica sand were described in 2.2.2. The surface area of the prepared char, Fe_2O_3 and ZrO_2-supported Fe_2O_3 was measured by BET method, as described in 2.4.3, which are 307.14, 0.25, and 1.18 m^2/g, respectively.

3.2.2 Experiments

Gasification of the char in silica sand in a quartz tube fluidised bed reactor from 1123 to 1248 K with CO_2 concentration varying from 20% to 100% (balance N_2) was first investigated. For a typical experiment, ~ 0.04 g of char was added into fluidised bed from the top of the reactor. Investigation of the gasification in the presence of active oxygen carriers were carried out only in 20% CO_2, with temperature ranging from 1123 to 1248 K. ~ 0.1 g char, instead of 0.04 g, was added into the fluidised bed for a typical experiment when in Fe_2O_3-based oxygen carriers. This was to amplify the obtained signals, without affecting the mixing behaviour in the fluidised bed (*i.e*. the rate was normalised, and no evidence of mixing was observed). For all gasification experiments here, the volume of the bed (unfluidised) was ~ 20 ml and the fluidising gas flowrate was at 50 ml/s (leading to a U/U_{mf} between 6.6 – 9.0, depending on bed materials and temperatures), and the

operating pressure of the fluidised bed was at atmospheric. The detailed description of the experimental set-up and procedures were illustrated in 2.3.2. It should be noted that here, the effect of the change in the flow rate on the gas compositions due to the reaction inside the fluidised bed, was considered negligible.

3.3 Results

3.3.1 Reproducibility of the gasification experiment

Each single experiment was repeated for at least another two times to ensure the reliability of the results. Figures 3-3 to 3-4 show two runs of char gasification in silica sand at 1173 K in 100% CO_2, on two separate days. The results show good agreement of the two runs, indicating high reproducibility of the gasification experiments. Carbon balance, defined as the ratio of the increased amount of carbon in gaseous phase to the amount of carbon in the char fed into the reactor, fell between 95% and 104%, implying high reliability of the experimental data obtained. The gasification rate (*i.e.* rate of production of CO per unit mass of carbon) firstly reached a peak (1.4%) at a conversion, X, of 0.2, and then gradually dropped to zero. The conversion of carbon, X, was defined by the initial mass of char fed into the reactor m_o, the accumulated increased amount of carbon in the gaseous phase m_t, and the fraction of carbon in the char (0.484 as seen in Table 2-4):

$$X = \frac{m_t}{m_o \times 0.484}.$$

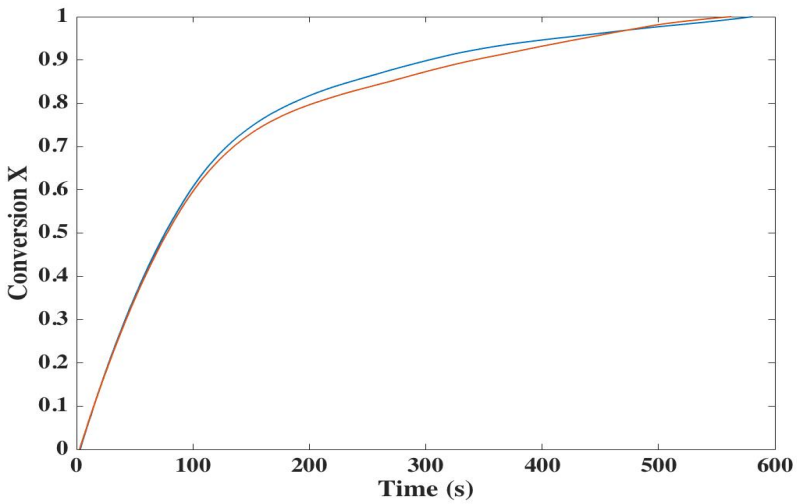

Figure 3-3 Carbon conversion of gasification of the char over time by 100% CO_2 at 1173 K in the quartz-tube silica sand-loaded fluidised bed of two experimental runs. ~ 0.042 g char with a particle size fraction of 600 – 850 μm was added into the bed in a single run.

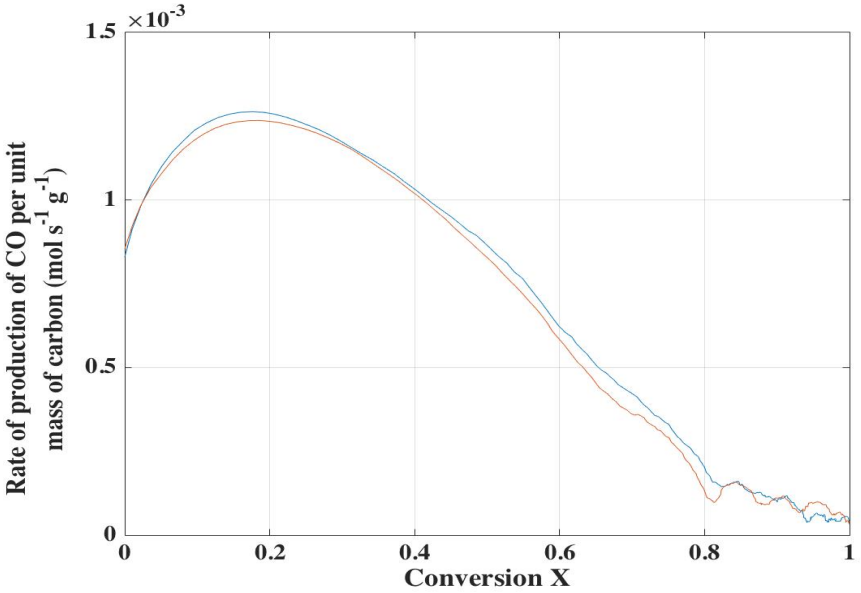

Figure 3-4 Rate of gasification (rate of production of CO per unit mass of carbon) of the char over conversion by 100% CO_2 at 1173 K in the quartz-tube silica sand-loaded fluidised bed of two experimental runs. ~ 0.042 g char with a particle size fraction of 600 – 850 μm was added into the bed in a single run.

3.3.2 Effect of temperature on char gasification

Figures 3-5 to 3-7 show the results of gasification of the char in 100% CO_2 with the operating temperatures from 1123 to 1248 K. The results are presented in mole fraction of CO over time, rate of gasification over conversion X, and normalised rate (= $\frac{Rate\ of\ gasification,\ R_g'}{Initial\ rate\ of\ gasification,\ R_{g,0}'}$) over conversion X, respectively.

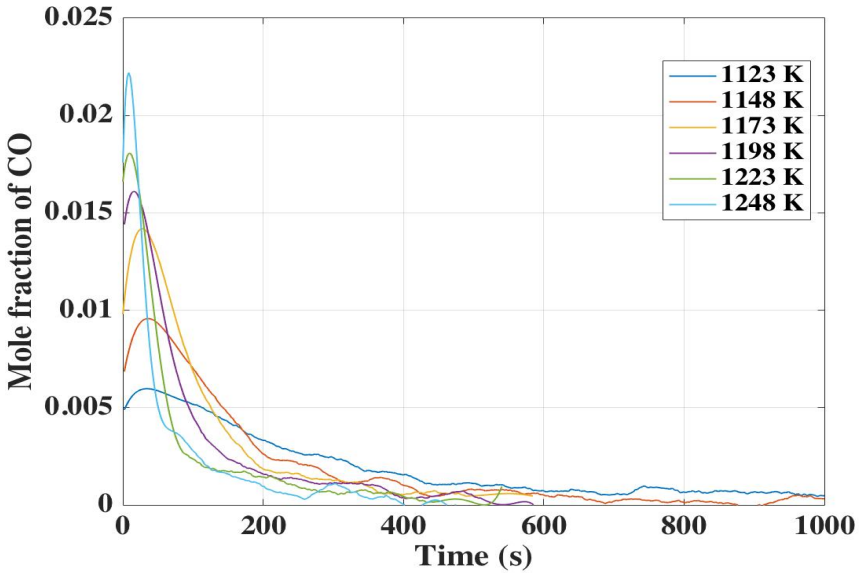

Figure 3-5 Mole fraction of the char over time by 100% CO_2 from 1123 to 1248 K in the silica sand-loaded fluidised bed. ~ 0.042 g char with a particle size fraction of 600 – 850 μm was added into the bed.

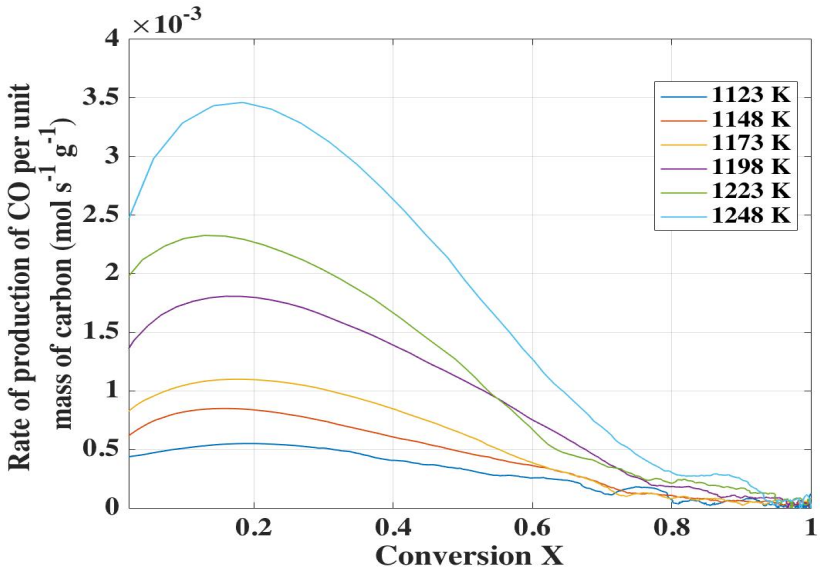

Figure 3-6 Rate of gasification of the char over conversion by 100% CO_2 from 1123 to 1248 K in the silica sand-loaded fluidised bed. ~ 0.042 g char with a particle size fraction of 600 – 850 μm was added into the bed.

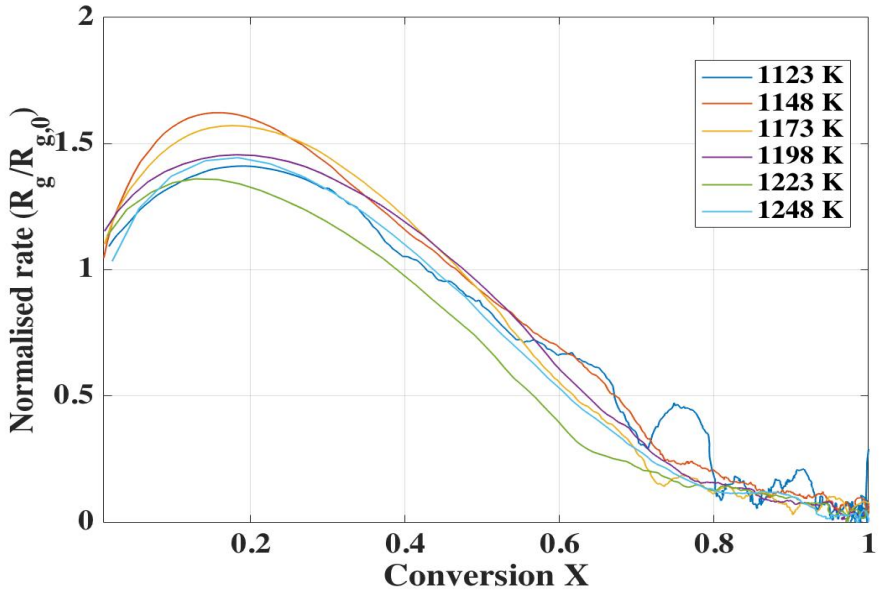

Figure 3-7 Normalised rate of gasification of the char over conversion by 100% CO_2 from 1123 to 1248 K in the silica sand-loaded fluidised bed. ~ 0.042 g char with a particle size fraction of 600 – 850 μm was added into the bed.

According to Fig. 3-5, temperature exhibited a positive effect on the measured CO in the sampled product stream. The peak of the mole fraction of CO reached the highest at 1248 K, giving a value of ~ 0.023, and the lowest peak was 0.007 at 1123 K. The residence time of the analyser, FTIR, is ~ 3 s, which is negligible compared to the gasification time (*e.g.* 400 s for the gasification at 1248 K, and over 1500 s for that at 1123 K); thus, the effect of gas mixing on FTIR signal can be ignored. The trends of gasification rate curves, as shown in Fig. 3-6, are similar to the mole fraction curves. In a typical gasification experiment, the gasification rate always increased to a peak value when the conversion X reached between 0.1 and 0.2. Figure 3-7 presents the normalised rate, $\frac{R\prime g}{R\prime g,0}$, the ratio of the gasification rate to the initial gasification rate (at t = 0), over conversion X. In the kinetically controlled regime this plot should give $f(X)$, which describes the pore structure evolution and change in rate as conversion increases. A change in the shape of $f(X)$, would give indication of a change in the controlling regime, or imply that the gasification is in the mass transfer limited regime. The results shown here did not reveal significant variation in the trend of $f(X)$ curves, suggesting no strong evidence for a change in the temperature range studied. This shape of $f(X)$ can be explained by the change in pore structure [14,140] that in the beginning period of gasification, the

chemical reaction was slow enough to allow the CO_2 diffuses into the particle. The pore size first increased to a threshold, below which it led to an increase in the total surface area and active sites and thus the rate of production of CO gradually reached to a maximum. Increase in the pore size above the threshold value led to a decrease in the total surface area due to coalesce of the pores, resulting in the decrease in the gasification rate.

3.3.3 Effect of CO_2 concentration on char gasification

Results of the effect of CO_2 concentration from 20% to 100% in the temperature range from 1123 to 1248 K were presented in Figs. 3-8 to 3-11. The increase in the CO_2 concentration, in general, promoted the gasification. According to Figs. 3-11 and 3-13, the maximum rate of production of CO in the gasification experiments with CO_2 content from 20% to 100% always fell into a char conversion range between 0.1 and 0.2 both at 1248 K, and this is also representative for the results at other temperatures.

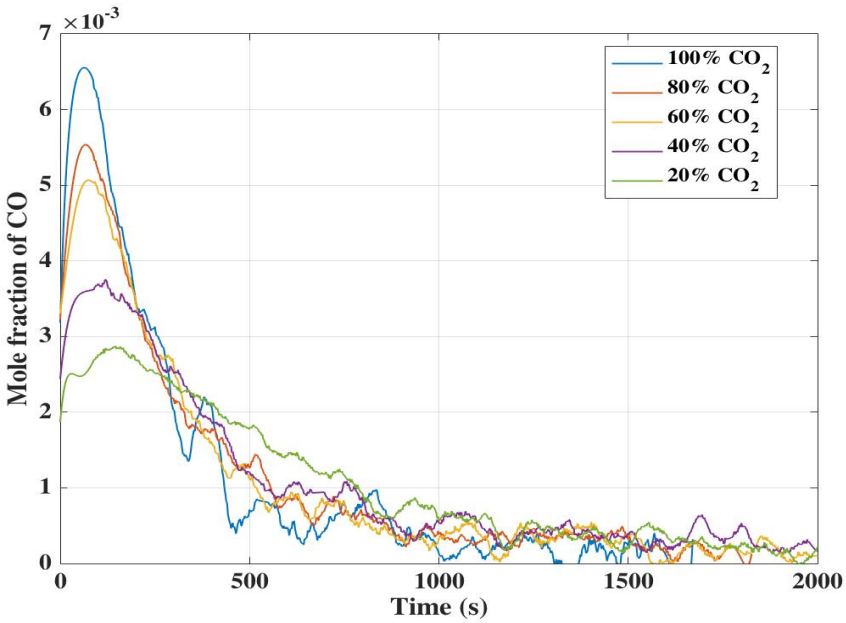

Figure 3-8 Mole fraction of CO from the gasification of the char over time with CO_2 concentration from 20% to 100% CO_2 at 1123 K in the silica sand-loaded fluidised bed. ~ 0.042 g char with a particle size fraction of 600 - 850 µm was added into the bed.

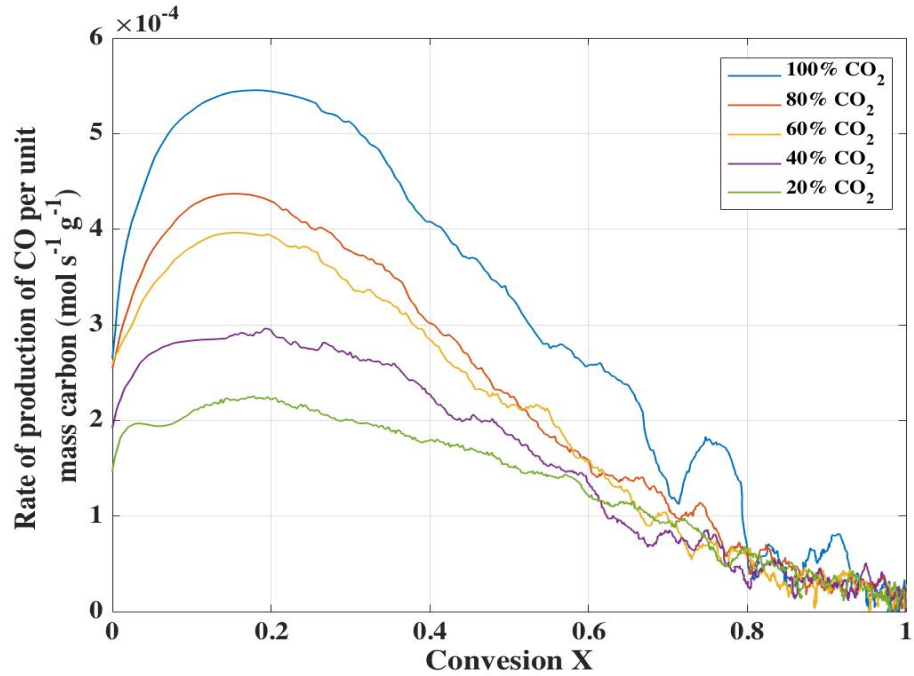

Figure 3-9 Rate of gasification of the char over conversion with CO_2 concentration from 20% to 100% CO_2 at 1123 K in the silica sand-loaded fluidised bed. ~ 0.042 g char with a particle size fraction of 600 - 850 µm was added into the bed.

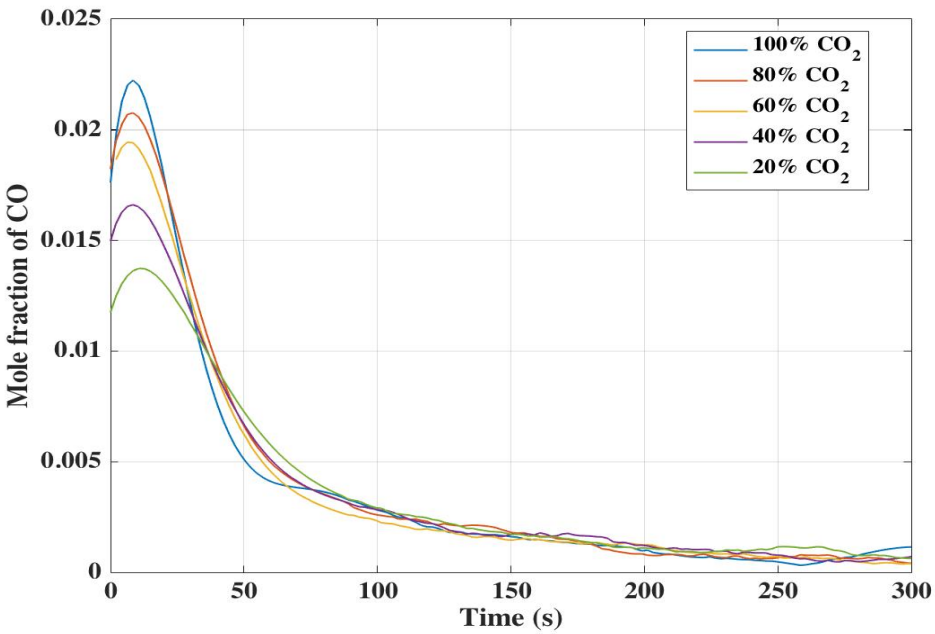

Figure 3-10 Mole fraction of CO from the gasification of the char over time with CO_2 concentration from 20% to 100% CO_2 at 1248 K in the silica sand-loaded fluidised bed. ~ 0.042 g char with a particle size fraction of 600 - 850 µm was added into the bed.

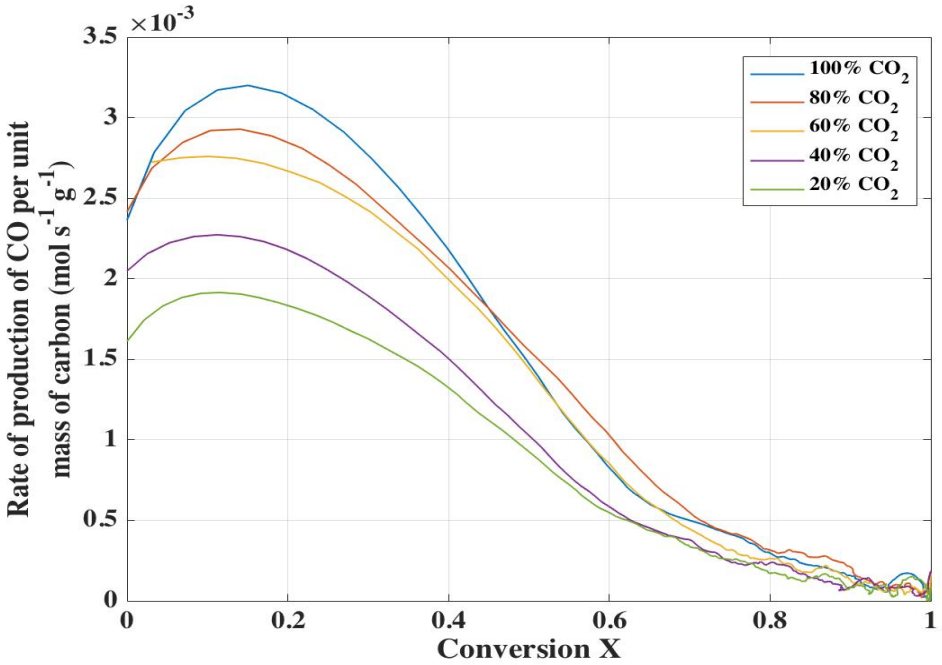

Figure 3-11 Rate of gasification of the char over conversion with CO_2 concentration from 20% to 100% CO_2 at 1248 K in the silica sand-loaded fluidised bed. ~ 0.042 g char with a particle size fraction of 600 - 850 µm was added into the bed.

3.3.4 The effect of Fe_2O_3 on *in situ* char gasification

Gasification in the presence of oxygen carriers were performed in 20% CO_2 from 1123 to 1248 K. The presence of Fe_2O_3 consumed CO produced from *in situ* gasification, and generated CO_2. Therefore, the additional CO_2 measured by the FTIR resulted from a combination of char gasification and combustion of CO by Fe_2O_3. To improve the CO_2 signals (distinguishable from the background CO_2 level) detected by the FTIR, the amount of the char fed to the bed was increased to ~ 0.1 g (still in the range where the gasification was not affected by the amount of char fed). The final reduced phase of Fe_2O_3 should be limited by the ratio of CO_2 to CO in the bed. It was noticed that in the work carried out here, a CO_2 to CO ratio larger than 15 (refer to Fig. 3-2) over the gasification time was always obtained. This ensures that Fe_2O_3 should only be reduced to the magnetite phase, Fe_3O_4.

To express the gasification rate of the char, different from the measured overall change in CO, the consumption of CO by the oxygen carriers to generate CO_2 should be considered. For char gasification only (in silica sand):

The overall rate of production of CO_2: $R_{CO_2,silica} = -r$.

The overall rate of production of CO: $R_{CO,silica} = 2r$.

For char gasification in the presence oxygen carrier:

The overall rate of production of CO_2: $R_{CO_2,oc} = -r + r_{oc}$.

The overall rate of production of CO: $R_{CO,oc} = 2r - r_{oc}$.

r_{oc} is the rate of production of CO_2 from the reaction between the CO and oxygen carriers.

Rate of char gasification (based on production of CO) can be expressed as

$2r = 2 \times (R_{CO_2,oc} + R_{CO,oc})$.

Figure 3-12 gives an example of the CO and CO_2 measured from gasification in silica sand at 1223 K. For carbon gasification in CO_2, consuming one mole of CO_2 should generate two moles of CO, which was also observed in Fig. 3-12. In Fig. 3-13, rate of CO in Fe_2O_3, CO_2 in silica sand and in Fe_2O_3 at 1223 K were presented. Good carbon balances between 97% to 105% were obtained in the Fe_2O_3 beds.

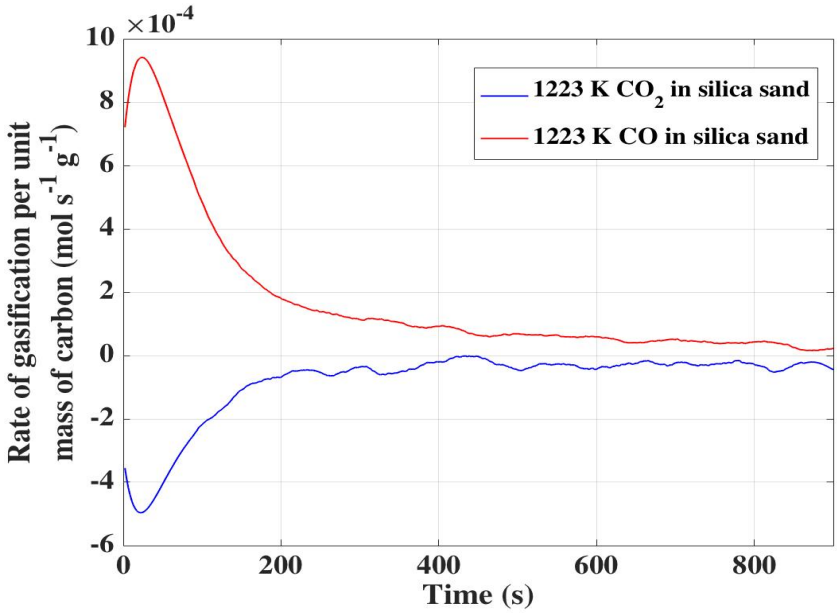

Figure 3-12 $R_{CO,silica}$ and $R_{CO_2,silica}$ at 1223 K, where the rates here represent the overall rate of production of CO, and CO_2 per unit mass of carbon of carbon in a bed of silica sand.

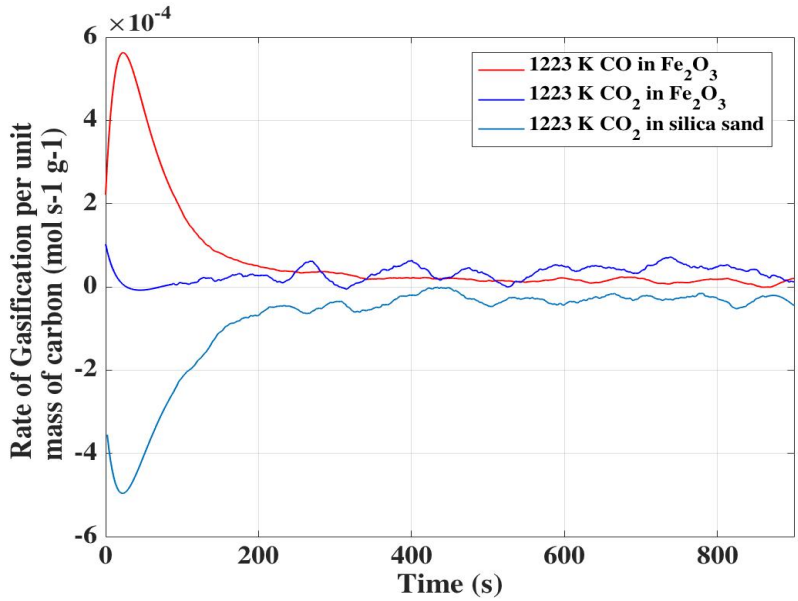

Figure 3-13 $R_{CO,oc}$, $R_{CO_2,oc}$ and $R_{CO_2,silica\ sand}$ at 1223 K, where $R_{CO,oc}$ and $R_{CO_2,oc}$ here represent the overall rate of production of CO, and CO_2 per unit mass of carbon of carbon in a bed of Fe_2O_3, respectively, and $R_{CO_2,silica\ sand}$ is the overall rate of production of CO_2 in a bed of silica sand.

Figures 3-14 to 3-16 show the comparison of overall char gasification rates (based on the total production of CO per unit mass of carbon) in silica sand and Fe_2O_3 at different temperatures, and no significant difference in the rates in the two beds were observed.

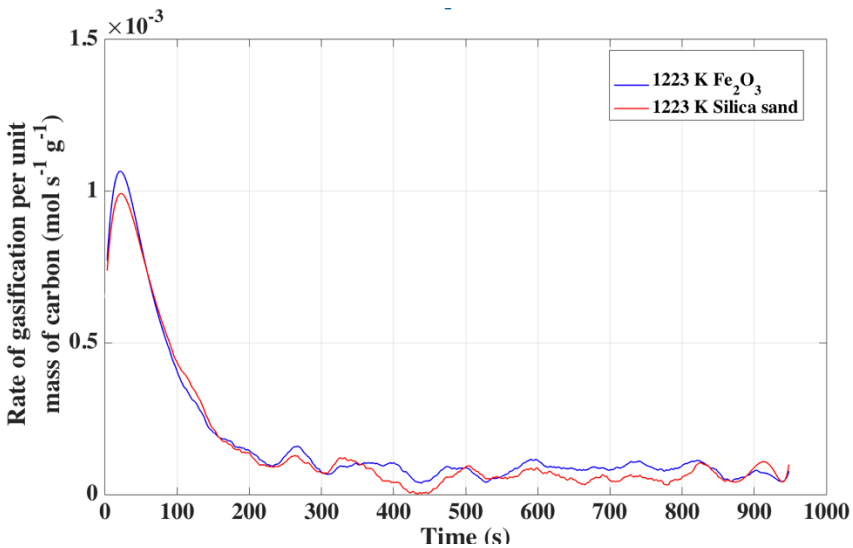

Figure 3-14 Comparison of overall rate of char gasification in beds of silica sand Fe_2O_3 at 1223 K.

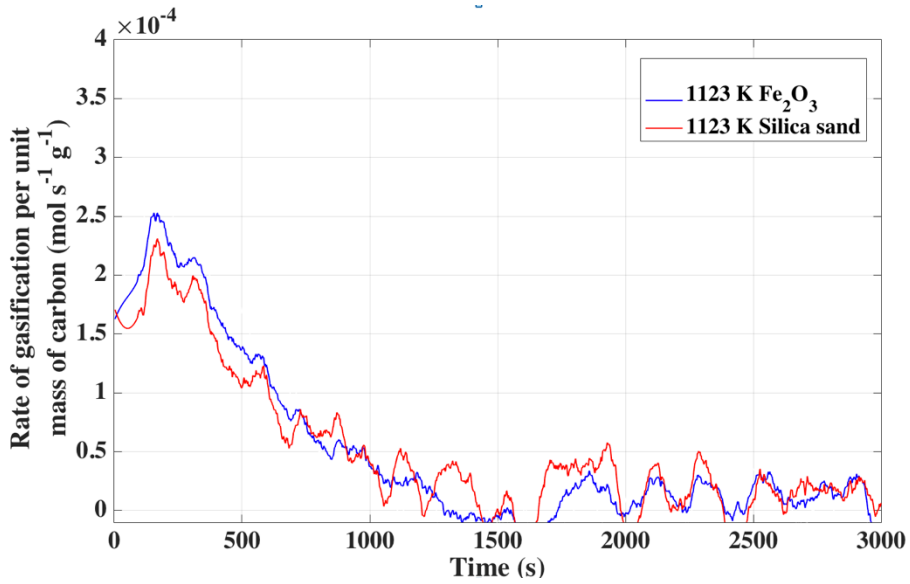

Figure 3-15 Comparison of overall rate of char gasification in beds of silica sand and Fe_2O_3 at 1123 K.

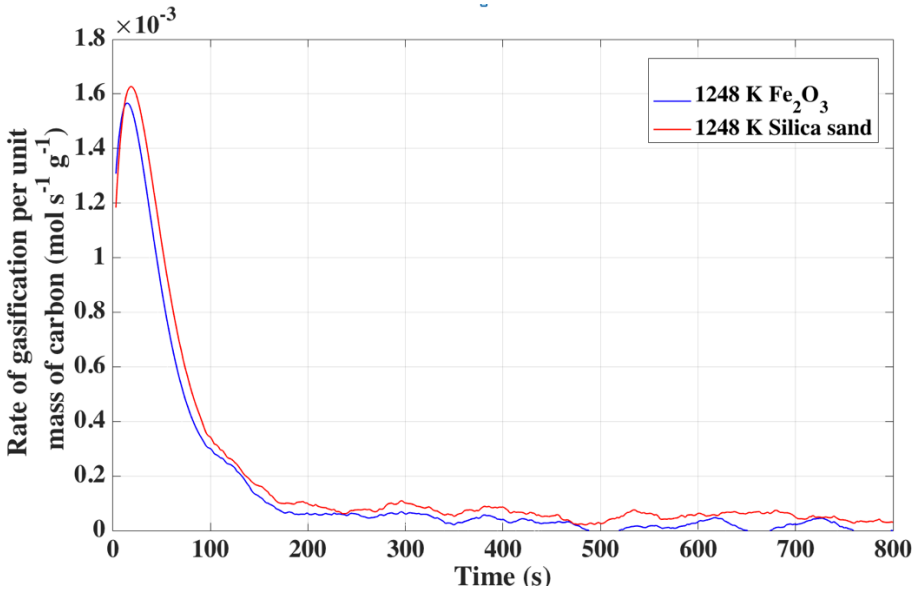

Figure 3-16 Comparison of overall rate of char gasification in beds of silica sand and Fe_2O_3 at 1248 K.

3.3.5 The effect of ZrO_2-supported Fe_2O_3 (FeZr) on *in situ* char gasification

Figure 3-17 shows the rate of CO in FeZr, CO_2 in FeZr and silica sand, and the overall gasification rate (based on total CO production rate per unit mass of carbon). Figures 3-18 to 3-20 present the comparisons of the overall gasification rate in silica sand, and FeZr at 1123, 1173 and 1248 K, respectively. Different from the results in a bed of Fe_2O_3, clear differences in the rates at each temperature were found, where the gasification rate was in silica sand was always higher. The carbon balances (over the period until no change in

mole fractions of each gas was observed) in FeZr were 84%, 81% and 79%, corresponding to each temperature from 1123 to 1248 K. The results seem to suggest an inhibition effect of FeZr on the char gasification, leading to some unreacted carbon remaining in the bed.

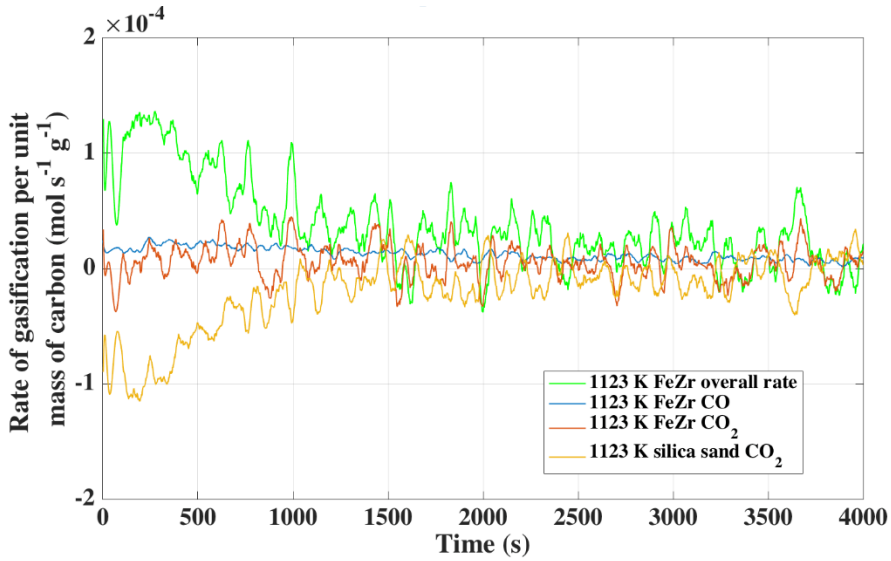

Figure 3-17 $R_{CO,oc}$, $R_{CO_2,oc}$, $R_{CO_2,silica\ sand}$ and the overall rate of gasification at 1123 K and by 20% CO_2, where $R_{CO,oc}$ and $R_{CO_2,oc}$represent the overall rate of production of CO, and CO_2 per unit mass of carbon of carbon in a bed of FeZr and $R_{CO_2,silica\ sand}$ is the overall rate of production of CO in a bed of silica sand.

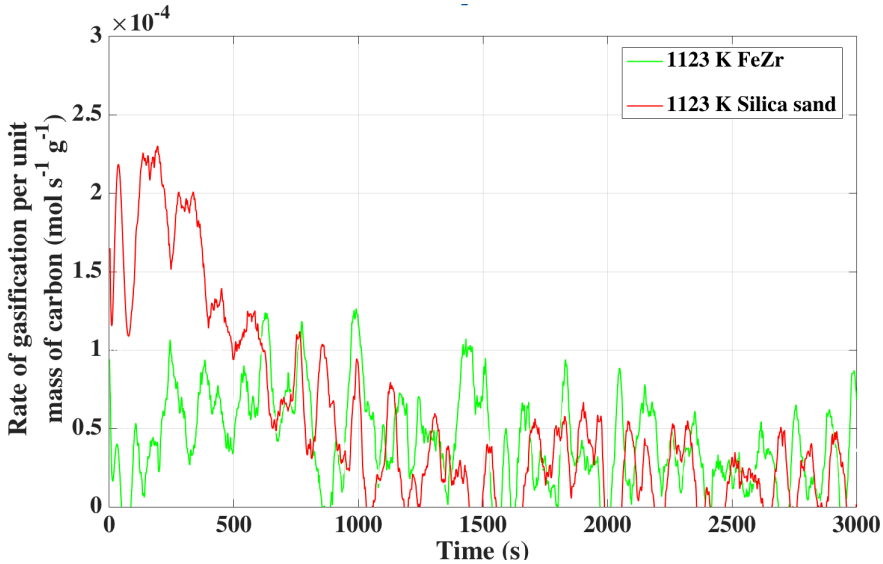

Figure 3-18 Overall gasification rate over time by 20% CO_2 at 1123 K in beds of silica sand and FeZr.

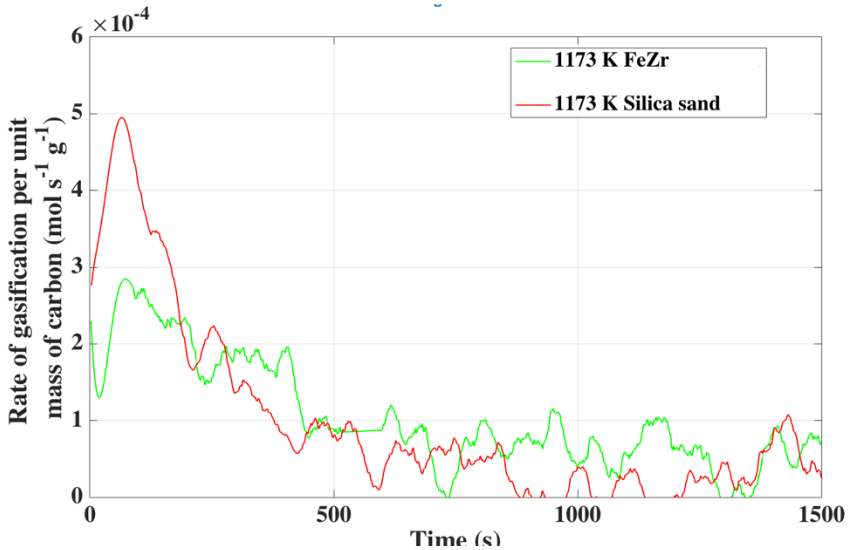

Figure 3-19 Overall gasification rate over time by 20% CO_2 at 1173 K in beds of silica sand and FeZr.

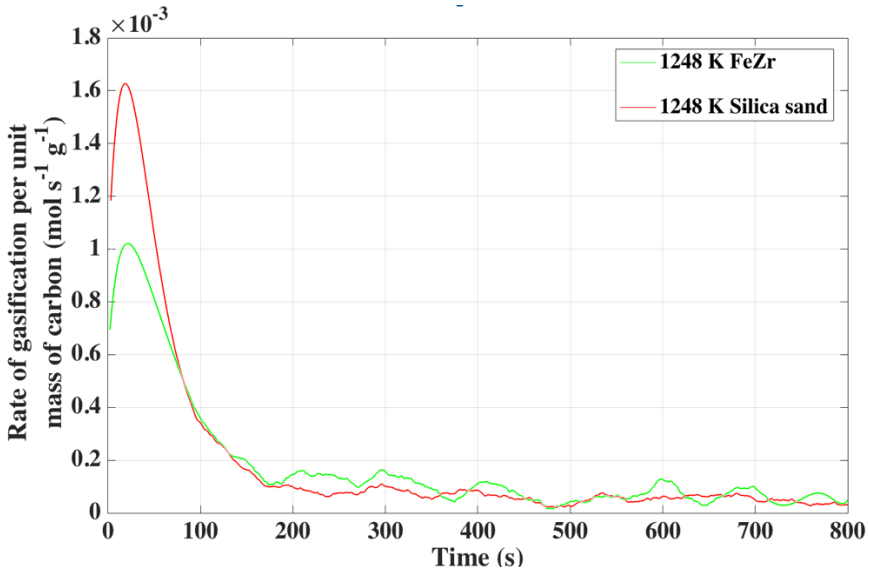

Figure 3-20 Overall gasification rate over time by 20% CO_2 at 1248 K in beds of silica sand and FeZr.

3.4 Discussion

3.4.1 Kinetic evaluation of the gasification of the char (in silica sand)

In this work, prior to investigating the gasification performance in the presence of active oxygen carriers, understanding of whether the gasification of Polish char was affected by mass transfer limitation is necessary. The measured gasification rate was first compared with the external mass transfer rate, which is also the maximum rate

approachable for gasification reaction. If the rate is liminted by the diffusion of the reactant to the surfance, the maxium rate can be estimated based on Eq. 3-1 [141]:

$$R_{\max} = 2 \times \frac{Sh}{1.102} \times ([CO_2]_{bulk} - [CO_2]_{surface}) \times D_{CO_2} \times \frac{6}{d_p{}^2 \times \rho}. \quad \text{Equation 3-1}$$

The surface concentration of CO_2 is close to zero when the reaction is totally controlled by external mass transfer. The constant 1.102 is introduced to account for the fact of the non-equiomolar counter diffusion [142]. Sherwood number (a dimensionless number describing the ratio of convection mass transfer rate to that of diffusive mass transfer), Sh, of the reacting char particle in the fluidising situation was obtained from the correlation [141]

$$Sh = 2\varepsilon_{mf} + 0.69\left(\frac{U_{mf}d}{v\varepsilon_{mf}}\right)^{1/2}\left(\frac{v}{D_{CO_2}}\right)^{1/3}, \quad \text{Equation 3-2}$$

where ε_{mf} is the voidage at incipient fluidisation, v is the kinematic viscosity of fluidising gas, d is the diameter of the reacting particle, and D_{CO_2} is the diffusivity of CO_2 in a gas mixture. Table 3-1 compares the maximum char gasification rate observed from the experiments and the limiting maximum rates, at different temperatures. For example, at 1123 K, the maximum gasification rate by 20% CO_2 is 2.1×10^{-4} mol s^{-1} g^{-1}, whereas the corresponding limiting rate of 0.0090 mol s^{-1} g^{-1} is significantly faster. At the highest temperatue 1248 K, the limiting rate is ~ 0.0097 mol s^{-1} g^{-1}, and this is still more than five times the maximum gasification rate, which is 1.8×10^{-3} mol s^{-1} g^{-1}. The significant differences in the rates suggest that the gasification of the char was less likely to be influenced by external mass transfer.

Table 3-1 R_{max} at different temepratures by 20% CO_2.

Temperature (K)	$[CO_2]_{bulk}$ (mol/m^3)	D (m^2/s)	Sh	R_{max} (mol s^{-1} g^{-1})	$R_{max,\,measured}$ (mol s^{-1} g^{-1})
1123	2.1686	0.00017	1.5605	0.0090	2.1×10^{-4}
1148	2.1213	0.00017	1.5576	0.0091	3.7×10^{-4}
1173	2.0761	0.00018	1.5550	0.0093	5.5×10^{-4}
1198	2.0328	0.00019	1.5522	0.0094	8.9×10^{-4}
1223	1.9912	0.00019	1.5495	0.0095	1.3×10^{-3}
1248	1.9514	0.00020	1.5468	0.0097	1.8×10^{-3}

The value of the slope from Arrhenius plot would give indication of the controlling regime of a reaction. The gasification of the solid fuel can usually be described as:

$$r = k'(T, C)f(X),$$

where $k'(T, C)$ is the effective rate constant, which is a function of gas concentration C and temeprature T. Assuming that the overall CO_2 gasification of the char obeys the Arrhenius law ($k = Ae^{-\frac{E}{R_{ideal}T}}$), Eq. 3-3 can be obtained

$$r = G(C)Ae^{-\frac{E}{R_{ideal}T}}f(X), \qquad \text{Equation 3-3}$$

where A is the frequency factor, E is the effective activation energy, R_{ideal} is the ideal gas constant. By taking the natural logithm of Eq. 3-3, and apply the initial gasification rates, $R_{g,0}{}'$, the following equation was obtained:

$$\ln\left(R_{g,0}{}'\right) = \ln(A \cdot G(C)) - \frac{E}{R_{ideal}T}.$$

For constant gas concentrations, the effective activation energy E can be obtaiend from the slope of the Arrhenius plot $\ln\left(R_{g,0}{}'\right)$ versus $1/T$. Arrhenius plot of the initial gasification rate for different CO_2 concentrations was shown in Fig. 3-21. The values of various parameters of the trendlines for the Arrhenius plots are presented in Table 3-2. According to Fig. 3-21, the data points of the initial gasification rates for different CO_2 concentrations were well fitted to linear lines, with high values of R-squared values, R^2, as shown in Table 3-2. This further indicates no clear change in the controlling regime from 1123 to 1248 K. The observed activation energy, E, was calculated from the slope of the trendline, and the frequency factor, A, was obtained from the intercept. Activation energy values between 196 to 216 kJ mol^{-1}, and frequency factor values between 6.2×10^4 mol $s^{-1}g^{-1}$ to 1.67×10^5 mol $s^{-1}g^{-1}$ were obtained for CO_2 concentrations from 20% to 100%. The apparent activation energy estimated here is close to those reported in literature for CO_2 gasification of other lignite chars, which were around 190 kJ mol^{-1} [143,144]. Therefore, it is reasonable to believe that intra-particle mass transfer limitation is less of our concern here.

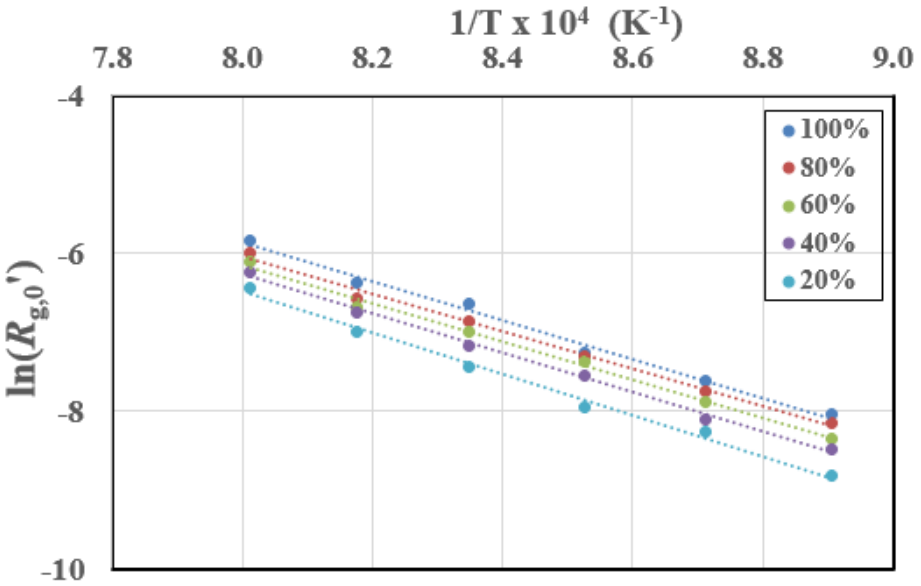

Figure 3-21 Arrhenius plot of the natural logarithm of the initial gasification rate versus the inverse of temperature from 1123 to 1248 K for CO_2 concentrations from 20% to 100%.

Table 3-2 Values for the parameters of the trendlines in for the Arrhenius plots in Fig. 3-23.

	100% CO_2	80% CO_2	60% CO_2	40% CO_2	20% CO_2
Intercept = ln(A)	13.82	12.81	13.34	13.78	14.33
Slope = $\frac{-E}{R_{ideal}}$, (K)	-24612	-23575	-24356	-25052	-26025
R^2	0.991	0.993	0.994	0.996	0.993

3.4.2 Gasification in the presence of Fe_2O_3

The discussion in 3.4.1 suggest that gasification of Polish char was mainly controlled by intrinsic chemical kinetics from 1123 to 1248 K. Based on Saucedo *et al.*'s results in Ref.[14] that the overall gasification rate was improved by the presence of Fe_2O_3 due to the removal of surface CO, given that gasification was limited by mass transfer. In the current study, for the kinetically controlled gasification of Polish char, Fe_2O_3 did not have much effect on the char gasification rate, *i.e.* the overall gasification rates between in silica sand and Fe_2O_3 beds were very comparable. This is consistent with the mechanism extrapolated from the study by Saucedo *et al.* that the removal of CO by Fe_2O_3 so as to improve the gasification rate is mainly effective when the gasification is external mass

transfer limited. On the other hand, the presence of Fe_2O_3 increased the CO_2 concentration due the combustion of the produced CO, which might improve the gasification rate; however, the increased amount (*i.e.* between 0.2% to 0.7% in 20% CO_2,depending on the temperature) is negligible compared to the bulk 20% CO_2 gasification environment.

According to Fig. 3-11, a significant amount of CO was still observed in the presence of Fe_2O_3, suggesting relatively slow combustion of produced CO from the gasification step. For the application of CLC for CCS, chemical looping oxygen carriers with higher oxidation activity, are needed in this case.

3.4.3 Gasification in the presence of FeZr

Based on the results in 3.3.4, over the whole temperature range, gasification of Polish char in FeZr exhibited lower rates than those in silica sand and Fe_2O_3 beds. This suggests some 'inhibition' effect in the presence of FeZr, either chemically or physically. The chemical reactivity of the prepared FeZr was first investigated by comparing the reduction of FeZr and Fe_2O_3 by CO.

- **Comparison of the reduction between FeZr and Fe_2O_3 by 10% CO**

The reduction experiment was carried out in a quartz tube fluidised bed reactor at 1173 K, as described in 2.3.2. Around 8 g of FeZr or Fe_2O_3 particles were fed into the bed. The feed gas, 10% CO in N_2, was introduced into the reactor at a flowrate of 1.8 L/min. Figures 3-22 and 3-23 show mole fractions of CO, CO_2, and the sum of the two in the reduction. The produced CO_2 should only come from the oxidation of CO. Therefore, the sum of the mole fractions of CO and CO_2 should always be around 0.1 through the whole reduction period, as seen in Figs. 3-22 and 3-23. For FeZr, the experiment was terminated at ~ 550 s due to de-fluidisation of the bed; whilst for Fe_2O_3, up to 1000 s, there was no significant de-fluidisation. Significant difference in the reduction behavior was observed in the two beds. Three stages were seen in the reduction of FeZr, which are t = 0 to t = 80 s (stage 1), t = 80 to t = 300 s (stage 2), t = 300 to = 500 s (stage 3), and t > 500 s, respectively. Assuming that the three stages correspond to the phase transitions of reduction of Fe_2O_3 (*i.e.* $Fe_2O_3 \rightarrow Fe_3O_4$, $Fe_3O_4 \rightarrow FeO$, and $FeO_x \rightarrow Fe$) in FeZr (given that ZrO will not lose oxygen), the oxygen balances (defined as the ratio amount of increased oxygen in the gas phase to the estimated amount of oxygen released from phase

reduction) were obtained as follow: 0.98 for stage 1, 0.94 for stage 2, and 0.18 for stage 3. The first two stages exhibit good oxygen balances, indicating the presence of appropriate phase transitions. Apparently, the reduction from wustite, FeO_x, to Fe has not completed. In the bed of Fe_2O_3, however, there was no separation of stages. Fe_2O_3 also seems to be less reactive than FeZr for CO reduction. This probably can be partly explained by the larger BET surface area of FeZr.

It is also suspected that carbon deposition from CO *via* $2\ CO \rightarrow C + CO_2$, onto the solids, could lead to a lower amount of CO measured at the outlet. Direct identification of the deposited carbon was difficult here, whilst there is some evidence showing that at least no significant carbon deposition occurs. For carbon deposition from CO, the stoichiometric ratio of the consumption of CO to the production of CO_2 is 2, and for Fe_2O_3 reduction in CO, this ratio is 1. If carbon deposition is significant during reduction, the ratio should fall between 2 and 1. The experimental data gave a ratio of around 1 over the whole reduction period, suggesting little carbon deposition. It seems that the low CO amount and the apparent gasification rate in the gasification experiments are highly likely to have resulted from other factors.

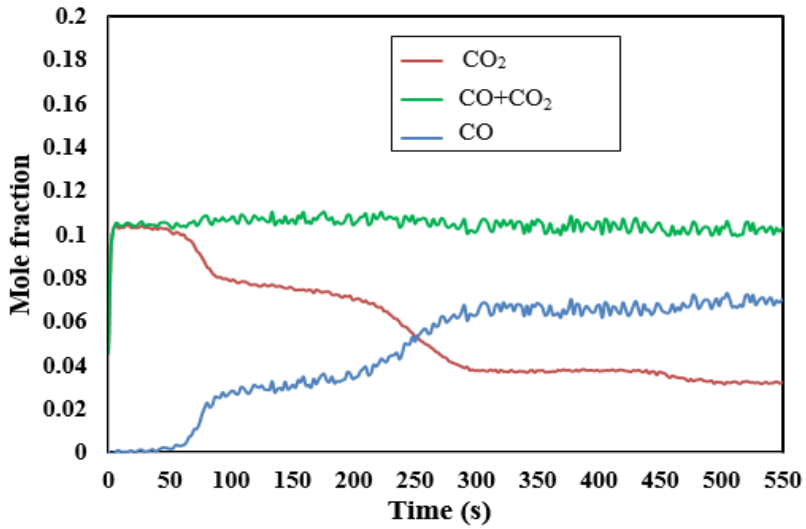

Figure 3-22 FeZr reduction by 10% CO in fluidised bed at 1173 K.

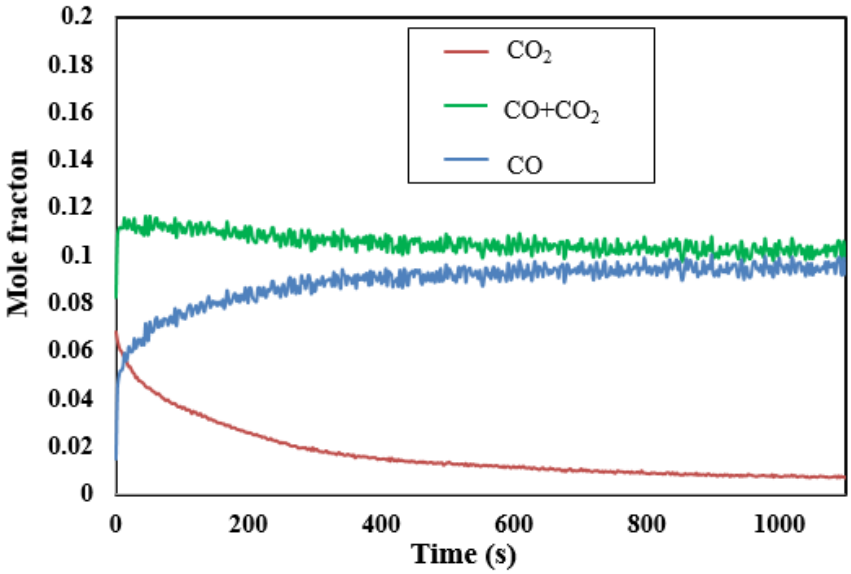

Figure 3-23 Fe_2O_3 reduction by 10% CO in fluidised bed at 1173 K.

- **Investigation of the low carbon balance in char gasification in FeZr**

Char gasification in FeZr shows lower carbon balance (79% to 84%), suggesting some carbon remaining in the fluidised bed. The possible amount of carbon left inside the bed was examined by air burn-off. Air was used to burn the bed after CO_2 gasification of the char at 1173 K and 1248 K for 2000 s. After the completion of CO_2 gasification, the gas was firstly switched to N_2 to flush our any CO_2 remaining in the bed. The N_2 purge took about 60 s, before being switched to air for burning off. For reference, the CO_2 gasification – N_2 – air experiments were also carried out in silica sand bed and in FeZr without adding char into the bed (blank experiment).

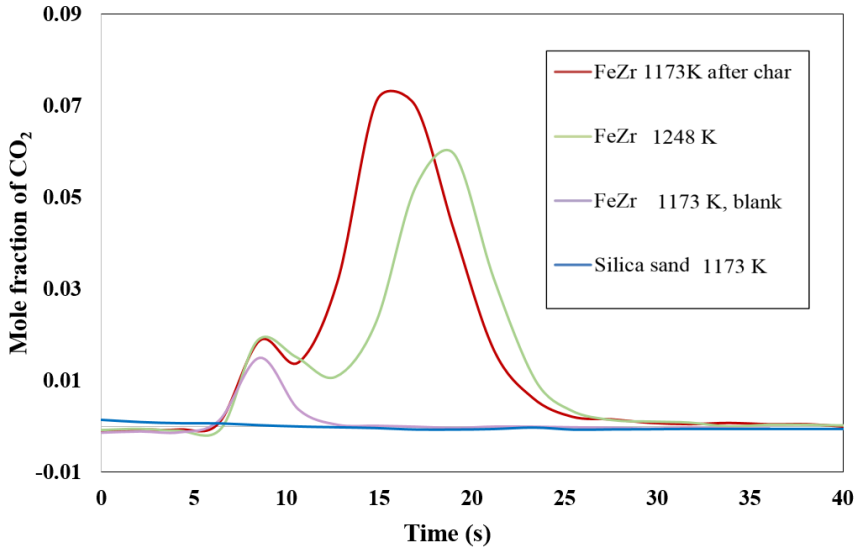

Figure 3-24 Air burning-off of the fluidised beds after CO_2 gasification. The experimental curve labelled 'blank' in FeZr bed at 1173 K means no char was fed into the fluidised bed in the CO_2 gasification stage.

Figure 3-24 shows the CO_2 mole fraction during the air burn-off (from t = 6 s). For the char gasification in silica sand at 1173 K, there is no CO_2 peak, meaning that all the carbon in the char was gasified. However, in the FeZr bed with char fed in the gasification stage, two peaks (a small peak, followed by a bigger one) were always observed. In the blank experiment in FeZr, where no char was added, a small peak was found. At 1173 K, the amount of carbon in CO_2 during the air burn-off accounted for 19% of the total carbon (as char) fed into the FeZr bed; at 1248 K, the value was 16%. These data balance the lower carbon balances previously reported for char gasification in FeZ, implying that FeZr was causing some carbon remaining during gasification. There are two possible reasons for this: (1) FeZr is inhibiting the gasification of char thus causing some carbon in the char unreacted; (2) there was some carbon deposition from the CO produced. (2) was thermodynamically unstable, as CO carbon deposition on iron-based materials have been reported [145,146] only at low temperatures (below 1073K). Carbon deposits would react with iron to form iron carbides and free carbon, depending on specific operating temperatures. For the carbon deposition from $2\,CO \rightarrow C + CO_2$, at the lowest gasification temperature 1123 K, P_{CO_2}/P_{CO}^2 is ~ 0.06 [147], and the value decreases with increasing temperature. This theoretically rules out the possibility of (2) at gasification temperatures studied (where $P_{CO_2}/P_{CO}^2 \gg 1$). Alternatively, (2) might become possible if the thermodynamics is different: *e.g.* CO bound to zirconia.

- **Comparison of char gasification between in pure ZrO_2 and silica sand**

So far, the results seem to suggest an 'inhibition' effect of FeZr on CO_2 gasification of Polish char. Further investigation on the effect of ZrO_2 was carried out by performing char gasification in ZrO_2 (prepared from $Zr(OH)_4$ powder, the detailed preparation method is presented in 2.2.2). Figure 3-25 presents the comparison of char gasification by 20% CO_2 in ZrO_2 and silica sands at 1173K. Same amount of char (~ 0.1 g $\pm$ 0.004 g) was added to the beds. According Fig. 3-25, the amount of CO produced in silica sand was much higher than that in ZrO_2. Char gasification in silica sand finished at around 1800 s; while in ZrO_2, after 6000 s (not shown in this Fig. 3-25), there was still CO detected. The difference is also a function of temperature. At the highest temperature of 1248 K, the maximum rate in ZrO_2 is about two thirds of the latter; at the lowest temperature of 1123 K, the difference is about a factor of 7.

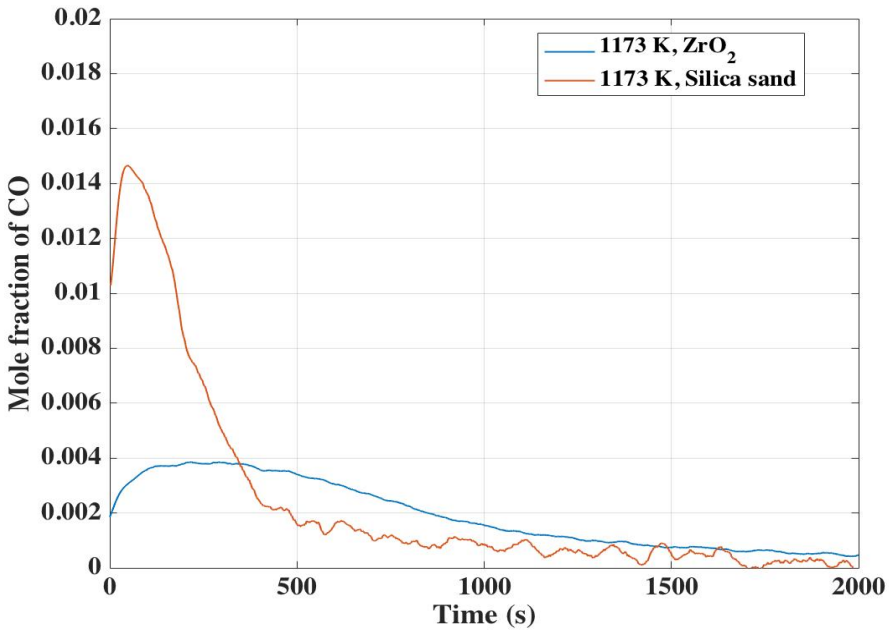

Figure 3-25 Mole fraction of CO of char gasification by 20% CO_2 at 1173 K in ZrO_2 and silica sand beds, respectively.

Based on the above results, it seems that the presence of ZrO_2 could be the main reason accounting for decreased apparent char gasification rate in FeZr. However, it is still unclear by which mechanism ZrO_2 affects the char gasification. Maitre and Lefort [148] studied the reaction between solid carbon and ZrO_2 at temperatures above 1600 K, where zirconia carbide was formed. Though this temperature is much higher than the

temperatures studied here, it is widely recognised [148,149] that an intermediate product zirconium oxycarbide $Zr(C_xO_y)$ was formed prior to the transformation to ZrC, and the formation temperature for zirconium oxycarbide is still unclear. XRD characterization of fresh ZrO_2, ZrO_2 which has experienced CO_2 gasification, and ZrO_2 which has experienced gasification and followed by air oxidation have been carried out. For the gasified and oxidised samples, they were quenched to room temperature for testing. The results showed no difference between the three samples, which indicates less likelihood of the formation of zirconium carbide. Further work on this could be focused on the interaction between ZrO_2 for CO to investigate whether the apparent inhibition effect was due to the product CO being absorbed by the ZrO_2.

3.5 Conclusions

The main results from the investigation carried out in this chapter are summarised below:

a) CO_2 gasification of Polish char in the temperature range from 1123 to 1248 K was found to be free of external mass transfer limitation. The high apparent activation energy found, between 196 to 216 kJ mol^{-1}, suggests that it is mostly likely to be in the kinetically controlled regime.

b) The presence of Fe_2O_3 was found to have no significant effect on the gasification of the char, mainly due to the face that gasification of the char was not influenced by external mass transfer (*i.e.* the external mass transfer rate is more than 5 times higher than the maximum rate of gasification over conversion).

c) The results of char gasification in ZrO_2-supported Fe_2O_3 (FeZr) showed a much decreased apparent rate of gasification of Polish char, compared with sand. Auxiliary experiments were carried out to explore the reason behind. Results of reduction of FeZr and Fe_2O_3 respectively in 10% CO (balance N_2) show that CO reacted much faster with FeZr, indicating that the reduction of FeZr by CO is fast enough. Further investigation of char gasification in pure ZrO_2 was carried out and it showed that the apparent rate of char gasification in ZrO_2 was much lower than that in silica sand, suggesting an 'inhibition' effect of ZrO_2 on char gasification, and the inhibition effect decreases with increasing temperature. However, the mechanism of ZrO_2 for 'inhibiting' the gasification requires further investigation. Future work could focus on the interaction between ZrO_2 surfaces and CO.

4.0 Numerical study of CO_2 gasification of Polish char and the investigation of the CO inhibition effect on gasification

4.1 Introduction

Experimental investigation of the gasification of a Polish char was carried out in Chapter 3. The results suggested that the gasification of the char was mainly controlled by chemical kinetics (perhaps with some influence of intra-particle diffusion). A numerical model for the gasification is developed in this chapter. The kinetic parameters to be substituted into the numerical model were obtained based on the gasification results in Chapter 3. More importantly, this chapter aims at understanding the effect of CO on CO_2 gasification by intentionally introducing some CO into the fluidised bed.

4.1.1 Mechanisms of CO_2 gasification of carbon and the effect of CO

The effect of the gasification product, CO, on reaction kinetics has been studied in literature [150–152]. Any attempt to understand the underlying mechanism requires the gasification itself free of mass transfer limitation. For intrinsic kinetics, the models can be categorised into two kinds: chemical reactions mainly take place on the surfaces for nonporous particles, and reactions initiate on pore surfaces within the solid for porous particles [140]. For instance, the unreacted shrinking core model applies to relatively non-porous particles, where the rate-limiting step that can be one of the following: diffusion through a fluid film surrounding the solid particle, diffusion through the ash/inert solid layer, and chemical reaction at the core surface [153]. The volumetric model, on the other hand, is applied to porous particles and when the intrinsic reaction rate is relatively slow [154]. The reaction rate can be considered uniform throughout the reacting particle. The random pore model is suitable for situations where reaction depends strongly on the total internal surface area of the pores [140]. The results shown in Chapter 3 show periods of increase in the observed rates as the conversion increased in the initial stage, is a typical example of the gasification of porous particle and the increase in the rate is largely because of the increase in the surface area due to pore evolution [14,140]. To account for this effect, the rate R'_g can be expressed as [137,155–157]:

$$R'_g(X) = R'_{g,0} \times f(X), \qquad \text{Equation 4-1}$$

where $R'_{g,0}$ is the initial rate, when the pore parameters are at initial conditions. The function $f(X)$ is the term introduced to describe the change in pore structure over the

conversion of carbon of the particle. It should be noted that $R'_g(X)$ should be a function of local conversion, which will vary across the particle. For example, for a spherical particle, there can be radial gradient in gas concentrations if intra-particle mass transfer limitation exists. Saucedo *et al*. [14] proposed the idea of using an arbitrary function, $f(X)$, which can be experimentally determined in the kinetically controlled regime. For simplicity, the local conversion, X, was replaced by an average conversion across the particle. This was later improved by Dai *et al*. [158] by using the local conversion within a particle. The idea of implementing an experimentally determined $f(X)$ instead of using a mathematical pore model for $f(X)$ was continued in this work. The advantage is that it avoids the process of selecting between different models that may give a good fit to experimental results.

The mechanism of carbon-carbon dioxide gasification, which determines the intrinsic reaction rate expression, can consist of multiple elementary steps [159] including

$$C_f + CO_2\,(g) \rightleftharpoons C(CO_2)$$

$$C_f + C(CO_2) \rightleftharpoons C(CO)_A + C(O)$$

$$C_f + C(O) \rightleftharpoons C(CO)_B$$

$$C(CO)_A \longrightarrow CO(g) + nC_f$$

$$C(CO)_B \longrightarrow CO(g) + nC_f$$

$$C_f + C(O) \rightleftharpoons C(CO)_C$$

, where C_f represents a free active carbon site, $C(CO_2)$ and $C(O)$ are the carbon site occupied by CO_2 and an oxygen atom respectively. $C(CO)$ represents the site occupied by CO, with the subscripts A, B and C indicating the sites formed *via* different reactions. A very complex rate expression would result if all proposed reactions were taken into account.

On the other hand, an application of Langmuir-Hinshelwood mechanism to describe the C-CO_2 reaction kinetics, results in the rate expression as [150,151,160] follow

$$R'_g = \frac{k_a N_t p_{co_2}}{(1+k_b p_{co}+k_c p_{co_2})}, \qquad \text{Equation 4-2}$$

where k_a, k_b, and k_c are the rate or ratio of rate constants, N_t is the total number of active sites. Equation 4-2 is consistent with a subset of the above elementary reactions [160], and two commonly recognised gasification mechanisms, (Mechanism A [150,151,161,162] and Mechanism B [15], below), with different meanings of k_a, k_b and k_c [164].

Mechanism A:

$$C_f + CO_2\,(g) \underset{k_{-1}}{\overset{k_1}{\rightleftharpoons}} C(CO) + C(O) \qquad \text{R.4-1}$$

$$C(CO) \xrightarrow{k_2} CO(g) + nC_f \qquad \text{R.4-2}$$

Mechanism B:

$$C_f + CO_2\,(g) \xrightarrow{k_1} C(CO) + C(O) \qquad \text{R.4-3}$$

$$C_f + CO(g) \underset{k_{-2}}{\overset{k_2}{\rightleftharpoons}} C(CO) \qquad \text{R.4-4}$$

$$C(CO) \xrightarrow{k_3} CO(g) + nC_f \qquad \text{R.4-5}$$

In mechanism A, CO retards the gasification due to the reaction of chemisorbed oxygen with gaseous CO to generate CO_2. In mechanism B, the retardation happens *via* the adsorption of CO on a free active carbon site. Debates over the two mechanisms will not be reviewed here but can be found elsewhere [165]. In general, mechanism A, also known as the Ergun's mechanism, has been studied to a wider extent. The above mechanisms were fitted to the experimental data at pressures of CO_2 up to 1 atm. At higher pressures, up to 40 atm, Blackwood and Ingeme [160] found their data to be best fitted with a rate expression as

$$R'_g = k_a N_t p_{co_2} + \frac{k_b N_t {p_{co_2}}^2}{(1 + k_c p_{co_2} + k_d p_{co})}. \qquad \text{Equation 4-3}$$

Studies focusing on high CO partial pressure in a gasification environment have been carried out to a lesser extent in previous work. The amount of produced CO from C-CO_2 gasification is usually too low to exhibit its effect on the gasification rate. Only when the partial pressure of CO in the system reach certain amount, does it become possible to

validate the CO term in rate expressions. In this study, CO was intentionally introduced to the system at different concentrations to investigate its effect on gasification. A numerical model based on Mechanism A was developed to describe the gasification of Polish char. The literature reported values of the activation energy of R.4-1, 95 kJ/mol [161] , was used as the starting point for the fitting of other kinetic data. The kinetic data, obtained by taking the initial conditions at different temperatures and CO_2 concentrations were substituted into the model to fit the experimental results.

4.2 Experimental methods

The experimental investigation was carried out in a quartz tube reactor loaded with silica sand, the same as the one used for Chapter 3, in a bubbling fluidised bed, as described in 2.3.2. CO with various concentrations (0.5%, 1%, or 3.5%) mixed with 20% CO_2 (balance N_2) was used as the fluidising gas. The temperature investigated was from 1148 to 1248 K. Around 0.04 g of Polish coal derived char (the same fuel used in Chapter 3) was fed into the fluidised bed for every single experiment. The product gas was sampled and analysed by a FTIR. Refer to 2.3.2 for more detailed experimental conditions.

4.3 Theory of the numerical model

As described in Chapter 3, gasification of Polish char was mainly controlled by chemical kinetics. However, there was no strong evidence showing that the gasification is purely free of intra-particle diffusion limitation. A numerical model, containing both the kinetic part and the intra-particle diffusion is developed. Assuming that the gasification is totally free of intra-particle diffusion limitation, the obtained kinetic parameters can be directly substituted into the model. Good fitting of the modelled results with the experimental results imply the validity of the assumption. The intra-particle diffusion part in the model should not affect the results if gasification is free of diffusion limitation. Otherwise, the experimental results would be underestimated, and the presence of the diffusion part in the model would then increase the difference between the experimental and modelling results. The intrinsic kinetics of the model is developed based on the Ergun's two-step mechanism [161], and the diffusion part is built from Cylindrical Pore Interpolation Method (CPIM) [166], a method based on Maxwell Stefan equations for describing multicomponent diffusions.

4.3.1 Intrinsic kinetics of gasification in CO_2 based on Ergun's mechanism (Mechanism A)

In Chapter 3, kinetic data based on Arrhenius law was obtained. However, this can only be thought as a preliminary treatment of the experimental results. CO_2 gasification of carbon, known as the Boudouard reaction (R. 4-6), is better described by Ergun's two step (R. 4-1 and 4-2) mechanism [161], which is also widely recognised.

$$C + CO_2 \rightleftharpoons 2CO \qquad \text{R. 4-6}$$

By applying a pseudo steady state assumption for the concentration of $C(O)$, the rate of the production of CO can be expressed as [161]

$$R'_{g,0} = \frac{2ck_2\left(p_{CO_2} - \frac{p_{CO}^2}{K_p}\right)}{p_{CO_2} + \frac{k_2}{k_1} + \frac{k_{-1}}{k_1} \times p_{CO}}. \qquad \text{Equation 4-4}$$

The term $\frac{p_{CO}^2}{K_p}$ was later introduced to account for the reversibility of step two in Mechanism A [165]. In this expression, k_i represents rate constant per active site with an activation energy of E_i; p_{CO_2} and p_{co} are partial pressures of CO_2 and CO, respectively; c is the concentration of active sites per unit mass of carbon; K_p is the equilibrium constant. In this chapter, the experimental data were retreated to obtain kinetic data based on Eq. 4-4. The equation shows that the overall rate does not follow the Arrhenius law, while individual steps do. Ergun [167] found the equilibrium constant for R.4-1, and the activation energy of ck_2 by carrying out experiments for three types of carbons:

$$K_1 = \frac{k_1}{k_{-1}} = 4150 \times \exp\left(\frac{E}{R_{ideal}T}\right) \qquad \text{Equation 4-5}$$

$$E_{ck_2} = 247 \text{ kJ/mol}, \qquad \text{Equation 4-6}$$

where E was found to be -95 kJ/mol, K_1 is the equilibrium constant of R. 4-1. K_1 was found to be only a function of temperature, regardless of the type of carbon. Likewise, the activation energy of ck_2 was independent of carbon types. If the concentration of active site is independent of temperature, and k_2 changes exponentially with $1/T$, this indicates that k_2 is the same for each of all types of carbon. The primary property accounting for the differences in reactivity between carbons is the variation of the number of active sites per unit mass of carbon, c. It is not possible to directly measure the rate

constants k_1 and k_2, without measuring the concentration of active sites c of the char [161]. c also changes as the gasification proceeds, which can be expressed as a function of X, the conversion of the char. $f(X)$ was obtained experimentally from the regime, which has the least mass transfer effect (*i.e.* at 1123 K) if there is any.

4.3.2 Intra-particle mass transfer

For the diffusion part of the numerical model, it assumes: 1). a spherical porous carbon particle with cylindrical pores of uniform pore diameter; 2). negligible temperature variation within the particle; 3). negligible internal pressure variation from the centre to the surface; 4). the fluxes J can be linked *via* the reaction stoichiometry with a constraint that N_2 is stagnant, *i.e.* $J_{co} = -2J_{co_2}$, and $J_{N_2} = 0$. This last assumption is only valid if the gas concentrations are assumed to be in steady state throughout, which is not overly restrictive given that the time constant needed here to establish a steady state was about in milliseconds (*i.e.* the time constant for diffusion is estimated from $\frac{R^2}{D}$, where R is the radius of the particle, and D here is the diffusion coefficient of CO_2), *i.e.* much shorter than the time to fully convert the particle.

A material balance on the gaseous species within the spherical reacting char particle gives:

$$\frac{dy_a}{dt} = \frac{R_{ideal}T}{P}\left(\frac{1}{r^2}\left(\frac{d(r^2 J_a)}{dr}\right) - r_g\right), \qquad \text{Equation 4-7}$$

where y_a is the molar fraction of component a, r is the radial coordinate and a = 1 for CO, 2 for CO_2 and 3 for N_2. R_{ideal} is the ideal gas constant. The reaction term is

$$r_g = \frac{v_a}{2} \times R'_g(X) \times \rho_{in} \qquad \text{Equation 4-8}$$

$$R'_g(X) = R'_{g,0} \times f(X). \qquad \text{Equation 4-9}$$

$R'_g(X)$ and $R'_{g,o}$ are respectively the rate of gasification at a conversion X and zero, in mol s^{-1} g^{-1} and v_a is the stoichiometric coefficient for species a. r_g is the gasification rate per unit volume of carbon, in mol s^{-1} m^{-3}. The rate of change of local conversion then be obtained by

$$\frac{dX}{dt} = R'_g(X) \times \frac{M_{carbon}}{2}, \qquad \text{Equation 4-10}$$

where M_{carbon} is the molar mass of carbon, in g mol^{-1}.

The overall gasification is non-equimolar and N_2 is present as a third gas species, thus a simple binary diffusion model for description is inappropriate. CPIM, which describes diffusion of multi-components, and accounts for the effects on pore size, is applied [166]. The model is simplified here by noting that CO produced from the gasification by CO_2 is at low concentrations, thus the pressure gradient term in the original CPIM is eliminated. The pseudo steady assumption means that $J_1 = -2J_2$, and $J_3 = 0$; so that only the flux of CO needs to be calculated. Now, the diffusion terms have the following forms:

$$\frac{dy_1}{dr} = \frac{\tau^2 R_{ideal} T}{\varepsilon P}\left[\frac{y_1 J_2}{(D_A)_{21}} - \frac{y_2 J_1}{(D_A)_{12}} - \frac{y_3 J_1}{(D_A)_{13}}\right] \qquad \text{Equation 4-11}$$

$$\frac{dy_2}{dr} = \frac{\tau^2 R_{ideal} T}{\varepsilon P}\left[\frac{y_2 J_1}{(D_A)_{12}} - \frac{y_1 J_2}{(D_A)_{21}} - \frac{y_3 J_2}{(D_A)_{23}}\right] \qquad \text{Equation 4-12}$$

$$\frac{dy_3}{dr} = \frac{\tau^2 R_{ideal} T}{\varepsilon P}\left[\frac{y_3 J_1}{(D_A)_{13}} + \frac{y_3 J_2}{(D_A)_{23}}\right], \qquad \text{Equation 4-13}$$

where y_i is the molar fraction of species i, J_i is the molar flux, $(D_A)_{ij}$ is the molar diffusivity. ε and τ^2 are the porosity and the tortuosity factor of the particle, respectively. P is the total pressure. $(D_A)_{ij}$ is obtained by interpolating between the extremes of continuum and Knudsen flow

$$\frac{1}{(D_A)_{ij}} = \frac{1}{(D_K)_i} + \frac{1}{(D_B)_{ij}}. \qquad \text{Equation 4-14}$$

$(D_K)_i$and $(D_B)_{ij}$ are the Knudsen diffusivity and the molecular diffusivity, respectively.

$(D_K)_i$ and $(D_B)_{ij}$ are given by:

$$(D_K)_i = \frac{d_{pore}}{3}\sqrt{\frac{8R_{ideal}T}{\pi M_i}} \qquad \text{Equation 4-15}$$

$$(D_B)_{ij} = \frac{1.00\times10^{-8}T^{1.75}(\frac{1}{M_i}+\frac{1}{M_j})^{1/2}}{p[(\sum_i v'_a)^{\frac{1}{3}}+(\sum_j v'_a)^{\frac{1}{3}}]^2}.$$ Equation 4-16

For estimating $(D_B)_{ij}$, which was determined by Fuller *et al*. [168] is used. d_{pore} is the pore diameter, M_i is the molar mass of species i, v'_a is the atomic diffusion volume of an element in species i, or j. In this study, Knudsen diffusion, $(D_K)_i$, was found the rate limiting step that governs the overall molar diffusion, $(D_A)_{ij}$, *i.e*. the values of $(D_B)_{ij}$ are usually more than twice those of $(D_K)_i$.

The porosity ε and pore diameter d_{pore} change with conversion of the carbon X, which could affect the diffusion. The correlations of porosity and pore diameter proposed by Dai *et. al*. [158] are used in the study, assuming that the crossover between uniform pore channels can be neglected, and the enlargement of pores occurs only in a radial direction:

$$\frac{\varepsilon(r)}{\varepsilon_o} = (\frac{d_{pore}}{d_{pore,o}})^2$$ Equation 4-17

$$d_{pore} = d_{pore,o}\sqrt{(\varepsilon_o + X(1-\varepsilon_o))/\varepsilon_o}\,.$$ Equation 4-18

ε_o and $d_{pore,o}$ are respectively the initial porosity and pore diameter. The values are determined by N_2 adsorption and mercury intrusion porosimetry in Table 4-1.

The model assumes following initial and boundary conditions:

For t = 0:

$P_{co}(r) = P_{co,bulk}, P_{co_2}(r) = P_{co_2,bulk}, X(r) = 0$

For r = 0:

$J_{co}(t) = 0,\ J_{co_2}(t) = 0$

For r = R:

$P_{co}(t) = P_{co,bulk}, P_{co_2}(t) = P_{co_2,bulk}$

, where $P_{co,bulk}$ and $P_{co_2,bulk}$ are respectively the partial pressure of CO and CO_2 in the bulk phase, R is the radius of the particle.

4.3.3 Solution of the model

Parameters of the char particles were listed in Table 4-1. The tortuosity value was assumed to be the reciprocal of the porosity, as suggested by Bhatia and Perlmetter [169].

Table 4-1 Model parameters

Initial porosity ε_o	0.69
Initial pore diameter $d_{pore,o}$	160 nm
Tortuosity factor τ^2	1.43
Surface area	240 m^2/g
Pore volume	1.44 cm^3/g

The pseudo-steady assumption for the gas phase allows the equations describing the diffusion to be simplified. By substituting $J_1 = -2J_2$ into Eq. 4-11, gives

$$\frac{dy_1}{dr} = \frac{\tau^2 RTJ_1}{\varepsilon P}\left[\frac{-2y_1}{(D_A)_{21}} - \frac{y_2}{(D_A)_{12}} - \frac{y_3}{(D_A)_{13}}\right]. \qquad \text{Equation 4-19}$$

This assumption reduces the number of gas phase species, which need to be solved, to one, since $J_1 = -2J_2$, and $y_1+y_2+y_3=1$, which is valid when the generated CO concentration is relatively low. Despite a pseudo-steady state in the gas phase being assumed, the model was solved firstly by discretising the gas and solid phase balance equations, and marching forward in time (finite difference method) the time-dependent mass balance equations. The model was solved in Matlab using ODE15s.

4.4 Results

4.4.1 Experimental investigation of the effect of CO on char gasification

Experiments of introducing CO along with the gasification agent, 20% CO_2, were carried out at temperatures from 1148 to 1248 K. Typical experimental results of gasification at various CO concentrations (0%, 0.5%, 1%, and ~ 3.5% CO) at 1173 K, were presented in Fig. 4-1. Apparently, the presence of CO significantly decreased the gasification rate. Around 0.5% of CO decreased the gasification rate to about half of the rate when no CO

was introduced. Interestingly, further increase in the CO amount did not lead to significant drop in the gasification rate: the rates with 1% CO and 3.4% CO were comparable and not much lower than that in the presence of 0.5% CO.

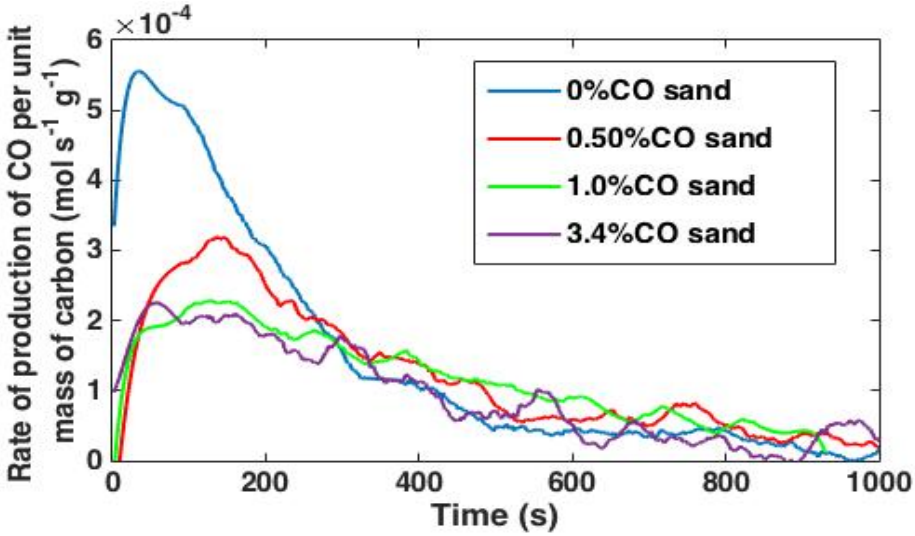

Figure 4-1 Gasification of Polish char in a fluidised bed at 1173 K by a mixed stream of CO, CO_2 and N_2, where CO_2 was always at 20% and CO from 0% to 3.4 % CO (balance N_2).

4.4.2 Determination of the kinetic data based on Ergun's equation

By rearraging the rate expression of gasifcation Eq. 4-4, and neglecting the term $\frac{{p_{co}}^2}{K_p}$, Eq. 4-20 is obtained. At $X = 0$, ck_1 and ck_2 are obtained from the slope and intercept of the rearranged equation. Substiting p_{co_2}, p_{co} at X = 0, and varying $\frac{k_{-1}}{k_1}$ (based on varying a value of activation energy between -92 to -98 kJ/mol [161]), the slope and intercept were detemined by having the least squared value of the initial rates. Table 4-2 gives the obtained kinetic parameters results, and the activation energy of $\frac{k_{-1}}{k_1}$ is -93 kJ/mol (by fitting). These experimentally obtaiend kinetic parameters (*i.e.* ck_1, ck_2 and k_{-1}/k_1), which were the main variables for the numerical model at different operating conditions, were substituted into the model to predict the gasification profiles.

$$\frac{p_{co_2}}{R_{g,0}} = \frac{1}{2ck_2}\left(p_{co_2} + \frac{k_{-1}}{k_1}p_{co}\right) + \frac{1}{2ck_1} \qquad \text{Equation 4-20}$$

Table 4-2 Kinetic results of char gasification based on Ergun's equation, from the experiemntal data of CO_2 concentrations varying from 20% to 100%.

T (K)	ck_1(mol s^{-1} g^{-1} bar^{-1})	ck_2(mol s^{-1} g^{-1})	k_2/k_1 (bar)	k_{-1}/k_1
1123	4.863x10^{-4}	2.336x10^{-4}	0.4804	5.083
1148	6.248x10^{-4}	4.678x10^{-4}	0.7487	4.092
1173	1.660x10^{-3}	4.845x10^{-4}	0.2919	3.324
1223	3.488x10^{-3}	1.050x10^{-3}	0.3011	2.251
1248	6.317x10^{-3}	1.815x10^{-3}	0.2873	1.874

Based on the values of ck_1 and ck_2 shown in Table 4-2, the correpsonding activation energies, E_{ck_1} and E_{ck_2} are obtained, which are -244 and -176 kJ/mol respectively. The values of E_{2ck_1} and E_{2ck_2} are within the value ranges reported previously in literature [14,170], and the overall value of overall activation energy of gasification would fall into the range between -244 and -176 kJ/mol, silimilar the range of values estimated from Arrhenius law, which is between 196 to 216 kJ/mol. The high value of the activation energy also suggests less likelihood of being limited by the diffusion for gasification.

4.4.3 Comparison of experimental and model results based on Ergun's equation

- **Validation of model**

The model assumes a fixed radius, but this is only valid when the local conversion at the boundary does not reach 100%. Figure 4-2 gives the computed local conversion as as function of dimensionless time (defined as the ratio of the ongoing gasification time to the total time required for the completion of the gasification). It shows that the difference in the local conversion between the center and the surface boudary at 1173 K is not as significant as that at 1248 K. Under these conditions, the local converstion at the center was predicted to be ~ 0.98 when the outer surface reached the coversion of unity (and when the particle boundary would begin to move). Therefore, for this Polish char, the entire char particle is almost fully converted before a moving boundary appears, characteristic of the gasification not being limited by diffusion through the particle.

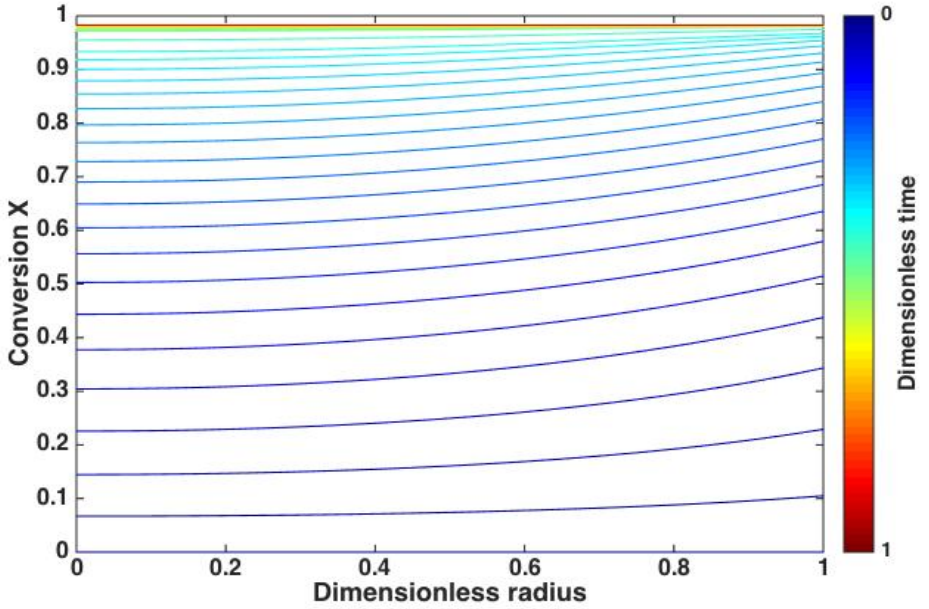

(a)

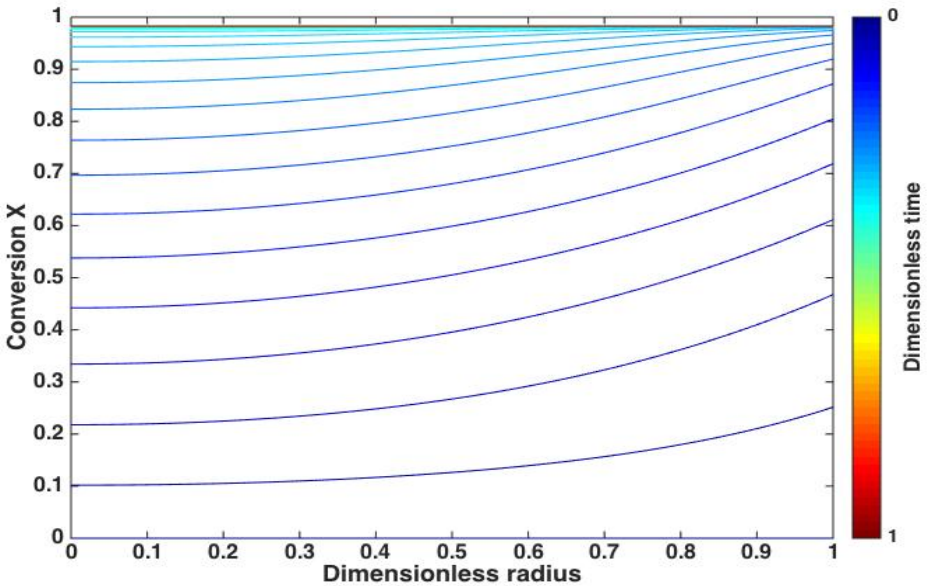

(b)

Figure 4-2 Local conversion profiles of the modelled (based on Ergun's mechanism) results from gasifiation of Polish char by 20% CO_2 at (a). 1173 K, and (b). 1248 K.

- **Modelled results based on Ergun's equation**

$f(X)$ that could describe the change in pore structure is obtained experimentally at 1123 K. Gasification at 1123 K, which is the lowest operating temperature in this study, should

be of least mass transfer limitation, if there is any. Experimental gasification of char particles of a wide range of sizes (from 250 to 1180 μm) was performed to confirm that it is not mass transfer limited, as shown in Fig. 4-3. No noticeable difference in obtained rates was observed, indicating the gasification being fully kinetically controlled at 1123 K.

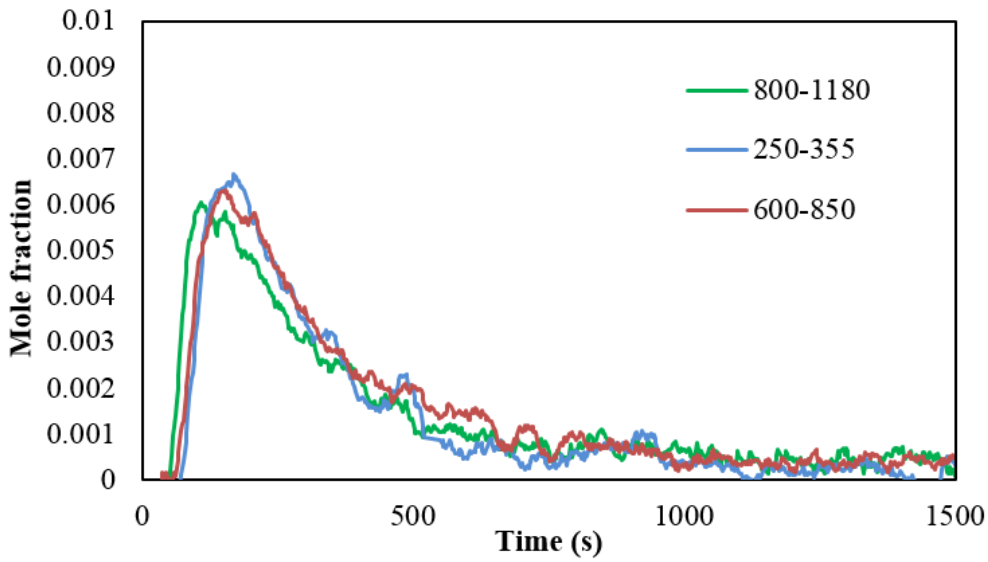

Figure 4-3 Gasification of Polish char in FB at 1123 K, by 100% CO_2, with different particle size fractions, in μm.

The $f(X)$ expression obtained at 1123 K was then applied to the model to compute experimental results at all temperatures. Figure 4-4 presents the comparison of the rate of gasification under different operating conditions (whilst no CO was intentionally introduced into the reactor at this stage) between experimental and modelled results. It shows good agreement between the experimental and modelled data from 1123 to 1248 K, and at various CO_2 concentrations.

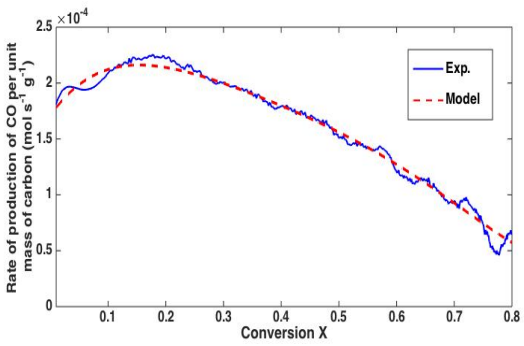

(a)

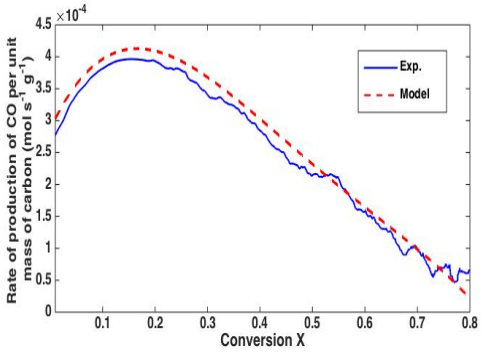

(b)

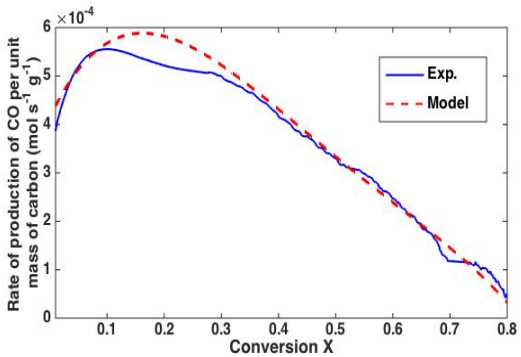

(c)

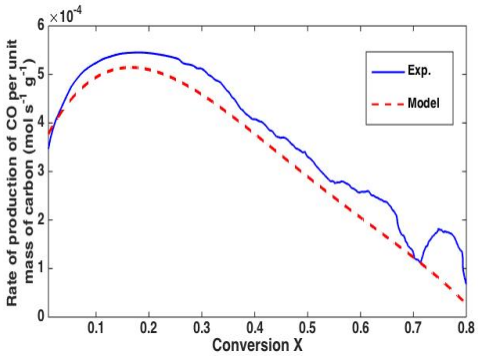

(d)

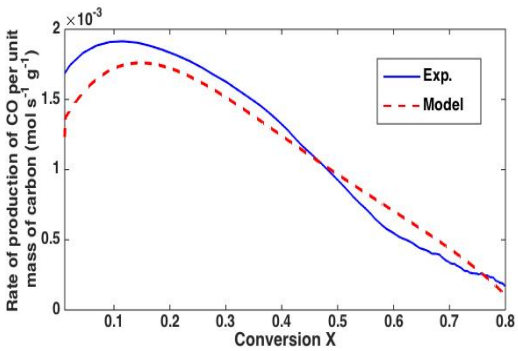

(e)

Figure 4-4 Comparison of experimental and model (based on Ergun's mechanism) results of gasification with conditions (a). at 1123 K, by 20% CO_2, (b). at 1123 K, by 60% CO_2, (c). at 1123 K, by 100% CO_2, (d). at 1173 K, by 20% CO_2, and (e). at 1248 K, by 20% CO_2.

The comparison of the concentration of CO within the char particle over gasification were modelled, with results at 1123 K and 1248 K were shown in Fig. 4-5. The concentration of CO depends on the rate at which it is produced by the reaction and the rate at which it

diffuses from the particle. As illustrated in Fig. 4-5a, at 1123 K, the local CO mole fraction at the particle centre firstly increases to a maximum (~ 0.021) from an initial value of ~ 0.018, followed by a gradual decrease to zero. As the temperature increases to 1248 K (Fig. 4-5b), the change in the [CO] at the centre was from 0.135, to 0.150, and to 0. The corresponding maximum deviations from the boundary value to the centre of CO_2 (not shown here) is 0.07, *i.e.* 0.2 at the boundary and 0.13 at the centre. From the deviation in the concentration of CO_2 across the particle, no significant influence from diffusion was expected, yet the large changes in CO concentration might have still imposed some diffusion limitation. For a system, in which the reaction rate is a non-linear function of both the product and the reactant, the effect of diffusional resistance depends on the sensitivity of the rate to the concentration of these species. The large amount of CO that builds up (suggested by Fig. 4-5b) and the lack of apparent limitation on the gasification indicates that the gasification rate is relatively insensitive to the concentration of CO. The form of the Ergun expression and the values of the constants used, mean that the apparent kinetics are not greatly affected by a large CO concentration.

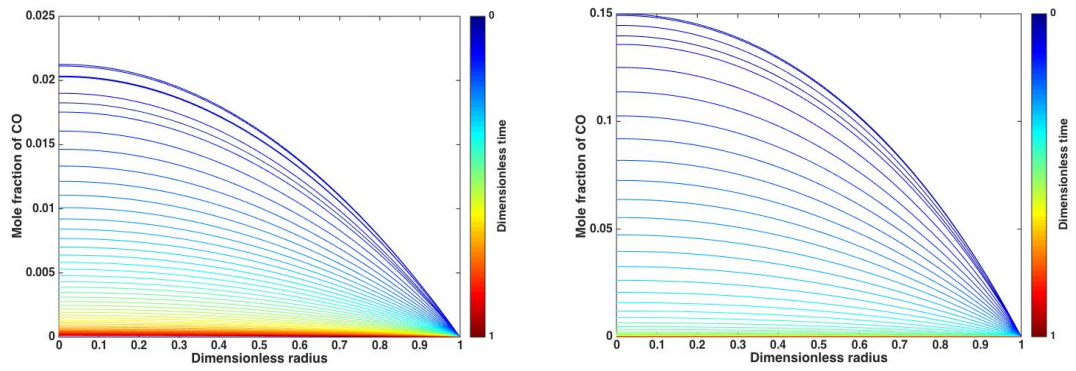

(a) (b)

Figure 4-5 Modelled (based on Ergun's mechanism) CO mole fractions inside the char particle gasified by 20 % CO_2 at (a). 1123 K, and (b). 1248 K.

4.4.4 The effect of CO

The modelled (*i.e.* based on Ergun's expression), and experimental results of gasification agreed reasonably well in the cases presented previously, in which the background levels of CO in the experiments were small. However, as shown in Fig. 4-6, when CO was present in the fluidising gas, the fitting was very poor for both the two concentrations of CO. The modelled results significantly over-estimated the gasification rates.

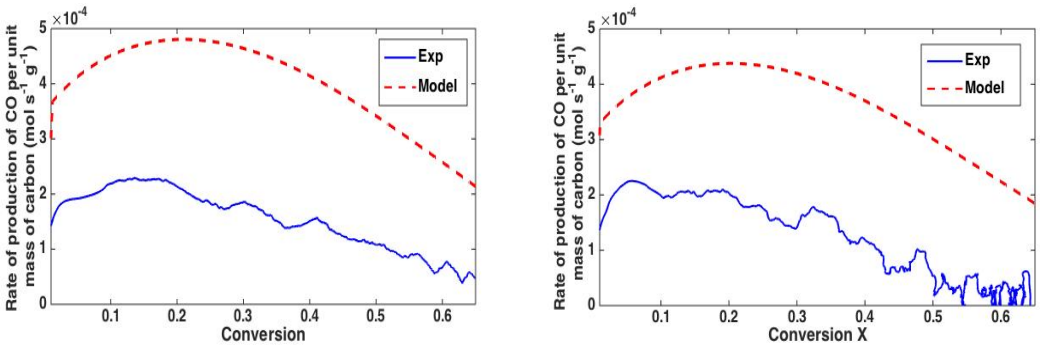

(a) (b)

Figure 4-6 Comparison of experimental and modelled results (based on Ergun's mechanism) of gasification by 20% CO_2 at 1173 K, mixed with (a). 1% CO, and (b). 3.4% CO.

4.5 Discussion

4.5.1 Refitting the results based on different CO concentrations

The model, based on Ergun's mechanism, fitted well with the experimental data without any intentionally introduced CO in the background; whilst it over-estimates the experimental data when CO was applied. It should be aware that the kinetic data used for the model was obtained from the experimental results at various temperature and CO_2 concentrations from 20% to 100%. For these conditions, the measured initial CO concentrations were low, and their effect on the estimation of kinetic data might not be significant. The obtained kinetic data, in this case, might only suit for low CO concentrations at a wide range of CO_2 concentrations. This means the only term that describes the inhibition effect of C, $\frac{k_{-1}}{k_1}$, might have been underestimated, and the underestimated effect only becomes significant and noticeable when [CO] is significant. Therefore, to be able to predict the conditions with 1% and ~3.5 % CO in the background gas, the kinetic data were re-fitted by taking into account all levels of CO at different CO_2 concentrations. Table 4-3 gives the refitted kinetic data, based on Ergun's mechanism. The activation energy of $\frac{k_{-1}}{k_1}$ obtained this time was -108 kJ/mol (with a fixed the pre-exponential factor A = 4150), much higher the originally obtained - 93 kJ/mol. The much higher values of $\frac{k_{-1}}{k_1}$ from the re-fitting, as shown in Table 4-3, suggests more pronounced effect of CO inhibition. Figure 4-7 presents the results based on the re-fitted kinetic data at various conditions at 1173 K. Much improved fitting of the experimental results was obtained with the new kinetic data for all the conditions, compared to Fig. 4-6.

Table 4-3. Re-fitted kinetic data based on CO at various concentrations.

Temperature (K)	ck_1	ck_2	k_2/k_1	k_{-1}/k_1
1148	0.0061	0.0002	0.036	19.699
1173	0.0196	0.0003	0.017	15.478
1223	0.0176	0.0008	0.046	9.842
1248	0.0466	0.0013	0.027	7.956

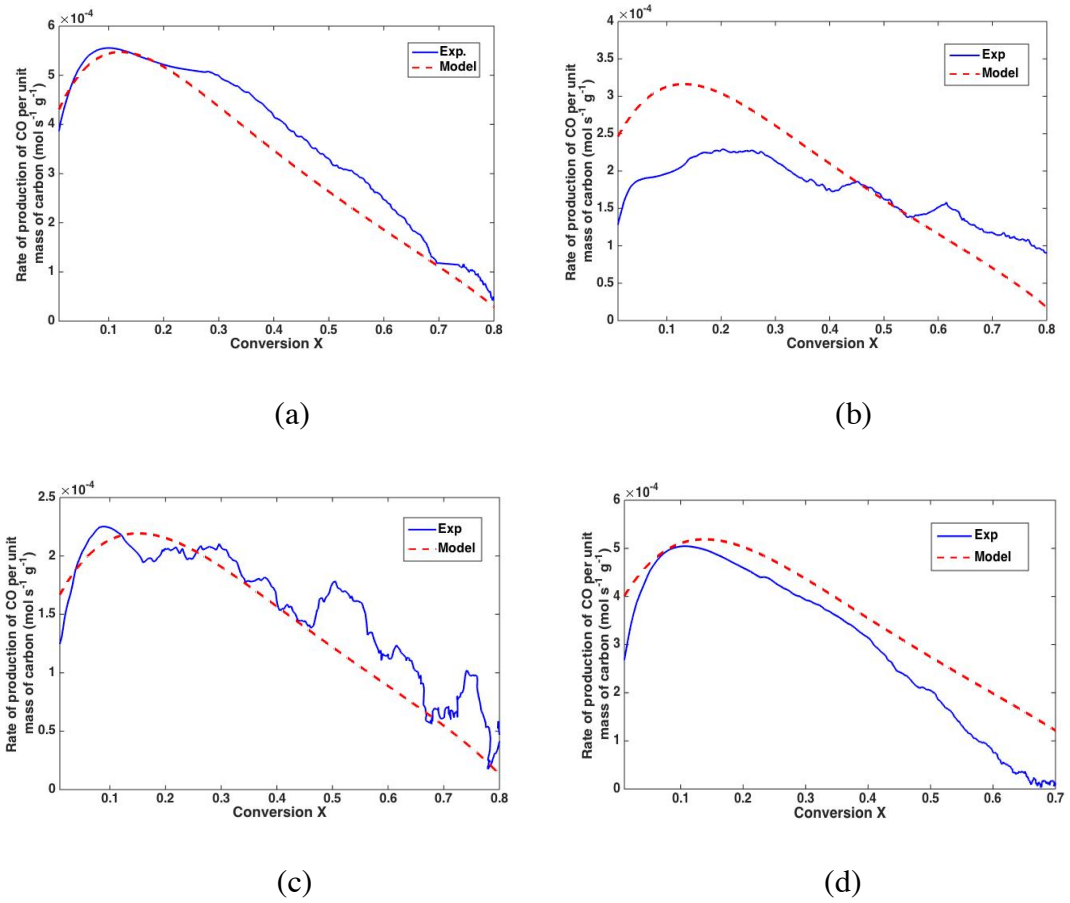

Figure 4-7 Gasification results using the re-fitted kinetic data at 1173 K in (a). 20% CO_2 + 0% CO, (b). 20% CO_2 + 1% CO, (c). 20% CO_2 + 3.4 % CO, and (d). 60% CO_2 + 1% CO.

4.5.2 Rate expression based on a three-step mechanism

A new rate expression based on a three-step mechanism is deduced as follow. The intra-particle mass transfer in the model remains the same as previously described. The new

mechanism is a combination of Mechanisms A (Ergun's) and B. It differs from Ergun's mechanism by taking into account the situation when CO gas molecules can block the active sites to form C(CO):

$$CO_2(g) + C_f \underset{k_{-1}}{\overset{k_1}{\rightleftharpoons}} CO(g) + C(O)$$

$$C(O) \xrightarrow{k_2} CO(g) + nC_f$$

$$CO(g) + C_f \underset{k_{-3}}{\overset{k_3}{\rightleftharpoons}} C(CO).$$

By applying assumptions from the Langmuir adsorption isotherm [171], and at steady state, the rate of formation of $C(O)$ equals the rate of disappearance of $C(O)$:

$$\frac{d\theta_1}{dt} = k_1 p_{co_2}(1 - \theta_1 - \theta_2) - k_{-1} p_{co} \theta_1 - k_2 \theta_1 = 0.$$

Similarly, for $C(CO)$:

$$\frac{d\theta_2}{dt} = k_3 p_{co}(1 - \theta_1 - \theta_2) - k_{-3} \theta_2 = 0.$$

θ_1 and θ_2 are respectively the surface active coverage by $C(O)$ and $C(CO)$.

The rate of carbon transfer per unit mass of carbon from solid phase to the gas phase is then $R'_g = ck_2\theta_1$, giving a final rate expression of

$$R'_g = \frac{2ck_2 \times p_{co_2}}{p_{co_2} + \left(\frac{k_{-1}}{k_1} + \frac{k_2}{k_1} K_3\right) \times p_{co} + \frac{k_{-1}}{k_1} K_3 \times {p_{co}}^2 + \frac{k_2}{k_1}} f(X), \qquad \text{Equation 4-21}$$

where

$K_3 = \frac{k_3}{k_{-3}}$.

To obtain the values of the kinetic terms, Eq. 4-19 is rearranged into:

$$\frac{p_{co_2}}{R'_g} = \frac{1}{2ck_2}\left(p_{co_2} + \left(\frac{k_{-1}}{k_1} + \frac{k_2}{k_1} K_3\right) p_{co} + \frac{k_{-1}}{k_1} K_3 {p_{co}}^2\right) + \frac{1}{2ck_1}. \qquad \text{Equation 4-22}$$

This new rate expression has an extra term describing the inhibition effect of CO, depending on the square of the partial pressure of CO. By taking the slope and the intercept of $\frac{p_{co_2}}{R\prime_g}$ versus $\left(p_{co_2}+\left(\frac{k_{-1}}{k_1}+\frac{k_2}{k_1}K_3\right)p_{co}+\frac{k_{-1}}{k_1}K_3{p_{co}}^2\right)$, $2ck_2$ and $2ck_1$ are obtained. The kinetic data are obtained by achieving least squared values of the initial rates. k_{-1}/k_1 and K_3 are constrained to follow the Arrhenius relation. Table 4-4 presents the values of the kinetic data for the new equation, and the new modelled results, in comparison to the experimental results, are shown in Fig. 4-8.

Table 4-4 Kinetic results of char gasification based on the new rate equation.

Temperature (K)	ck_1	ck_2	k_2/k_1	k_{-1}/k_1	K_3
1148	0.0054	0.00022	0.0405	19.751	0.570
1173	0.0087	0.00034	0.0366	15.470	0.558
1223	0.0096	0.00082	0.0897	9.954	0.535
1248	0.0371	0.0012	0.0337	8.090	0.524

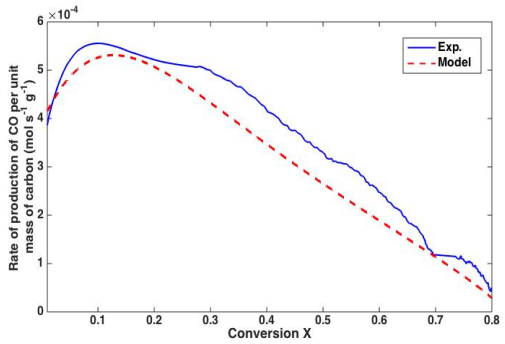

(a)

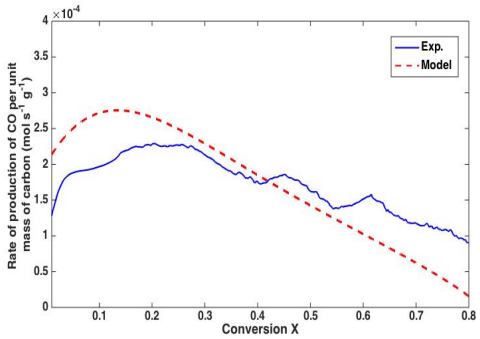

(b)

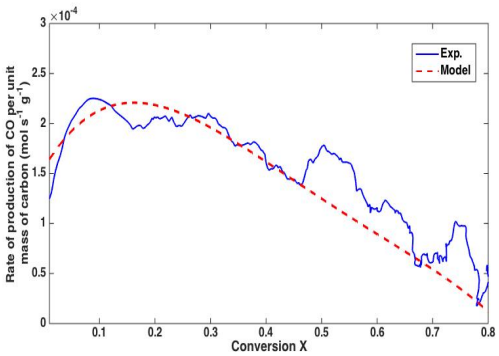

(c)

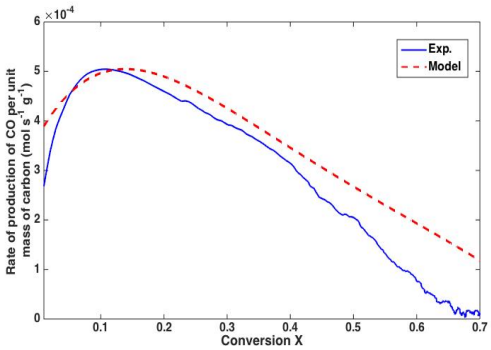

(d)

Figure 4-8 Gasification results of the new rate equation (three-step mechanism) at 1173 K by (a). 20% CO_2 + 0% CO, (b). 20% CO_2 + 1% CO, (c). 20% CO_2 + 3.5 % CO, and (d). 60% CO_2 + 1% CO.

According to Fig. 4-8, good fitting of the experimental data with the results from the three-step mechanism, was achieved for various combinations of CO and CO_2 concentrations. Comparing Figs. 4-7 and 4-8, the new rate equation model even gave a slightly better fit for the conditions at 20% CO_2 + 1% CO. At this stage, it is difficult to determine which rate expression is significantly is better for describing the gasification of Polish char, but both show higher sensitivity to the presence of CO than the results based on Ergun's mechanism with no introduction of CO. The mole fractions of CO across the radius of a char particle over gasification by 20% CO_2 modelled from the three conditions: Ergun's mechanism with kinetic data obtained at no introduction of CO, Ergun's mechanism with kinetic data involving introduction of CO, and three-step mechanism, were compared and shown in Fig. 4-9. The mole fractions of CO inside the char particle from Fig. 4-9b and 4-9c are much lower than the one from Ergun's mechanism with kinetic data obtained without CO addition experiments (Fig. 4-9a). However, the modelled overall gasification rates of the char particle from the three conditions all fitted well of the experimental data, as shown in Figs. 4-4d, 4-7a, and 4-8a, indicating higher sensitivity to CO locally with the latter two situations.

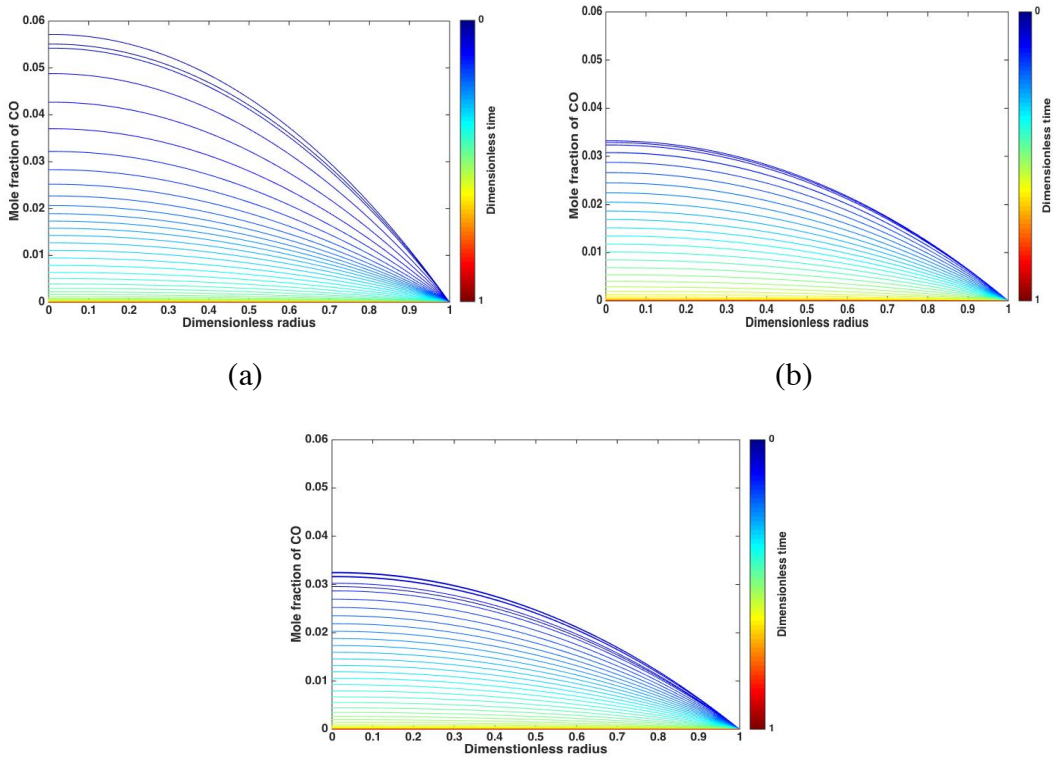

Figure 4-9 Modelled CO mole fraction across the radius of the char particle over gasification by 0 % CO and 20 % CO_2 at 1173 K, based on (a). Ergun's mechanism with kinetic data obtained at no introduction of CO, (b). Ergun's mechanism with the kinetic data obtained involving the introduction of CO, and (c). three-step mechanism.

The local gasification rate across the char particle from the three-step mechanism was also presented to understand the effect of local CO on the gasification rate. Figure 4-10 shows the local rates under various introduced CO concentrations at 1173 K. Some difference, whilst not significant, in the gasification rate between the particle center in the initial period was observed when gasified by 20% CO_2 (no introduced CO), as shown in Fig. 4-10a, corresponding to the case when a maximum of ~ 3% accumulation of CO in the particle center and 0% at the surface in Fig. 4-9c. This indicates less effect of the [CO] gradient on the local gasification rate in the beginning of gasification. The overall gasification rate, as shown in Fig. 4-8a, also seems to be similar to the roughly averaged local gasification rates from the center to the surface. In the later stage of gasification, larger differences in the local rate across the particle were observed in Fig. 4-10a. This probably mainly resulted from the difference in local conversion, caused by the differences in local $f(X)$values.

When there is the intentionally introduced CO in the background (1% and 3.4%), as seen in Fig. 4-10b and 4-10c, the presence of the high [CO] in the background significantly decreased the local rates across the radius. Furthermore, the rates in the center decreased to much lower values than the rate of in the presence of 3% locally produced CO (Figs. 4-9c and 4-10a). This indicates a higher sensitivity of the gasification rate to the externally added CO rather than locally self-produced CO. In addition, the rate gradients across the particle when CO was intentionally introduced in Fig. 4-10b and 4-10c, are lower than over the whole gasification period. The dimensionless radius here was defined as the ratio of distance between a radial position and the particle center, over the initial radius of the particle.

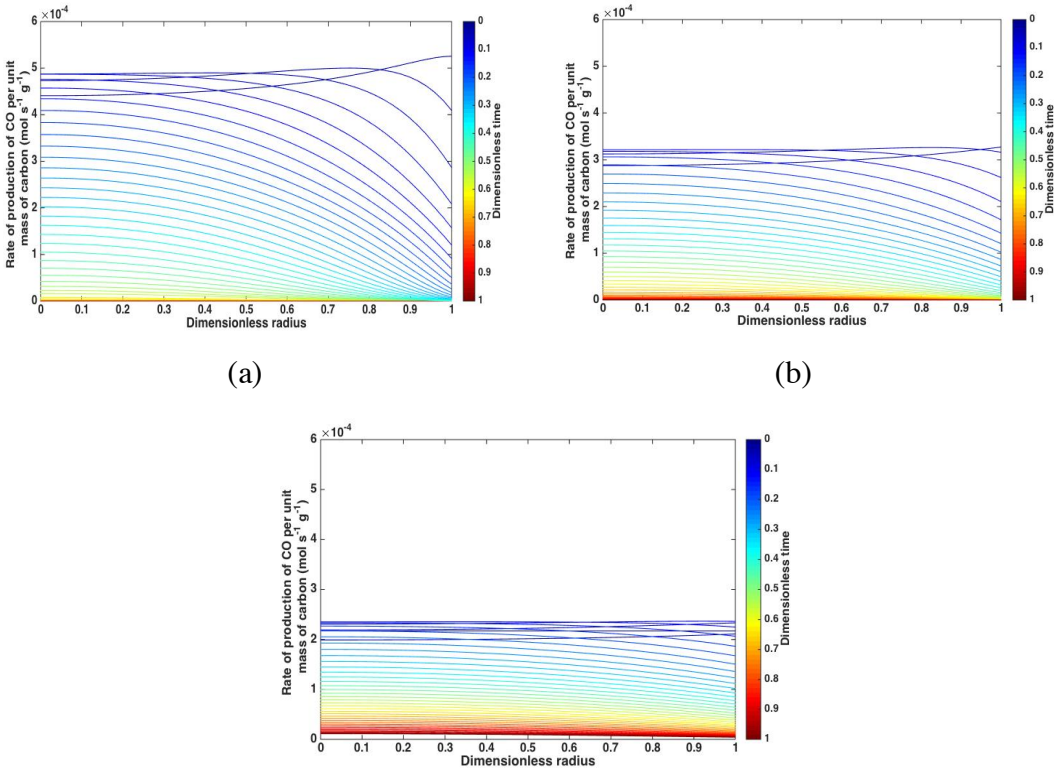

(a) (b)

(c)

Figure 4-10 Local gasification rate (modelled based on the three-step mechanism) across the radius of the char particle over gasification time at 1173 K, in 20% CO_2 mixed with (a). 0% CO, (b). 1% CO, and (c). 3.4 % CO as gasification agent.

Investigation of the effect of the intentionally introduced CO in the background on the gasification rates is carried out here. Roberts and Satterfield [172] defined a modified Thiele modulus, for a reaction with a rate expressed as:

$$r = \frac{kp_A}{1+K_A p_A+\sum_l K_l p_l}, \qquad \text{Equation 4-23}$$

where l is used to denote any reaction product other than the reactant A. According to Eqs. 4-4, 4-8, 4-9 and 4-23, the following relations can be obtained

$k = ck_1\rho_{in} \times f(X)$

$K_A = \frac{k_1}{k_2}$

$K_i = \frac{k_{-1}}{k_2}$.

The modified Thiele modulus by Roberts and Satterfield is:

$$\phi_m = L(\frac{k'' R_{ideal} T}{D_{co_2}^{eff}})^{1/2},$$

where

$$k'' = \frac{k}{\omega}$$

$$\omega = 1 + K_i[p_{co,s} + (2p_{co_2,s} D_{co_2}^{eff}/D_{co}^{eff}].$$

$D_{co_2}^{eff}$ and D_{co}^{eff} are the effective diffusivity of CO_2 and CO. $p_{co,s}$ and $p_{co_2,s}$ refer to the partial pressures of CO and CO_2 at the particle surface. L refers to the characteristic length of a particle. Without the addition of CO to the system, the surface CO partial pressure, $p_{co,s}$, is always zero (the boundary condition used in the study), as a result, $p_{co,s}$ in the denominator of the ϕ_m can be removed. Whereas, when CO is added to the fluidising agent, the presence of $p_{co,s}$ results in a decrease of ϕ_m. This means that the addition of CO suppresses the rate gradient across the particle. As seen in Fig. 4-10, the change of externally introduced CO from 0% to 3.4% CO results in a decrease of concentration gradient across the particle. With higher level of CO present on the surface, the local rate at the center becomes more sensitive to the surface high CO concentration. The boundary condition of high CO restrained the overall gasification of the particle.

4.6 Conclusions

The main results from the numerical study of the gasification of Polish char and the investigation of the inhibition effect of CO are summarised as follow:

a). A numerical model based on Ergun's two step mechanism and the kinetic data obtained without the addition of CO to the system, was used to fit the experimental gasification results. It gave good fit of the experimental results of gasification at various CO_2 concentrations (without CO introduced externally) at different temperatures. However, the model significantly over-estimated the gasification rates when CO was intentionally added.

b). By including the experimental results of adding CO, new kinetic data from Ergun's mechanism was obtained. With the re-fitted data, the fitting of the experimental results was significantly improved. The higher $\frac{k_{-1}}{k_1}$ values for Ergun's two step mechanism suggest enhanced inhibition effect of CO. Based on a fixed pre-exponential factor A (A= 4150), an activation energy of $\frac{k_{-1}}{k_1}$ of -108 kJ/mol was obtained for the newly fitted kinetic data, much higher than the previously suggested ~ -95 kJ/mol.

c). A new rate expression developed from a three-step mechanism was developed, and it has an extra term (depending on the square of p_{co}) describing the inhibition effect of CO. The model based on this three-step mechanism fitted well of the experimental data both without and with (*i.e.* 1 % and 3.4 % CO) the introduction of CO.

d). The study showed more pronounced inhibition effect of CO than expected, especially when CO was intentionally introduced in the system, along with the gasification of CO_2. According to the modified Thiele modulus, the added CO suppresses the rate gradient across the particle. This is probably the main reason for the gasification rate being more sensitive to the surface CO concentration than the local produced CO.

5.0 Development of a combined system of fluidised bed and a plasma reactor for the quantification of biomass-derived tar and investigation of the effect of oxygen carriers and the presence of CO_2 on biomass product distribution

5.1 Introduction

The effect of Fe-based oxygen carriers on CO_2 gasification of a clean solid fuel, a Polish coal-derived char, has been studied in Chapter 3. Practically, raw fuels, instead of de-volatised fuels, would be used directly in industries. Direct use of un-pretreated solid fuels such as coal and raw biomass, would make the process more complicated, introducing multiple phases of products under thermal treatment, including gaseous products such as CO, CO_2, organic acids, condensable volatiles, and solid char.

CLC of liquid fuels has been studied only recently and has been normally based on model compounds due to the complexity of liquid fuels or tar. Mendiara *et al*. [173] investigated tar (toluene) removal by selective reforming in a chemical looping system (in TGA and a lab-scale fixed bed reactor), using four oxygen carriers (60% $NiO/MgAl_2O_4$, 40% $NiO/NiAl_2O_4$, 40% Mn_3O_4/Mg-ZrO_2, and $FeTiO_3$). The study compared the extent of carbon deposition of toluene on the four oxygen carriers. 40% $NiO/NiAl_2O_4$ and 40% Mn_3O_4/Mg-ZrO_2 were reported to have good reactivity with toluene, but 40% $NiO/NiAl_2O_4$ showed a high tendency for carbon deposition. They also found that the addition of H_2O reduced carbon deposition. However, the characterization of the products (apart from the deposited carbon) from the reaction between the oxygen carriers and toluene were not mentioned in this study; therefore it is not clear how these oxygen carriers further affect the distribution of the products. Ryden *et al*. [174] investigated CLC of kerosene with Ni-, Mn-, Cu- and Fe-based oxygen carriers in continuous operation. They reported 95% - 99% conversion of the fuel carbon converted to CO_2. CLC of solid fuels such as raw biomass or coal, rather than the derived char has been studied to a lesser extent. Some work [175–177] on char has been carried out in inter-connected fluidised CLC systems with continuous operation. However, the quantification of the amounts or character of the volatile matter and tar produced (other than CH_4) has not been undertaken. The effect of oxygen carriers on tars is not fully understood, and, it would be helpful to understand how the product distribution varies under thermal treatment (pyrolysis), and in the presence of different oxygen carriers.

This chapter aims to understand the effect of oxygen carriers on the processing of biomass, which is renewable and cleaner than raw coals, in a fluidised bed. In particular, the effect of oxygen carriers on the distribution of products under thermal treatment (pyrolysis) is examined. In addition, how the presence of gasification agent, CO_2, affects the distribution of the product is studied, and compared with the effects of oxygen carriers. The main challenge for the current study was the quantification of the condensable volatile product (liquid fuels), referred as tar in this work. Therefore, an online continuous tar measurement system needs to be first developed.

5.1.1 Tar measurement system

For the continuous quantification of the tar produced from the upstream, an online tar measurement system, based on the conversion of tar to light carbon-containing gaseous products at mild temperatures is developed. Dielectric barrier discharge (DBD) is a promising technique to achieve this conversion. DBD reactors have been widely studied for the abatement of VOCs [88,96,97,99]. In the current study, a DBD reactor was developed to convert the tar produced to species such as CO and CO_2, which enables the quantification of the tar to be achieved by measuring these non-condensable carbon-containing species. If the developed system is successful in the quantification of the tar, the investigation of the product distribution from biomass pyrolysis and gasification/reforming in the presence of oxygen carriers can then be carried out. In the current study, two typical oxygen carriers: Fe_2O_3, and CuO (supported on mayenite) were selected as the oxygen carriers.

5.2 Experimental methods

Pyrolysis of a biomass fuel, wood chips, was carried out in a quartz tube reactor, as described in 2.3.3. The pyrolysis results from a bed of active oxygen carrier (Fe_2O_3 or mayenite-supported CuO) were compared with the reference conditions in alumina sand. The temperature range of interest was from 773 to 1173 K. In addition to the fluidising pyrolysis gas being N_2, the effect of the presence of gasification agent CO_2 (~18% CO_2) on the distribution of product from the fluidised is investigated. The CO_2 experiments were carried only in alumina sand bed. The products generated from the fluidised bed including non-condensable gases, condensable volatiles and solid char were measured by different approaches. Non-condensable gases were measured by FTIR, the condensable

volatiles (referred as tar here), was measured by the tar quantification system. The quantification of char was performed by burning off the bed with air after the pyrolysis or gasification stage. For the quantification of the tar, a plasma reactor was developed and positioned downstream of the fluidised bed. For every experiment, two single runs with plasma reactor on and off (other conditions kept the same), were carried out to allow quantify the tar. A side stream of air was introduced into the plasma reactor and converted the tar into light carbon-containing gaseous species (when plasma on) that were measurable by FTIR. The difference in the signals detected by the FTIR in the two runs indicated the amount of the carbon content in the tar from the upstream. The oxygen level in the sampling line was measured by a paramagnetic oxygen analyser (ABB, EL3020). For a typical experiment, around 20 ml of bed material was fed into the quartz tube and fluidised with a flow at 3 L/min. To avoid the condensation of the tar before it reaches the plasma reactor, both the sampling system and the plasma reactor were externally heated to 573 and 523 K, respectively. More detailed experimental conditions are presented in 2.3.3.

5.3 Results

5.3.1 Tar measurement

- **Identification of the product species**

DBD plasma is effective in activating chemical reactions, and even N_2 (as an inert gas for most conventional chemical reactions) can react easily with other species by plasma effect. Understanding the effect of plasma on some reference gas conditions is important. Figure 5-1 shows the IR spectra (from FTIR) in the following gases passing through to the DBD reactor: pure N_2 or air/N_2 mixture (~ 8.3 vol% oxygen). The gas passing through the FB was N_2 in both cases. Additionally, the effect of plasma on the gases containing product of wood pyrolysis from the fluidised bed was also examined. In Fig. 5-1, the significant peaks at around 630 - 710 cm^{-1}, 2280 - 2380 cm^{-1}, and 3580 - 3770 cm^{-1} are the typical peaks of CO_2. The main species detected from plasma running in N_2 was CO_2 (< 100 ppm). The CO_2 peaks in N_2 might have come from contamination in the system or have been an artefact of the background subtraction. No nitrogen-containing species were detected by the FTIR. When the stream of air joined the N_2 and was passed through the plasma reactor, the products detected were N_2O, NO_2, NO, and CO_2. In Fig. 5-1, only the main peaks of N_2O and NO are marked, because the secondary peaks overlapped those

for CO, CH_4 and CO_2. Ozone is often formed in plasma reactor in the presence of air [178], but was not observed here. This might be due to the excess of N_2 and the external heating of the plasma reactor. It could be that any ozone produced quickly decomposed in the heated environment and reacted with N_2 to form more stable species such as NO, N_2O or NO_2. This is in agreement with the findings of Huu *et al*. [97]. They studied methane removal using a plasma-catalytic hybrid reactor, showing that increasing the temperature of a plasma reactor significantly decreased the ozone concentration in the product stream, *e.g*. with a clear ozone signal at 303 K to no signal detected at 573 K.

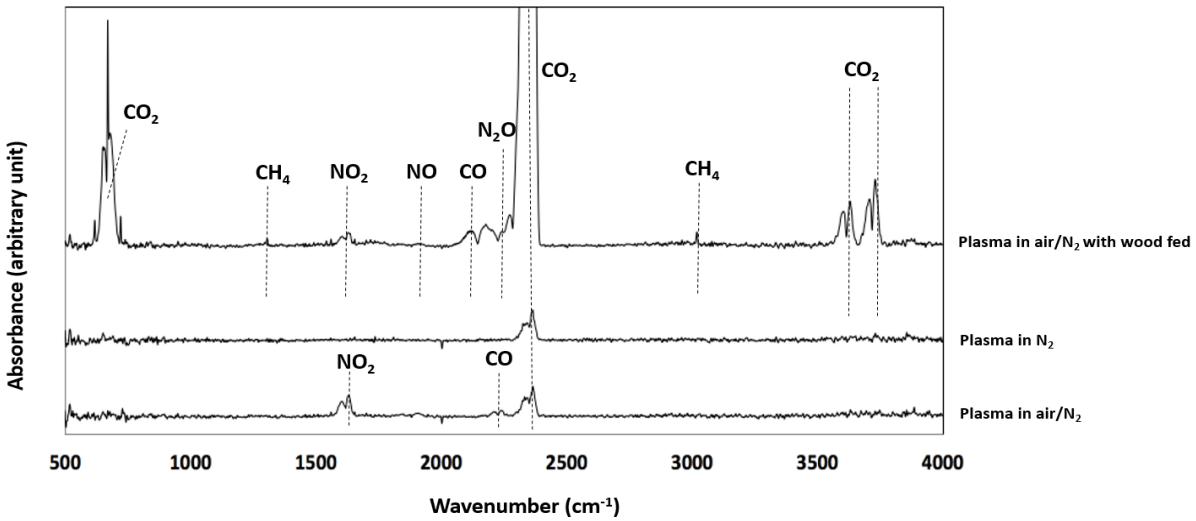

Figure 5-1 Spectrum of species in different gaseous environment in the presence of plasma discharge with FB fluidised in pure N_2 (SED of 1027 J/L).

When wood chips were fed into the fluidised bed, the pyrolysis products entered the sampling system. A comparison between the spectra with wood fed into a fluidised bed of alumina sand at 873 K with the plasma on and off, is presented in Fig. 5-2**.** With the plasma running, the products after the plasma reactor, and having passed through the cold trap, were mainly N_2O, NO_2, NO, CO_2, CH_4 and CO. Whereas, the main gaseous products without downstream plasma running, were CO, CO_2, and CH_4. Some other absorption peaks at ~ 950, 1700, and 3050 cm^{-1} were also observed without plasma running. They seem to match the peaks of acetic acid, CH_3COOH. The fact that no acetic acid signal was detected in the plasma-treated case suggests that plasma converted the acetic acid to other species, mostly likely CO or/and CO_2. The plasma reactor also seems to have converted some of CH_4 due to lower intensity of CH_4 signals observed with plasma running. It should also be remembered that any heavier hydrocarbons, which do pass

through the sampling system unconverted, would be removed before the FTIR by the cold trap.

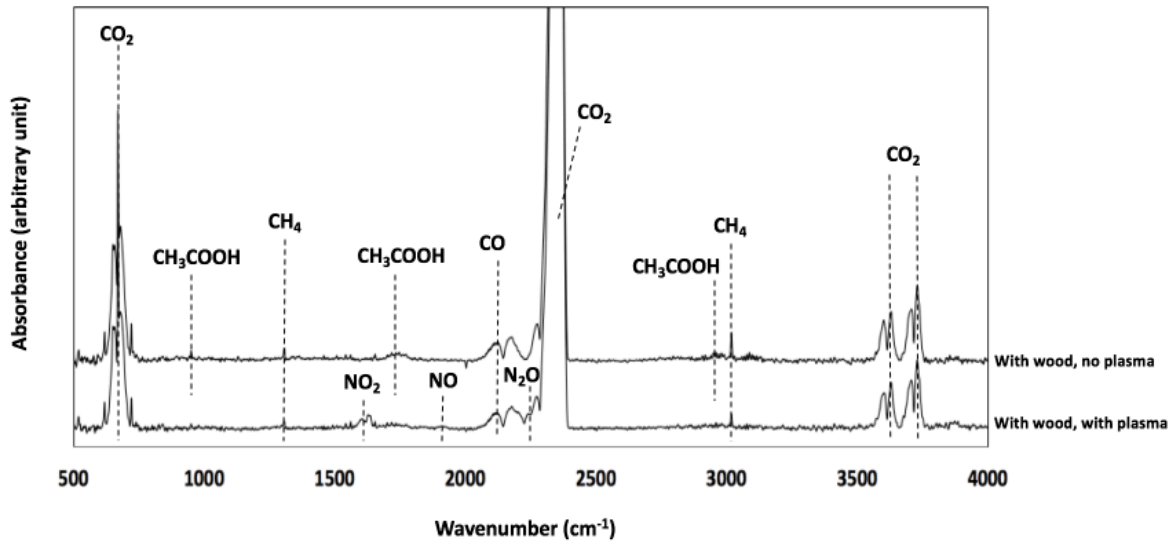

Figure 5-2 Spectrum of gaseous products with/without plasma running with wood fed into the fluidised bed (in N_2) of alumina sand at 873 K (SED of 1027 J/L).

- **Characterisation of the flow**

The change in composition of the gases can change appreciably the total flow rate through the sample line. In particular, the generated tar (without plasma running) appeared to block the sampling line, leading to an increased pressure drop, and causing a change in the total flow rate through the line. To resolve the issue, correction of the change in the flow was applied. For the condition without plasma running, the oxygen introduced by the side air stream can be treated as the tracing element for the estimation of the total flow in the sampling line. Whilst in the case with plasma running, the oxygen was consumed in the plasma reactor for the conversion of the tar. In this case, some model tar compounds were assumed to estimate the amount of oxygen consumed in the DBD reactor and thus work back to the total flow rate in the sampling line.

Without plasma

The air flow, F_{air}, introduced to mix with the product flow sampled from the fluidised bed was controlled by a variable area flow meter and assumed to be constant at 0.45 L/min. When there was no plasma ($i.e.$ oxygen was not consumed), the oxygen in the air

flow was used as a tracer. The total flow rate in the sampling line during the experiment, F_{total}, could therefore be obtained by

$$F_{total} = \frac{F_{air} \times 0.21}{x_{O_2}}. \qquad \text{Equation 5-1}$$

Here, x_{O_2} is the mole fraction of oxygen detected by the ABB analyser, with 0.21 being the measured mole fraction of oxygen in the supplied laboratory air. If no change in sampled gas flow occured, the "ideal" mole fractions of product species detected by the analyser would be

$$x_{i,ideal} = \frac{F_{FB,initial} \times y_i}{F_{FB,initial} + F_{air}} \qquad \text{Equation 5-2}$$

$$x_i = \frac{F_{FB} \times y_i}{F_{FB} + F_{air}}. \qquad \text{Equation 5-3}$$

In Eq.5-2, $x_{i,ideal}$ is the "ideal" mole fraction of the product species *i* detected by the analyser, assuming negligible change in the total flow rate due to change in the pressure drop. $F_{FB,initial}$ is initial flow rate of the gas stream that entered to the sampling line and y_i is the mole fraction of species *i* in the gas flow from the fluidised bed. For the non-ideal case, where the flow rate from the fluidised bed upstream changed due to condensation or trapping of tar or water in the sampling line, F_{FB}, would be lower than $F_{FB,initial}$, leading to lower measured mole fractions of the product species i, x_i. By combining Eqs.5-2 and 5-3, the rearrangement gives

$$x_{i,corrected} = \frac{x_i \times F_{total} \times F_{FB,initial}}{F_{total,initial} \times F_{FB}},$$

where

$$F_{total} = F_{FB} + F_{air}.$$

Corrected, "ideal" mole fractions of the product species were used for the calculation of yields.

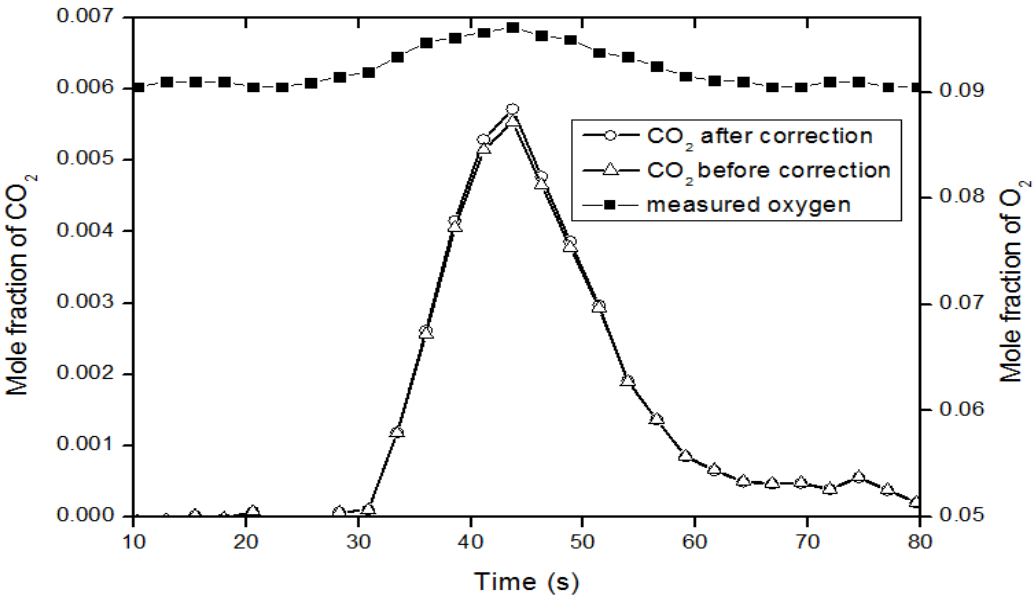

Figure 5-3 Mole fractions of CO_2 before and after the correction of the flow, with operating in a Fe_2O_3 bed at 873 K in the FB without plasma discharge in the DBD reactor. The measured mole fraction of O_2 is also shown. Note that the wood was fed into the fluidised bed at t = 30 s.

Figure 5-3 shows the results of wood pyrolysis in a fluidised bed of Fe_2O_3 at 873 K, without plasma running. The oxygen, which was expected to be inert, increased a little when the wood was fed into the bed. The corrected CO_2 curve based on the measured oxygen curve is very similar to that before correction, suggesting that the change in the flow did not have a significant effect on the concentration of CO_2 measured. A similar observation was made when using other gases and at different temperatures. In the gas environment of CO_2, however, there was a significant difference between the measured and corrected mole fraction profiles of the product species. Figure 5-4 compares the results without and with the correction of the total flow rate when no plasma was running. According to Fig. 5-4a, when the wood chips were fed into the fluidised bed, a sharp increase in [CO] and [CH_4] were seen. After t = 25 s, the fraction of CO_2 started to drop to below the initial stable background level (from 0.088 to 0.068). At the same time, the measured mole fraction of O_2 increased from 0.094 to 0.118 and stabilised at 0.118, unless the flow was manually adjusted. The correlated change (~ 1:1) in the mole fraction of CO_2 and O_2 strongly suggests that this change might be due to change in the flow rate in the sampling line. With the correction of the total flow, as shown in Fig. 5-4b, the mole

fraction of CO_2 and O_2 (after pyrolysis) returned to the initial stable levels. In terms of CO and CH_4, no significant difference in the mole fraction curves between the two cases was observed.

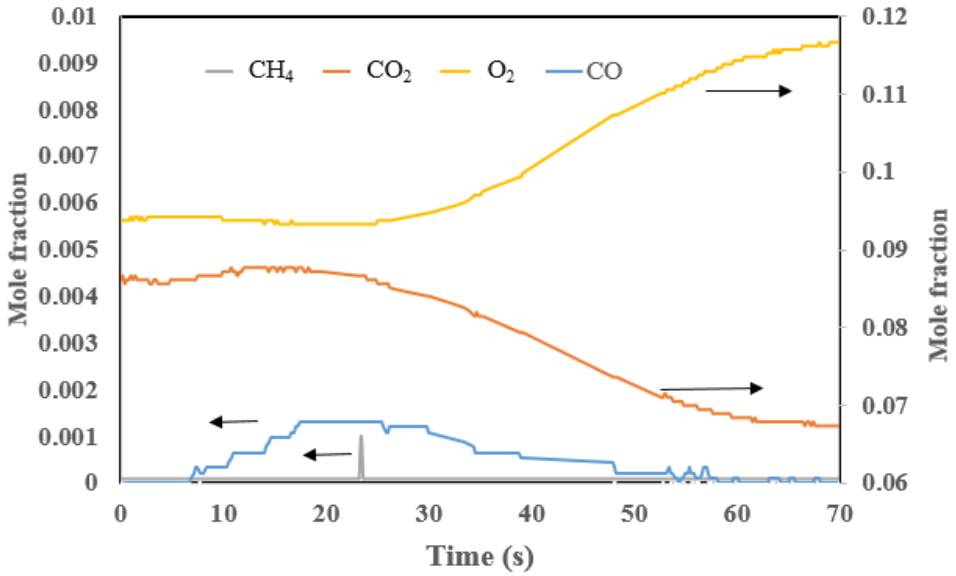

(a)

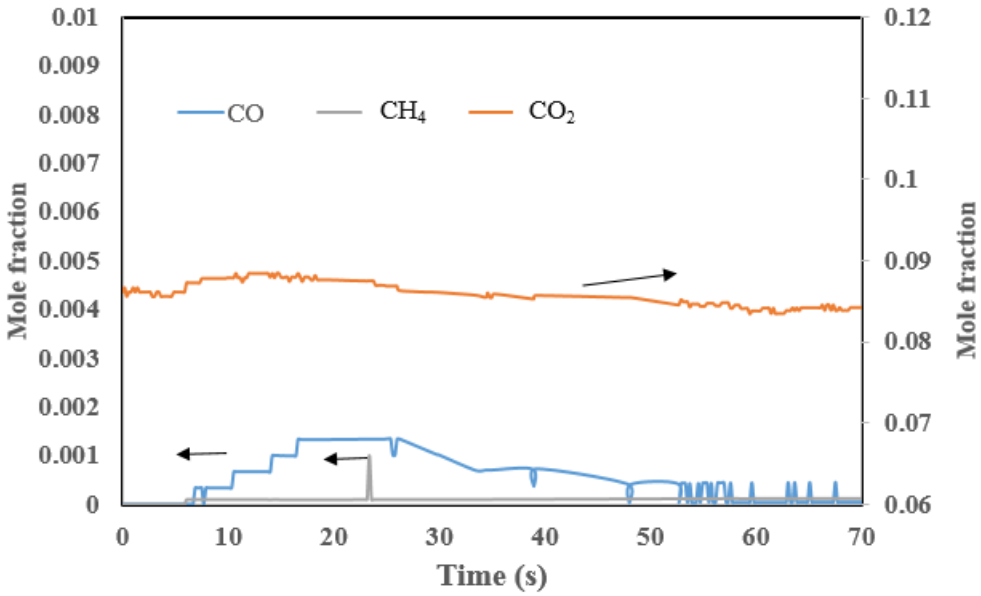

(b)

Figure 5-4 Mole fractions of each gas species from FB at 773 K, fluidised by 18% CO_2, without plasma running: (a). before, and (b). after correction for the changes in the flow rate. Note that the wood was fed into the fluidised bed at t = 7 s.

With plasma

In the case when there is plasma discharge, oxygen was consumed for converting the tar and no longer used as a tracer. In order to correct for changes in the dilution, the oxygen concentration before the plasma reactor was required. It was assumed that the drop in the measured oxygen level is all used to burn the tar and possibly convert CO to CO_2. Assuming that the tar is oxygen-free, then the difference in total O_2 content in the CO and CO_2 between the experiments with and without plasma all comes from the oxygen being consumed. Oxygen is also being consumed to produce water during tar combustion, and this amount depends on the chemical formula of the tar:

$$C_xH_y + \left(x + \frac{1}{4}y\right)O_2 = xCO_2 + \frac{1}{2}y\,H_2O.$$

The amount of oxygen consumed for converting the carbon in tar to CO and CO_2, $F_{O_2,C}$, is

$$F_{O_2,C} = \left(\frac{1}{2}F_{co,on} + F_{CO_2,on}\right) - \left(\frac{1}{2}F_{co,off} + F_{CO_2,off}\right).$$

Here $F_{O_2,C}$ is the molar flow rate of oxygen consumed for burning the carbon content of tar, $F_{co,on}$ and $F_{CO_2,on}$ are respectively the mole flow rates of CO and CO_2 with plasma running, and *off* indicates the condition without plasma. Taking into account the stoichiometry of the tar, $F_{O_2,tar}$, the mole flow rate of oxygen consumed burning the tar is

$$F_{O_2,tar} = F_{O_2,C} * \left(1 + \frac{\frac{1}{4}y}{x}\right).$$

The flow of oxygen through the sampling line, in the absence of combustion, is then

$$F_{O_2} = F_{O_2,tar} + F_{O_2,measured}.$$

Figure 5-5 shows the comparison of flowrates of the mole fractions from pyrolysis of wood chips in a bed of Fe_2O_3 at 873 K of before and after correction. In Fig. 5-5a, the measured oxygen level significantly decreased when the wood was fed into the bed. All the three tar compounds could restore the oxygen profile to the inlet of the plasma reactor, to close to the initial value, among which the correction based on pure carbon appeared to be the best. However, a tar compound usually contains some hydrogen. The fact that

pure carbon could restore the oxygen profile best is a combined effect of: 1) the tar itself might be mainly aromatics, which has very high C to H ratio; 2) the tar might contain some oxygen, which would lead to an over-estimation of the oxygen consumed for burning the carbon content in the tar; 3) incomplete combustion in the plasma reactor; 4) fluctuation in the background flow itself.

Figure 5-5b gives the corrected CO_2 mole fraction based on an oxygen level restored using pure carbon tar compound. There is little difference between the corrected and the measured values, suggesting that with plasma running there is no need to correct for changes in dilution in the sampling line with N_2 in the fluidised bed; qualitatively, very little change in flow was observed when the plasma was active.

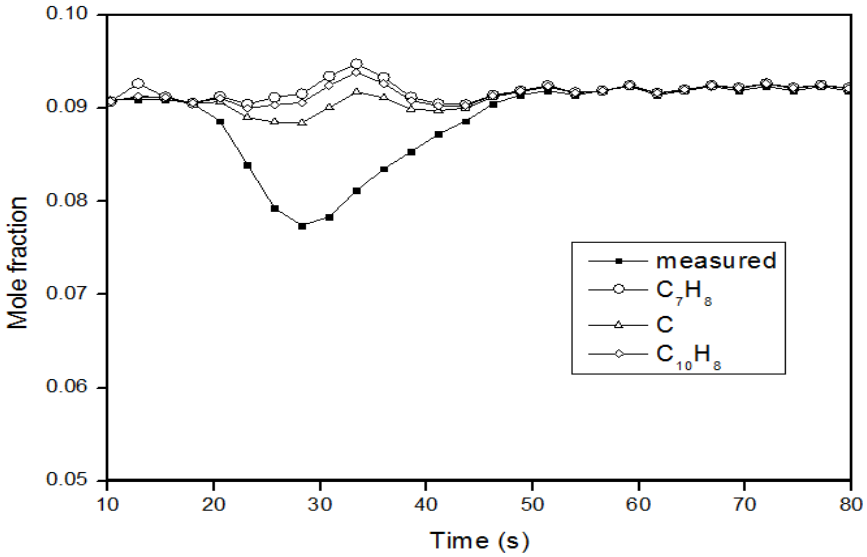

(a)

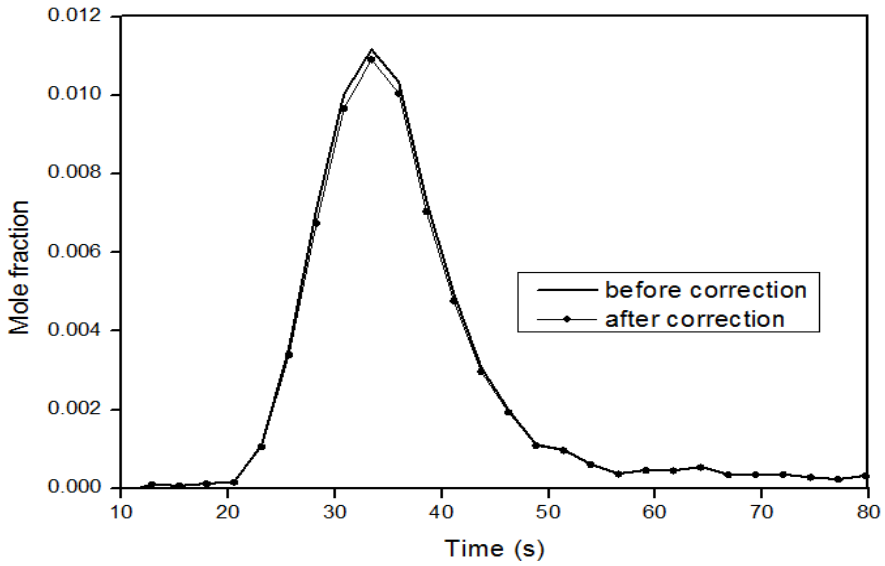

(b)

Figure 5-5 Mole fraction of CO_2 from pyrolysis of wood chips at 873 K in a Fe_2O_3 bed with plasma discharge (a). measured oxygen mole fraction and calculated mole fraction at the inlet to the plasma reactor, based on different tar compound; (b). comparison of the CO_2 before and after correction of the flow. Note that the plasma was turned on at t = 10 s, and wood was fed into the FB at t = 20 s.

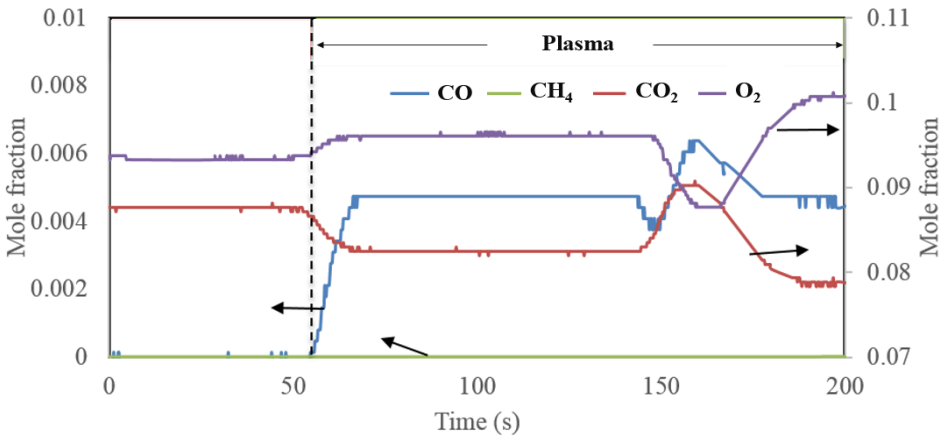

(a)

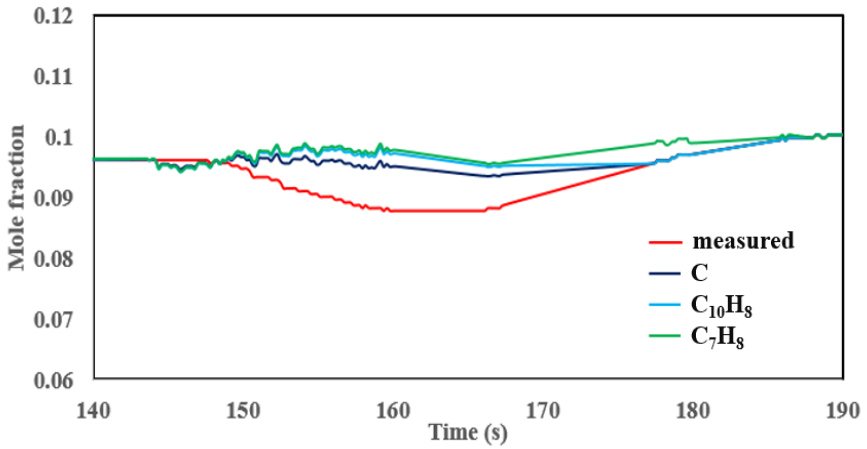

(b)

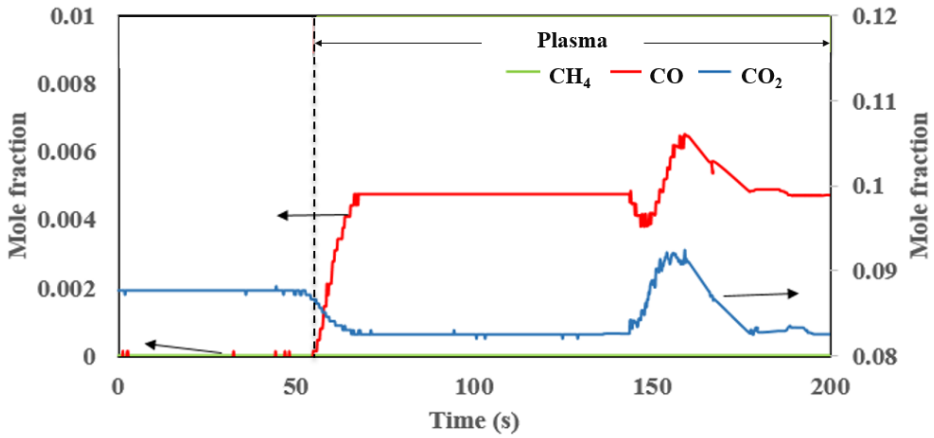

(c)

Figure 5-6 Mole fraction profiles of different species from wood processing at 773 K, with the bed fluidised in 18% CO_2, with plasma running: (a). before correction (b). ideal oxygen mole fraction based on different tar model compounds, and (c). after correction

based on carbon as the tar model. Note that the plasma was turned on at t = 55 s, and wood was fed into the fluidised bed at t = 144 s.

The results from an experiment with the plasma active and with the fluidised bed in 18% CO_2 are shown in Fig. 5-6. When plasma was active, after wood processing in the fluidised bed and the reactions in the plasma reactor, there was an increase in the oxygen level, together with a decrease in the CO_2 level. As seen in Fig. 5-6a, the level of oxygen dropped during the reaction period when the plasma was active. To be able to correct the flow rate, the oxygen profile needs to be 'returned' to the condition where O_2 was 'not consumed' for tar combustion. According to Fig. 5-6b, all the three tar compounds can restore the oxygen profile reasonably well. Figure 5-6c presented the corrected product mole fractions based on an oxygen level restored using pure carbon tar compound. With correction, after the wood processing, the mole fraction of CO_2 returned to the background level.

- **The effect of plasma power**

The plasma power input would affect the type of products after the DBD reactor and the conversion efficiency of the tar in plasma discharge. The effect of the supplied power on the destruction or conversion of the carbon-containing compounds inside the plasma reactor was investigated. This was carried out with the fluidised bed loaded with mayenite-supported CuO in pure N_2 at 873 K. The reason for testing the system in the mayenite-supported CuO bed was that it is more reactive than Fe_2O_3 for combustion and thus expected to result in less tar from the fluidised bed. Therefore, mayenite-supported CuO requires the most sensitive measurements. Figure 5-7 gives the mole fraction of primary carbon-containing species leaving the plasma reactor after a batch of wood chips has been added, as a function of increasing plasma input power (from 0 to 17.1 W, corresponding to SED values from 0 to 1027 J/L). The time taken for completing pyrolysis in each experiment was reproducible (~30 s), as shown in Fig. 5-7. It can be seen that as SED increased, the mole fraction of CO increased accordingly, while CO_2 was not affected significantly. The apparent rate of production of CH_4 decreased with the increase in the plasma power. This suggests that when the tar was transported into the hot plasma reactor, most of the tar was converted to CO. Meanwhile, some of the CH_4 produced from pyrolysis, was burned and probably converted to CO or CO_2. Huu *et al*.

[97], and Baylet *et al*. [179] both have investigated CH_4 conversion using DBD. Under operating conditions similar to the current study (> 473 K, and a gas mixture of $N_2/O_2/CO_2$ in the plasma reactor, and a similar DBD geometry), they found CH_4 in plasma was converted primarily into CO, and a small proportion of CO_2.

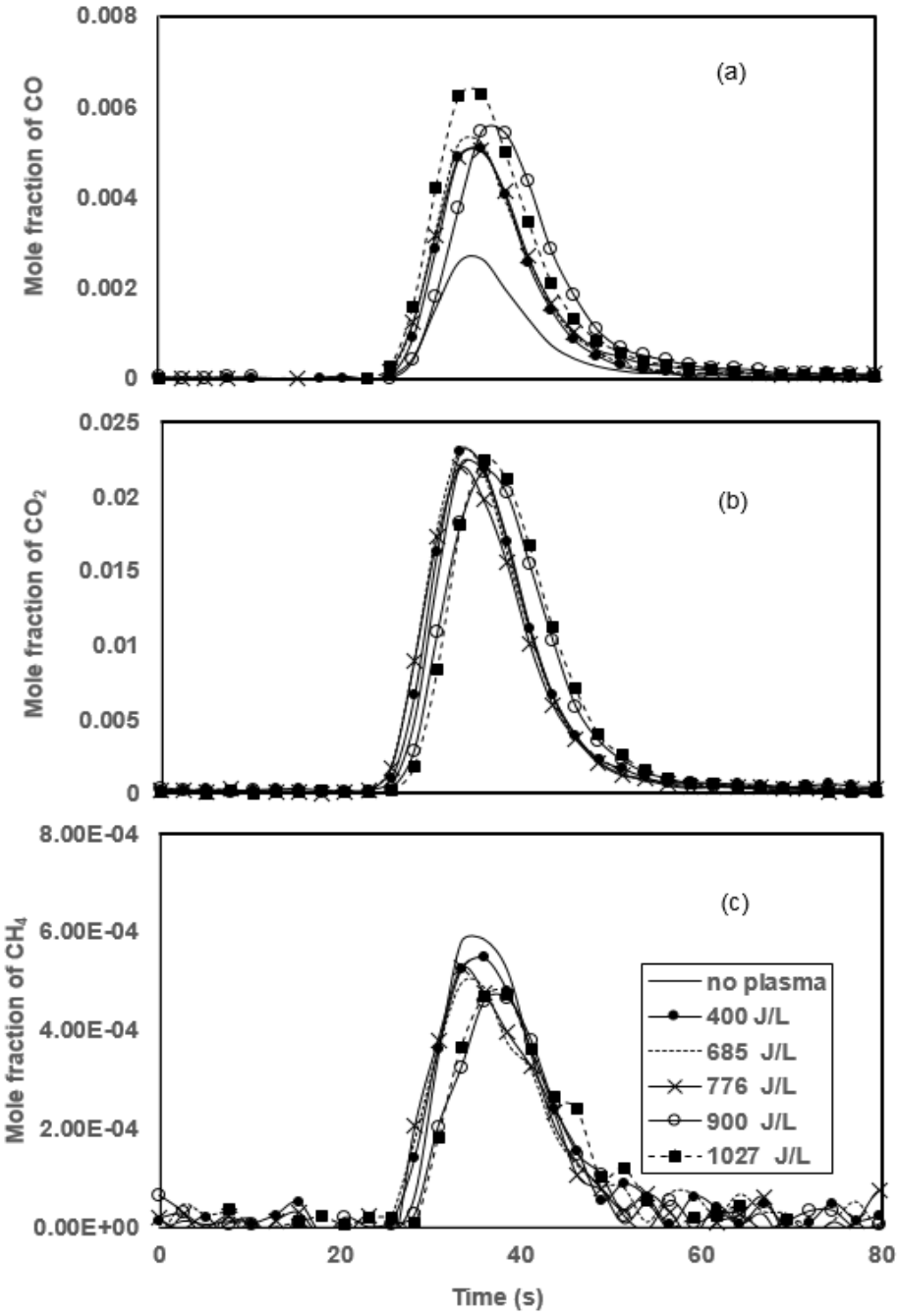

Figure 5-7 Mole fraction of carbon-containing gaseous species detected (with dilution by air) at 873 K in FB for different SED values of the plasma reactor, (a) CO, (b) CO_2, (c) CH_4.

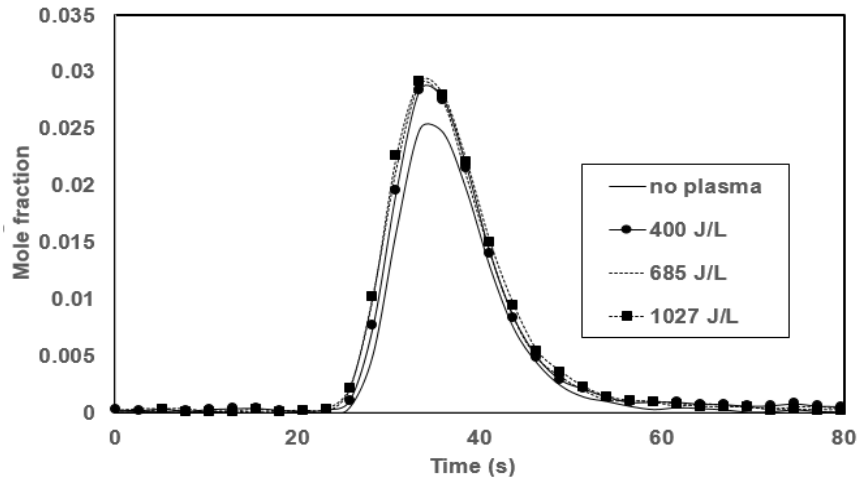

Figure 5-8 Overall mole fraction profiles of carbon-containing gaseous species (CO + CO_2 + CH_4) detected (with dilution by air) with the fluidised bed at 873 K, under different SED values of the DBD reactor.

Figure 5-8 illustrates the overall mole fraction of all carbon-containing species (CO, CO_2 and CH_4) detected by FTIR. The measurement system has ~ 18 seconds residence time (time taken for the FTIR signal change from 5% to 95 % of full response to a step change). Any difference between the curves would suggest a difference in the amount of carbon in the tar being converted in plasma. No obvious deposits of tar were observed in the cold trapping tube. The amount of carbon without plasma discharge was the lowest, and the other three with plasma were higher. On the other hand, the increase in the plasma power from 400 to 1027 J/L did not lead to a clear difference in the measured carbon amount, but higher plasma power seems to cause conversion of CH_4 to CO or CO_2, as suggested in Fig. 5-6 (c). The results indicate that most of the produced tar in fluidised bed has been combusted (or converted to methane) in the presence of plasma at low power, further increase in the power did not result in a clear increase in the overall rate of conversion to (CH_4 + CO + CO_2), but the conversion of CH_4 to CO or CO_2. Table 5-1 presents the overall carbon balances at different plasma power ratings, where the carbon balance was defined as the ratio of total amount of carbon in the carbon-containing products (gases + char that measured by air burn-off after processing in N_2), as expressed in 2.3.3. The carbon balances do not reach 100%; this is probably due to some condensation of tar in the sampling tube. It was found that higher temperature in the fluidised bed led to better carbon balance, as shown in Table 5-2, suggesting either easier conversion of higher temperature-produced tar (from the fluidised bed) in the DBD reactor, or less

condensation of tar in the sampling system as it produced from hotter bed. The investigations of the effects of temperature and bed materials in the following sections were all carried out with a plasma SED of 1027 J/L.

Table 5-1 Total carbon as CO, CO_2 and CH_4 under different plasma SED (base on pure carbon as the tar compound).

SED (J/L)	Total carbon balance (air-dried)
0 (no plasma)	0.73±0.02
400	0.89±0.02
685	0.90±0.03
776	0.92±0.02
900	0.93±0.02
1027	0.94±0.02

Table 5-2 Total carbon balance under various operating conditions (based on pure carbon as the tar compound).

Bed material	FB temperature (K)	Carbon balance
N_2 fluidised bed with alumina sand	773	0.86±0.02
	873	0.88±0.03
	973	0.96±0.02
	1073	0.99±0.02
	1173	1.04±0.01
N_2 fluidised bed with Fe_2O_3	773	0.85±0.03
	873	0.88±0.03
	973	0.98±0.02
	1073	0.94±0.03
	1173	1.01±0.02
N_2 fluidised bed with mayenite-supported CuO	773	0.91±0.03
	873	0.94±0.01
	973	0.96±0.02
	1073	0.99±0.02
	1173	0.97±0.03
N_2 fluidised bed with mayenite-supported Cu_2O	773	0.92±0.03
	873	0.96±0.02
	973	0.98±0.03
	1073	1.00±0.02
	1173	0.99±0.03
CO_2 fluidised bed with alumina sand	773	0.83±0.03
	873	0.86±0.02
	973	0.87±0.04
	1073	0.97±0.03
	1173	0.98±0.03

5.3.2 Pyrolysis of wood in alumina sand

Figure 5-9 shows the yield of each carbon-containing species including gaseous species, tar and char from wood pyrolysis in a fluidised bed of alumina sand from 773 to 1173 K. The error bars show the range of results for three repetitions. Alumina sand is relatively inert, thus chemical interaction with the wood particle is expected to be minimal. According to Fig. 5-9, an increase in the operating temperature improved the production of gases. The yield of CH_4 increased from less than 0.1% to 1.9% on a weight basis from 773 to 1073 K, with a maximum value of 2.5% at 973 K. A sharp increase in CH_4 yield was observed when further increasing the temperature from 1073 to 1173 K; at the same time, there was a decrease in the yield of tar (the tar yield increased gradually from 773 to 1073 K, followed by a drop from 1073 to 1173 K). This suggests that the significantly increased amount of CH_4 might come from the cracking of tar from 1073 to 1173 K. The yield of char was determined from the CO and CO_2 produced during the burn-off period after pyrolysis. The char content gradually decreased from ~ 29% to ~ 17% from 773 to 1173 K, probably due to its decomposition as the temperature increased.

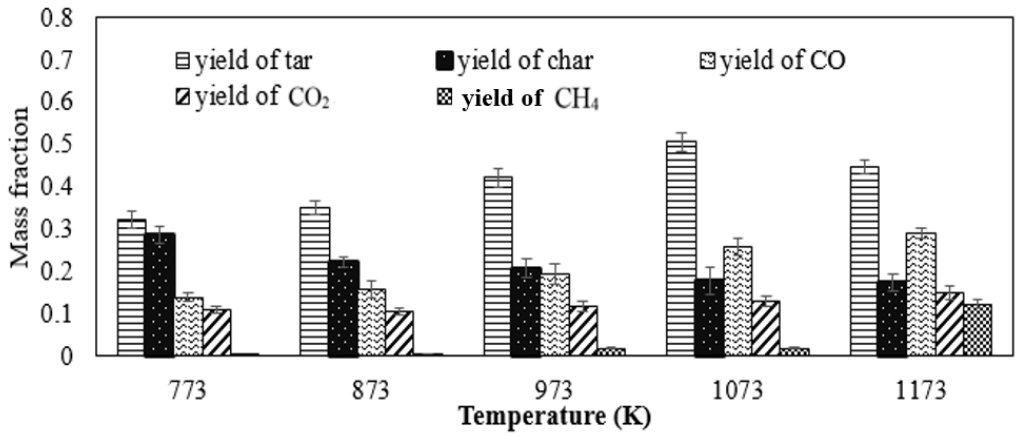

Figure 5-9 Mass fraction of different carbon-containing product species in a bed of alumina sand from 773 to 1173 K with a fluidising gas of N_2.

5.3.3 Pyrolysis of wood in the presence of Fe_2O_3

The results of pyrolysis of wood chips in the presence of Fe_2O_3 is presented in Figure 5-10. Comparing the results from Fig. 5-9, the yields of CO are similar in alumina sand and Fe_2O_3 from 773 to 973 K; beyond 973 K, the amount of CO produced in the Fe_2O_3 bed dropped. As discussed in Chapter 3, the presence of Fe_2O_3 mainly affects the gaseous products by reacting with CO around the surface of the char particle , and no evidence of

catalytic effect of Fe_2O_3 was found. The decrease in the CO from 973 K here is most likely due to the combustion of the CO by Fe_2O_3. The yield of tar is also found lower in Fe_2O_3 from 873 to 1173 K, whilst the yield of CO_2 is much higher. This indicates that the tar produced from wood pyrolysis started to be converted by Fe_2O_3 when the temperature exceeds 773 K, and most of the tar was combusted to CO_2. From 773 to 1073 K, the yield of CH_4 in Fe_2O_3 is higher than that in alumina sand; whilst at 1173 K, the value is lower. It seems that CH_4 is also a product from the reaction between tar and Fe_2O_3 from 773 to 1073 K. When the temperature increased to 1173 K, Fe_2O_3 became highly reactive with CH_4, resulting in its decrease. This is somewhat consistent with the findings in literature [180,181] that the conversion of CH_4 by Fe_2O_3-based materials usually occurred at temperatures above 1123 K, depending on the composition, preparation method and particle size of the material. The char yields in the beds of alumina sand and Fe_2O_3 are similar, indicating no direct solid-solid reaction between char and Fe_2O_3.

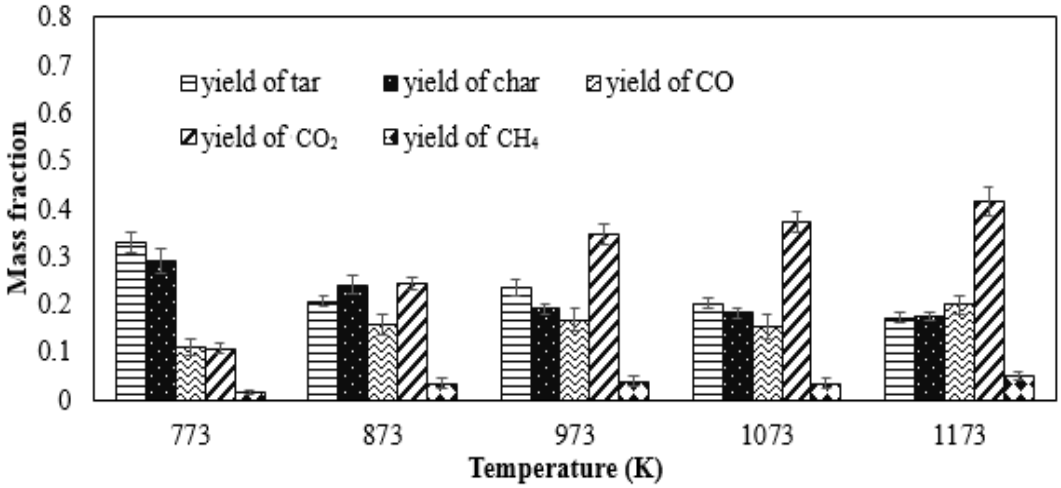

Figure 5-10 Mass fraction of different carbon-containing species in a bed of Fe_2O_3 from 773 to 1173 K with a fluidising gas of N_2.

5.3.4 Pyrolysis of wood in the presence of mayenite-supported CuO

Figure 5-11 shows results from a bed of mayenite-supported CuO. Comparing Figs. 5-11 and 5-9, mayenite-supported CuO seems to be effective in converting pyrolysis products *in situ*. The products of pyrolysis were converted mainly to CO_2, especially at 1173 K, where CO_2 constitutes of ~ 87 % of the products. Comparing the results with the pyrolysis in Fe_2O_3, mayenite-supported CuO exhibited higher reactivity for combustion of the pyrolysis products. Similar to Fe_2O_3 and alumina sand, there seems to have been no

significant solid-solid reaction between mayenite-supported CuO and char from 773 K to 1073 K. However, when the temperature reached 1173 K, mayenite-supported CuO consumed most of the char generated. This high reactivity of CuO at 1173 K mainly comes from the change in the form of oxygen supply. CuO tends to release significant amount of gaseous oxygen [182] and form Cu_2O: $CuO \rightarrow Cu_2O + O_2$. The effect of released oxygen from CuO at higher temperatures is further discussed in 5.4.2. At temperatures below 1073 K, this effect can be ignored. Thus, at 1173 K, both gas-gas reaction between gaseous pyrolysis products and released oxygen, and solid-gas reaction between char and the released oxygen were taking place.

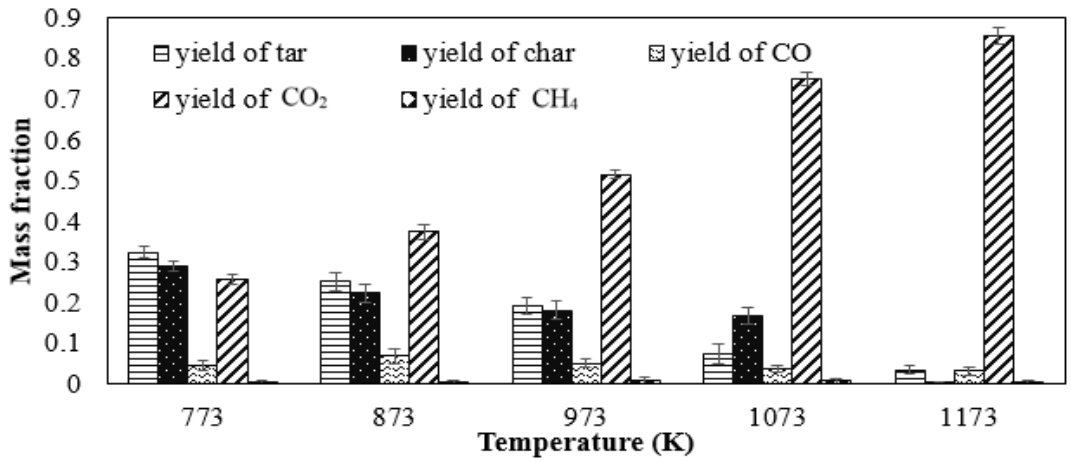

Figure 5-11 Mass fraction of different carbon-containing products species in a bed of mayenite-supported CuO from 773 to 1173 K with a fluidising gas of N_2.

5.3.5 The effect of CO_2 on the distribution of products from wood

The results of wood processing in a fluidised bed of alumina sand supplied with 18% CO_2 (balance N_2) are shown in Fig. 5-12. As the change in the CO_2 was obtained by taking the difference of the experimentally measured CO_2 profile and the inlet CO_2 concentration (*i.e.* 18% CO_2), the negative mass fraction means an overall consumption of CO_2. According to Figs. 5-12 and 5-9, at the lowest temperature, 773 K, the distribution of the products shows no significant difference between pure N_2 and 18% CO_2, indicating little effect of the presence of CO_2 to the pyrolysis products at such temperature. A clear difference appeared when the bed temperature was increased to 973 K. An overall consumption of CO_2 in the fluidised bed, together with decreased tar yield and increased CO and CH_4 (compared to the yields in N_2), was observed. The consumption of CO_2 is

mainly due to the reforming of tar produced *in situ*, and the main products from this reaction are CO and CH_4. Further increases in the temperature led to more consumption of CO_2 and generation of CO and CH_4. In terms of the char yield, from 773 to 973 K, there seems to be no difference in the products in the two gaseous environments; however, from 1073 K, the char yield in 18% CO_2 is lower than that in N_2. This is probably caused by the gasification of the char, which takes place at the same time as the pyrolysis of the wood. Gasification of the char generated CO, leading to an increase in the CO yield. The starting temperature for char gasification found here, 1073 K, was also comparable to the temperature conducted for the gasification of Polish char (refer to Chapter 3). Unlike the conditions at lower temperatures, the char yield would be very sensitive to the time span (pyrolysis time) selected once the gasification of the char starts: the longer the time, the higher the proportion of carbon in the char is converted to CO. The yield of CO and char at 1073 and 1173 K in Fig. 5-12 was determined by defining the end of pyrolysis as being when CH_4 was no longer detected. At this point, the fluidising gas was quickly switched to pure N_2.

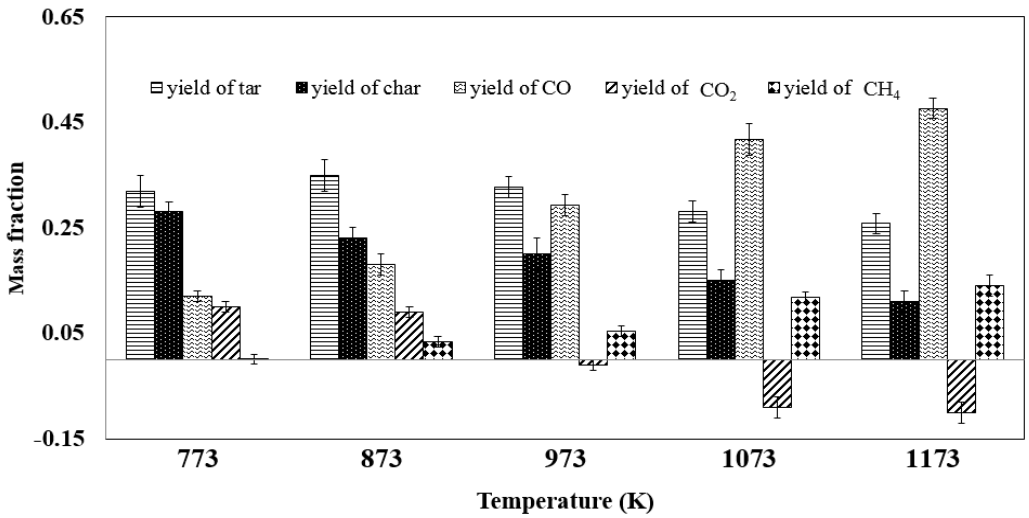

Figure 5-12 Distribution of each product species in a bed of alumina sand fluidised by 18% CO_2. The negative CO_2 mass fraction indicates the consumption of background CO_2.

5.4 Discussion

5.4.1 Carbon balance in the two fluidising gas environment

The carbon balances of the conversion of the wood chips in the two fluidising agents are presented in Table 5-2. Both N_2 and 18% CO_2 gave high carbon balances, but the values in N_2 at each temperature was even nearer to closure. The lower carbon balance in 18%

CO_2 could mainly come from the shift in the CO_2 level in the background. Although the correction of the flow was conducted and the CO_2 mole fraction after correction is more reliable for the determination of tar and CO_2, there still might be some limitations. Firstly, for the correction, it was assumed that the air flow rate was constant so that the oxygen could be used as a tracer. Practically, it is hard to control the flow rate perfectly and any fluctuation in the air flow rate would result in the shift in the CO_2 background. For the experiments with no CO_2 in the background, changes in the air flow rate were less of a problem because the background level would always be nearly zero. Secondly, when the plasma was turned on, the tar compound was assumed to be oxygen-free and even the best fit did not return the oxygen mole fraction curve to a perfectly stable one, meaning that the corrected oxygen is not a perfect 'tracer'. Thirdly, the effect on the sampling flow rate due to CO_2 splitting in the plasma reactor was not taken into account when characterising the flow. These accumulated errors probably caused the less ideal carbon balance in 18% CO_2. Generally, to improve the carbon balance, a well-engineered system that could control the flow rate (*e.g.* feedback control loop of the flow to the analysers) more accurately, and more precise flow measurements is required. However, this is difficult as flow measurement devices generally require clean gases, and often the calibration of the flow device depends on species present (here both the sampled gas and the injected air must be controlled).

When the plasma was running in N_2/air mixed environment, the product species detected were primarily NO_x. In the presence of CO_2, it was found that CO and O_2 were also generated, as seen in Fig. 5-6. When the plasma was turned on, there was a quick drop in the CO_2 background level (from a mole fraction of 0.088 to 0.084), correspondingly the [CO] increased from 0.000 to 0.005 and [O_2] increased from 0.094 to 0.096. The change in the mole fractions in the different species suggests that reaction of CO_2 splitting, $CO_2 \rightarrow CO + O_2$, might have taken place when the plasma was running in the CO_2/air mixed gas environment. As reported by Yap *et al.* [183], non-thermal plasma can promote the highly endothermic reaction of CO_2 splitting. Whether there was a significant effect of the generation of some O_2 from CO_2 splitting on the other reactions taking place in the DBD reactor is indicated in Fig. 5-13. Fig. 5-13 summarised the results of the change in the mole fraction of CO and CO_2 from the two fluidising gases in a bed of alumina sand at 773 K, when plasma was active. The higher background level of CO in the 18% CO_2 comes from the splitting of CO_2. At 773 K, there was minimal tar reforming in the

fluidised bed (refer to Fig. 5-12). If the reactions taking place in the plasma reactor in the two gaseous environments are the same, the CO and CO_2 signals after dropping in the wood chips, should follow the same patterns. According to Fig. 5-13, however, there was more significant rise of CO_2 and lower rise of CO (*i.e.* from t = 52 s, after the initial drop of CO) in a bed fluidised by CO_2 (the sums of change in the two product species are similar in the two gas conditions). This seems to suggest a conversion of the sampled CO (from the upstream) to CO_2 in the DBD reactor when running in CO_2/air mixed atmosphere. The conversion of CO to CO_2 might be from the reaction between the CO in the sampled gas and the oxygen generated by the dissociation of CO_2 in plasma. The temperature (523 K) for the conversion of CO to CO_2 in the plasma reactor is much lower than the auto-ignition temperature of CO (882 K). This reaction, however, can be initiated in a DBD reactor if singlet O_2, which is an excited species and was found to be a product from CO_2 splitting in plasma [184], is generated. One of the possible routes for the dissociation of CO_2 is to excite CO_2 to vibrational levels of the ground excited state [185]. Provided with energy just exceeding the threshold for dissociation, CO_2 dissociates into ground electronic state CO and singlet oxygen. Starik *et al.* [186] studied the influence of singlet oxygen molecules on homogenous charge compression ignition (HCCI) combustion and found a much diminished temperature needed for combustion in the presence of singlet oxygen. The concentration of by-product CO also significantly decreased. This strongly suggests that some CO might have been combusted by singlet O in the current study.

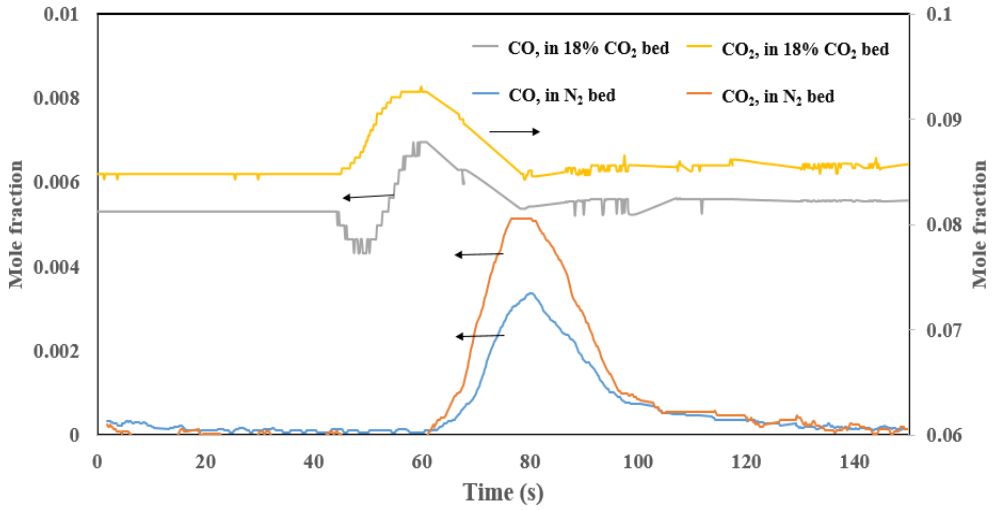

Figure 5-13 Mole fractions of CO and CO_2 with plasma running, with FB fluidised in N_2 and 18% CO_2 at 773 K. Note biomass was fed into the fluidised bed at t = 48 s with the bed fluidised in 18% CO_2, and at t = 62 s with the bed fluidised in N_2.

5.4.2 Reactivity of products

The order of reactivity of pyrolysis products including CO, CH_4 and tar, with the active bed materials could be determined by comparing the results in Figs. 5-9, 5-10, and 5-11. According to Figs. 5-9 and 5-10, at the lowest temperature, 773 K, the presence of Fe_2O_3 caused a slight decrease in CO and tar yields; the yield of CH_4 increased a little, probably due to tar decomposition. The comparison suggested that CO and tar are more reactive than CH_4 for combustion/conversion. Comparing the product distribution at 773 K in the bed of alumina sand and mayenite-supported CuO, as shown in Figs. 5-9 and 5-11, there was a clear increase in the yield of CO_2 and a decrease in CO, while no drop in the tar yield in mayenite-supported CuO was observed. In this case, CO is considered to react more readily with active bed materials. An order of the reactivity of pyrolysis products with the oxygen carriers can then be obtained: CO > tar > CH_4.

Both the active bed materials and the presence of CO_2 help tar abatement inside the fluidised bed within the short residence time (~ 1s), as shown in Fig. 5-14. The increase in the temperature improves the conversion of tar. The effect of oxygen carriers for tar reduction is more significant than CO_2, and mayenite-supported CuO is especially effective at high temperatures. Mayenite-supported CuO is a promising material for *in*

situ tar reduction in a fluidised bed reactor; it also shows great potential as an oxidant for the direct combustion of biomass.

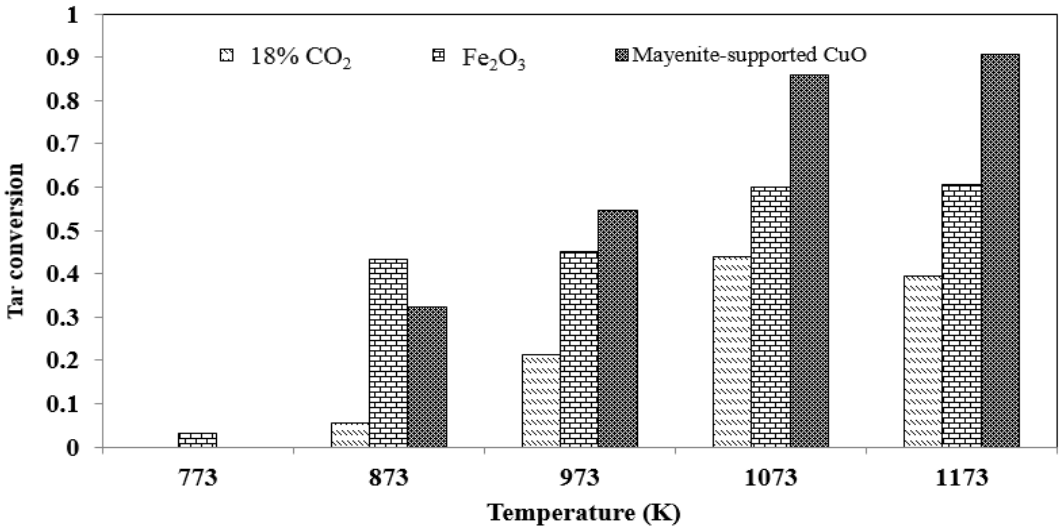

Figure 5-14 Tar conversions in different fluidised bed conditions.

5.4.3 The effect of released oxygen from CuO on product distribution

Figure 5-15 shows the phase diagram of the Ca-Al-Cu-O system (which is identical to the Cu-O phase diagram, for the range of compositions over which the aluminum and calcium bind preferentially into calcium aluminates). At 1073 K, the oxygen mole fraction at atmospheric pressure produced by CuO is about 0.0016; at 1173 K, it reaches 0.018. Thus, at 1173 K, there can be both gas-gas reaction between gaseous pyrolysis products and released oxygen, and solid-gas reaction between char. Whether it was the released gaseous oxygen from CuO that led to the significant drop in the tar yield from 1073 to 1173 K, was investigated by performing pyrolysis of the wood chips in the bed of mayenite-supported Cu_2O. The particles were prepared from mayenite-supported CuO, by first fluidising the bed in N_2 at 1173 K until no oxygen was detected. Fluidised in N_2, which is assumed to have an O_2 partial pressure of 1×10^{-5} bar, CuO decomposes to Cu_2O; further decomposition to Cu was avoided either by its own equilibrium with the trace amount of O_2 with the ambient and/or the slow reaction kinetics. For a typical group of experiments, the prepared Cu_2O was divided into five equal portions, for pyrolysis at each temperature from 773 to 1173 K, with and without plasma (*i.e.* two individual runs for one portion). The amount of oxygen available in the Cu_2O was always in excess of that needed for complete combustion of the fuel (*i.e.* a maximum of 0.88 g of Cu_2O is needed for every 0.0538 g wood). At each temperature, between the two runs, the Cu_2O

was not regenerated. Although the bed material was not regenerated prior to the second run, repeated experiments by switching the order of the two runs (*i.e*. without and with plasma running) showed that the results were not influenced by the conversion of the oxygen carrier. After two runs at each temperature, the bed was burned off in air to quantify the amount of char. The amount of char at each temperature can be obtained by taking half of carbon content in CO and CO_2 generated during burn-off. Figure 5-16 shows the results in mayenite-supported Cu_2O. Comparing the mole fractions of CO, tar and CH_4 in Fig.s 5-11 and 5-16, the reactivity of Cu_2O and CuO for the conversion of CO and tar are similar from 773 to 973 K. More CH_4 was detected in Cu_2O, indicating that CuO is more reactive than Cu_2O towards CH_4. When the temperature reached 1073 K, the yield of tar in CuO dropped whilst that in Cu_2O still remained high. At 1173 K, the difference is more significant in that both tar and char still contribute a big portion to the total yield in a Cu_2O bed, but not in CuO. The clear difference observed at 1073 and 1173 K suggests that gaseous oxygen from CuO is very likely to be the primary cause for the reduction of char and tar at 1173 K.

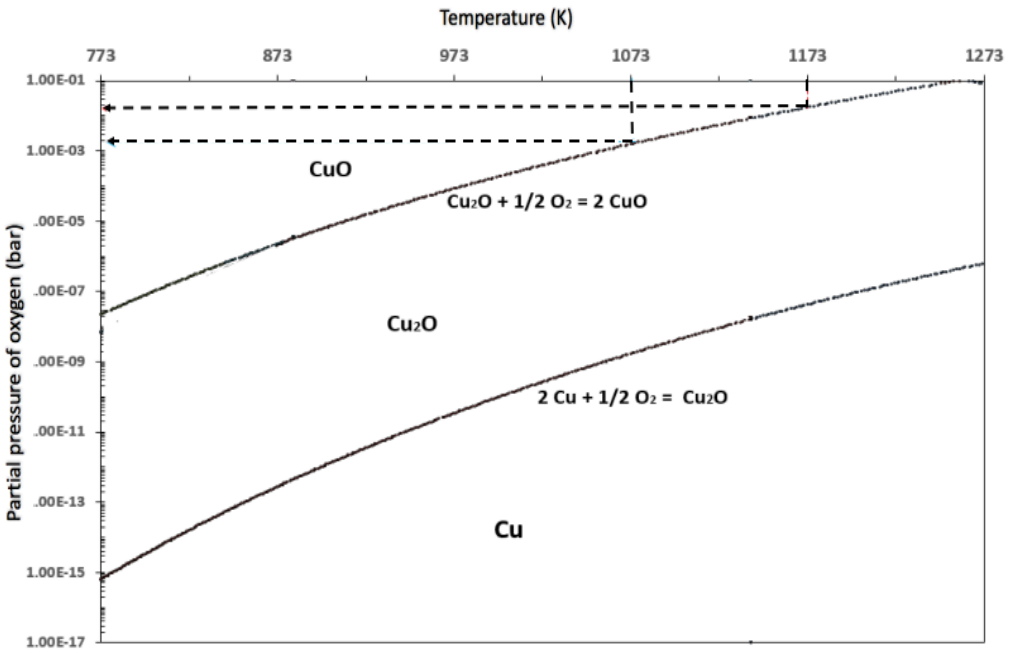

Figure 5-15 Equilibrium phase diagram of Ca-Al-Cu-O system (refer to 2.2.2 for the composition of the system) from 773 to 1273 K, where the phases of Ca and Al are not shown in the figure. The diagram was generated from MTDATA software [139] using NPL database.

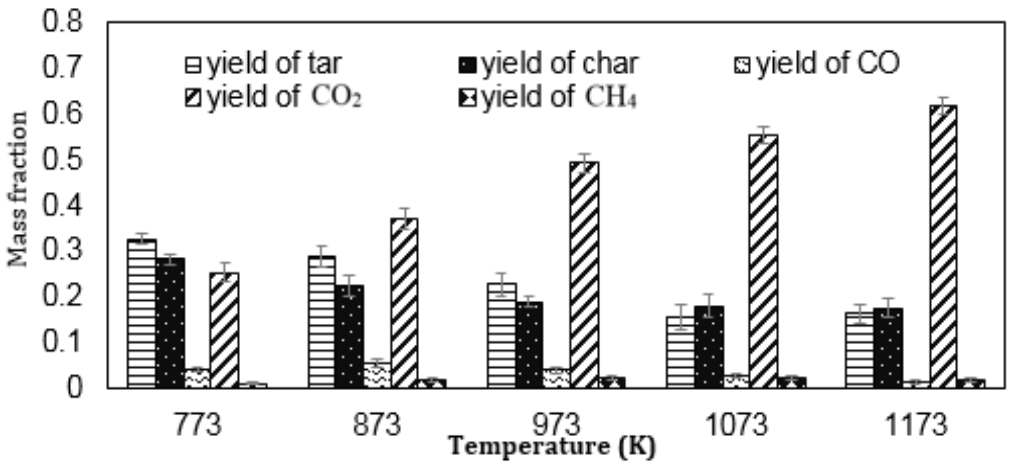

Figure 5-16 Mass fraction of different carbon-containing products species in a bed of mayenite-supported Cu_2O from 773 to 1173 K.

5.4.4 Methods for tar measurement

In the current study, to quantify the tar produced at one experimental condition, two identical experiments were required, with and without plasma discharge. To have exactly the same experimental conditions, the wood mass, flow rate, N_2 to air ratio of the two experiments need to be strictly controlled. The results showed good repeatability of the approach, but it is time-consuming and does not give an instantaneous online measurement. Other ways of carrying out the tar measurement were also attempted. Firstly, the idea of using two sampling lines was tested. The sampling line from the fluidised bed to the point where the air was introduced was unchanged, after the air mixing, the stream was divided into two, with 50% of the flow going to a "blank" reactor with the same dimensions as the plasma reactor prior to an analyser, the other going to the plasma reactor prior to FTIR. The difference between the signals from the two analysers indicates the amount of tar entering each sampling line. This method simplified the experimental procedure, as only one experiment was needed to measure the tar yield. However, practically, it was difficult to control the flow conditions in the two sampling lines to be exactly the same. Although the two sampling lines were engineered to be the same, any tiny variation between the two flow rates led to significant differences in the results. The error caused by the difference in calibration, and residence time of the two analysers could not be neglected. Secondly, the plasma was pulsed on and off plasma during one experiment. However, the idea was quickly found unsuitable for the experiment because this method requires a sufficiently fast response of the plasma reactor

(*i.e.* on/off), compared to the pyrolysis time. The plasma system has ~ 5 seconds response delay when turning on or off, which is not sufficiently short compared to ~ 40 seconds pyrolysis time here. However, for a continuous process in which changes took longer, this method would be suitable. Alternatively, a bypass line could be introduced around the plasma reactor. The plasma reactor could then be kept running, allowing the gas to be (periodically) sent to the analyser directly or alternatively *via* the plasma reactor. This would allow two curves to be obtained from the FTIR in one experimental run. However, this method would be limited by the response time of the valves and the analyser. For the short experiments carried out here, using two experiments was found to be more practical, however, if the pyrolysis was continuous, using gas switching or turning the plasma on or off may be more practical.

5.4.5 Apparent rate of tar production

The plasma system used in this study allows direct on-line measurement of tar generated during fuel processing. As Fig. 5-17 illustrates, the difference in the curves between plasma on and off accounts for the tar converted. Here, good carbon balances are obtained for most conditions (as shown in Table 5-2) and no clear evidence of tar was found in the trapping tube after the plasma reactor, indicating that for most conditions, tar condensation in the sampling line and tar remaining after plasma reactor were negligible. Assuming that all the tar can be cracked and converted to CO, CO_2 and CH_4 in the plasma reactor, the rate of the conversion of tar, $R_{conversion,tar}$, can be obtained as follow

$$R_{conversion,tar} = R_{production,tar\ in\ FB} \times \frac{F_{sampling}}{F_{FB}} \times \frac{F_{sampling}}{(F_{sampling}+F_{air})}.$$

F_{air} is the flow rate of air introduced into the sampling system prior to plasma reactor, $R_{conversion,tar}$ is the rate of tar cracking/conversion by plasma, and $R_{production,tar\ in\ FB}$ is the rate of production of tar from the fluidised bed. The rate curves are proportional to the mole fraction curves obtained. Figure 5-17 presents the mole fraction profile of tar cracking/conversion from a mayenite-supported CuO bed at 873 K with the DBD reactor having a SED of 1027 J/L, from which the apparent rate of tar production can be predicted. A true tar production profile over time can be further estimated by deconvolution of the system, assuming a continuous stirred tank reactor (CSTR, to

account for the ~ 18 seconds residence time) plus a plug flow reactor (PFR). Further work on this was not displayed in this study.

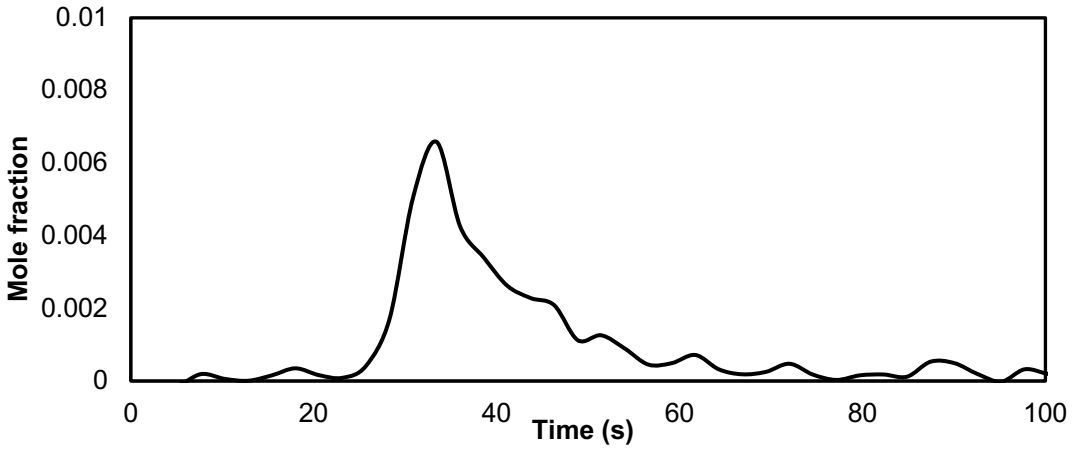

Figure 5-17 Mole fraction of tar based on the detection by FTIR, with the fluidised bed at 873 K, a SED of 1027 J/L in a bed of mayenite-supported CuO.

5.5 Conclusions

The main findings from the investigating the effect of oxygen carriers and CO_2 on the product distribution from wood chips in a fluidised bed are as follow:

(a) A plasma system for the on-line continuous quantification of tar was developed and placed in the downstream of a fluidised bed. The plasma system was found to be effective for tar conversion. The method for tar quantitation worked well and gave carbon balances close to unity. The apparent rate of tar production over time could also be obtained. Though further characterisation work was required to establish true rate profile, it provides a promising solution for the kinetic study of the generation of tar. Improvements to the response time of the gas analysers, and better control of the flow rates would allow more rapid measurements of the rates of tar production.

(b) For the pyrolysis of the wood chips, it was found that higher temperature promoted the production of gaseous products. Tar was the primary product from

pyrolysis from 773 to 1173 K. When the bed temperature increased above 1073 K, the tar formed cracked to CH_4 (from 50 wt% at 1073 K to 45 wt% at 1173 K).

(c) Fe_2O_3 and mayenite-supported CuO were found to be effective for *in situ* reduction of tar in the fluidised bed. The decreased tar was mostly combusted to CO_2. The reactivity of mayenite-supported CuO for the reaction with the pyrolysis products was higher than Fe_2O_3, and particularly effective for the conversion of tar and char at 1173 K due to its oxygen uncoupling property, resulting ~ 87% CO_2 in the products. The results showed promising feasibility of CLC/CLOU of biomass, without any active fluidising agent.

(d) With CO_2 fluidising the bed, the tar released from the biomass could be dry-reformed *in situ* at temperatures above 973 K. The reforming products were mainly CH_4 and CO. The char derived from the biomass started to be gasified in CO_2 at 1073 K.

6.0 Development of a plasma-assisted packed bed reactor for H_2 production from CH_4

6.1 Introduction

The DBD reactor developed for the quantification of tar measurement *via* tar cracking and combustion in Chapter 5, has revealed the potential of fuel conversion at low operating temperatures in such a plasma discharge system. The aim of the current chapter is to design a plasma-assisted reactor that allows for the conversion of gaseous fuel, in this case, CH_4. The electrical characteristics of the system and the controlling parameter for the conversion of CH_4 are to be investigated. As a preliminary study, the two packing materials: alumina sand, which is widely considered inert and low dielectric constant material, and $SrFeO_{3-\delta}$, a reactive oxygen carrier with a higher dielectric constant, are studied.

6.1.1 Electric discharge

An ideal DBD reactor is supposed to generate silent glow discharge; however, in reality,

current pulses are often observed in DBD applications. A discharge that contains a significant amount of current pulses is characterised as filamentary discharge. However, these filaments are transient states and exit only for a short time [187]. When ac voltage is applied to a DBD reactor, there are periods with discharges (when the voltage inside the gas gap is high enough to initiate breakdown and maintain a discharge), and without discharges (when the gap voltage falls below the value). The Lissajous figure is a useful tool for understanding the plasma properties. Figure 6-1 shows a resulting charge-voltage Q-V Lissajous figure of a DBD system when applied with sinusoidal voltage. Depending on the shapes, there are several types of Lissajous figures usually seen in a DBD system [187]:

1) A straight line in a Lissajous plot represents an ideal capacitance. The capacitive load has a current wave form leading the voltage, and thus the voltage and current peaks are not in phase.

2) For a resistive load, the current and voltage are in phase, and it results in an ellipse, and this normally indicates the presence of residual ions at all times. This is due to insufficient time for the ions to decay or to be removed between two succeeding half waves.

3) In most DBD applications, the figure is close to a parallelogram.

Figure 6-1 Voltage - Charge Lissajous figure of a dielectric barrier discharge cycle. U here stands for voltage, and Q is the charge. The figure was reproduced from [187]. For copyright issue, the figure is removed here.

For a discharge cycle, as shown in Fig. 6-1, ① → ② and ③ → ④ represent stages with discharge; and ② → ③ and ④ → ① are stages when discharge is off [187]. $\widehat{U}$ is the peak voltage in a discharge cycle. For the discharge to occur, the peak to peak voltage, $2\widehat{U}$, needs to be equal or higher than 2 U_{min} (the minimum voltage required for discharge to start). The capacitances can be estimated from the slopes of the Lissajous figure. In Fig. 6-1, the total capacitance of the electrode configuration, C_{Total}, can be calculated from the slope of the discharge stages:

$$C_{Total} = \frac{1}{\tan \alpha}.$$

The capacitance of the dielectric for a fully bridged gap, C_D, can be obtained *via* the slope of the discharge-off stages:

$$C_D = \frac{1}{\tan \gamma}.$$

The value of C_D should be a constant for a particular reactor set-up. However, in many cases, the gap is not fully bridged when in discharge [188,189] , in which case the measured gradient is lower than C_D, and is termed as the effective dielectric capacitance C_d.

The capacitances follow the correlation below:

$$\frac{1}{C_{Total}} = \frac{1}{C_{gap}} + \frac{1}{C_d}.$$

Where C_{gap} is the overall capacitance of the gap. The electrical pathway of the plasma system, which is supplied with ac power, can be illustrated by a simple equivalent circuit, as shown in Fig. 6-2. The switch turns on or off when the magnitude of the voltage is above or below the breakdown threshold.

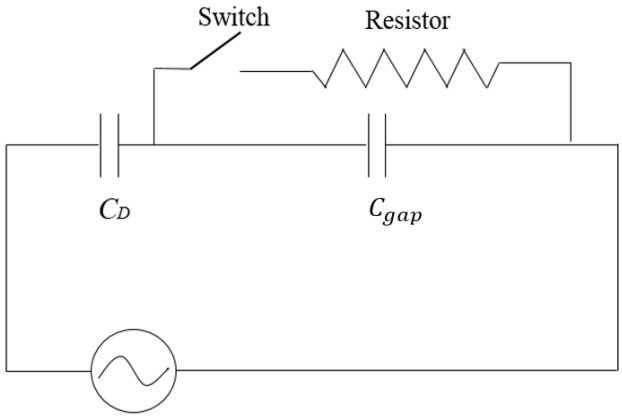

Figure 6-2 Equivalent circuit of the DBD system applied with ac voltage.

6.1.2 Estimation of the mean electron energy

The mean electron energy can indicate how much energy input is supplied to the system. In this study, it will be estimated from Einstein's equation,

$$\frac{k_B T_e}{e} = \frac{D_e}{\mu_e},$$

where k_B, D_e and μ_e are the Boltzmann constant ($1.38 \times 10^{-23}\ J/K$), diffusion constant, and drift mobility respectively. e is the elementary electron charge ($1.60 \times 10^{-19}\ C$). T_e is the electron temperature. The mean electron energy, $< \varepsilon >$, can be calculated from the electron temperature: $< \varepsilon > = \frac{3}{2} k_B T_e$ [101]. The electron temperature, the mean electron energy and the value of $\frac{D_e}{\mu_e}$, is typically a function of the reduced electric field, $\frac{E}{N}$ (E is the electric field and N is the density of neutral gas particles) [190] . Given the experimental valves of $\frac{E}{N}$, empirical values of $\frac{D_e}{\mu_e}$ reported in literature can be used to estimate the mean electron energy. Figure 6-3 presents the experimentally measured $\frac{D_e}{\mu}$ over a wide range of $\frac{E}{N}$ by Al-Amin [191].

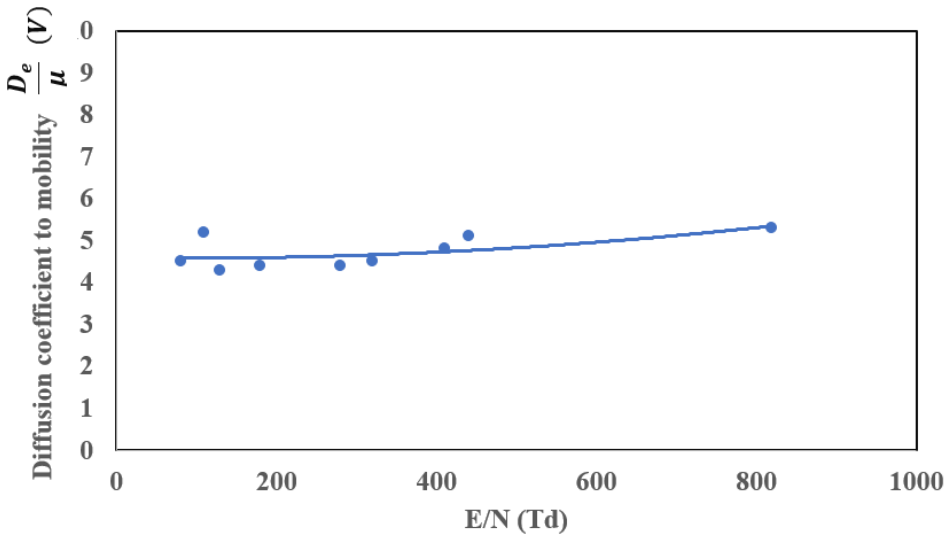

Figure 6-3 Ratio of diffusion coefficient to mobility over E/N for in methane (99.2% with impurities of 0.7% for N_2, BOC), where 1 Td = 10^{-21} V · m^2. Note that the data are cited from Ref. [191].

6.2 Experiments and calculation of the parameters

6.2.1 Development of a plasma-assisted chemical reactor

A DBD reactor consists of two electrodes (planar, co-axial, or adjacent cylinders, refer to Fig. 1-4) made of metals, covered or separated by a dielectric material (s). Recent research on the conversion of fuels employing non-thermal plasma, largely used cylindrical configurations [123,179,189,192–194]. This is mainly because it is easier to directly couple such a plasma system configuration to the existing chemical reactors, such as plug flow reactors and packed bed reactors. In this chapter, a plasma-assisted chemical reactor is first developed. The design is based on a cylindrical quartz tube, as described in 2.3.4, with a distributor plate and allowing gas flowing in from the bottom of the tube. Stainless-steel mesh is used to cover the quartz tube, acting as the ground electrode; the high voltage electrode is a stainless-steel rod, sitting on the distributor with the other end supported by a cap on top of the quartz tube. The initial idea was to apply non-thermal plasma to a fluidised bed system. However, de-fluidisation inside the bed was observed when subjected to plasma discharge. This phenomenon did not improve regardless of varying the particle size (from 180 – 250 μm to 800 – 1000 μm), and flow rate through the bed (from just on fluidisation to $U/U_{mf} > 10$). It is suspected with the supply of plasma

discharge, the particles inside the fluildised bed quickly become charged and the intra-particle forces between the charging particles led to the de-fluildisation of the bed. Understanding of the effect of plasma on fluidisation and development of a stable fluidised bed in the presence of plasma discharge would be necessary prior to the investigation of the chemical reactions in such systems. However, systems involving plasma in a fluidised bed have received little attention in the literature [195–198] have not been well understood. The main interest of this study (Chapters 6, 7 and 8) is on the reaction side, and a plasma-assisted packed bed reactor is investigated. For a packed bed reactor, the gas inflow is also introduced from the bottom of the reactor, whilst the flow rate is controlled to be low enough to avoid fluidisation. The details are described in 2.3.4.

6.2.2 Experiments

Characterisation of the electrical signals and the investigation of their effect on the conversion of CH_4 in the developed plasma-assisted packed bed, as described in 2.3.4, was carried out here. The experiments were conducted at temperatures from 293 to 723 K, with 100% CH_4 as the feeding gas at a flow rate of 0.5 L/min. The gas from the packed bed was sampled at 0.2 L/min and mixed with a N_2 dilution stream at 0.8 L/min, giving a total flow rate of 1 L/min entering the analysers. The effect of applied voltage from 7 to 19 kV, and frequency from 20 to 29 kHz on the electrical signals and conversion of CH_4 were studied. For a typical experiment, when the gas flow through the DBD reactor stabilised, the plasma was then applied for 2.5 $\pm$ 0.2 min. $SrFeO_{3-\delta}$, with a particle size fraction of 600 - 850 μm, prepared from solid mixing (as presented in 2.2.2) was used as the bed material packing the DBD reactor, giving a height of the plasma discharge region of ~ 20 mm. The non-stoichiometry of $SrFeO_{3-\delta}$ was found to be $SrFeO_{2.820}$, which is presented in 7.3.1. As a control, alumina sand (600 - 850 μm), which was considered chemically inert, was also studied. In addition to the difference in chemical reactivity of the two materials, $SrFeO_{3-\delta}$ has a much higher dielectric constant (between 200 – 400 in the applied AC frequency of 20 - 30 kHz [199]) than alumina sand (8 - 11, [200]).

6.2.3 Estimation of the parameters

- **Capacitance of the dielectric C_D**

The capacitance of the dielectric (quartz reactor), which is independent of the experimental conditions, can be calculated based on the geometry of the reactor set-up. The following equation [201] is used:

$$C_D = \frac{2\pi\varepsilon_{vaccum}\varepsilon_D l}{\ln((r+x)/r)},$$

where ε_{vacuum} is the dielectric constant of the vacuum (8.854×10^{-12} Fm^{-1}); ε_D is the relative dielectric constant of quartz tube ($i.e.$ ~ 4.7); l is the discharge length, which is 25 mm. r is the inner diameter of the quartz tube, and x is thickness of the quartz tube. Based on the above values, C_D of the reactor is 9.0×10^{-11} F.

- **Conversion of CH_4**

The term, conversion of CH_4, studied here refers to the averaged conversion of CH_4 over the plasma discharge time ($e.g.$ ~ 2.5 min in this case), and was obtained from

$$X_{CH_4} = \frac{\frac{\int_{t_0}^{t_{end}} (F_{total,0} \cdot x_{CH_4,0} - F_{total} \cdot x_{CH_4}) dt}{t_{end} - t_0}}{F_{total,0} \cdot x_{CH_4,0}},$$

where $x_{CH_4,0}$ and x_{CH_4} are CH_4 mole fractions measured at the reactor inlet and outlet, respectively. $F_{total,0}$ and F_{total} are the corresponding total flow rates. The converted CH_4 was averaged for the period with plasma discharge from t_o to t_{end}.

The methods for obtaining other electrical properties including the dissipated power and the estimated mean electron energy, can be found in 2.3.3 and 6.1.2, respectively.

6.3 Results and discussion

6.3.1 Understanding the electrical signals

- **Discharge behaviour**

Figure 6-4 presents the electrical signals of CH_4 plasma discharge with the DBD reactor packed with alumina sand at 293 K under two supplied plasma conditions. The electrical signals were captured when voltage and current signals were stable. The current

waveforms were obtained by differentiation of the measured charge waveforms, followed by smoothing using a moving average filter with a window size of 5% of the total data points. According to Fig. 6-4a, with the alumina sand-packed DBD reactor operated with a dissipated power of 22 W, some current pulses were observed. The plasma power was gradually increased to 22 W until conversion of CH_4 was observed. The number and the intensity of current pulses clearly increased when the plasma power increased to 32 W, as shown in Fig. 6-4b. A similar effect of plasma power on the discharge performance was also found at higher temperatures. In addition, a noisy sound was heard from the DBD reactor during plasma discharge. The presence of these current pulses and the noise indicate the presence of filamentary discharge in CH_4 plasma in the alumina sand bed, meaning the plasma formed cannot be homogeneously distributed. Ionised species and electrons in some areas can be very concentrated, which would result in sparks locally. Filamentary discharge like this is usually not favoured due to the significant noise level, and the waste of energy in the concentrated zone. In terms of the conversion of CH_4 in such bed at 293 K, when the voltage was only gradually increased to 15.4 kV (resulting a plasma power of 22 W and the frequency of 26.4 kHz), the conversion of CH_4 in the DBD reactor was observed. From this point, further increase in the voltage to 19 kV (resulting a plasma power of 32 W and the frequency of 23.8 kHz) led to an increase in the conversion of CH_4 (*i.e.* 0.051).

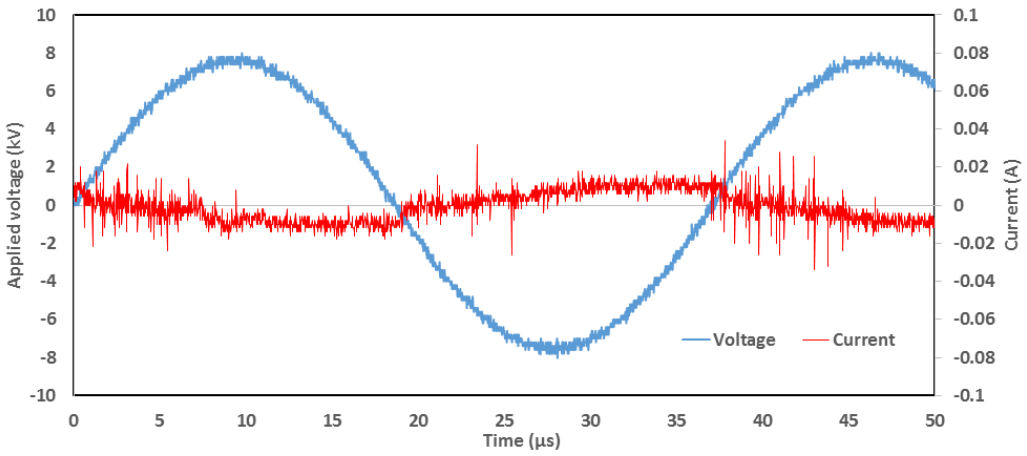

(a)

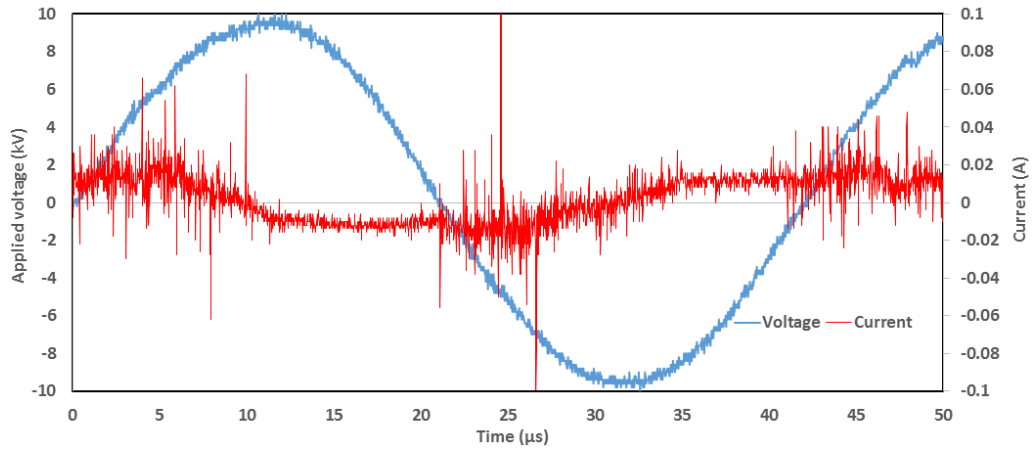

(b)

Figure 6-4 Voltage and current waveforms of plasma running in the alumina sand-packed DBD reactor at 293 K purged with 100% CH_4 (a). under the voltage of 15.4 kV at 26.8 kHz with a dissipated power of 22 W, giving an averaged conversion of CH_4 of 0.001; and (b). under the voltage of 19 kV at 23.8 kHz with a dissipated power of 32 W, giving an averaged conversion of CH_4 of 0.051.

The representative electrical signals in a $SrFeO_{3-\delta}$-packed bed are shown in Fig. 6-5. Similarly, the voltage was first gradually increased to the point where the conversion of CH_4 can just be observed. In the $SrFeO_{3-\delta}$-packed bed operated at 293 K, this value found was 11 kV (resulting a plasma power of 7 W and the frequency of 21.9 kHz). Compared to the case in the alumina sand bed, the voltage and power threshold required for starting CH_4 conversion in $SrFeO_{3-\delta}$-packed bed were significantly decreased. The amplitude (peak to peak value, ~ 0.06 A) of current in $SrFeO_{3-\delta}$, as shown in Fig. 6-5a, also increased

significantly (compared to the value of ~ 0.02 in Fig. 6-4a; however, the current pulses were not clearly observed in Fig. 6-5a. The increase in the voltage to 13.3 kV (resulting a plasma power of 16 W and the frequency of 20.5 kHz) also did not generate clear current pulses, as shown in Figure 6-5b. These observations suggest that the it is easier to generate CH_4 plasma in the bed of $SrFeO_{3-\delta}$, and the plasma formed in such case did not have much filaments. This is further supported by the fact that no sound was heard from the plasma in the $SrFeO_{3-\delta}$ bed. The silent discharge mode, known as diffuse plasma, was also found in $SrFeO_{3-\delta}$ at higher temperatures. The difference in the results from Figs. 6-4 and 6-5 is mainly due to the variation in the dielectric constant of the two materials. High dielectric constant materials could improve the stabilisation of plasma and reduce the number of filaments [93]. This is also supported by the Lissajous figures, as presented in Fig. 6-6. It shows a typical comparison of the Charge-Voltage Lissajous plots in the two bed materials at 293 K, where the conversion of CH_4 just initiated under the corresponding voltages. To achieve the same chemical conversions of CH_4 in the DBD reactor, the Lissajous figure changes from ellipse-shaped in alumina sand bed to parallelogram-shaped in the $SrFeO_{3-\delta}$ bed. It is reported [202] that during plasma discharge, some charges are not spread out uniformly over the surface of the dielectric (the quartz tube and alumina sand in this case) and accumulate at some points. When the applied voltage is reversed, these residual charges memorise the previous polarity and generate filamentary channels, leading to less sharp edges in the Lissajous figures. The observed sharp edges at the reversal points in the $SrFeO_{3-\delta}$ loop in Fig. 6-6, indicates few residual ions present between two succeeding half waves, which is ideal for DBD reactors.

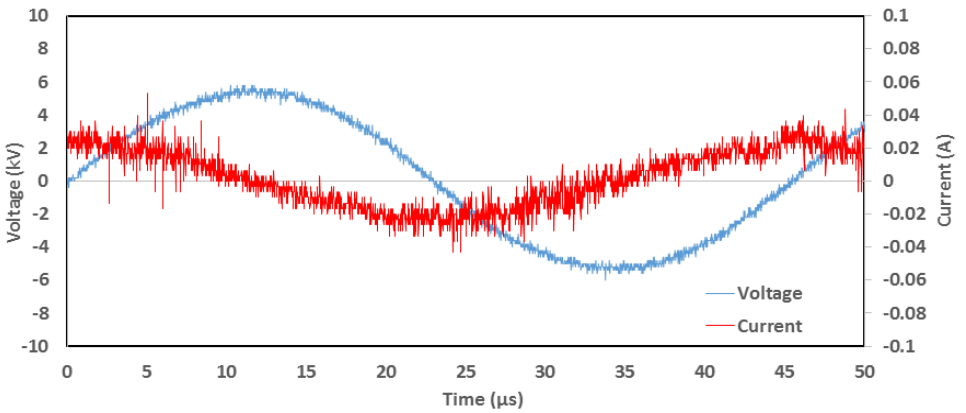

(a)

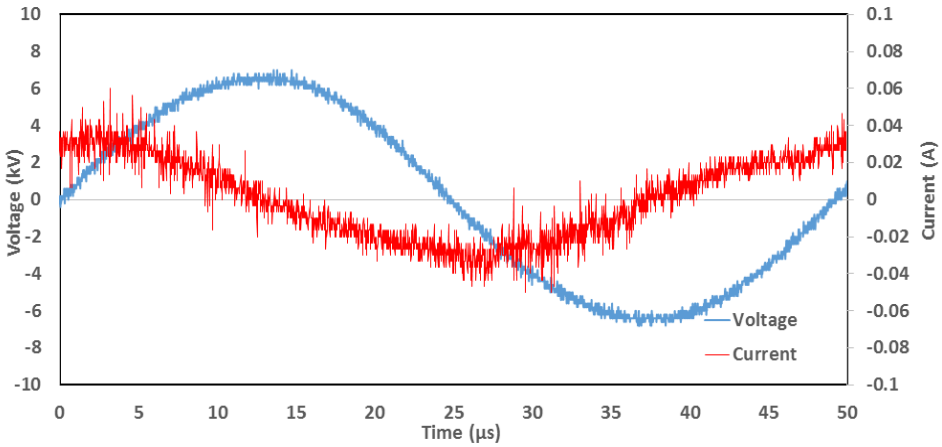

(b)

Figure 6-5 Voltage and current waveforms of plasma discharge in the $SrFeO_{3-\delta}$-packed DBD reactor at 293 K purged with 100% CH_4 (a). under voltage of 11 kV at 21.9 kHz with a dissipated plasma power of 7 W, giving an averaged conversion of CH_4 of 0.001; and (b). under voltage of 13.3 kV at 20.5 kHz with a dissipated plasma power of 16 W, giving an averaged conversion of CH_4 of 0.0210.

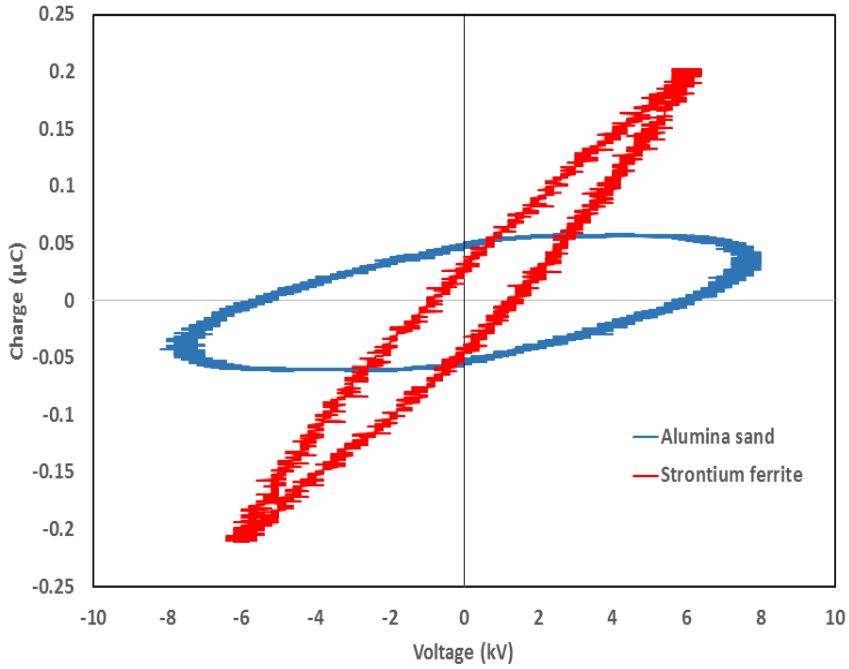

Figure 6-6 Lissajous figures of CH_4 plasma with the DBD reactor packed with the two bed materials at 293 K, both giving the conversion of CH_4 of 0.001. In the alumina sand bed, the electrical conditions were voltage of 15.4 kV, frequency of 26.8 kHz and plasma power of 22 W; in the strontium ferrite ($SrFeO_{3-\delta}$) bed, the voltage, the frequency and the plasma power were 13.3 kV, 20.5 kHz, and 16 W, respectively.

- **Correlation between voltage, plasma power and frequency**

The correlation between the applied voltage, power, and frequency to the DBD reactor are investigated. Figure 6-7 illustrates the plots of voltage versus plasmas power, and voltage versus frequency in $SrFeO_{3-\delta}$-packed DBD reactor at 293, 623 and 723 K. According to Fig. 6-7a, higher applied voltage to the plasma reactor results in higher dissipated plasma power at each temperature. In addition, based on the trendline of the data points collected, it seems that under the same applied voltage, higher temperature led to higher plasma power. For the relation between frequency and applied voltage, as shown in Fig. 6-7b, it seems that the increase in the applied voltage resulted in a decrease in frequency. This correlation may only apply to this particular plasma system, and the understanding of the system was only for the purpose of controlling the operating conditions for experiments in Chapters 7 and 8. The plasma generator used here was designed in a way that only the applied voltage can be manually controlled, and the

generator itself has a built-in tuning function to adjust the corresponding frequency in order to achieve stablisation of the system. At a same applied voltage, the increase in temperature seems to result in lower frequency; however, this trend is not decisive due to lack of data points available. In summary, from Fig. 6-7, low frequency appears together with high applied voltage and plasma power.

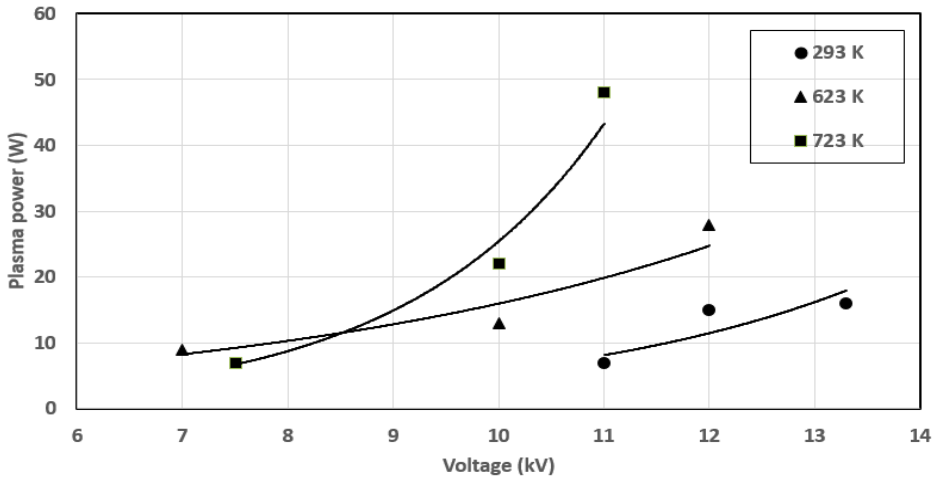

(a)

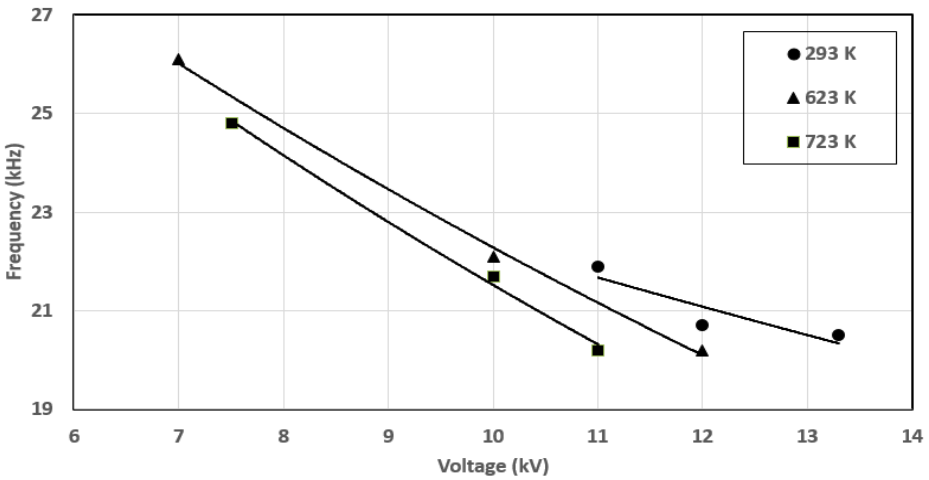

(b)

Figure 6-7 The correlations between voltage, frequency, and plasma power at different operating temperatures in the $SrFeO_{3-\delta}$-packed DBD reactor, (a). voltage versus plasma power, (b). voltage versus frequency.

Figure 6-8 shows the effect of plasma power on the effective capacitance of the quartz reactor at different temperatures. In the temperature range studied, the effective capacitance measured was from 3.6×10^{-11} to 8.3×10^{-11} F, which are below the

capacitance of the quartz C_D(9.0×10^{-11} F), indicating non-fully bridged gap in plasma discharge. On the other hand, the increase in the plasma power improved the effective capacitance, suggesting an increased bridging in the gaps. It is also found that, from 293 to 623 K, the increase in the temperature improved the effective capacitance; whilst from 623 to 723 K, there was no clear improvement.

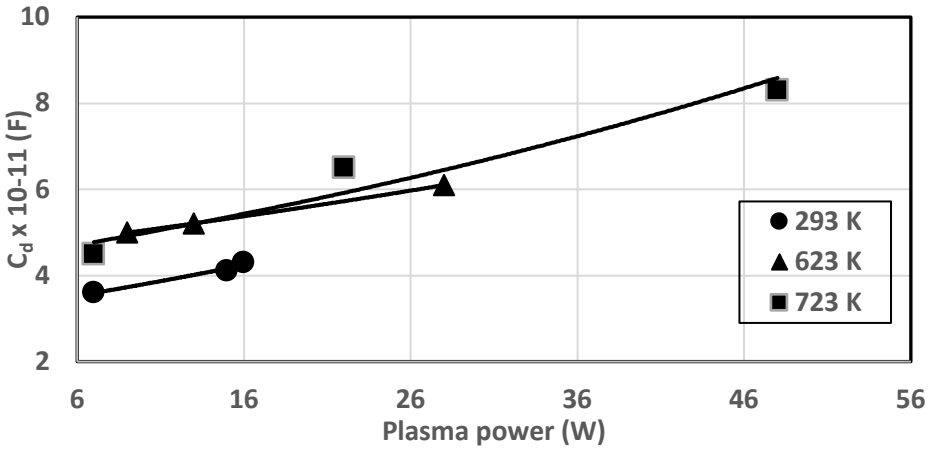

Figure 6-8 The correlation between effective capacitance of the dielectric C_d and the plasma power under different operating temperatures in a $SrFeO_{3-\delta}$-packed DBD reactor.

6.3.2 CH_4 conversion and mean electron energy

Table 6-1 Summary of the averaged conversion under different operating conditions in the alumina sand-packed DBD reactor.

Temperature (K)	Frequency (kHz)	Power dissipation (W)	Voltage (kV)	Averaged conversion of CH_4	Mean electron energy (eV)
293	26.8	22	15.4	0.001	4.60
	23.8	32	19.0	0.035	4.61
473	25.6	23	16.0	0.020	4.60
	23.1	40	16.2	0.039	4.60
573	26.3	21	14.0	0.007	4.59
	23.1	25	15.0	0.041	4.60
	20.4	92	16.0	0.053	4.60
723	28.6	33	12.6	0.001	4.59
	25.5	43	13.8	0.019	4.59
	21.2	77	14.0	0.029	4.59

Table 6-2 Summary of the averaged conversion under different operating conditions in the $SrFeO_{3-\delta}$-packed DBD reactor.

Temperature (K)	Frequency (kHz)	Power dissipation (W)	Voltage (kV)	Averaged conversion of CH_4	Mean electron energy (eV)
293	21.9	7	11	0	4.58
	20.7	15	12	0.021	4.59
	20.5	16	13.3	0.022	4.59
473	21.5	7	10.2	0	4.58
	20.4	17	12	0.015	4.59
573	21.3	16	11.5	0.010	4.58
	20.2	24	12.7	0.016	4.59
623	26.1	9	7	0.002	4.58
	20.2	28	12	0.075	4.59
	22.1	13	10	0.025	4.58
673	25.7	7	7.6	0	4.58
	20.0	54	10.4	0.093	4.58
	21.0	49	12	0.083	4.59
723	24.8	7	7.5	0.009	4.58
	20.2	48	11	0.100	4.58
	21.7	22	10	0.048	4.58

The conversions of CH_4 in the two different packing materials under each operating condition are presented in Tables 6-1 and 6-2, respectively. The conversion was averaged over the ~ 2.5 min plasma discharge. The mean electron energy was also estimated by calculating the reduced electric field, $\frac{E}{N}$, and referring to Fig. 6-3 to find corresponding values of $\frac{D_e}{\mu_e}$. For applied voltages below 12 kV (corresponding to 80 Td, or 8×10^{-20} V · m^2), the mean electron energy values were estimated by extrapolating the curve in Fig. 6-3 on the low side. As seen in the two tables, for both in the alumina sand and $SrFeO_{3-\delta}$ beds, higher conversion of CH_4 at each temperature was always achieved at higher plasma power (lower frequency and applied voltage). According to Fig. 6-3, the values of $\frac{D_e}{\mu_e}$ are stable over a wide range of $\frac{E}{N}$, thus the mean electron energy values obtained here do not vary significantly, from 4.58 to 4.61 eV. It has been found that in non-thermal plasma, the reactions stimulated by vibrational excitation are responsible for the major part of energy exchange, in which the electron energies required to initiate reactions are usually between 1 - 3 eV [101]. For CH_4 cracking to C and H_2, $CH_4 \rightarrow C + H_2$, the electron energy needed is about 0.9 eV [101]. Therefore, the energy supplied here should be sufficient to

initiate the cracking of CH_4. The fact that the conversion of CH_4 was observed also supports this.

In the alumina sand bed, as shown in Table 6-1, the conversion of CH_4 was between 0.001 to 0.053. For most of the experimental results, both increasing the temperature of the DBD reactor and the plasma power can lead to higher conversion of CH_4. However, this is not always true. The conversion of CH_4 at 723 K, with a plasma power of 77 W was 0.029; whilst this is lower than the conversion (0.035) at 293 K with a plasma power of 32 W. The higher plasma power would indicate higher degree of ionisation occurred in the plasma reactor, while this does not necessarily mean higher conversion of CH_4. As introduced in 1.4.2 (Chapter 1), DIEI (where the ionisation happens by collisions between neutrals and previously un-excited species by collisions with electrons) is a significant route for ionisation in the non-thermal plasma. Alternatively, SIEI, where some electron species needs to be excited and the excitation can include vibrational and rotational excitation, can also be a route to reaction. In order to have SIEI, some supplied energy needs to be used for excitation only. In addition to ionisation, chemical reactions can also be initiated by routes other than ionisation, for instance, vibration without going through ionisation. The mean electrode energy, which is dependent on the applied voltage, was found to have a slightly higher value at 293 K than that at 723 K (*i.e.* 4.61 > 4.59 eV). However, the applied voltage at 293 K was significantly higher. It suggests that in this case the applied voltage, and thus the electric field strength plays an important role in converting CH_4. According to Ref. [101], similar mean electron energy values do not always guarantee better overall performance in a system. The distribution of the electron energy is a complicated function of multiple parameters. Depending on the actual situation, different electron energy distribution functions can be obtained for the same value of mean electron energy (refer to Fig. 6-9), for instance Maxwell distribution for elastic collisions dominated cases and Druyvesteyn distribution for the situations where the electron mean free path can be treated as constant [101]. To initiate the conversion of CH_4, the electron energy needs to go beyond a threshold value for the reaction, and thus the not only the mean electron energy is important, the overall distribution of the electron energy in a system also matters. Here, it seems that the applied voltage might have led to a clear difference in the distribution of electron energy distribution at 723 and 293 K, which could then be responsible for the difference in the conversions. In summary, higher plasma power can be used as a first guide for achieving higher conversion, whilst it is not

the only influencing factor. High mean electron energy and applied voltage, which would give indication of the electron energy distribution, should also be considered.

Figure 6-9 Comparison of Maxwell and Druyvesteyn electron energy distribution functions for the same electron mean energy value. Note that the figure was reproduced from Ref. [101]). For copyright issue, the figure is removed here.

In a bed of $SrFeO_{3-\delta}$, according to Table 6-2, the electron energies are rather stable, between 4.58 and 4.59 eV. The conversion of CH_4 in $SrFeO_{3-\delta}$ is very low from 293 to 573 K. However, when increasing the temperature above 623 K, there is a significant increase in the conversion. At 623 K, with a plasma power of 28 W and electron energy of 4.58 eV, the conversion reached 0.075. Under similar conditions at 573 K (*i.e.* 24 W and 4.58 eV), the conversion was 0.016. This big difference seems less likely due to the small temperature difference (573 and 623 K) in the gas phase, but more reasonably from the activation of $SrFeO_{3-\delta}$. Alumina sand was considered inert and does not chemically involve in the conversion of CH_4. In this case, the conversion of CH_4 only would be ascribed to the decomposition of CH_4. $SrFeO_{3-\delta}$ can be chemically reactive at sufficiently high temperatures and participate in the conversion of CH_4, *i.e.* the oxygen in $SrFeO_{3-\delta}$ can react with CH_4. Therefore, compared to the CH_4 conversion trend in the alumina sand bed, the sharp increase in the CH_4 from 623 to 723 K should be mainly due to the reaction between CH_4 and $SrFeO_{3-\delta}$. Further investigation of this is presented in Chapter 7.

6.4 Conclusions

A packed-bed DBD reactor for CH_4 conversion was developed, and the electrical behavior with two packing materials: alumina sand and $SrFeO_{3-\delta}$, were studied. The main observations from the preliminary study are:

(a) Filamentary discharge was found in the alumina sand; whilst in the $SrFeO_{3-\delta}$, the discharge mode was close to silent discharge (diffuse plasma).

(b) Based on the current plasma generator, at each operating temperature of the DBD reactor, higher plasma voltage always resulted in higher plasma power and lower frequency, *e.g.* at 723 K, an increase in the voltage from 7.5 to 11 W resulted in a power increase from 7 to 48 W and a decrease in frequency from 24.8 kHz to 20.2 kHz.

(c) Higher plasma power and temperature led to higher discharge performance, *i.e.* closer to fully-bridged gap in the discharge zone with an effective capacitance from 3.6×10^{-11} to 8.3×10^{-11} F.

(d) For most cases, higher plasma power always led to higher conversion of CH_4, while it is not the only criteria. Higher mean electron energy and applied voltage that affect the electron energy distribution should also be considered.

7.0 H_2 production in a plasma-assisted chemical looping system in the presence of $SrFeO_{3-\delta}$

7.1 Introduction

A plasma-assisted packed bed reactor for the conversion of CH_4 was successfully developed in Chapter 6. In this chapter, the developed set-up was used for the investigation of H_2 production from the conversion of CH_4. The aim of this study is to achieve high yield of H_2 at mild temperatures (from 293 to 773 K). $SrFeO_{3-\delta}$, as an active oxygen-donating material and also a promising material for the stablisation of plasma, is studied here. To fully understand the chemical reactions taking place inside the DBD reactor, the process is studied in pure Ar, which provides an inert environment even in the plasma discharge condition, and ~ 8.5% CH_4/Ar respectively, instead of 100% CH_4.

7.1.1 $SrFeO_{3-\delta}$

Strontium ferrite, $SrFeO_{3-\delta}$, belongs to the family of perovskite materials, which possess a general formula of ABO_3 (*i.e.* A is usually an alkaline earth or rare earth cation, and B is a transitional metal cation). Perovskites have become increasingly attractive for chemical looping combustion, due to their high redox capability [203]. Particularly, $SrFeO_{3-\delta}$, was found promising from a recent study [42] of large scale *in silico* screening of materials. $SrFeO_{3-\delta}$, was able to release gaseous oxygen over multiple redox cycles (decomposition in N_2 or CO_2 followed by re-oxidation in air) at mild temperatures (~ 823 K), showing its promising chemical potential of oxygen for combustion and fast kinetics in redox. The material also showed good resistance to carbonation. To fit the aim of converting CH_4 at low temperatures in this study, $SrFeO_{3-\delta}$ is adopted as a first trial in the developed DBD reactor for H_2 production.

7.1.2 H_2 production from chemical looping

As described in 1.5.1 in Chapter 1, steam reforming of natural gas is a main approach used industrially for the production of H_2-rich gas and normally carried out at temperatures above 1073 K. A water-gas shift stage, operated at much lower temperatures (~ 673 K), is usually employed for higher yield and selectivity for H_2. Overall, the process is endothermic, meaning the need for external heating. Non-thermal plasma-assisted reforming of CH_4, particularly DBD configuration, has been widely investigated as an

alternative process for H_2-rich gas production [123]. The feasibility of using a DBD reactor for H_2 production from CH_4 reforming, either in the presence of CO_2 or H_2O, has been demonstrated in recent studies [123,124]; whilst its possibility for employing active chemical looping materials for the conversion of fuels for H_2 production has never been studied. In contrast to conventional plasma-assisted systems, an active oxygen carrier, $SrFeO_{3-\delta}$, is employed to provide a source of oxygen for CH_4 (ideally partial oxidation of CH_4) and suppress carbon deposition, without introducing a separate oxygen stream. Once depleted of oxygen, the oxygen carrier can be regenerated using air, allowing the cycle to be repeated. Thus, this plasma-assisted chemical looping H_2 production (PCLH) from CH_4, which is first proposed here, is similar to conventional chemical looping reforming [13] but can operate at much lower temperatures, where the water-gas shift equilibrium favours H_2.

7.2 Experimental methods

Around 7.5 ml of $SrFeO_{3-\delta}$, with a size fraction of 600 - 850 μm, prepared from solid mixing (as presented in 2.2.2) and calcination in air at 1273 K for 19 h, was used to pack the plasma-assisted quartz tube reactor. The experiments were carried out either in pure Ar or a mixed stream of CH_4 and Ar. Ar is considered relatively more chemically inert than other gases (such as N_2) both for conventional thermal conditions and in plasma. The investigation in Ar helps to understand the effect of plasma on the $SrFeO_{3-\delta}$, provided as a reference condition. The temperatures studied were from 293 K to 773 K. For a typical experiment, the gas inflow, either pure Ar or ~ 8.5% CH_4 (balance Ar) entered the packed bed at a flow rate of 0.72 L/min, equivalent to an hourly space velocity of 4670 h^{-1}. The gas from the packed bed was sampled at 0.5 L/min to the analysers. For a typical experiment with the feed gas being 8.5% $\pm$ 0.5% CH_4, the reactor was flowing in Ar to purge the system before the start of the experiment. Later, Ar was switched to the mixed stream of CH_4 and Ar. Plasma was then introduced for 2.5 $\pm$ 0.2 min. After CH_4/Ar plasma discharge, the gas was switched to air to burn off any deposited carbon as well as re-oxidise the bed materials. Plasma discharge was later introduced to assist the process of de-coking and re-oxidation of the bed material. For the experiment with the bed material treated in Ar plasma only, the plasma on and off operation kept the same, with only that the gas medium flowing through the DBD reactor being different. The applied voltage was controlled at 8.5 $\pm$ 0.5 kV, resulting a plasma power at 16.0 $\pm$ 1.5 W. More detailed description of the experimental set-up and the process was presented in 2.3.3.

For data analysis (refer to 6.2), the change in the total flow (as a result of conversion of CH_4) at the reactor inlet and outlet, $F_{total,0}$ and F_{total}, was corrected based on the assumption that Ar did not change over time, only CO, CO_2, H_2, C_2H_2, C_2H_4 and Ar were present in the measured flow at the outlet, the total flow rate at the outlet (dry basis), F_{total}, can be obtained from the Ar balance:

$$F_{total,0} \cdot \left(1 - x_{CH_{4,0}}\right) = F_{total} \cdot (1 - x_{CH_4} - x_{CO} - x_{CO_2} - x_{C_2H_2} - x_{C_2H_4} - x_{H_2}).$$

7.3 Results

7.3.1 Identification of the non-stoichiometry of $SrFeO_{3-\delta}$

The non-stoichiometry, 3-δ, was determined by performing reduction of the prepared fresh $SrFeO_{3-\delta}$ (600 - 850 μm), in H_2 in Thermogravimetric analysis (TGA), as described in Ref. [40]. The non-stoichiometry was found to be 2.820, giving $SrFeO_{3-\delta}$. The fresh $SrFeO_{3-\delta}$ (600 - 850 μm) was also XRD scanned, where the particles were first crushed to a particle size below 50 μm before scanning. The running parameters of the XRD scanning was presented in 2.4.1. Figure 7-1 shows the spectrum of the $SrFeO_{3-\delta}$ sample. The reference data of $SrFeO_{2.8064}$ with an angle range from 10° to 60°, was found to fit the sample spectrum well, not far from the results determined by TGA.

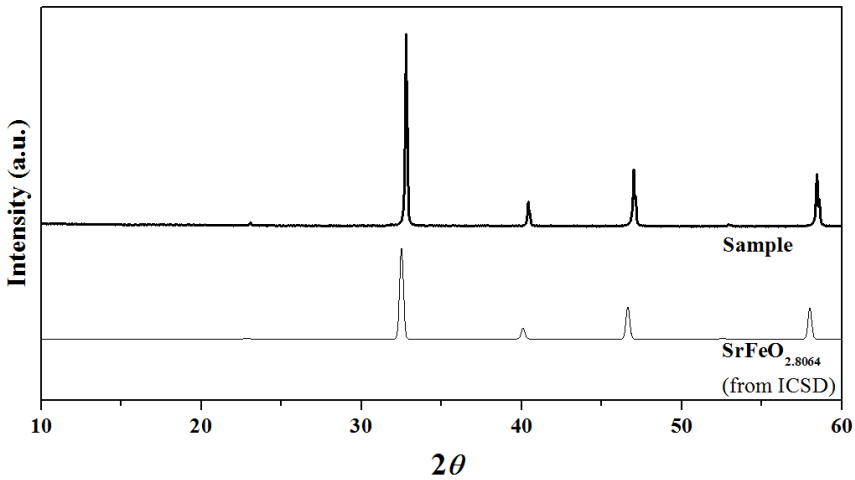

Figure 7-1 XRD spectrum of the prepared $SrFeO_{3-\delta}$, in comparison to the reference spectra of $SrFeO_{2.8064}$ (with a collection code of 154928, from ICSD).

7.3.2 Identification of the gaseous products

The product species in UV-Vis and IR regions in the gas phase was identified. The investigation of CH_4 conversion in a plasma environment was initially carried out in the

mixed gas of CH_4 and N_2. However, N_2, which is generally considered inert for traditional chemical processes in the temperature range studied, was found to chemically react with the bed material to generate species such as N_2O in the presence of plasma here. Therefore, the background gas changed to Ar, a chemically inert gas in plasma discharge.

- **Identification of products in the UV-Vis region**

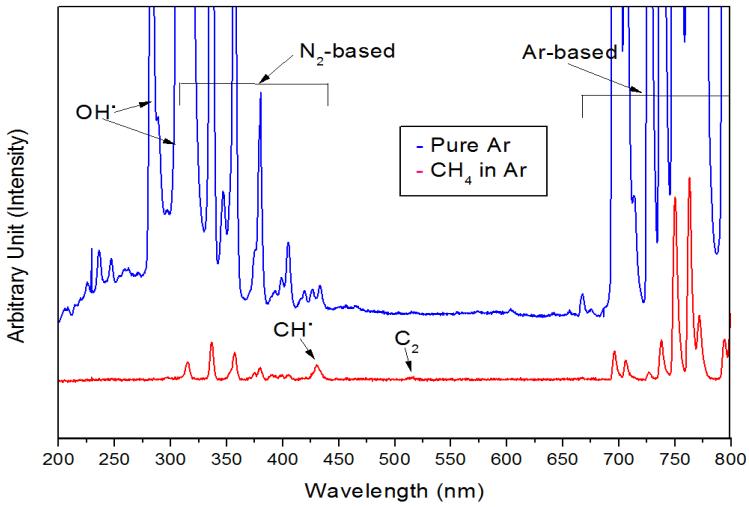

Figure 7-2 UV-Vis spectrum results in the $SrFeO_{3-\delta}$-packed DBD reactor at 293 K in the two gases: pure Ar, and ~ 8.5 % CH_4 (balance Ar).

Figure 7-2 shows the uv-vis spectrums (from 200 to 800 nm) in the two gas mediums with the bed packed with $SrFeO_{3-\delta}$ and operated at 293 K. For the wavelength region below 275 nm, the peaks have not been assigned and identified, as they are not strong peaks of any species of interest here. Most of the peaks of interest fell into the range from 275 to 800 nm. Data from National Institute of Standard and Technology (NIST) Atomic Spectra Database Lines Form [204] were used for identification. According to Fig. 7-1, in pure Ar, the species detected were mainly Ar-based species (mostly > 650 nm), N_2-based species (mainly between 300 to 450 nm), and OH· radicals. The presence of N_2-based species and OH· radicals should mainly come from the excitation of the trace amounts of N_2 and moisture that entered the DBD reactor. Especially for the spectrum of OH· at 309.3 nm, which is generally found in plasma systems when there is moisture present [205]. In Fig. 7-1, however, it cannot show a complete OH· spectrum at ~ 309.3 nm, as it overlapped with the spectrum of a N_2-based excited species at ~ 313.0 nm. When a proportion of CH_4 (resulting 8.5% CH_4 in N_2) was introduced into the DBD reactor, the

intensity of most spectrums significantly decreased. One of the OH· radical spectrums (*i.e.* at ~ 295 nm) even became too weak to be detected in the presence of CH_4. On the other hand, there were two extra peaks found: ~ 430.1 nm, and ~ 517.0 nm. They match the spectrums of CH· radical, and C_2 swan band (with the peak at close to 517.0 nm) respectively. In general, the results are in agreement with the spectrum of CH_4 plasma; however, no strong H-based spectrum lines/peaks were observed here. The difference in the intensity of the Ar- and N_2-based spectrums in the two gas medium might be due to the difference in the plasma stability in pure Ar and 8.5% CH_4/Ar (see detailed discussion in 7.4.1).

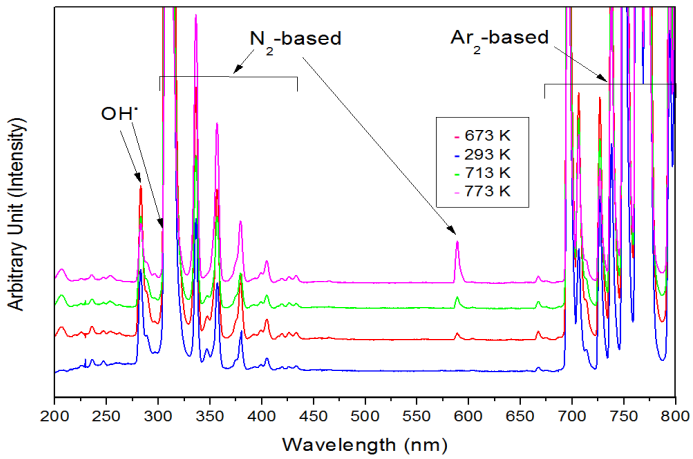

Figure 7-3 UV-Vis spectrum results in the $SrFeO_{3-\delta}$-packed DBD reactor in pure Ar at different temperatures of 293, 673, 713 and 773 K.

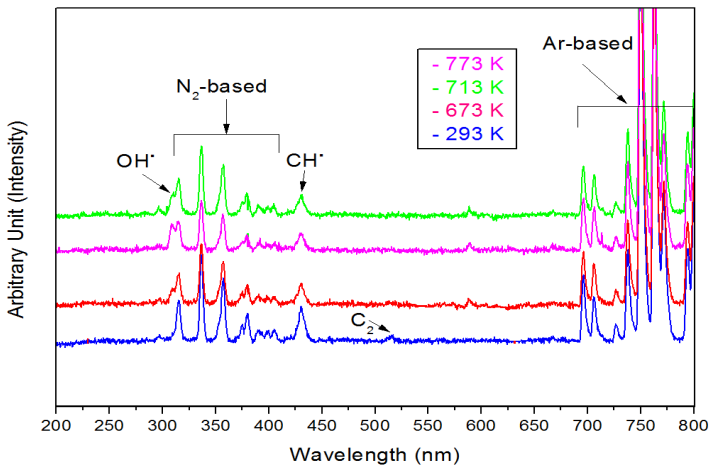

Figure 7-4 UV-Vis spectrum results in the $SrFeO_{3-\delta}$-packed DBD reactor in ~ 8.5% CH_4 (balance Ar) at different temperatures of 293, 673, 713 and 773 K.

Figures 7-3 and 7-4 present the emission spectrums from the $SrFeO_{3-\delta}$-packed DBD reactor from 293 K to 773 K in pure Ar (Fig. 7-2) and ~ 8.5% CH_4 (Fig. 7-3). According to Fig. 7-3, at 293 K, no strong peak was observed at 590 nm in pure Ar; whilst as the temperature increased to beyond 673 K, the peak at 590 nm was observed and most likely to be a N_2-based excited species. Ar-based excited species are relatively inert to other components. For other species including N_2-based species, OH· radicals and C-based excited species, whether they would influence any chemical reactions inside the DBD reactor is unknown. For instance, OH· radicals, is an oxygen source, understanding of its contribution to the conversion of CH_4 would be interesting. However, as the N_2-based excited species and OH· radicals are only from the trace amounts of N_2 and H_2O, their effect is assumed to be negligible in this study. When a portion of CH_4 joined the Ar to enter the DBD reactor, the spectrums were shown in Fig. 7-4. In general, the intensity of the spectrums at different temperatures were comparable. C_2 and CH· peaks in the spectrum were found at the 293 and 673 K; whilst when the temperature increased further, C_2 spectrum became invisible and CH· radical was the only C-containing species found in the UV-Vis region.

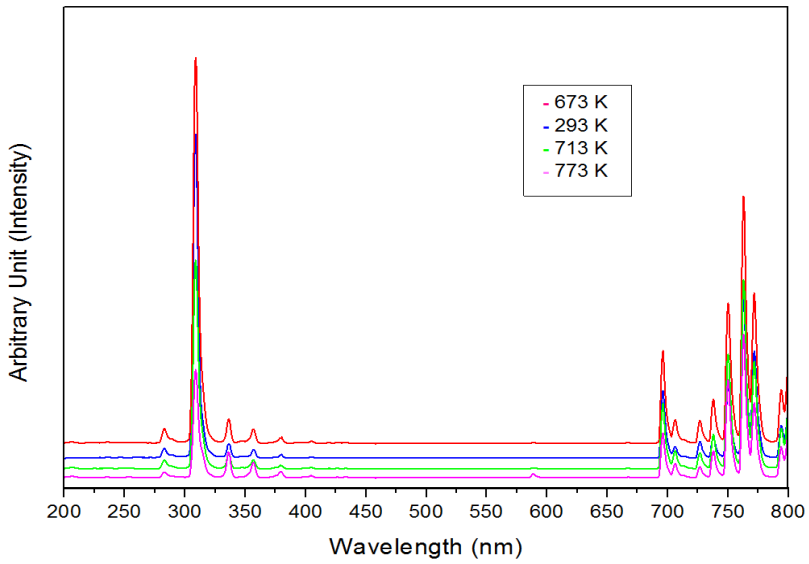

Figure 7-5 Full scale of the UV-Vis spectrum results in pure Ar at 293, 673, 713 and 773 K.

Figure 7-5 shows the full scale of spectrum in Fig. 7-2. It can be seen that unlike the conditions in ~ 8.5% CH_4 (where the intensities of the spectrums at different temperatures are similar), the intensity of the spectrums in the pure Ar vary significantly as a change

of temperature. The intensity of the spectrums of most excited species reached maximum at 673 K, much higher than those at 713 and 773 K (refer to the N_2- and Ar-based species in Fig. 7-5). In the meantime, gaseous oxygen from the DBD reactor was detected at 713 and 773 K, and the decreased intensity might be linked with the presence of these gaseous oxygen (refer to further discussion in 7.4.1).

- **Identification of products in the IR region**

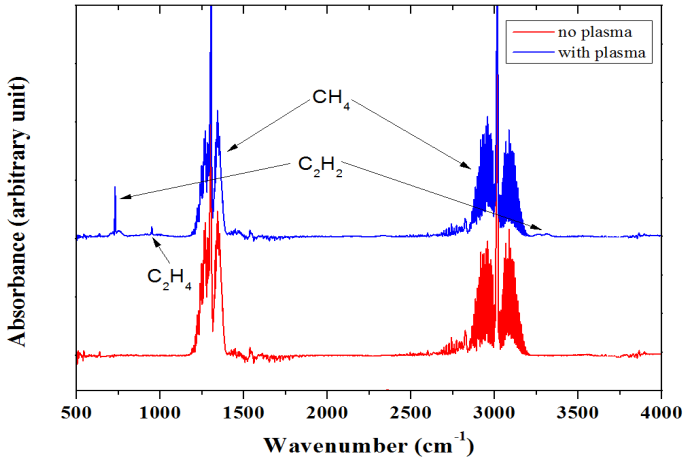

(a)

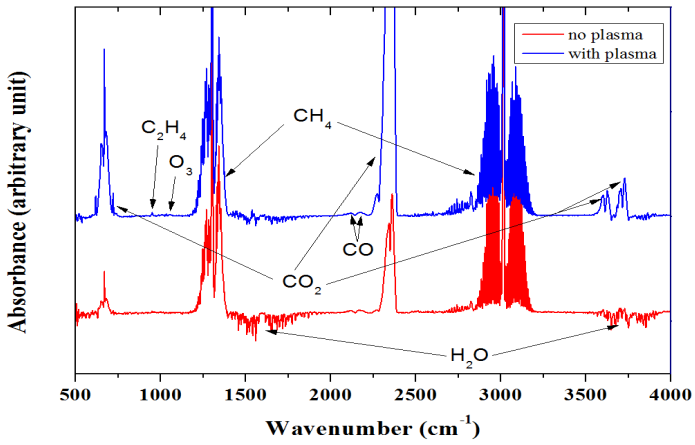

(b)

Figure 7-6 IR spectrums by FTIR from $SrFeO_{3-\delta}$-packed DBD reactor in ~ 8.5% CH_4 with/without plasma discharge, at a bed temperature of (a). 293 K, (b). 773 K.

Product species in the range of IR (with a wavenumber from 500 cm^{-1} to 4000 cm^{-1}) were identified from the measurement in the FTIR. No product was detected in pure Ar during

plasma discharge. Figure 7-6 presents the FTIR results of with/without plasma discharge in 8.5% CH_4 (balance Ar) at 293 and 773 K, respectively. According to Fig. 7-6a, without plasma discharge in 8.5% CH_4, in addition to CH_4 peaks, only some fluctuation in the moisture level was observed. When plasma was introduced to the DBD reactor, some extra peaks were seen. The peaks at 650 - 800 cm^{-1} and 3200 - 3360 cm^{-1} are assigned with C_2H_2 peaks (with another peak in the range of 1300-1400 cm^{-1} overlapped one of the CH_4 peaks), and the peak at 900 - 1000 cm^{-1} is assigned with C_2H_4 (with its other peaks overlapped the CH_4 peaks). At 773 K, according to Fig. 7-6b, some CO_2 was observed even without plasma discharging the bed, suggesting the direct reaction between CH_4 and $SrFeO_{3-\delta}$ to generate CO_2 at this temperature. The C_2H_2 peaks, seen at 293 K, were not found at 773 K. It is most likely that the reactivity of $SrFeO_{3-\delta}$ at 773 K does not allow the existence of C_2H_2. C_2H_2 peaks were only observed at temperatures below 673 K. Combining the results in Fig. 7-4, it seems that C_2H_2 and C_2 always appeared simultaneously here. C_2H_2 was reported to be an important intermediate species in the combustion of hydrocarbons and a key species for soot formation and growth, and C_2 always appears together with the generation of C_2H_2 [206]. The fact that C_2H_2 and C_2 were only found at the low temperature is consistent with the very low carbon balance at ambient temperature (refer to Table 7-1 in discussion), indicating higher amount of solid phase carbon formed inside the DBD reactor.

7.3.3 H_2 production from plasma-assisted redox cycle

According to 7.3.2, the main gas species involved in the conversion of CH_4in the UV-Vis and IR regions include CH_4, CO, CO_2, C_2H_2, C_2H_4, and O_3. C_2H_2, C_2H_4 and O_3 were only found at trace amounts, thus not considered in the following analysis. The generated H_2 from the system was measured by a separate conductivity analyser. In addition, O_2 was also produced under some conditions and was measured by a paramagnetic analyser. The results of the mole fractions with the $SrFeO_{3-\delta}$-packed DBD reactor in Ar and 8.5% CH_4/Ar were shown as follow.

- **Results with the DBD reactor in pure Ar**

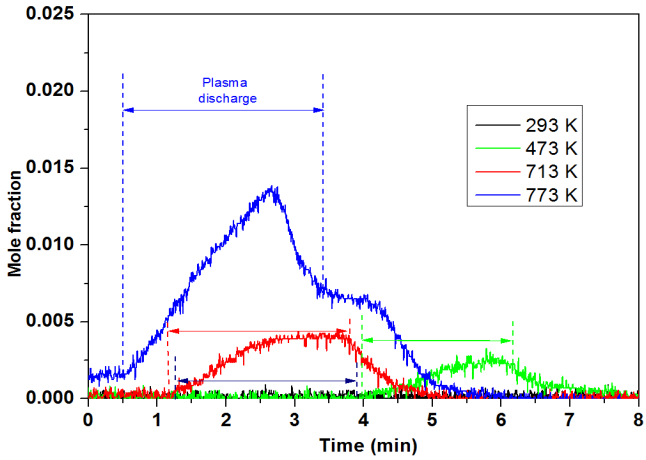

Figure 7-7 Mole fraction of oxygen released from $SrFeO_{3-\delta}$-packed DBD reactor in pure Ar at 293 K. The plasma discharge time span was about 2.5 min.

Figure 7-7 shows the amount of gaseous oxygen, which was the only product detected in the gas phase, released from $SrFeO_{3-\delta}$ bed in Ar plasma discharge at temperatures from 293 to 773 K. At ambient temperature, there was no significant release of gaseous oxygen for both with and without plasma discharge periods. When the bed temperature increased to 473 and 713 K, gaseous oxygen was observed when subjected to plasma discharge. At the highest temperature 773 K, some gaseous oxygen (~ 0.0015) was observed even without plasma; more oxygen was produced when plasma was applied. More interestingly, at 473 and 713 K, the released gaseous oxygen quickly dropped to zero; whist at 773 K, the level of released gaseous oxygen was maintained at 0.006 for 0.7 min, followed by a decrease to zero (*i.e.* below its initial equilibrium level). It suggests that plasma might have led to some heating effect on the solids, resulting in release of oxygen. The surface temperature in non-equilibrium discharges can be much higher than the bulk gas temperature by having the species such as charge carriers, photons, metastable and excited neutrals hitting the surface of the materials [207]. The heating effect depends on the power coupled into the plasma and could have led to an increase in the bulk temperature of the solid bed, or/and formation of "hot spots". Owing to this effect, the surface oxide reduction processes can be stimulated. When the plasma discharge was off, the solid beds require some time to fall back to its equilibrium temperature, as a result, 'post-plasma' effect of releasing oxygen at 773 K was observed. Additionally, according

to Fig. 7-7, after plasma discharge, $SrFeO_{3-\delta}$ has been reduced to a state that no longer released significant amount of gaseous oxygen.

- **Results with the DBD reactor in 8.5% ± 0.5% CH_4 (balance Ar)**

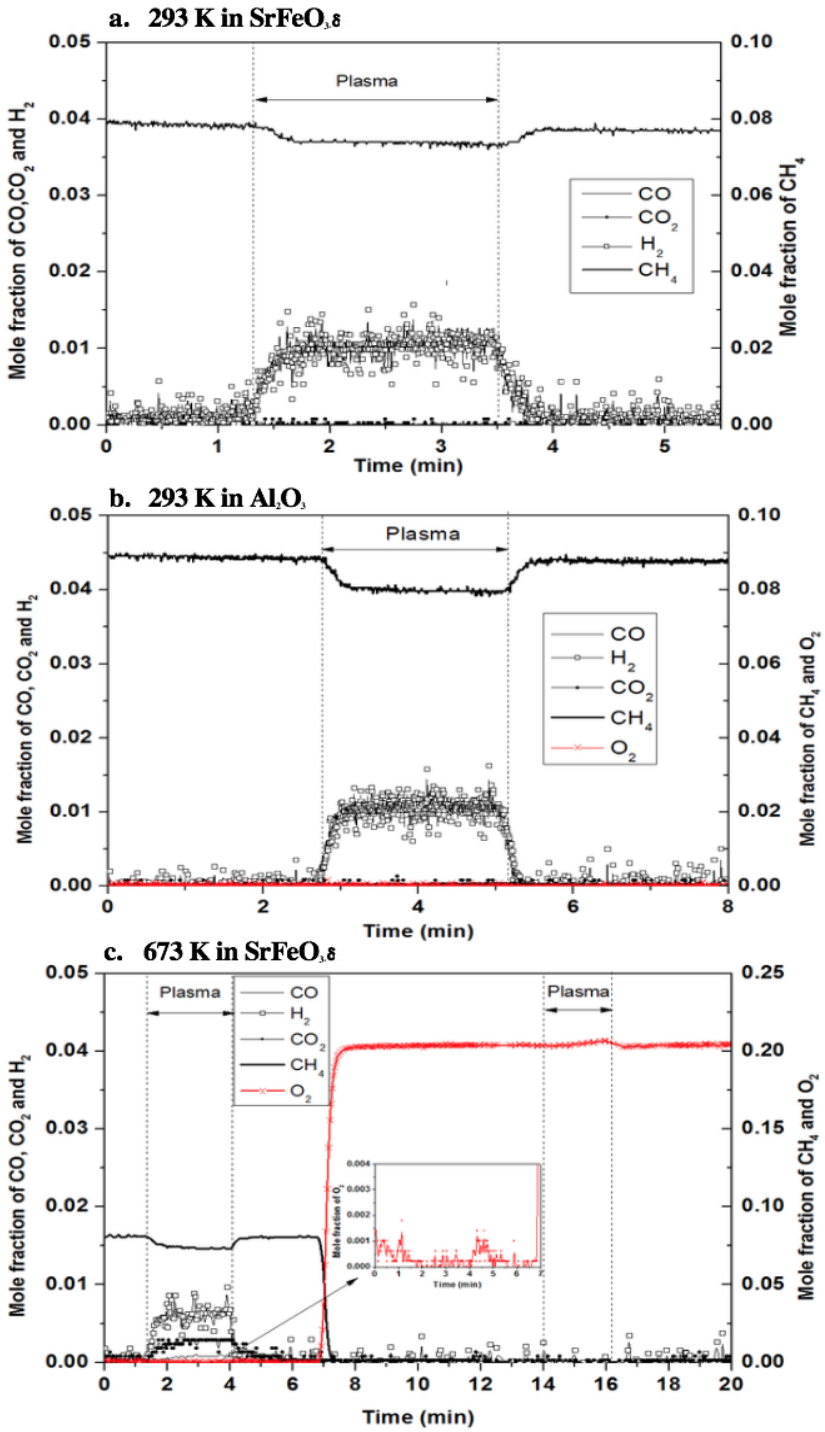

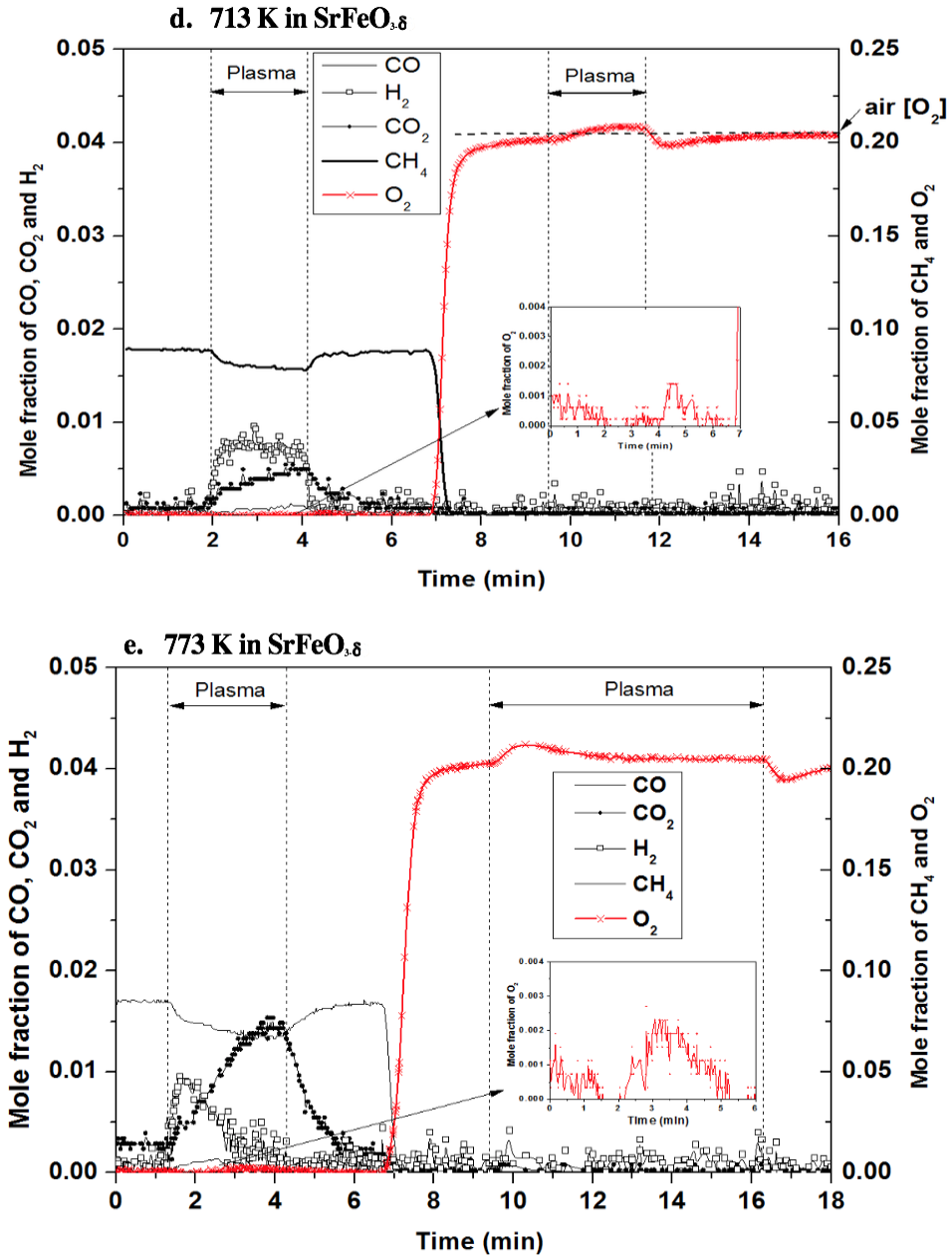

Figure 7-8 Mole fractions of different gaseous species from the DBD reactor with the conditions being a. at 293 K in $SrFeO_{3-\delta}$; b. at 293 K in Al_2O_3; c. at 673 K in $SrFeO_{3-\delta}$; d. at 713 K in $SrFeO_{3-\delta}$; e. at 773 K in $SrFeO_{3-\delta}$. The plasma discharge time span in ~ 8.5% CH_4 was about 2.5 min.

Figure 7-8 presents the results of the gases observed from the DBD reactor including CO, CO_2, CH_4, O_2 and H_2, from 293 to 773 K in ~ 8.5% CH_4. A complete cycle of the bed first experiencing the reduction in ~ 8.5% CH_4, followed by the re-oxidation or regeneration in air at temperatures above 673 K is shown. According to Fig. 7-8a, when the packed

bed was purged with ~ 8.5% CH_4 at 293 K, there was a constant conversion of CH_4 when subjected to plasma discharge. Uniform generation of H_2 was observed over the entire plasma discharge period in ~ 8.5% CH_4. Other gaseous products formed include C_2H_2 and C_2H_4, but at trace amounts. The extreme low carbon balance (Table 7-1), which is defined as the ratio of the amount of carbon in the carbon-containing gaseous products over a complete redox cycle to the amount of converted CH_4 in the reduction stage, and the uniform generation of H_2 during plasma discharge suggest the formation of solid carbon inside the DBD reactor from direct CH_4 cracking by plasma. The results were compared to the condition when the DBD reactor was loaded with Al_2O_3, where Al_2O_3 is considered chemically inert. According to Fig. 7-8a and 7-8b, similar levels of CH_4 conversion and H_2 production were observed, implying that at this temperature, $SrFeO_{3-\delta}$ was chemically inactive. When the operating temperature of the DBD reactor increased to 673 K, according to Fig. 7-8c, CH_4 was converted when plasma was active. Together with the conversion of CH_4, the production of CO_2 (~ 0.0025), CO (~ 0.0009) and H_2 (~ 0.007) were observed. The generation of CO and CO_2 means that $SrFeO_{3-\delta}$ was activated by plasma and stimulated the conversion of CH_4. This can either be *via* a gas-gas reaction between CH_4 and gaseous oxygen (released from $SrFeO_{3-\delta}$, as shown in Fig.7-7 in Ar), or direct gas-solid reaction between CH_4 and $SrFeO_{3-\delta}$. It was noticed that there was some amount of gaseous oxygen detected in CH_4/Ar before plasma discharge, whilst the oxygen level dropped to zero when the plasma was active; some oxygen was detected again as soon as plasma was tuned off. $SrFeO_{3-\delta}$ seems to have become active in donating oxygen at 673 K, and it suggests that at least gas-gas reaction between CH_4 and gaseous oxygen exist in this system. Comparing the amounts of H_2 produced at 293 and 673 K, lower amounts of H_2 were seen at 673 K, suggesting that some H_2 might have been oxidised to other species by $SrFeO_{3-\delta}$, most probably H_2O. In the air regeneration stage, no species other than O_2 were observed before plasma discharge; and higher [O_2] than that in air was detected during air plasma discharge, indicating a release of gaseous oxygen from the solid bed.

When the bed temperature increased to 713 K, according to Fig. 7-8d, similarly, CO_2, CO, and H_2 were observed during plasma discharge. A decrease in the [O_2] over the discharge period in ~ 8.5% CH_4 was also found. The generation of CO_2 and H_2 were not as uniform as those at lower temperatures (Fig. 7-8a and 7-8c), the amount of H_2 was gradually

decreasing. As the cracking of CH_4 (by plasma) always takes place, regardless of the interaction between CH_4 and $SrFeO_{3-\delta}$, the gradually reduced [H_2] seems to suggest an increasing consumption of the generated H_2 due to an increase in the activity of the solid bed. In the meantime, the CO_2, CO and O_2 concentrations gradually increased to ~ 0.006, 0.0015, and 0.0002, respectively. Referring to the oxygen level with that (gradually increased to ~ 0.0035) in pure Ar at 713 K (Fig. 7-7), the sum of the oxygen amount from CO and CO_2 was higher than in the gaseous O_2 released in Ar, suggesting that either more gaseous oxygen was pulled off from $SrFeO_{3-\delta}$ in CH_4/Ar in the presence of plasma, or there is direct gas-solid reaction between CH_4 and $SrFeO_{3-\delta}$. More oxygen was detected when plasma was turned off (with the bed still in 8.5% CH_4) than that before plasma discharge. This indicates 1) the presence of post plasma heating effect; 2) the $SrFeO_{3-\delta}$ contributes to the conversion of CH_4 and gas-gas reaction between CH_4 and gaseous O_2 was present. Whether gas-gas combustion will be dominant, however, is still not clear. In terms of the air regeneration of the bed material, similar to the results from lower temperatures, oxygen was pulled out from $SrFeO_{3-\delta}$ during plasma discharge; interestingly, while plasma was stopped, [O_2] dropped to a level slightly lower than the air O_2 level, followed by a gradual increase to the expected [O_2] in air. Further discussion on this is presented in 7.4.4.

When the bed temperature increased to 773 K, as seen in Fig. 7-8e, some CO_2 (mole fraction of ~ 0.0028) was generated even without plasma. Meanwhile, an oxygen mole fraction of ~ 0.001 was detected. In Fig. 7-7, without plasma discharge in Ar, there was a mole fraction of around 0.0015 oxygen released from the solid bed. As it is expected that even more gaseous oxygen should be released from $SrFeO_{3-\delta}$ in 8.5% CH_4 due to much lower partial pressure of oxygen (*i.e.* pure CH_4 is with $p_{O2} \sim 10^{-35}$ bar) in the reducing environment, the lower detected amount of oxygen level in 8.5% CH_4 than that in Ar at least suggests the presence of direct combustion of CH_4 by the released O_2. The auto-ignition temperature of CH_4 is about 810 K [208], indicating a catalytic effect of $SrFeO_{3-\delta}$ on the combustion of CH_4. Falcon *et al*. [209] observed similar catalytic effect of $SrFeO_{3-\delta}$ for the combustion of CH_4. Whether there was direct gas-solid reaction between CH_4 and $SrFeO_{3-\delta}$ is still unknown. When plasma was applied to the DBD reactor at t = 1.3 min, CO_2 was found to be the primary product from the conversion of CH_4. The generation of CO started at about the same time with the generation of CO_2. [H_2] firstly

reached a maximum with a peak value of around 0.009, followed by its quick decrease, whilst CO_2 and CO concentrations kept rising. [O_2] first dropped in the presence of plasma discharge, however, it quickly increased, and this might suggest some phase change of $SrFeO_{3-\delta}$, where $SrFeO_{3-\delta}$ became more reactive for releasing oxygen or the oxygen decoupling rate has become faster. In the air regeneration stage, similar to the conditions at 713 K (Fig. 7-7d), a quick drop to lower than air level [O_2] after plasma discharge was observed at 773 K.

7.3.4 Results of conversion, selectivity and material balance

Table 7-1 shows the summarised results including the averaged conversion of CH_4, selectivity for different gaseous products, and hydrogen and carbon balances at different operating temperatures of the DBD reactor. The equation for obtaining the averaged conversion of CH_4, X_{CH_4}, has been described in 6.5.3. Other parameters were calculated based on the equations as follow.

The averaged selectivities, $S_{a=CO\ or\ CO_2}$ for CO or CO_2, and S_{H_2} for H_2, are given as:

$$S_a = \frac{\int_{t_0}^{t_{end}} F_{total} \cdot x_a dt}{\int_{t_0}^{t_{end}} (F_{total,0} \cdot x_{CH_4,0} - F_{total} \cdot x_{CH_4}) dt}$$

$$S_{H_2} = \frac{\int_{t_0}^{t_{end}} F_{total} \cdot x_{H_2}\, dt}{2\int_{t_0}^{t_{end}} (F_{total,0} \cdot x_{CH_4,0} - F_{total} \cdot x_{CH_4}) dt},$$

where S_a is based on C in CH_4, and S_{H_2} is based on H in CH_4. The average yield for each product, Y_i, was defined as the amount of component *i* produced for every mole of CH_4 introduced into the DBD reactor:

$$Y_i = \frac{\frac{\int_{t_0}^{t_{end}} F_{total} \cdot x_i\, dt}{t_{end} - t_0}}{F_{total,0} \cdot x_{CH_4,0}}.$$

The fraction of carbon deposited was estimated from the difference between the carbon input and that detected at the outlet during the reduction period:

$$d_c = 1 - \frac{\int_{t_0}^{t_{end}} F_{total} \cdot (x_{co} + x_{co_2} + 2x_{C_2H_4} + 2x_{C_2H_2})\, dt}{\int_{t_0}^{t_{end}} (F_{total,0} \cdot x_{CH_4,0} - F_{total} \cdot x_{CH_4}) dt}.$$

The carbon and hydrogen balances, defined as the ratio of carbon/hydrogen-containing species measured to the carbon/hydrogen in the converted CH_4 in a complete redox looping cycle (*i.e.* CH_4/Ar plasma discharge followed by air plasma discharge stage), were also estimated. According to Table 7-1, the increase in the temperature leads to an increase in the conversion of CH_4; however, the production of H_2 does not benefit from the increase in temperature. This might be due to the too high activity of $SrFeO_{3-\delta}$ at high temperatures that resulted in the oxidation of the produced H_2. In the meantime, higher selectivity towards CO_2 was observed with an increase in temperature; whereas for CO, the selectivity from 673 to 773 K seems to be stable. Similar to H_2, both the selectivity towards C_2H_2 and C_2H_4 decreased. Due to the increased oxidising activity of $SrFeO_{3-\delta}$ with an increase in temperature, the carbon balance over a complete plasma-assisted redox cycle increased significantly. If the poor carbon balance was mainly due to deposited carbon in the DBD reactor, it seems that the even with the assistance of plasma discharge in the regeneration stage, not all the deposited carbon was removed, as no significant amount of CO or CO_2 was detected, as shown in Fig. 7-8.

Table 7-1 Summarised results of conversion of CH_4, product selectivity and material balances.

Parameters	Temperature (K)			
	293	673	713	773
Gas medium	CH_4/Ar	CH_4/Ar	CH_4/Ar	CH_4/Ar
X_{CH4}	0.075	0.082	0.117	0.171
S_{CO}	0	0.113	0.108	0.111
S_{CO2}	0	0.391	0.472	0.692
S_{H2}	0.782	0.489	0.359	0.093
S_{C2H4}	0.181	0.061	0.042	0.024
S_{C2H2}	0.191	0.03	0	0
$Y_{CO} \times 10^3$	0	9	12	18
$Y_{CO2} \times 10^3$	0	30	57	118
$Y_{H2} \times 10^3$	115	81	84	32
H balance	0.918	0.537	0.395	0.113
C balance	0.311	0.594	0.650	0.847

7.4 Discussion

7.4.1 The effect of Ar on plasma intensity and conversion of CH_4

As described in Fig. 7-2, significantly higher intensity of the UV-Vis spectrum was observed in pure Ar plasma than that in CH_4/Ar, indicating that it was easier to form plasma species in pure Ar. The first ionisation energy of Ar is about 1520 kJ/mol, higher than that for CH_4 (~ 1220 kJ/mol) [210,211]. However, this does not mean it is easier to generate plasma in CH_4. CH_4 is more chemically active compare to Ar, and this would mean that some of the applied energy has been used for other routes besides ionisation, such as vibrational and rotational excitation. While in Ar, the routes to spread the energy of electrons are very limited, suggesting that the energy efficiency for ionisation in Ar would be higher than that in CH_4. Additionally, because there are many possible routes to spread the energy of electrons in CH_4 plasma, the mean free path of the electrons, the average distance traveled between successive collisions [212], in Ar plasma is estimated to be around 1.3 times that in CH_4 plasma (based on $\lambda = 1/(n\sigma)$, where n is the number density of the particles, σ is the cross section of a two-particle collision, and λ is the mean free path between collisions) [213]. Given identical electric field, the electrons are accelerated by electric field to higher velocities, and therefore energies, in Ar compared

to CH_4 before they experience a collision. As a result, the energy density of the electrons in Ar would be higher, giving a more stable plasma in Ar. The addition of CH_4 to the Ar gas is actually contaminating the Ar plasma environment, leading to a decrease in the plasma intensity. This is consistent with what has been reported by Matsumoto *et al.* [214] that only the addition of 2% CH_4 into pure Ar in a DBD reactor dramatically decreased the degree of Ar excitation.

The effect of the purity of Ar on plasma can also be responsible for the difference in the spectra intensity in Fig. 7-5. The Ar spectra at 293 and 673 K were much higher than those at 713 and 773 K. At 293 and 673 K, during plasma discharge, no gaseous oxygen was produced to 'contaminate' the pure Ar environment; therefore, the intensity would be high. When the bed was increased to between 713 and 773 K, oxygen started to be released from $SrFeO_{3-\delta}$, especially at 773 K, where the oxygen mole fraction reached close to 0.015 (at its peak). This significantly affected the plasma intensity. This is because, compared to Ar, oxygen molecule is also much more chemically active. With its first ionisation energy (~ 1314 kJ/mol, [210,211]) being similar to that of Ar, the energy density of electrons in the presence of gas phase oxygen would also be much lower.

7.4.2 Investigation of the effects of plasma catalysis and plasma heating

The dissipated plasma power was determined by taking the integration of the parallelograms of the voltage-charge figures, as described in 2.3.3. To understand whether the plasma energy input is a significant amount, the thermal energy required for heating the DBD reactor was estimated for comparison. It was assumed that the thermal energy was only used for heating the bed of $SrFeO_{3-\delta}$ and the flowing gas through the DBD reactor. Heat capacities of each medium in each temperature range was estimated by taking the average of the values of the starting and end temperatures. The values of the heat capacity used are presented in Table 7-2:

Table 7-2 Heat capacities.

Medium	Heat capacity (J/mol/K)		
	from 293 to 773 K	from 673 to 773 K	from 293 to 713 K
$SrFeO_{3-\delta}$ (data based on [215]	106	111	106
CH_4 (data from NIST [131])	48.4	59.0	46.8
Ar (data from NIST [131])	20.8	20.8	20.8

Table 7-3 Estimated thermal energy input (assuming negligible heat loss from the bed).

Temperature increase (K)	Heat for heating $SrFeO_{3-\delta}$ (J)	Heating power for the flowing gas (W)
100	585	1.67
420	2346	6.67
480	2682	7.99

According to Fig. 7-8, in the absence of plasma discharge, up to 713 K, no significant conversion of CH_4 was observed. The thermal energy required to heat the bed from 293 to 713 K was about 2346 J, and heating power for the flowing gas was about 6.67 W. The effects of plasma power and thermal energy input were compared. For a bed of $SrFeO_{3-\delta}$ at 293 K, plasma power supplied to the DBD reactor was gradually increased to the point where the conversion of CH_4 was just observable (converted mole fraction of CH_4 of ~ 0.001). The corresponding supplied power was 4.13 W and it took about 0.5 min to reach a stable conversion of CH_4, resulting in a plasma energy of about 123.9 J. This plasma input was much lower than the thermal heat input required to initiate the conversion of CH_4. Based on the observation that $SrFeO_{3-\delta}$ was chemically inert at 293 K, the conversion of CH_4 at such low temperature should be mainly due to the plasma catalysis, rather than plasma heating effect. A comparison of conversion of CH_4 between thermal approach and the plasma-assisted one was carried out in [101], as presented in Fig. 7-9. Line 1 is the thermodynamic equilibrium conversion of methane as a function

of specific energy input. Line 2 represents experimental results achieved by thermal preheating without plasma discharge, where the growth of methane conversion and increase of temperature happen at the same time. Lines 4, 5, and others represent the isotherms in the range between 250 and 650°C. Curves 3, 6, and 7 mean preheating the temperatures to 550, 500, and 600°C, followed by plasma discharge (generated from microwave) at different powers. According to curves 3, 6, and 7, non-equilibrium plasma drives the conversion curves closer to thermodynamic equilibrium. A small amount of plasma energy input can lead to significant decrease in the thermal energy, suggesting the effect of plasma catalysis.

Figure 7-9 Plasma conversion of methane (from steam methane reforming, where the methane to steam ratio varies from 1:1 to 1:2): results of experiments and simulations presented as the methane conversion dependence on specific energy input: (1) thermodynamic calculations of the quasi-equilibrium states; (2) experiments with purely thermal energy input; (3, 6, 7) experiments with a discharge; (4, 5) theoretical lines representing isotherms (fixed temperature T). The figure was cited from [101]. For copyright issue, the figure is removed here.

The plasma effect on the gas phase, CH_4, has now been understood as plasma catalysis. The plasma effect on the solid bed, $SrFeO_{3-\delta}$, is also studied here. The comparison of the electrical and thermal energy input to activate $SrFeO_{3-\delta}$ for donating gaseous oxygen was

conducted. According to Fig. 7-7, at 673 K, it took about 0.8 min to reach an O_2(g) mole fraction of 0.0018 during plasma discharge. A similar release of gaseous oxygen (~ 0.0018) was found when the bed was increased to temperature 773 K without plasma discharge. The thermal energy input (585 J to heat the $SrFeO_{3-\delta}$ bed, and 1.67 W to heat the flowing gas, as shown in Table 7-3) to raise the whole DBD reactor from 673 to 773 K was compared with the plasma energy input with the DBD reactor at 673 K. Taking out the plasma power needed to heating the gas flow (1.67W), the actual plasma power supplied to the $SrFeO_{3-\delta}$ bed would be 13.33 W (= 15 W- 1.67 W), resulting a total energy of 640 J to reach the oxygen concentration of 0.0018 at 673 K. This was comparable to the thermal heat required to drive $SrFeO_{3-\delta}$ to release the same amount of oxygen. Therefore, the activation of $SrFeO_{3-\delta}$ might be more of a thermal effect caused by plasma. The results and discussion in the current study agree with the findings reported in literature [101] that for heterogeneous non-thermal plasma processes, the production of actives species in plasma was usually controlled by the temperature of the electrons; whilst the surface reactions are usually controlled by the surface temperature and limiting the total kinetics.

7.4.3 Investigation of longer plasma discharge period in the $SrFeO_{3-\delta}$-packed DBD reactor

It has been found that when $SrFeO_{3-\delta}$ became chemically reactive during plasma discharge, the production of CO_2 became significant. It seems that the produced H_2 can be oxidised by the activated $SrFeO_{3-\delta}$ so that [H_2] dropped. The over-expected activity of $SrFeO_{3-\delta}$ for the suppression of coking, is not an advantage here as it lowered the productivity of H_2, though the conversion of CH_4 improved. $SrFeO_{3-\delta}$ has non-stoichiometry of oxygen and goes through phase transitions in a reducing environment, from perovskite ($2.5 < 3-\delta < 3$) to brownmillerite structure ($3-\delta < 2.5$) [39]. It would be interesting to know if there is a state of $SrFeO_{3-\delta}$ that helps promote the oxidation of CH_4, whilst still maintain a high selectivity for H_2 as a product. Therefore, an experiment with a much longer plasma discharge period inside the DBD reactor at 773 K, as shown in Fig. 7-10, was carried out.

According to Fig. 7-10, plasma was introduced at t = 2.3 min, and the results in the first 2.5 min of the plasma discharge period appeared similar to those from Fig. 7-8e: [H_2] firstly increased to a peak value and then dropped, this was then followed by an increase in the CO_2 and CO. If the drop in the H_2 concentration as plasma was introduced, was believed due to its oxidation to H_2O by $SrFeO_{3-\delta}$, it seems the sequence for oxidation is H_2 > CO. After the first 2.5 min of plasma discharge, [CO] and [CO_2] gradually dropped to zero, whilst [H_2] dropped and seemed to finally stabilise at 0.002. A proposed reaction sequence which might have happened here is: at 773 K, before plasma discharge, a low amount of CH_4 was oxidised by the $SrFeO_{3-\delta}$, either directly with the solid $SrFeO_{3-\delta}$ or with gaseous oxygen released from $SrFeO_{3-\delta}$. As plasma was introduced, H_2 was generated, mainly through the cracking of CH_4. As the plasma acted on the $SrFeO_{3-\delta}$ bed, the bed became active and started to oxidise the H_2 produced to H_2O, and also CO and CO_2. In the meantime, $SrFeO_{3-\delta}$ also improved overall conversion of CH_4, mostly to CO and CO_2 (very likely *via* the route of direct combustion of CH_4 by $SrFeO_{3-\delta}$ to CO, CO_2 and H_2O). Later on, $SrFeO_{3-\delta}$ seemed less reactive, [CO] and [CO_2] was gradually dropped to zero, and some H_2 was observed. The conversion of CH_4 also dropped and gradually reached a stable value. The measured low level of H_2 after t = 15 min should be a combined effect of the cracking of CH_4 to H_2, and some oxidation of H_2 to H_2O by the less reactive $SrFeO_{3-\delta}$, where $SrFeO_{3-\delta}$ no longer react with CH_4. The hypothesis is supported by that the conversion of CH_4 when [H_2] became stabilised (from t = 15 to 27.5 min), 0.078, similar to the conversion of CH_4 at 293 K, 0.075 (refer to Table 7-1 and Fig.7-8a) where only cracking of CH_4 by plasma was believed to dominate in the DBD reactor.

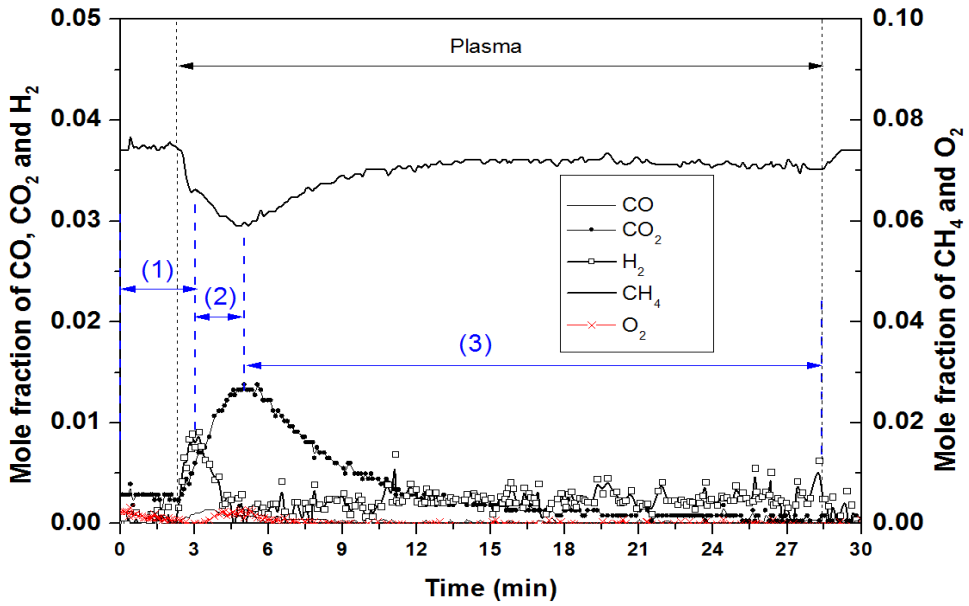

Figure 7-10 Mole fraction of gaseous from the $SrFeO_{3-\delta}$-packed DBD reactor at 773 K with a long period (*i.e.* 26 min) of plasma discharge.

Overall, in a 26 min's long plasma-assisted reduction period, $SrFeO_{3-\delta}$ did not help promote H_2 production in such systems, in different stages of the reduction process: (1) high [H_2] was detected when subjected to plasma discharge; (2) [H_2] quickly dropped, in the meantime, [CO_2] increased substantially and the conversion of CH_4 also improved; (3) [H_2] was maintained at a relatively constant level, whilst CO and CO_2 was no longer produced in a large amount and the conversion of CH_4 dropped. It was not clear what led to the change in the apparent activity of $SrFeO_{3-\delta}$, but the corresponding amounts of oxygen consumption from $SrFeO_{3-\delta}$ in each stage was estimated. Assuming that the cracking process of CH_4 by plasma catalysis was not affected by the change of $SrFeO_{3-\delta}$, and that the expected amounts of H_2 produced at 773 K was the same as those produced at 293 K, the lowered amount of H_2 in this case is believed due to oxidation from H_2 to H_2O by $SrFeO_{3-\delta}$. If the solid bed was converted uniformly over the plasma discharge period, and by calculating the amounts of oxygen in the products (*i.e.* CO, CO_2, O_2 and estimated H_2O) at stages (1), (2) and (3), the corresponding phase transformation or change in the non-stoichiometry in $SrFeO_{3-\delta}$ in each stage can be estimated. According to Fig.7-1, the prepared fresh $SrFeO_{3-\delta}$ was with an oxygen non-stoichiometry of 2.820. Stages (1), (2) and (3) correspond to a change in $SrFeO_{3-\delta}$ from $SrFeO_{2.820}$→ $SrFeO_{2.808}$→ $SrFeO_{2.755}$→ $SrFeO_{2.648}$. A recent study on the determination of 'δ - p_{O2} - T' diagrams for perovskite related oxides including $SrFeO_{3-\delta}$ carried out by Starkov *et al.* [39] showed that

the sequence of equilibrium phase transformation in a reducing environment for $SrFeO_{3-\delta}$ at 773 K was $SrFeO_{2.81} \rightarrow SrFeO_{2.66} \rightarrow SrFeO_{2.51}$, where $SrFeO_{2.81} \rightarrow SrFeO_{2.66}$ corresponded to the change in oxygen vacancy in the perovskite phase and $SrFeO_{2.66} \rightarrow SrFeO_{2.51}$ was the phase transition from perovskite to brownmillerite phase. Based on non-stoichiometry, it appears that here, $SrFeO_{3-\delta}$ was still in perovskite phase in stages (1) and (2). The reduced particles (after stages (1) amd (2)) were collected (with the bed quench in ~ 8.5% CH_4) and carefully observed. Some brown particles, indicating brownmillerite structure, were found randomly distributed. This implies inhomogeneous effect of plasma on the solid bed. In stage (3), some part of the bed (based on the non-stoichiometry) were in brownmillerate phase, whilst it still did not help H_2 production. In summary, the results suggest that $SrFeO_{3-\delta}$ might not be a good candidate for hydrogen production.

7.4.4 Investigation of O_2 release from $SrFeO_{3-\delta}$ in air regeneration stage

In the air regeneration stage at 713 and 773 K (Fig. 7-8d and 7-8e), gaseous oxygen from $SrFeO_{3-\delta}$ was released during plasma discharge, resulting in a higher $[O_2]$ than that in the air. Interestingly, after the plasma was stopped, a decrease in $[O_2]$ to lower than that in air was observed, indicating a transport of oxygen from the air to $SrFeO_{3-\delta}$. Extrapolating the results from Starkov *et al*. [39], at temperatures $\leq$ 773 K, $SrFeO_{3-\delta}$ with $(3-\delta) \geq 2.81$ would be the expected forms in thermodynamic equilibrium with air ($[O_2] = 0.21$). In the results shown here, for CH_4/Ar plasma treated $SrFeO_{3-\delta}$, where $(3-\delta)$ is usually below 2.81 (*e.g*. 2.76 at 773 K, as shown in Fig. 7-8), a significant release of gaseous oxygen from $SrFeO_{3-\delta}$ to air was not expected. The observed increase in gaseous oxygen in plasma discharge, together with the transporting of oxygen to the solid bed after plasma stopped, means that plasma has forced $SrFeO_{3-\delta}$ to release more gaseous oxygen than that from the bulk thermal equilibrium. This is very likely due to plasma local or surface heating on the solids. On the other hand, even with the improved oxygen-donating ability of $SrFeO_{3-\delta}$ in plasma, it did not result in the burn off any of the deposited carbon on the solids in the air regeneration stage. This implies that the deposited carbon formed in the reduction stage was hard to be removed by the presence of ($SrFeO_{3-\delta}$ + gaseous O_2 + plasma), the significant generation of CO_2 (and some CO) during reduction period should mainly come from the direct combustion of CH_4, rather than experiencing an intermediate step *via* solid carbon.

7.4.5 Comparison of the system for H_2 generation and other industrial means of H_2 generation

The results from the current study suggest a $SrFeO_{3-\delta}$-packed DBD reactor is not promising for H_2-rich gas production due to its over-reactivity. An estimation of the energy cost for this process was compared with some processes for H_2 production. There are many ways to categorise the energy cost. Two definitions of energy cost were used here for comparison with other processes reported, EC_a and EC_b.

$$EC_a = \frac{(\frac{W}{B_{CH_4} \cdot \eta} + n_{CH_4}) \cdot HHV_{CH_4}}{n_{H_2}}$$

$$EC_b = \frac{W}{n_{H_2}}$$

W is the applied plasma power, measured from the Lissajous figure; n_{H_2} is the amount of H_2 produced over time. B_{CH_4} is the chemical exergy of CH_4, which is ~ 52 MJ/kg [216]. η is the efficiency from thermal to electricity energy and a value of 60% is assumed here. n_{CH_4} is the converted amount of CH_4. HHV_{CH_4} is the high heating value of CH_4, 55.5 MJ/kg. EC_b only takes into account the energy from the applied plasma for the production of H_2, whereas EC_a converts the plasma energy back to the thermal energy equivalent to that from the combustion of CH_4, and also considers the chemical energy of converted CH_4. The definition of EC_a here tries to normalise the energy cost from different approaches based on the energy in CH_4, allowing easy comparison between various H_2 production techniques. It should be noted that for both EC_a and EC_b, the energy of maintaining the reactor at the operating temperature has not been taken into account. For industrial H_2 production techniques such as steam reforming of CH_4, electricity input only accounts for a small amount of total energy input. In this study, the adoption of plasma generates heat inside the reactor, and this might account for the energy required to maintain the operating temperature; however, for simplicity, this reactor heating energy is not included in the estimation of the energy cost here.

Table 7-4 presents EC_a and EC_b of this study, with the temperature from 293 to 773 K. EC_a is first compared with other conventional H_2 production processes such as steam reforming of CH_4 and water electrolysis. According to Table 7-4, EC_a varies from 2680 to 4070 MJ/kg, depending on the temperature. For conventional steam reforming of CH_4, the energy cost (EC_a) is reported to be less than 160 MJ/kg [104], significantly lower

than the values obtained here. However, steam reforming, which requires multiple stages to achieve high H_2 yield, is more suited for large-scale H_2 production. For small scales or point-of-use, water electrolysis (water splitting) is one of the popular approaches, with its energy cost for was reported to be from 320 to 510 MJ/kg [217] (estimated based on the original data of electricity consumption 50 kWh/kg to 79 kWh/kg). Still, the energy cost from the current study is too high. However, these are only preliminary results without optimization of the process and reactor set-up. The increase in the scale can usually lead to a decrease in the production cost. On the other hand, the biggest issue revealed from the preliminary results is that $SrFeO_{3-\delta}$ did not to show apparent advantage in improving the hydrogen production from such process. The lowest hydrogen production cost was found at 293 K, where $SrFeO_{3-\delta}$ was considered to be chemically inert. $SrFeO_{3-\delta}$ seems to be too reactive here. The positive side is that the presence of local oxygen source did help decrease the coking. Therefore, suitable oxygen carriers that are reactive enough to suppress coking but not too reactive to combust hydrogen are needed.

Table 7-4 Energy cost EC_b from 293 to 773 K.

Temperature (K)	EC_a （MJ/kg)	EC_b （MJ/kg)
293	2680 ± 80	1400 ± 40
673	4070 ± 70	2080 ± 60
713	4040 ± 110	1940 ± 60
773	3680 ± 90	2300 ± 70

Improving the energy cost by varying other parameters is also possible. Nozaki *et al.* [218] carried out extensive experimental work in a non-thermal plasma-assisted system and the results are summarised in Table 7-5. The energy cost, EC_b, as shown in Table 7-4, can be compared with those obtained by Nozaki *et al.* Here EC_b is between 2680 to 4070 MJ/kg; compared with 136 to 8080 MJ/kg. According to Table 7-5, the use of Ni/SiO_2 and increase in temperature substantially improved hydrogen production by reducing the energy cost from 8080 to 1004 MJ/kg at 673 K when the DBD reactor was loaded with Ni/SiO_2, and from 1330 to 136 MJ/kg when increasing the bed temperature from 673 to 873 K. In addition, the increase in operating frequency also contributed to the reduction of energy cost. From this perspective, though the current energy cost is

significantly higher than the conventional H_2 production techniques, especially for steam reforming of CH_4, there are opportunities for improvement, particularly by employing some catalyst such as Ni.

Table 7-5 Comparison of the energy cost. Data from [218].

Reactor type	Operating temperature (K)	Operating frequency (kHz)	EC_b(MJ/kg H_2)
DBD	473	10	5974
DBD	673	76	8080
DBD + Ni/SiO_2	673	10	1330
DBD + Ni/SiO_2	673	76	1004
DBD + Ni/SiO_2	873	10	136

7.4.6 Investigation of Ni on $SrFeO_{3-\delta}$ for hydrogen production

As shown in 7.4.5, the presence of Ni could significantly improve the production of H_2, and thus decrease the energy cost. Ni was found to be an efficient catalyst for H_2 production. However, the use of Ni usually results in severe coking. For a DBD system therefore, an optimum material is likely to be a catalyst such as Ni, coupled with an oxygen carrier such as $SrFeO_{3-\delta}$ to prevent coking. The concept is tested here. Ni was doped onto the previously prepared $SrFeO_{3-\delta}$ by dry-impregation from nickel nitrate hexahydrate. The resulting particles, with a particle size fraction of 600 – 850 μm, had a molar ratio of Ni to total metals (*i.e.* Ni + Sr + Fe) of 1: 10. The detailed preparation protocol was presented in 2.2.2. The fresh Ni-doped $SrFeO_{3-\delta}$ sample was XRD performed to identify the phases formed, and the spectra is shown in Fig. 7-11. As seen in Fig. 7-11, in the fresh sample, the peaks were assigned to NiO and $SrFeO_{3-\delta}$ (the XRD patterns of the recovered samples are discussed below in appropriate section).

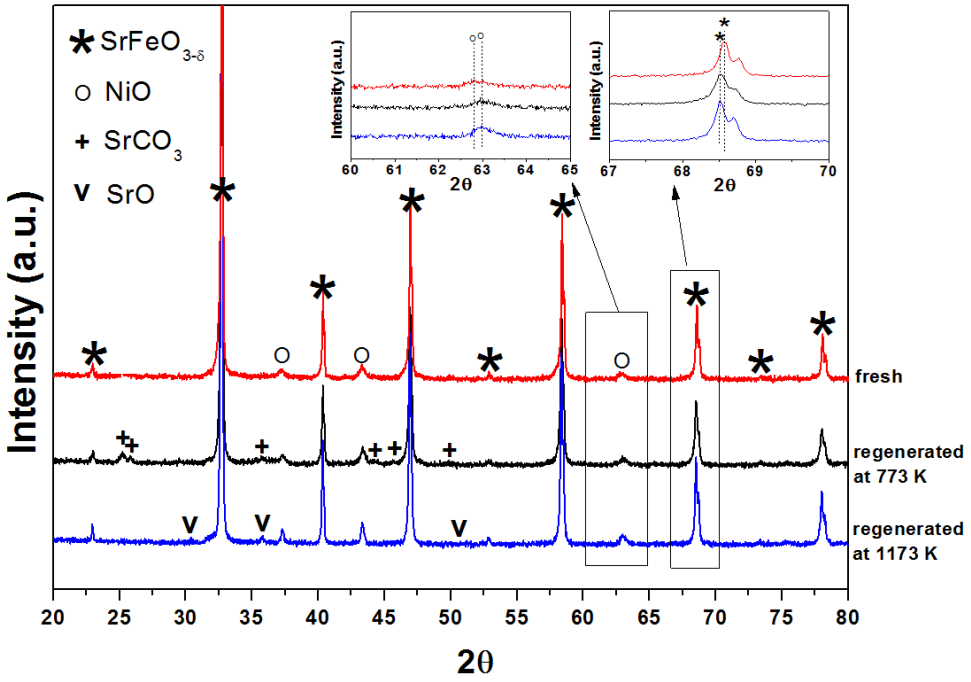

Figure 7-11 XRD spectra of fresh NiO/$SrFeO_{3-\delta}$, NiO/$SrFeO_{3-\delta}$ regenerated at 773 K and NiO/$SrFeO_{3-\delta}$ regenerated at 1273 K.

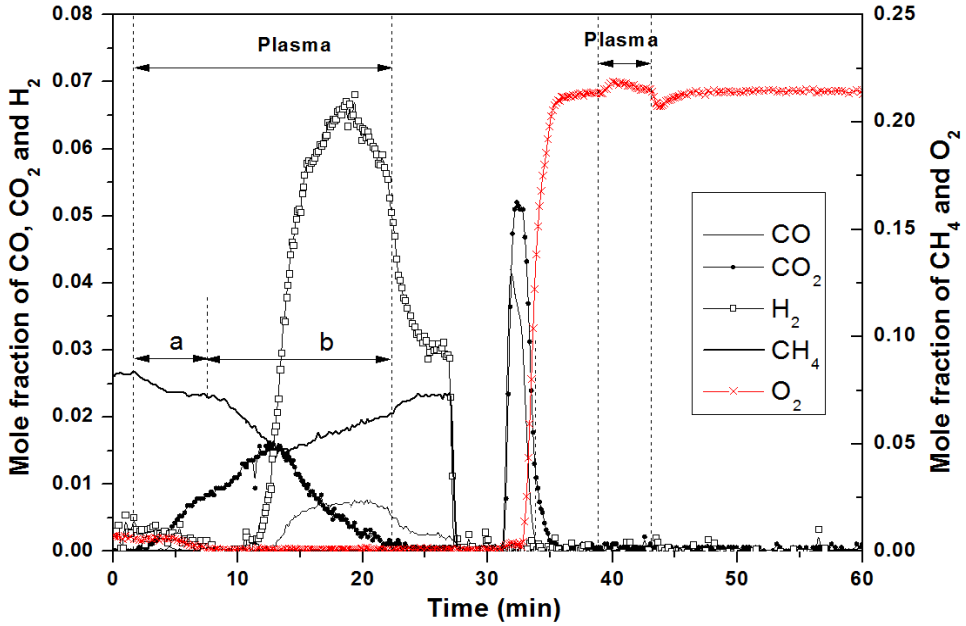

Figure 7-12 Plasma-assisted cracking/partial oxidation of CH_4 at 773 K in fresh NiO/$SrFeO_{3-\delta}$.

The result of converting CH_4 in the fresh NiO/$SrFeO_{3-\delta}$-packed DBD reactor is shown in Fig. 7-12. In the bed of fresh NiO/$SrFeO_{3-\delta}$, similar to the bed of $SrFeO_{3-\delta}$, gaseous O_2 was detected before introducing plasma; however, CO_2 was not observed here. From t = 2.0

to t = 22.4 min, the packed bed was subjected to plasma, where periods **a** and **b** correspond to plasma power of 13.1 W and 16.2 W, respectively. A decrease in [CH_4], and an increase in [CO_2] were clearly seen as soon as the plasma was applied, suggesting that CH_4 was largely converted to CO_2 as a result of plasma discharge. The [H_2] and [O_2] also dropped from t = 2 to t = 8 min, indicating the consumption of gaseous oxygen (released from $SrFeO_{3-\delta}$) and H_2 during this period. An increase in the plasma power from 13.1 to 16.2 W from t = 8 min led to subsequent increase in CH_4 conversion and CO_2 production. No H_2 was detected from t = 8 min to t =11 min. However, from t = 11 min, [H_2] started to sharply increase; in the meantime, production of CO was observed; whilst [CO_2] dropped and the conversion of CH_4 started to decrease. Both the concentrations of H_2 and CO reached a maximum first, followed by their gradual drop. After the plasma was stopped at t = 22.5 min, the bed still showed a relatively high activity for H_2 production. What happens in the NiO/$SrFeO_{3-\delta}$ in the initial period seems very similar to that in the $SrFeO_{3-\delta}$ bed: the solid oxygen carrier seems to be too reactive to maintain the H_2 produced from CH_4 cracking, the H_2 was oxidised probably to H_2O. However, when the reduction of the oxygen carrier reached a certain stage, the bed seemed to be less oxidising and exhibited very high selectivity for H_2 and CO, though CH_4 was converted less due to lower reactive of the bed. That fact that both high [H_2] and [CO] were observed in the second half of the reduction stage suggests that during this period, the system seems to be in the state where the overall process was very likely controlled by thermodynamics of $SrFeO_{3-\delta}$. The mechanism giving the much-increased production of H_2 is unclear, whether it is NiO or the reduced metal phase, Ni, or some other phase responsible for H_2 production is uncertain here.

According to Fig. 7-12, NiO/$SrFeO_{3-\delta}$, denoted as NSFO1 in the following text, showed great potential (when sufficiently reduced) for H_2-rich gas production in a plasma-assisted system. To test its cyclability, the material was regenerated in air plasma at 773 K, as shown from t = 31 min in Fig. 7-12. During regeneration, substantial amounts of CO_2 and CO were observed as soon as the bed was switched from Ar to air, indicating a large amount of solid carbon deposited in the bed; this carbon was easily removed. Plasma was later applied to assist carbon removal, though no clear carbon-containing species were detected. The regenerated sample was denoted as NSFO2 and tested in the second reduction. Figure 7-13 shows the results of converting CH_4 in the NSFO2 with a plasma

power of 16.3 W. It was found that H_2 production was insignificant over the 17 min's plasma-assisted reduction period. There was no period of the reduction that favored the generation of H_2 and CO over CO_2 (and H_2O). To understand what might have happened here, NSFO2 was XRD scanned and its spectra was presented in Fig. 7-11. In addition to NiO and the perovskite structure ($SrFeO_{2.820}$), $SrCO_3$ was detected.

The perovskite structure peaks, $SrFeO_{3-\delta}$, in NSFO2 shifted towards lower angle (*e.g.* the peaks between 65° and 80° shifted towards left by ~ 0.1°). On the other hand, the NiO peaks in NSFO2 shifted towards higher angle by 0.1°. In combination with the fact that $SrCO_3$ phase was also detected, it suggests some Sr segregated from the perovskite structure, indicating the segregation of Fe from $SrFeO_{3-\delta}$. The segregated Fe might have diffused into the NiO crystal structure, leading to a shift of NiO (probably resulting in <Ni, Fe,O>, compounds containing Ni, Fe, and O, where the main crystal structure is still governed by NiO). The deactivation of NSFO2 might be very likely due to this segregation. To further investigate this, NSFO2 was calcined at 1273 K for 6 h, which was intended to regenerate perovskite from the segregated $SrCO_3$ and possibly segregated Fe. The re-calcined particles, denoted as NSFO3, was also tested for H_2 production at 773 K from CH_4. However, similar results to those of NSFO2 were obtained. The XRD spectra of NSFO3 was also presented in Fig. 7-11. In NSFO3, apart from the shifted perovskite phase and shifted NiO phase, peaks of SrO were observed, whereas the $SrCO_3$ disappeared. This implies that the segregation of Sr and probably Fe from $NiO/SrFeO_{3-\delta}$ cannot be easily recovered.

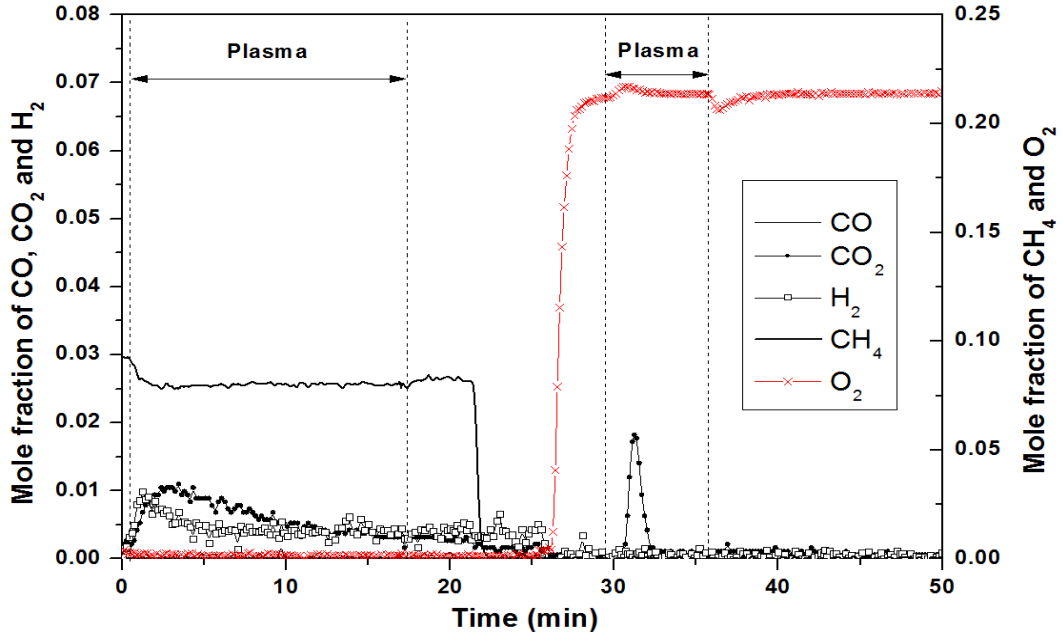

Figure 7-13 Plasma-assisted cracking/partial oxidation of CH_4 at 773 K in the bed of regenerated NiO/$SrFeO_{3-\delta}$ (NSFO2).

7.5 Conclusions

Preliminary study of H_2 production from a $SrFeO_{3-\delta}$-packed DBD reactor at temperatures from 293 to 773 K was carried out in this chapter, and the main results are:

(a) The intensity of plasma-generated excited species in pure Ar was significantly higher than that in the mixed gas of CH_4 and Ar.

(b) To achieve similar level of CH_4 conversion (without the chemical interaction with the solid beds), the plasma and thermal energy input were compared. It was found that plamsa input (*i.e.* 123.9 J) was significantly lower than that of thermal input (*i.e.* 2346 J), suggesting plasma catalysis effect for the cracking of CH_4. For the effect of plasma on $SrFeO_{3-\delta}$, the plasma energy input (*i.e.* 640 J) was comparable to thermal input (*i.e.* 585 J), indicating a heating effect by plasma on the solids.

(c) $SrFeO_{3-\delta}$ was found to have very low yield of H_2 (< 0.12 mole for every mole of CH_4 introduced into the system) at all temperatures studied. The yield of H_2 decreased with an increase in temperature (*i.e.* from 0.115 at 293 K to 0.032 at 773 K) due to its high oxidising property. Therefore, it is not a good candidate for H_2 production in such system.

(d) $NiO/SrFeO_{3-\delta}$ was found effective for H_2 production, whilst the bed lost activity after being regenerated.

8 H_2 production from partial oxidation of CH_4 by Fe_2O_3-supported Ni-based catalysts in a plasma-assisted packed bed reactor

8.1 Introduction

$SrFeO_{3-\delta}$ and $NiO/SrFeO_{3-\delta}$ proved over-oxidising for hydrogen production, when used in the DBD reactor for chemical looping H_2 production. In the current chapter, a conventional and less oxidative oxygen carrier, Fe_2O_3, is studied as the support, and NiO was doped onto Fe_2O_3 to hopefully promote the production of H_2, with the DBD reactor operated at 673 K.

8.2 Experimental methods and data analysis

8.2.1 Experiments

Two Fe_2O_3-supported catalysts were prepared: NiO/Fe_2O_3 and $NiFe_2O_4/Fe_2O_3$, where $NiFe_2O_4$ is the stable equilibrium phase to be formed in a Ni-Fe-O system under the experimental conditions. Pure Fe_2O_3 was also studied for comparison. Fe_2O_3 particles were prepared from iron oxide powders, followed by calcination. The Ni-based Fe_2O_3-supported materials were then prepared by dry-impregnating with Nickel nitrate hexahydrate onto the Fe_2O_3. NiO/Fe_2O_3 was first obtained by calcination at 823 K for 5 h, and to obtain $NiFe_2O_4/Fe_2O_3$, further calcination of NiO/Fe_2O_3 in air at 1123 K was required. As a control, materials were also prepared with Al_2O_3 instead of Fe_2O_3, giving Ni/Al_2O_3 and NiO/Al_2O_3. The detailed preparation procedures for the materials were described in 2.2.2. The experiments were carried out in the same set-up as that in Chapters 6 and 7, which was illustrated in 2.3.4. The gas stream entered the DBD reactor from the bottom at a flow rate of 0.75 L/min. The product gas was sampled at 0.5 L/min. For a typical experiment, the reactor was heated to 673 K in flowing air, followed by Ar to purge the system before the start of the experiment. During an experiment, a stream of CH_4 was mixed with Ar to give 8.5% $\pm$ 0.5% CH_4. After the mixed gas flow stabilised, the plasma was applied. For each experiment, the plasma discharge period was about 5.6 $\pm$ 0.5 min. After CH_4/Ar plasma discharge, the gas was switched to air to burn off any deposited carbon as well as re-oxidise the bed materials. Plasma discharge was later introduced to assist the process of de-coking and re-oxidation. The reduction-oxidation cycle was

repeated 2 more times. Ac power (primary) supplied to the DBD reactor was with a voltage of 10.5 ± 1.0 kV and frequency 26.0 ± 3.0 kHz. The dissipated plasma power (determined by Q-V Lissajous plot) was controlled at 7.2 ± 0.7 W.

8.2.2 Data analysis

Similar to the results shown in Chapter 7 that the main gaseous products observed were H_2, CO, CO_2, and traces of C_2H_2, and C_2H_4 (< 150 ppm). The study mainly focuses on parameters including averaged conversion of CH_4, selectivity and yield for different products, and material balances, where the equations for obtaining the values were presented in 7.3.4. Due to the low amounts of C_2H_2 and C_2H_4, the selectivity for the two were out of the interest here.

8.3 Results

8.3.1 The results of Al_2O_3 and Fe_2O_3

The results of plasma-assisted cracking or/and partial oxidation of CH_4 in undoped Al_2O_3 and Fe_2O_3 beds are presented in Fig. 8-1. For both materials, CH_4 conversion was only observed when plasma discharge was applied. H_2 was found to be the main product and its generation over the discharge period in 8.5% ± 0.5% CH_4 was relatively uniform. CO and CO_2 were observed only at trace levels (< 250 ppm). This suggests that H_2 was primarily generated from CH_4 cracking by the plasma, and the carbon from the converted CH_4 became the solid phase. This agrees with the fact that the ratio of generated H_2 to converted CH_4 was 1.7 ± 0.1 (based on three cycles) for both materials. Taking into account the C_2H_2 and C_2H_4 generated during discharge period (at ppm levels), over 80% hydrogen balance was obtained for both materials (refer to Table 8-1). The conversion of CH_4, as well as the generation of H_2, in the Al_2O_3 and Fe_2O_3 beds were similar, suggesting that neither material is a good catalyst for CH_4 cracking. In the air regeneration (and plasma discharge) period, trace levels (< 100 ppm) of CO and CO_2 were observed, suggesting the presence of deposited carbon from the cracking process in the bed. However, the deposited carbon could not be removed completely at such low temperatures even with the assistance of plasma discharge. Further regeneration of the bed was carried out by raising the temperature of the reactor to 823 K for over 30 min until no CO and CO_2 were detected.

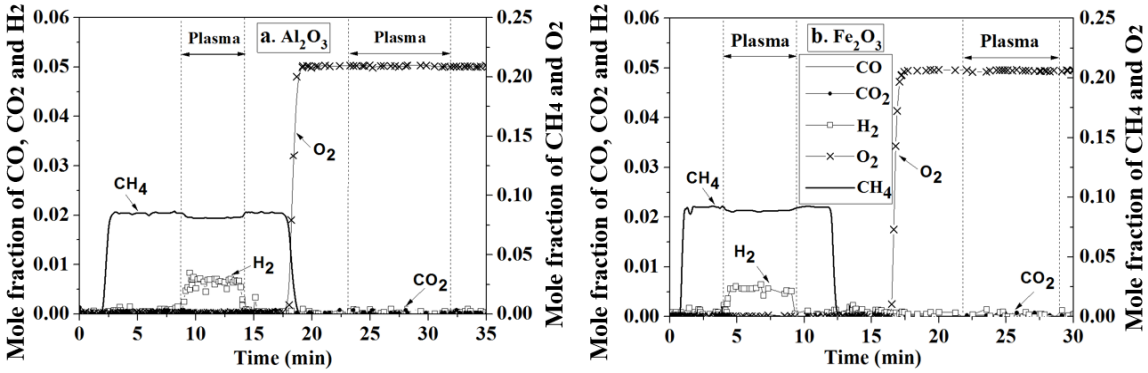

Figure 8-1 Plasma-assisted cracking/partial oxidation of CH_4 at 673 K with DBD reactor packed with (a). Al_2O_3, and (b). Fe_2O_3.

8.3.2 The results of NiO/Al_2O_3, Ni/Al_2O_3, NiO/Fe_2O_3 and $NiFe_2O_4/Fe_2O_3$

The results for Ni-doped Al_2O_3 and Fe_2O_3-supported materials are presented in Fig. 8-2. CH_4 conversion in the NiO/Al_2O_3 bed, as shown in Fig. 8-2a, is similar to those in the Al_2O_3 and Fe_2O_3 beds, suggesting that this material also has little effect on CH_4 reforming or partial oxidation. For Ni/Al_2O_3 as seen in Fig. 8-2b, a significant rise in [H_2] was observed when CH_4 was introduced into the reactor, without plasma. This was mainly due to the catalytic effect of Ni, as reported in Ref. [219]. However, the catalytic effect did not last long and the H_2 level dropped and gradually reached a mole fraction of 0.01, whilst in the meantime, no significant production of CO and CO_2 was observed. This suggests that the presence of Ni mainly improved the cracking of CH_4 to H_2 and solid carbon, and the deactivation of Ni was likely due to the formed carbon. In addition, the formation of some nickel aluminate, which can be confirmed by post-reaction XRD results shown in Fig. 8-3, could also contribute to this deactivation. When plasma discharge was applied from t = 9.5 to t = 15.6 min, higher degrees of CH_4 conversion and H_2 production were achieved. At t = 22.0 min, CH_4 was stopped, leaving the bed purging in Ar. Then, as soon as the gas was switched from Ar to air, a significant CO_2 peak together with a small CO peak was observed and an overall carbon balance of 94% was obtained.

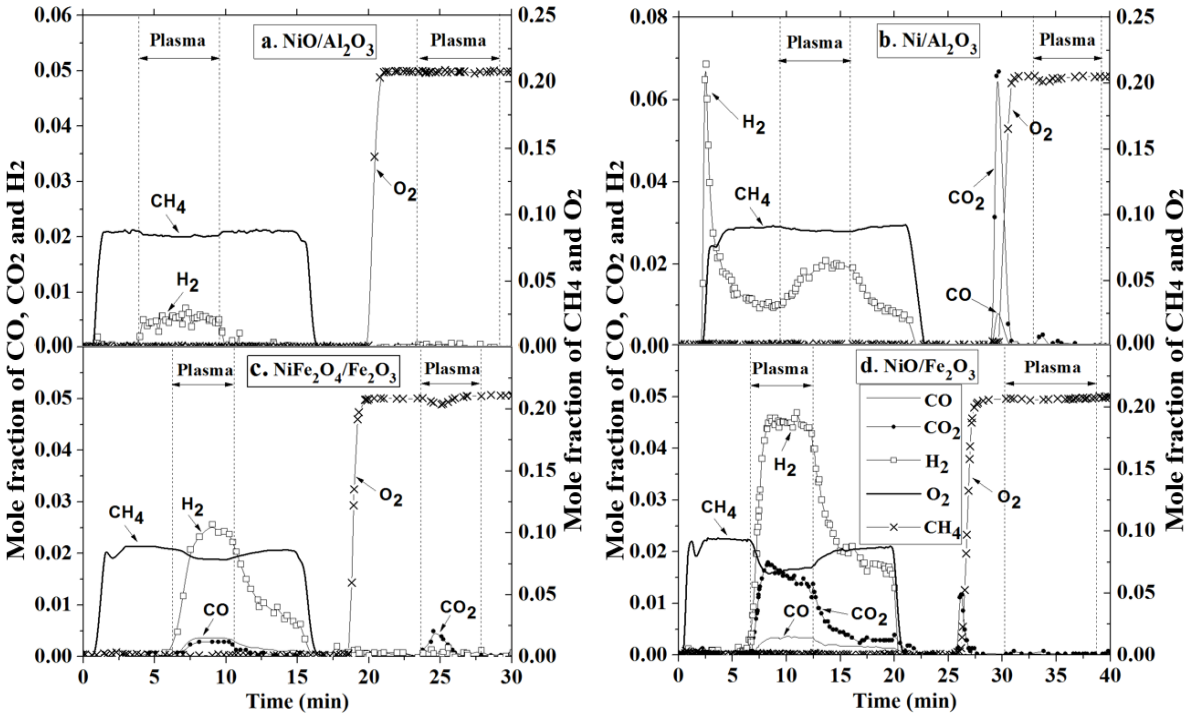

Figure 8-2 Plasma-assisted cracking/partial oxidation of CH_4 at 673 K with DBD reactor packed with (a) NiO/Al_2O_3; (b) Ni/Al_2O_3; (c) $NiFe_2O_4/Fe_2O_3$; (d) NiO/Fe_2O_3.

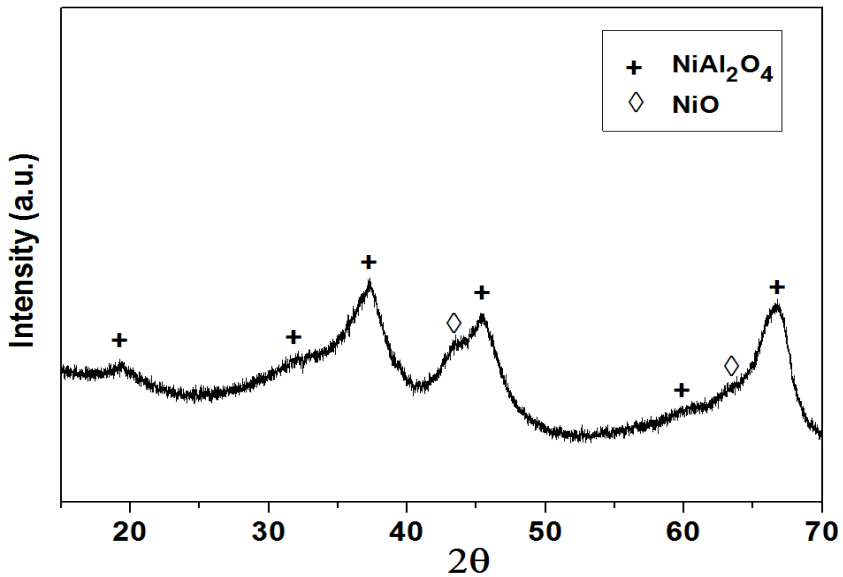

Figure 8-3 XRD spectra of CH_4/Ar plasma treated NiO/γ-Al_2O_3. Material was only reduced in 8.5% CH_4 plasma, and not regenerated with air (and plasma). The collection codes of the reference patterns from ICSD were presented in Table 8-2.

When the reactor was loaded with $NiFe_2O_4/Fe_2O_3$, according to Fig. 8-2c, no significant conversion of CH_4 was seen without plasma discharge. At t = 6.8 min, when plasma was

introduced, much improved generation of H_2 over the whole discharge period was observed; at the same time, there was a clear production of CO and CO_2, indicating that the reduction of the bed material, $NiFe_2O_4/Fe_2O_3$, occurred as it was the only source of oxygen in the system. The overall result was a partial oxidation of CH_4 by plasma discharge to H_2-rich gas that contains some CO and CO_2. When plasma discharge was stopped, H_2 was still produced from the $NiFe_2O_4/Fe_2O_3$ bed, though at lower levels. The fact that $NiFe_2O_4$ was not reactive for H_2 production before plasma discharge but was after, suggests the generation of some additional phase other than $NiFe_2O_4$ during plasma discharge, with this (probably reduced) phase having a catalytic effect even without plasma. In the air regeneration stage, CO_2 was only observed when plasma was applied. In the NiO/Fe_2O_3 bed, according to Fig. 8-2d, no conversion of CH_4 was observed until the plasma was applied, at which point a significant amount of H_2 was generated. The CO and CO_2 productions were also much higher than those from other beds during plasma discharge. CH_4 conversion reached 32% in this case. Similar to the case in the $NiFe_2O_4/Fe_2O_3$ bed, when plasma was switched off, there was still post-plasma H_2 production. Most of the deposited carbon was recovered in air, without the presence of plasma.

Table 8-1 Summarised results in different bed materials (errors show the range of three repeats)

Parameters	Al_2O_3	NiO/Al_2O_3	Ni/Al_2O_3	Fe_2O_3	NiO/Fe_2O_3	$NiFe_2O_4/Fe_2O_3$
d_c	0.75 ± 0.04	0.75 ± 0.03	0.90 ± 0.07	0.71 ± 0.05	0.15 ± 0.03	0.47± 0.08
C balance	0.26 ± 0.02	0.25 ± 0.02	0.94 ± 0.02	0.38 ± 0.02	0.94 ± 0.03	0.63 ± 0.04
H balance	0.93 ± 0.04	0.94 ± 0.03	0.96 ± 0.04	0.82 ± 0.02	0.82 ± 0.03	0.99 ± 0.06
X_{CH_4}	0.05 ± 0.01	0.05 ± 0.01	0.10 ± 0.02	0.04 ± 0.01	0.39 ± 0.07	0.19 ± 0.04
S_{co}	0.01 ± 0.01	0.01 ± 0.01	0.03 ± 0.01	0.01 ± 0.01	0.12 ± 0.01	0.25 ± 0.01
S_{co_2}	0.03 ± 0.01	0.06 ± 0.01	0.02 ± 0.01	0.08 ± 0.01	0.71 ± 0.02	0.27 ± 0.02
S_{H_2}	0.84 ± 0.01	0.85 ± 0.01	0.95 ± 0.01	0.74 ± 0.01	0.92 ± 0.01	0.98 ± 0.07
$Y_{co}\times10^3$	0. 3 ± 0. 1	0.3 ± 0.1	0.3 ± 0.1	0.2 ± 0.1	45.2 ± 4.9	38.4 ± 5.2
$Y_{co_2}\times10^3$	1.2 ± 0.3	2.7 ± 0.5	2.2 ± 0.6	3.2 ± 0.7	285.5 ± 15.1	45.4 ± 3.1
$Y_{H_2}\times10^3$	64.7 ± 1.4	81.3 ± 1.2	180.6 ± 11.2	58.9 ± 1.1	621.7 ± 32.3	319.0 ± 40.2

Table 8-1 presents the summarised results of degree of carbon deposition d_c (defined as in 7.3.4), conversion of CH_4, selectivity and yield for products, carbon and hydrogen balances. It should be noted that the results here show three redox looping

cycles of each material, starting from the fresh samples. No mechanical deterioration was observed for any of the tested materials in the repeated cycles. Overall, NiO/Fe_2O_3 seems to be the most promising material for H_2 production due to its low degree of carbon deposition, high carbon and hydrogen balances, and high selectivity and yield for H_2. The hydrogen balance in the case of NiO/Fe_2O_3 was slightly lower than those in other Ni-doped materials. This suggests that some H-containing products other than H_2 might have been generated, probably H_2O. $NiFe_2O_4/Fe_2O_3$ also exhibited very high selectivity towards the production of H_2, although its resistance to coking, carbon balance and the conversion of CH_4 were not as good as those of NiO/Fe_2O_3.

8.3.3 XRD characterization of NiO/Fe_2O_3 and $NiFe_2O_4/Fe_2O_3$

Based on 8.3.1 and 8.3.2, NiO/Fe_2O_3 and $NiFe_2O_4/Fe_2O_3$ show promising properties for hydrogen production. The evaluation of any possible change in the material structure after the plasma-assisted CH_4 conversion was carried out. The samples of NiO/Fe_2O_3 and $NiFe_2O_4/Fe_2O_3$ in different stages were collected for XRD scanning. The phases in the samples were identified using the reference patterns from ICSD database, as shown in Table 8-2.

Table 8-2 Collection Code of the XRD reference patterns used from ICSD database.

Component	Fe_2O_3	Fe_3O_4	NiO	Ni	$NiFe_2O_4$	(Ni, Fe)	$NiAl_2O_4$
Collection Code from ICSD	15840	30860	9866	260169	40040	56386	9556

- **NiO/Fe_2O_3**

Figure 8-4 shows the XRD patterns of NiO/Fe_2O_3 samples: freshly prepared, with CH_4/Ar plasma treatment and after regeneration in air plasma. Major peaks of each phase and an unknown peak (2θ = 26.7) are marked accordingly. For the freshly calcined NiO/Fe_2O_3, only patterns of NiO and Fe_2O_3 were detected. This suggests no chemical interaction between NiO and Fe_2O_3 during the initial preparation of NiO/Fe_2O_3. After CH_4/Ar plasma treatment, NiO was no longer detected; instead, other peaks, which were assigned with the patterns of metallic Ni and magnetite, Fe_3O_4, were detected. For the air regenerated NiO/Fe_2O_3, similar to the fresh sample, NiO and Fe_2O_3 were the only phases detected, suggesting that the NiO phase can remain separate during plasma discharge in air.

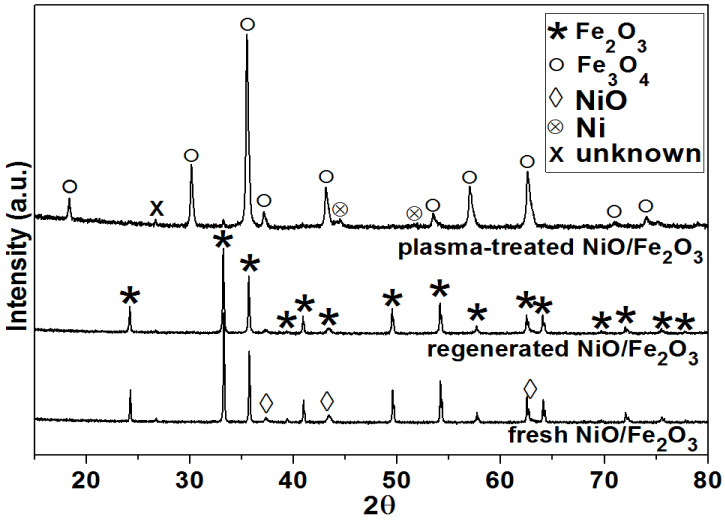

Figure 8-4 XRD spectra of fresh NiO/Fe_2O_3, CH_4/Ar plasma treated NiO/Fe_2O_3 and air plasma regenerated NiO/Fe_2O_3.

- **$NiFe_2O_4/Fe_2O_3$**

XRD results of $NiFe_2O_4/Fe_2O_3$ samples are presented in Fig. 8-5. Fe_2O_3 and $NiFe_2O_4$ phases were observed in the fresh sample. The formation of $NiFe_2O_4$ indicates the diffusion of NiO into the Fe_2O_3 crystal structure during calcination. In the XRD pattern of the CH_4/Ar plasma treated $NiFe_2O_4/Fe_2O_3$, there was a decrease in the intensity of the peaks for the $NiFe_2O_4$ phase; additionally, peaks assigned with metallic alloy of Ni-Fe, expresses as (Ni, Fe), were observed. There was no clear evidence of the presence of Fe_3O_4, suggesting that the oxygen in the produced CO and CO_2 in the CH_4/Ar discharge period probably came from the reduction of $NiFe_2O_4$ to the metallic (Ni, Fe). In the air regeneration stage, the (Ni, Fe) phase disappeared, but the intensity of $NiFe_2O_4$ peaks did not return to the higher level as seen in the fresh $NiFe_2O_4/Fe_2O_3$ sample.

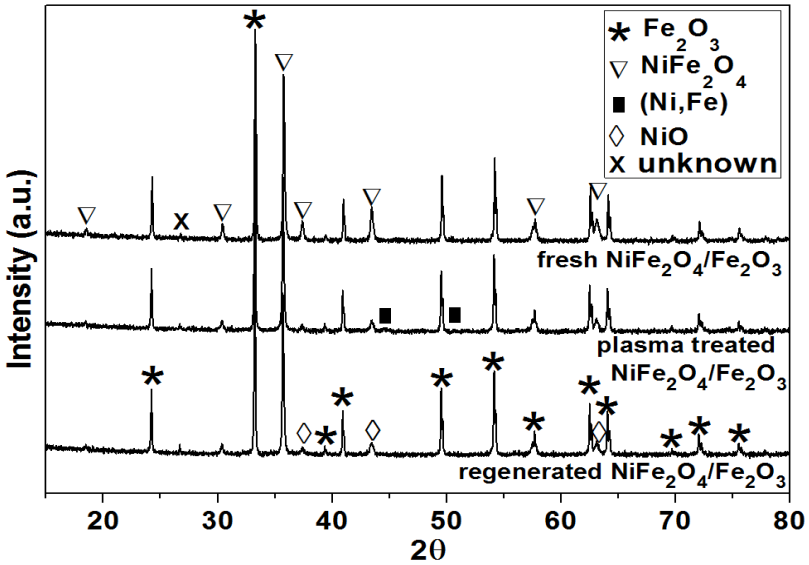

Figure 8-5 XRD spectra of fresh $NiFe_2O_4/Fe_2O_3$, CH_4/Ar plasma treated $NiFe_2O_4/Fe_2O_3$ and air plasma regenerated $NiFe_2O_4/Fe_2O_3$.

1

2

8.4 Discussion

8.4.1 Catalytic effect

As shown in Figs. 8-1 and 8-2, NiO (when supported on inert Al_2O_3) and Fe_2O_3 alone did not show good catalytic activity for the conversion of CH_4, even in the presence of the plasma discharge. However, the combination of NiO and Fe_2O_3, which resulted in NiO/Fe_2O_3 or $NiFe_2O_4/Fe_2O_3$, demonstrated significantly improved performance in the plasma, especially for NiO/Fe_2O_3. The catalytic mechanism is attempted to understand as follow.

- **NiO/Fe_2O_3**

The results in Fig. 8-4 show the formation of Ni when NiO/Fe_2O_3 was subjected to CH_4/Ar plasma discharge. Unlike Ni/Al_2O_3 experiment (in Fig. 8-2b), with which the production of H_2 was high at the very beginning of the plasma discharge but decreased quickly, the bed of NiO/Fe_2O_3 was able to produce significant amounts of H_2 over the entire plasma discharge period. The superior performance of NiO/Fe_2O_3 might result from lattice oxygen source in NiO/Fe_2O_3, which seems to suppress the coking of the solid bed, so that the catalytic activity of Ni can be maintained. This is supported by the smaller amount of carbon deposited in the NiO/Fe_2O_3 bed. Owing to the presence of Fe_3O_4, it was difficult to determine if NiO was still present in the plasma treated reduced NiO/Fe_2O_3 sample from the XRD (NiO peaks overlap with those from Fe_3O_4). However, calculation of the oxygen balances would give some indication of the presence of NiO phase. It was found that the amount of oxygen in the produced CO, CO_2 and H_2O (estimated from the hydrogen balance) during CH_4/Ar plasma discharge period accounted for 3.2 wt.% $\pm$ 0.2 wt.% of the total mass of NiO/Fe_2O_3. The NiO oxygen capacity (NiO $\rightarrow$ Ni) in the fresh material was 2.0 wt%, whilst the amount of oxygen from $Fe_2O_3 \rightarrow Fe_3O_4$ was 3.0 wt%. As most of the hematite was reduced (only low intensity of Fe_2O_3 peaks were detected), it is possible that some NiO might be still in the sample after being treated with CH_4/Ar plasma discharge.

Interestingly, the $NiFe_2O_4$ phase was not observed in the XRD patterns of the NiO/Fe_2O_3 (refer to Fig. 8-4), suggesting little interaction between NiO and Fe_2O_3, either during calcination or plasma treatment. The fact that NiO alone is inactive during plasma discharge, suggests the presence of some available oxygen in the NiO/Fe_2O_3 to suppress

coking. One of the two hypothesis might describe these conditions: 1) NiO itself is responsible for the partial oxidation of CH_4 *via* $NiO + CH_4 \rightarrow CO + CO_2 + H_2 + Ni$, and Fe_2O_3 helps the process to continue by transporting oxygen to the Ni sites; 2) metallic Ni is responsible for the catalytic effect of the generation of H_2 *via* $CH_4 \xrightarrow{Ni} C + H_2$, and the presence of Fe_2O_3 helps to remove the solid carbon from the Ni sites. The carbon formed in 2) is not necessarily solid carbon, it can also be some transient carbon that has not deposited. An illustration of the two hypothesis is shown in Fig. 8-6. In hypothesis 2, Ni is believed to be generated as soon as the system is subjected to plasma discharge, and triple-phase intimate contact (CH_4, Ni, and the incoming oxygen to Ni site) in crucial.

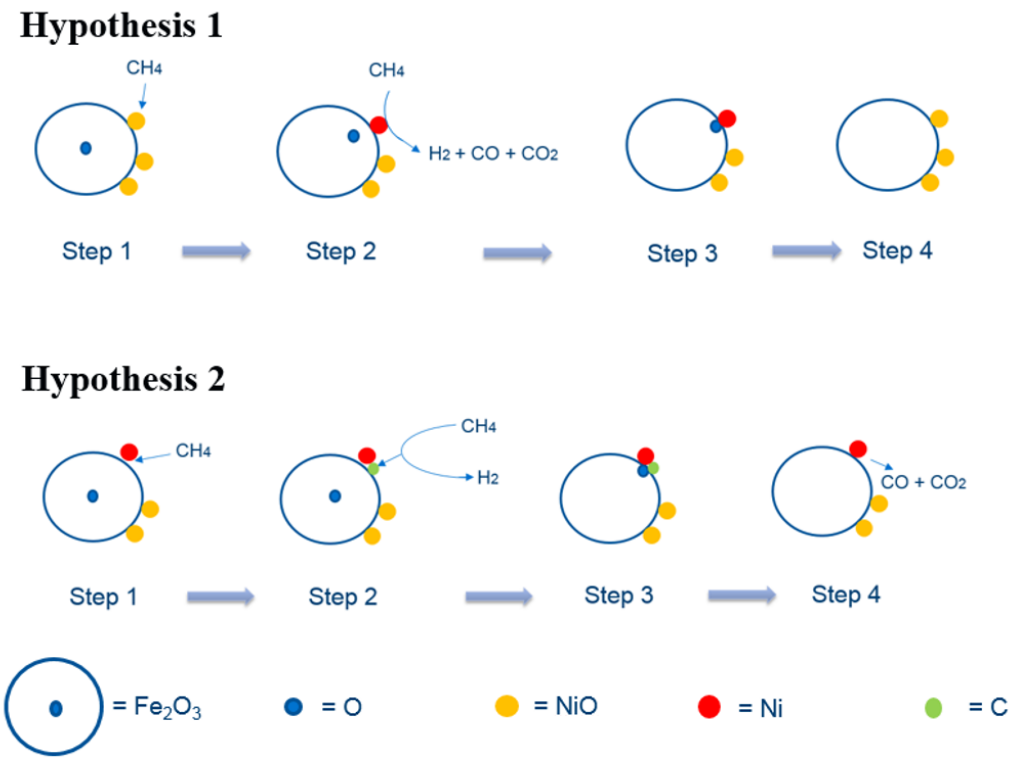

Figure 8-6 Graphic presentation of the two hypothesis accounting for the catalytic effect of H_2 production in NiO/Fe_2O_3.

The results obtained in this study indicate that hypothesis 2 seems to dominate. This is because (1) the H_2 production rate in the NiO/Fe_2O_3 bed was comparable to that when Ni/Al_2O_3 was just exposed to 8.5% CH_4/Ar (*i.e.* the initial H_2 peak); (2) SEM/EDX analysis of NiO/Fe_2O_3 particles (as shown in Fig. 8-7 and Table 8-3), where the particles was collected after CH_4/Ar plasma-assisted reduction (no air regeneration), showed that the surface of NiO/Fe_2O_3 particles was predominantly covered by Ni; (3) the trace amounts

of CO and CO_2 produced from NiO/Al_2O_3 subjected to CH_4/Ar plasma discharge were similar to those from Al_2O_3 and Fe_2O_3 beds, showing that NiO in the absence of Fe_2O_3 cokes easily, or does not react with CH_4.

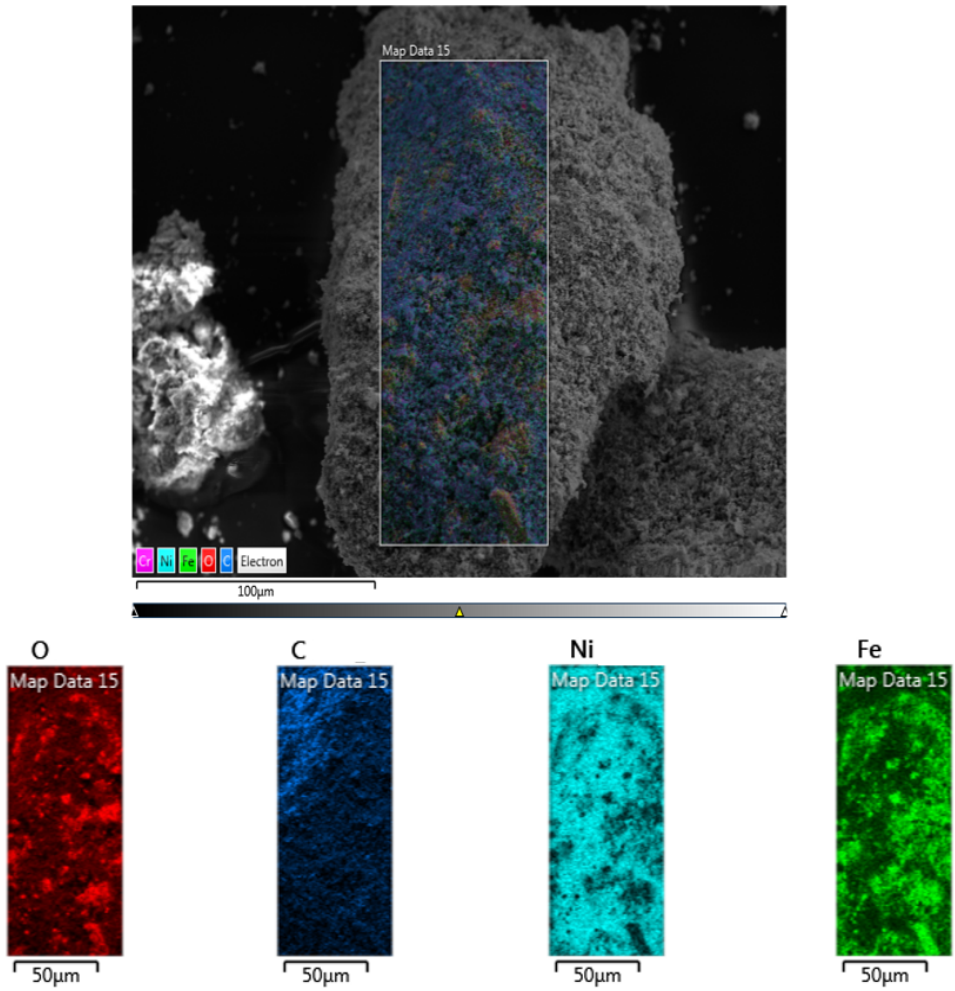

Figure 8-7 SEM micrograph combined with EDX analysis of NiO/Fe_2O_3 particle surface after experiment in the DBD reactor. The quantitative results from the EDX analysis are presented in Table 8-3.

Table 8-3 Results from the EDX analysis of NiO/Fe_2O_3 particle surface after experiment in the DBD reactor.

Element	Weight in wt%	σ in wt%
C	6.59	0.06
O	10.84	0.03
Fe	20.28	0.05
Ni	62.2	0.07

Due to the relative inertness between NiO and Fe_2O_3, it is reasonable to identify the sequence of phase transformation of NiO/Fe_2O_3 in the CH_4 reducing environment by referring to the Ni-O and Fe-O phase diagrams, as shown in Figs. 8-8 and 8-9, where the diagrams were computed by MTDATA [139]. Thermodynamically, at 673 K, the partial pressure of O_2, P_{O_2}, to cause a phase transition from NiO to Ni is lower than that for Fe_2O_3 to Fe_3O_4, but higher than that for Fe_3O_4 to Fe. This means that assuming negligible solubility of NiO into the Fe_2O_3 system, the sequence for reduction would be: Fe_2O_3 + NiO → NiO + Fe_3O_4 → Ni + Fe_3O_4. Therefore, thermodynamically, in a reducing environment, it is expected that if Ni was detected, Fe_3O_4 would then also be present. However, at the relatively mild temperatures in this study, reaction kinetics are important and Fe_2O_3 is un-reactive towards CH_4. A high level of H_2 production in NiO/Fe_2O_3 was observed as soon as the plasma discharge was applied. If the catalytic effect for H_2 production was only due to the presence of metallic Ni, then the formation of Ni must have happened as soon as NiO/Fe_2O_3 was subjected to plasma discharge. This contrasts with the pure NiO/Al_2O_3 material, which could also have reduced to Ni locally, but for some reason remained inactive. Such a different behaviour of NiO/Al_2O_3 might have been caused by coking, where carbon immediately deposited on any newly created Ni-metallic site. Additionally, the formation of nickel aluminate after plasma treatment also means that less Ni is available for CH_4 cracking. If Ni immediately formed when plasma was applied in the NiO/Fe_2O_3 bed, the suppression of coking was most likely due to the presence of an oxygen source, *i.e.* Fe_2O_3. The co-existence of Ni and Fe_2O_3 is thermodynamically unstable, and the system tends to form NiO and Fe_3O_4 at equilibrium. The transfer of oxygen to the Ni sites would then help remove any deposited carbon or prevent transiently formed absorbed carbon species from forming coke, and thus maintaining the catalytic activity of Ni. For NiO/Fe_2O_3, not only was less coke formed, the remaining coke was also more easily burned off during the air regeneration stage, compared with other materials *e.g.* NiO/Al_2O_3 and Fe_2O_3. The superior performance of the NiO/Fe_2O_3 for H_2 production and its easy regeneration demonstrate the proposed concept of having plasma-assisted chemical looping system for H_2 production at mild temperatures.

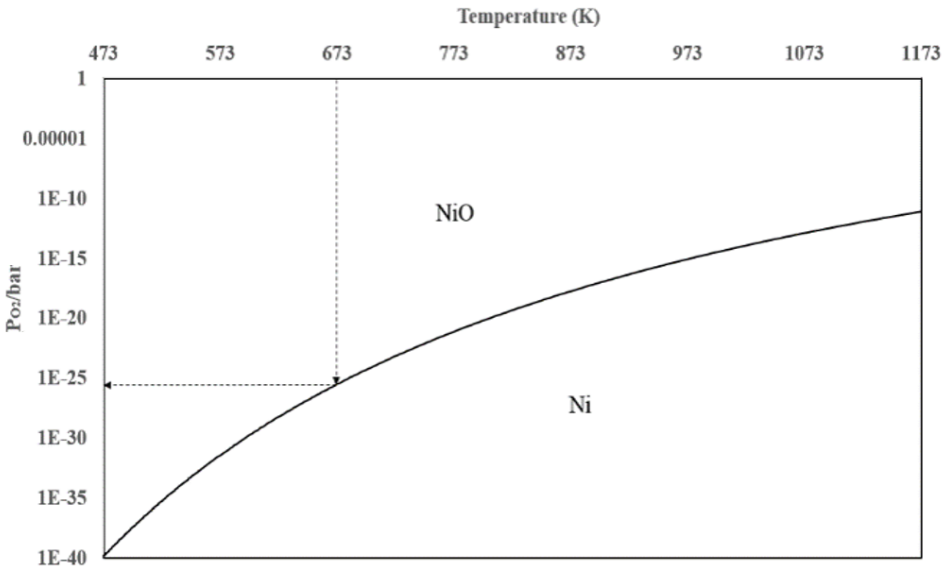

Figure 8-8 Phase diagram of Ni-O system, calculated with MTDATA [139] (SGTE database).

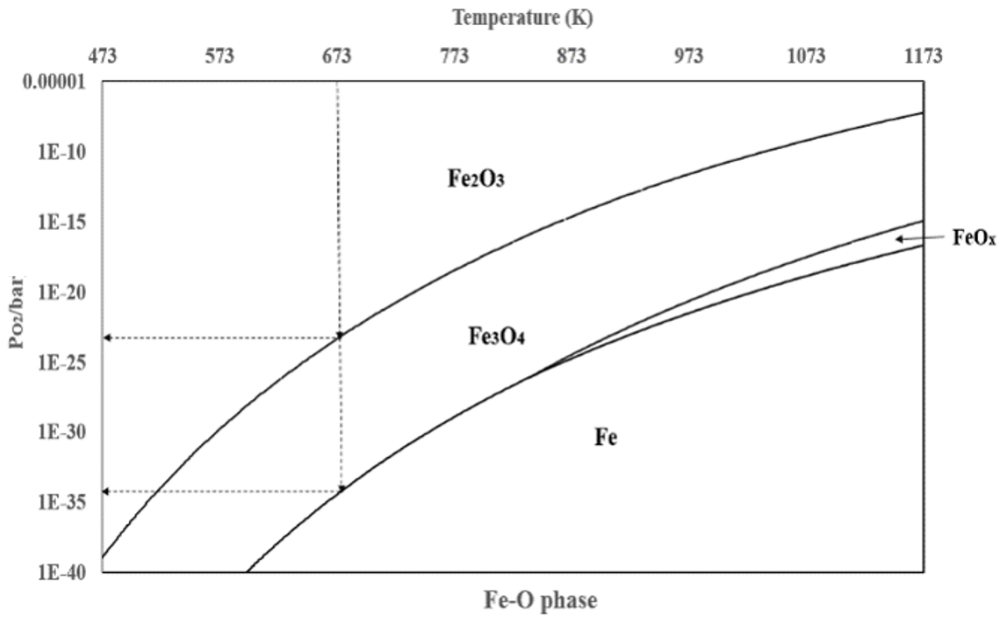

Figure 8-9 Phase diagram of Fe-O system with MTDATA [139] (NPL database).

- **$NiFe_2O_4/Fe_2O_3$**

In Fig. 8-5, the observed (Ni, Fe) phase together with the decreased intensity of $NiFe_2O_4$ peaks in the XRD spectra in the CH_4/Ar plasma treated sample, indicates the phase segregation of $NiFe_2O_4$ to (Ni,Fe). This seems to be consistent with study carried out by Raghavan [220]. At 1273 K and low P_{O_2} ($P_{O_2} < 10^{-11}$ bar), $NiFe_2O_4$ tends to reach equilibrium with $(Ni, Fe)_3O_4$ and (Ni, Fe). Extrapolating to the low temperatures used

here, it is reasonable to expect that the reduction follows $NiFe_2O_4 \rightarrow (Ni, Fe)_3O_4 + (Ni, Fe)$. In our study, when the $NiFe_2O_4$ material was regenerated in air plasma at 673 K, the (Ni, Fe) peaks disappeared (refer to Fig. 8-5). The most likely route for the oxidation of Ni is to create NiO. However, the presence of NiO was difficult to confirm, due to significant overlap of the NiO and $NiFe_2O_4$ peaks in the XRD pattern. For Fe, no evidence of wustite or magnetite phase was observed. The most likely route would then be $Fe \rightarrow Fe_2O_3$. In terms of the catalytic effect in the $NiFe_2O_4$ bed, it was found that the H_2 yield improved slightly in the second and third reduction cycles, especially in the initial plasma discharge period, as presented in Fig. 8-10. If NiO was indeed created in the regeneration stage, then it could have helped with the production of H_2 in subsequent reductions.

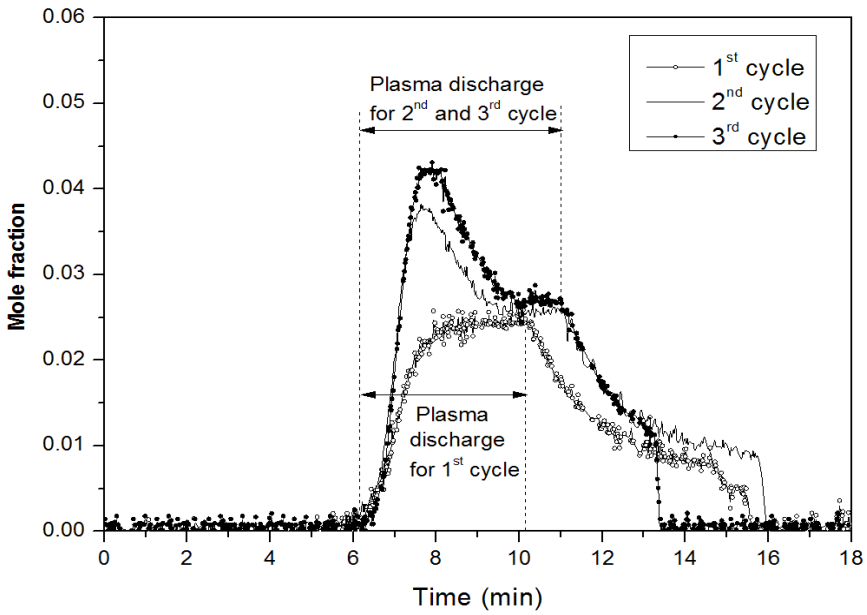

Figure 8-10 H_2 concentration measured during three subsequent CH_4/Ar plasma discharge experiments, using $NiFe_2O_4/Fe_2O_3$ as the bed material.

8.4.2 Comparison to water gas shift equilibrium

In the bed of NiO/Fe_2O_3, the products from CH_4/Ar plasma discharge were mainly H_2 and CO_2. A high yield of H_2 and CO_2 at such low temperature (673 K) could be linked with the water-gas shift reaction (WGSR: $H_2O + CO \rightarrow H_2 + CO_2$). Assuming that water was also produced in the NiO/Fe_2O_3 bed (which would also account for the discrepancy in the hydrogen balance, Table 1), then the reaction quotient, $\frac{[H_2][CO_2]}{[H_2O][CO]} = 64.6 \pm 19.1$, can be compared with the equilibrium constant of WGRS at 673 K, K_{eq} = 12.0 [221]. This

suggests that the plasma-assisted process tends to push production of H_2 and CO_2, beyond the thermodynamic equilibrium of WGSR. To achieve a K_{eq} close to the reaction quotient achieved here, the conventional WGSR would need to operate at a much lower temperature, where slow reaction kinetics may be problematic (though it should be noted that excess water is usually used to shift the equilibrium). The fact that such high production of H_2 and CO_2 was achieved within such a small bed (~ 7.5 ml) and at a low temperature indicates very fast reaction rates. For the WGSR to achieve a high conversion to H_2 and maintain favourable kinetics, multiple reaction stages are often employed (*e.g.* moving from high to low temperatures), and thus complicating the process. Therefore, the alternative H_2 and CO_2 production method described here, offers a promising new route. The high value of $\frac{[H_2][CO_2]}{[H_2O][CO]}$ found here seems to suggest that H_2 and CO_2 might be directly produced from the partial oxidation of CH_4 by the oxygen carrier, without going through some intermediate step involving WGSR. The unusually high ratio is likely to be a result of H_2 and CO_2 not having sufficient time to reach a WGSR equilibrium.

The energy cost, EC_a, as described in 7.4.5, is also estimated here, to compare with H_2 production with those in $SrFeO_{3-\delta}$ and for conventional industrial processes. The results are presented in Table 8-4. Compared to the $SrFeO_{3-\delta}$ bed (refer to Table 7-4), the energy cost in NiO/Fe_2O_3 and $NiFe_2O_4/Fe_2O_3$ beds is significantly decreased. More excitingly, the current values are in the same magnitude with the industrial water electrolysis (from 320 to 510 MJ/kg). Given that the current experimental set-up can be further modified to improve the H_2 production such as varying the dimension of the plasma region, changing the flow rate and *etc*., the results exhibit its promising application in the industry of H_2 production.

Table 8-4 The energy cost, EC_a for H_2 production in NiO/Fe_2O_3 and $NiFe_2O_4/Fe_2O_3$ (note: the error bar show the range of three repetitions), and in comparison to that from water electrolysis.

NiO/Fe_2O_3 (MJ/kg)	$NiFe_2O_4/Fe_2O_3$ (MJ/kg)	Water electrolysis (MJ/kg)
440 ± 20	550 ± 40	320 - 510

8.4.3 Discussion of the H_2 production in Fe_2O_3-based and $SrFeO_{3-\delta}$-based materials in the plasma-assisted chemical looping system

- **The catalytic effect in NiO/$SrFeO_{3-\delta}$**

In NiO/Fe_2O_3, the catalytic effect was considered due to hypothesis 2, *i.e.* the instantly generated Ni subjected to plasma discharge is responsible for the high generation of H_2. In the $SrFeO_{3-\delta}$-based system, as studied in Chapter 7, $SrFeO_{3-\delta}$ itself did not promote the production of H_2; on the contrary, it directly combusted the H_2 generated (from direct CH_4 cracking by plasma catalysis). The addition of NiO seems significant improved the generation of H_2 in the first reduction. It seems that hypothesis 2 can also explain what have happened to the NiO/$SrFeO_{3-\delta}$ system for H_2 production. The general idea is that for this plasma-assisted chemical looping H_2 production at low temperatures to work, an oxygen donor and a catalyst that promotes H_2 production, need both to be present. On the other hand, it was found that only the freshly prepared NiO/$SrFeO_{3-\delta}$, NSFO1, was active for H_2 production. Based on the change in the XRD patterns in the re-used material, NSFO2, as shown in Fig. 7-11, the decreased activity of NSFO2 might have resulted from the segregation of the material and the possibly segregated Fe could have deactivated NiO. This can be further supported by that the results in a bed of NSFO2 (Fig.7-13) are very similar to those in $SrFeO_{3-\delta}$ (Fig.7-10).

- **Comparison between NiO/Fe_2O_3 and NiO/$SrFeO_{3-\delta}$**

Regardless of the fact that NiO/$SrFeO_{3-\delta}$ was only active for one cycle, understanding of H_2 production in the both NiO/$SrFeO_{3-\delta}$ and NiO/Fe_2O_3 would provide important information of the selection of proper materials for the plasma-assisted chemical looping system for H_2 production. This is because Fe_2O_3 and $SrFeO_{3-\delta}$ are two typical examples of showing how oxygen carriers with very different activity would react in such a system.

Though hypothesis 2 can be used to explain high yield of H_2 for both NiO/$SrFeO_{3-\delta}$ and NiO/Fe_2O_3, as shown in Figs. 7-12 and 8-2d, they behaved very differently when subjected to plasma discharge. In NiO/$SrFeO_{3-\delta}$, a large amount of CO_2 was produced in the initial period of plasma discharge, and the catalytic effect of metallic Ni on H_2 production seems to be inhibited. H_2, together with some CO, was only observed when CO_2 was no longer generated, and this seems to be the stage that metallic Ni started to influence. The results

suggest that for NiO/$SrFeO_{3-\delta}$, n the initial period, the apparent reduction of NiO was not possible due to fast oxygen decoupling rate of $SrFeO_{3-\delta}$. Even if there was reduction of NiO to metallic Ni phase, the generated Ni can be quickly surrounded by the lattice oxygen from $SrFeO_{3-\delta}$, or the gaseous oxygen released from $SrFeO_{3-\delta}$ (due to high chemical potential of oxygen). The rate of CH_4 cracking for H_2 production over the catalytic Ni sites could have been much slower than the oxygen decoupling rate of $SrFeO_{3-\delta}$, and thus the oxidation rate of Ni (to NiO). Only when $SrFeO_{3-\delta}$ has been reduced to a state with lower chemical potential of oxygen, or/and lower oxygen decoupling rate, the presence of metallic Ni could be stable and exhibited its catalytic effect for H_2 production. As seen in Fig. 7-12d, after the initial period, [CO_2] dropped, CO and H_2 were significantly produced simultaneously, and this is where oxygen decoupling from $SrFeO_{3-\delta}$ became the rate-limiting step for the overall reaction.

In a NiO/Fe_2O_3 bed, according to Fig.8-2d, H_2 was immediately generated when plasma was applied to the DBD reactor. In the meantime, some CO_2 and CO were simultaneously generated. Based on hypothesis 2, NiO was immediately reduced to metallic Ni and promoted the H_2 production. This means that the oxygen decoupling rate, or the rate of oxygen transfer to the reduced Ni sites was just sufficient to suppress coking onto the Ni sites but not too fast to re-oxidise the Ni. The whole system seems to be in a perfect equilibrium of removal of any solid or transient carbon, and the transfer of lattice oxygen to the Ni sites, so that Ni can always be catalytic active.

The performance of NiO/Fe_2O_3 in the DBD reactor is stable for at least three looping cycles; whilst in the bed of NiO/$SrFeO_{3-\delta}$, it was only active in the fresh cycle. A holistic understanding of the deactivation needs further investigation. But the important message from the investigation of doping Ni/NiO onto the $SrFeO_{3-\delta}$ is that though the freshly prepared NiO/$SrFeO_{3-\delta}$ is promising for H_2 production, it has poor cyclability and thus not applicable in such system.

To summarise, a suitable chemical looping material for H_2 production in such as DBD reactor should meet the following requirements:

1) Contain a catalytic material for production or promotion of H_2 production.

2) Contain an oxygen source to remove coke and keep the catalytic active. More importantly, the oxygen carrier should not be too active.
3) Have good looping performance.

Theoretically, this idea would work for other systems that employing catalysts and oxygen carriers for fuel synthesis or production, depending on the product of interest.

8.5 Conclusions

The main novelty of this work is to convert a CH_4 stream to H_2-rich gas at a low temperature (673 K), without the addition of gaseous oxygen (which comes from the chemical loop here). In addition, this process can work without any steam input. For Ni-doped Fe_2O_3-based looping materials for H2 production, the results obtained are:

(a) The active nature of the supporting metal oxide, Fe_2O_3, positively influences the activity of the catalyst. Among the tested materials, NiO/Fe_2O_3 exhibited the best performance, resulting in the highest H_2 yield, whilst carbon deposition and the subsequent catalyst deactivation were significantly lower than those from NiO or Ni supported on alumina.
(b) The catalytic activity for H_2 production in the combined catalyst/oxygen carrier (NiO/Fe_2O_3) was attributed to the generation of metallic Ni, and the suppression of carbon deposition was connected to the presence of the active metal oxide, Fe_2O_3. The plasma-assisted CH_4 reforming and oxidation by the oxygen carrier significantly exceeded the theoretically expected performance if the water-gas shift equilibrium were applied.
(c) The energy cost estimated was found comparable to industrial water electrolysis, for instance, 440 +/- 20 MJ/kg of hydrogen in a NiO/Fe_2O_3 bed, compared to 320 - 510 MJ/kg for water electrolysis.

A comparison of $SrFeO_{3-\delta}$-based (studied in Chapter 7) and Fe_2O_3-based materials for H_2 production were carried out. It was found that oxygen carrier only with appropriate oxygen donating activity (not too active) works best for keeping the catalytic site active.

9.0 Conclusion

The dissertation was mainly concerned with investigating the effect of oxygen carriers on the conversion of fuels, for various processes including combustion of solid fuels (Polish coal-derived char and wood chips) as presented in Chapters 3 and 5, and hydrogen production from CH_4 in Chapters 6, 7 and 8.

In Chapter 3, to achieve effective overall combustion of Polish coal-derived char by Fe_2O_3 and ZrO_2-supported Fe_2O_3 in a fluidised bed from 1123 to 1248 K, gasification of Polish char by CO_2 was carried out *in situ*, prior to the combustion by the oxygen carriers. Before investigating the interaction between oxygen carriers and the gasification products, the gasification of Polish char was studied first. Comparing the measured experimental gasification rate and the estimated external mass transfer rate, the gasification was believed to be free of external mass transfer limitation. The activation energy values, based on the Arrhenius plot, were found to be 196 to 216 kJ mol^{-1}, suggesting a kinetically controlled regime for gasification. The replacement of the fluidising bed from inert silica sand to Fe_2O_3 particles initiated the combustion of the CO produced from gasification, to CO_2. Whilst Fe_2O_3 did not affect the gasification step, and this is mostly because the gasification was not affected by external mass transfer. The effect of ZrO_2-supported Fe_2O_3, however, significantly decreased the measured apparent rate of gasification. By comparing the reduction of ZrO_2-supported Fe_2O_3 and Fe_2O_3 in 10% CO, it was found that the reduction reactivity of ZrO_2-supported Fe_2O_3 with CO was higher, implying less likelihood of an inhibition effect from this step. Results with ZrO_2 as the fluidising bed for gasification exhibited much lower measured gasification rate, indicating that the inhibition effect of ZrO_2-supported Fe_2O_3 mainly came from ZrO_2. It is suspected that the inhibition is due to the interaction between CO and ZrO_2, whilst this requires future work to be conducted.

In chapter 4, a numerical model based on Ergun's two step mechanism was developed to describe the gasification of a Polish char particle. Using the kinetic data obtained from CO_2 gasification of the char, with CO_2 concentration varying from 0% to 100% (balance N_2), the modelled results fitted well of the experimental data. However, when CO was intentionally introduced into the system, the model did not give a good fit: the gasification rate was apparently over-estimated by the model. Two approaches were attempted to re-

fit the experimental data. In the first method, the kinetic data were re-calculated by including the experimental results of adding CO to the system. The new kinetic data showed higher inhibition effect of CO, and the re-substituted model exhibited good agreement of the experimental results at various conditions. The second approach modified the rate expression based on a three-step mechanism. The new model also amplified the effect of CO, and it described the gasification reasonably well. In summary, both the approaches showed that the inhibition effect of CO was more significant than previously expected. Referring to the modified Thiele modulus, as defined by Roberts and Satterfield [172], the added CO can suppress the rate gradient across the particle. This might be the main reason accounting for the gasification rate being more sensitive to the surface CO concentration than that locally.

Combustion of a biomass fuel, wood chips, at temperatures from 773 to 1173 K, was carried out in a fluidised bed reactor, by Fe_2O_3 and mayenite-supported CuO, respectively. The developed non-thermal plasma reactor, DBD reactor, was positioned in the downstream of the fluidised bed, for the continuous measurement of tar. It utilised the capability of the DBD reactor for cracking and converting heavy hydrocarbons into easily detectable gases (*e.g.* CO, CO_2), which allowed the quantification of the carbon content in the tar to be conducted. Based on the coupled system, both Fe_2O_3 and mayenite-supported CuO were effective in reducing tar *in situ*, and the tar was mostly converted to CO_2. Mayenite-supported CuO exhibited even higher reactivity due to its capability of releasing gaseous oxygen at temperatures above 1073 K, making it a promising candidate for the direct total combustion of biomass in the fluidised bed. The effect of the oxygen carriers on the distribution of the products from a pyrolysing environment was compared with that in the presence of CO_2. CO_2 was found to reform/gasify the biomass-derived products at temperatures above 973 K.

Oxygen carriers ($SrFeO_{3-\delta}$, Fe_2O_3, and NiO-doped $SrFeO_{3-\delta}$ and Fe_2O_3) were used to produce H_2 from CH_4 in Chapters 7 and 8. This was achieved using a plasma-assisted chemical reactor- that allowed H_2 production to occur at milder temperatures (~ 473 K) than those for conventional methane steam reforming for H_2 production. Oxygen carriers were packed in the DBD reactor in the plasma discharge zone, and enhanced the conversion of methane. The redox nature of the oxygen carriers provided the possibility of a chemical

looing scheme for H_2 production. The electrical behaviors of the developed plasma-assisted packed bed reactor were firstly studied in Chapter 6. It was found that the dielectric constant of packing materials affected the type of the discharge: noisy and filamentary discharge dominated in the bed with lower dielectric constant (*i.e.* alumina sand), whilst silent and diffuse discharge occurred in the $SrFeO_{3-\delta}$ bed with a significantly higher dielectric constant. Plasma power was observed to have the biggest influence on the conversion of CH_4; whereas the electron energy, a function of the applied voltage, also affected the conversion.

In Chapter 7, H_2 production from CH_4 was firstly investigated in a $SrFeO_{3-\delta}$-packed DBD reactor at temperatures from 293 to 773 K. The experiments were carried out in pure Ar and a mixed stream of CH_4 and Ar, where Ar can be treated as inert to other species in such a plasma system. The intensity of plasma-generated excited species in pure Ar was significantly higher than that in the mixed gas, due to the contamination effect of CH_4. Similarly, the presence of gaseous O_2 (released from $SrFeO_{3-\delta}$ at high temperatures) was also found to decrease the intensity of the plasma excited species. Direct cracking of CH_4 by plasma catalysis was observed; however, the effect of plasma on $SrFeO_{3-\delta}$ was mainly the surface heating. In general, $SrFeO_{3-\delta}$ was not promising for H_2 production in such system due to its over-reactivity, leading to the total combustion to CO_2 and H_2O. Ni was doped onto the surface of $SrFeO_{3-\delta}$ (resulting $NiO/SrFeO_{3-\delta}$). This significantly improved the yield of H_2; whilst the high reactivity towards H_2 production was observed in the fresh $NiO/SrFeO_{3-\delta}$ bed only.

Chapter 7 suggests that less reactive oxygen carriers are more suited for plasma-assisted chemical looping H_2 production. In Chapter 8, Fe_2O_3, NiO/Fe_2O_3 and $NiO/NiFe_2O_4$ were investigated, and compared with those from alumina-based beds. The experiments were carried out at 673 K. Fe_2O_3, on its own, was found inert to CH_4 even with plasma discharge. In contrast, the presence of Ni stimulated the production of H_2 for both the two forms of Ni-Fe-O system. A high H_2 yield in the two beds was maintained for three chemical looping cycles. NiO/Fe_2O_3 exhibited better performance, with a higher H_2 yield and carbon balance. In an inert alumina bed, low production of H_2 and severe carbon deposition were found. The catalytic activity for H_2 production in the combined catalyst/oxygen carrier (NiO/Fe_2O_3) could be most likley attributed to the generation of metallic Ni, and the

suppression of carbon deposition was connected to the presence of the active metal oxide, Fe_2O_3. The comparison between NiO/$SrFeO_{3-\delta}$ (studied in Chapter 7) and NiO/Fe_2O_3 for H_2 production indicated that oxygen carrier only with appropriate oxygen donating activity (not too active) works best for keeping the catalytic site active and effective. The high and repeatable H_2 yield in multiple cycles in a bed of NiO/Fe_2O_3, demonstrated the promising application of the proposed plasma system for H_2 production at mild temperatures. The estimated energy cost, 440 $\pm$ 20 MJ/kg of H_2, was also found comparable to that for water electrolysis.

10.0 Future Work

For Polish coal-derived char, the presence of ZrO_2-supported Fe_2O_3 was found to decrease the apparent gasification rate in a fluidised bed. The experimental results of much lower gasification rate in a bed of ZrO_2 than that in silica sand indicate that the 'inhibition' effect of ZrO_2-supported Fe_2O_3 on gasification mainly came from ZrO_2. This seems to be different from fact that ZrO_2 has been used as an inert support in many applications reported in literature. Further investigation on how ZrO_2 inhibited the gasification needs to be carried out in future. A most likely link to this might be to do with the surface of ZrO_2, for instance the surface interaction between ZrO_2 with CO, either chemically or physically.

In chapter 5, the developed tar measurement system allows an apparent rate profile of tar production to be obtained. Understanding the production of tar from the biomass over time, which is essentially the rate of devolatilisation, is of great importance for studying pyrolysis. To obtain a true tar production rate profile from the upstream, deconvolution of the system needs to be carried out further. This can be achieved by assuming a continuous stirred tank reactor coupled with a plug flow reactor.

The plasma-assisted packed bed reactor system for H_2 production from CH_4 partial oxidation by oxygen carriers exhibited its promising capability in chapters 7 and 8. Both $NiO/SrFeO_{3-\delta}$ and NiO/Fe_2O_3 showed high activity for producing H_2, but only the performance of NiO/Fe_2O_3 was maintained after multiple looping cycles. The deactivation of $NiO/SrFeO_{3-\delta}$ after the 1st (fresh) cycle should be further explored. So far, it seems that this might be due to the interaction between NiO and $SrFeO_{3-\delta}$ by plasma effect or reduction. Future work on the effect of Ni onto the $SrFeO_{3-\delta}$ perovskite structure on H_2 production would also be interesting. The current goal of chapters 7 and 8 was to introduce a new concept for H_2 production at mild temperatures. The focus has been on understanding the synergistic effect of NiO/Fe_2O_3 and $NiO/SrFeO_{3-\delta}$. In addition to these, process parameters can significantly influence the outcome of the investigated process. Further work, especially for NiO/Fe_2O_3, on exploring the effect such as of temperature, the flow rate, and the height of the packed bed is worth conducting. The results obtained here demonstrated the feasibility of PCLH. It is just the start of this exciting subject, and

this should be followed by investigation of other potential oxygen carriers and catalysts, to improve the H_2 yield further.

List of abbreviations and symbols

Abbreviations

a-CLR	Auto-thermal chemical looping reforming
BET	Brunauer-Emmett-Teller
BJH	Barrett-Joyner-Halenda
CCS	Carbon capture and storage
CLC	Chemical looping combustion
CLOU	Chemical looping oxygen uncoupling
DBD	Dielectric barrier discharge
DI	De-ionised water
DIEI	Direct ionisation by electron impact
FeZr	ZrO_2-supported Fe_2O_3
FTIR	Fourier transform infrared
GHG	Greenhouse gas
ICSD	Inorganic Crystal Structure Database
ICHIP	Ionisation by collision of heavy particles
IEA	International Energy Agency (IEA)
IPCC	Intergovernmental Panel On Climate Change
NIST	National Institute of Standards of Technology, USA
NPL	National Physical Laboratory, UK
PCLH	Plasma-assisted chemical looping hydrogen production
PI	Photo-ionisation
SR-CLC	Stem reforming with chemical looping combustion
SED	Specific energy density
SEM-EDX	Scanning electron microscope with energy dispersive X-ray spectroscopy (SEM/EDX)
SI	Surface ionisation
TGA	Thermogravimetric analyser
VOCs	Volatile organic compounds
XRD	X-Ray (powder) diffraction

Symbols

Symbols		units
A	frequency factor	mol s^{-1} g^{-1}
c	concentration of active sites per unit mass of carbon	g^{-1}
C_D	capacitance of the dielectric	F
C_d	effective dielectric capacitance	F
C_{gap}	overall capacitance of the gap	F
C_{Total}	total capacitance of the electrode configuration	F
D	diffusion coefficient	m^2 s^{-1}
$(D_A)_{ij}$	overall diffusivity	m^2 s^{-1}
$(D_B)_{ij}$	molecular diffusivity of component i in j	m^2 s^{-1}
$\boldsymbol{d_c}$	degree of carbon deposition	-
D_{CO_2}	diffusivity of CO_2	m^2 s^{-1}
$(D_K)_i$	Knudsen diffusivity of component i	m^2 s^{-1}
d_p	particle diameter	m
d_{pore}	pore diameter	m
E, E_i	activation energy	kJ mol^{-1}
EC_a, EC_b	energy cost	MJ/kg of H_2
g	acceleration due to gravity	m s^{-2}
F_{air}	air flow rate to mix with the sampled product flow from the fluidised bed	L/min
F_{total}	total flow rate in the sampling line	L/min
F_{FB}	total gas flow rate in the fluidised bed	L/min
F_{sampling}	flow rate of the sampling line from the fluidised bed	L/min
J_a	molar flux of component a	mol m^{-2} s^{-1}
k	volumetric rate constant	-
k’	Effective shrinking core rate constant	-
k_B	Boltzmann constant ($1.38 \times 10^{-23}\ J/K$)	J/K
k_i	rate constant per active site	-
K, K_p	equilibrium constant	-

M_{carbon}	molar mass of carbon	g mol^{-1}
$m_{\text{C,tar}}$	mass of carbon in the tar entering the sampling system	g
$M_{\text{C,tar}}$	total mass of carbon in the tar produced in the fluidised bed	g
$M_{\text{C,total}}$	total carbon content in the wood fed	g
m_i	mass of carbon in the carbon-containing species i	g
m_t	accumulated increased amount of carbon in the gaseous phase	g
m_o	initial mass of char fed into the reactor	g
$M_{\text{wood,total}}$	total mass of wood fed into the FB	g
m %	mass balance of carbon	-
N_{Ga}	Galileo number	-
n_{H_2}	amount of H_2 produced	kg
P	total pressure	Pa
p_{CO}	partial pressure of CO	Pa
p_{CO_2}	partial pressure of CO_2	Pa
R	sphere radius	m
R^2	R-squared values of fitting for kinetic parameters	-
$R_{co,burn-off}$	rate of production of CO during burn-off	mol s^{-1} g^{-1}
$R_{co_2,burn-off}$	rate of production of CO during burn-off	mol s^{-1} g^{-1}
$R_{CO,silica}$	overall rate of production of CO in silica sand	mol s^{-1} g^{-1}
$R_{CO_2,silica}$	overall rate of production of CO_2 in the presence of oxygen carriers	mol s^{-1} g^{-1}
$R_{CO,oc}$	overall rate of production of CO in the presence of oxygen carriers	mol s^{-1} g^{-1}
$R_{CO_2,oc}$	overall rate of production of CO_2 in silica sand	mol s^{-1} g^{-1}
r_g	gasification rate per unit volume of carbon	mol s^{-1} m^{-3}
Re_{mf}	Reynolds number at minimum fluidisation	-
R'_g	gasification rate over time	mol s^{-1} g^{-1}
$R'_{g,0}$	initial gasification rate (at t = 0)	mol s^{-1} g^{-1}
R_i	rate of production of carbon in the carbon-containing species i	g m^{-1}
R_{ideal}	ideal gas constant	J mol^{-1} K^{-1}

R_{max}	maximum rate of gasification (external mass transfer rate)	mol s^{-1} g^{-1}
r_{obs}	observed rate of reaction	-
r_{oc}	rate of production of CO_2 from the reaction between CO and oxygen carriers	mol s^{-1} g^{-1}
r_s	rate of reaction at the particle surface	-
Sh	Sherwood number	-
S_a	averaged selectivity of species a	-
T	temperature	K, or ℃
t_0	Initial pyrolysis time	s
t_a	processing at time a (pyrolysis)	s
t_b	processing time at time b (burn-off)	s
U	superficial velocity in a fluidised bed	m/s
$\widehat{U}$	peak voltage in a discharge cycle	kV
U_{mf}	minimum fluidisation velocity	m/s
U_{min}	minimum voltage required for discharge to start	kV
v	kinematic viscosity of fluidising gas	m^2 s^{-1}
v_a	stoichiometric coefficient for species a	-
v'_a	atomic diffusion volume	m^3
W	applied plasma power	J
X	conversion of carbon	-
x_C	weight fraction of elemental carbon in the wood	-
x_i	mole fraction of the product species *i*	-
Y_i	the yield of gaseous species *i*	-

Greek symbols		
ρ_f	the density of the fluidising gas	kg/m^3
ρ_s	the density of the solid particles	kg/m^3
μ	dynamic viscosity	Pa·s
μ_e	drift mobility	m^2 V^{-1} s^{-1}
ϕ	Thiele modulus	-
ϕ_m	modified Thiele modulus	-
η	effectiveness factor	-

$\eta_{with\ capture}$	power plant energy efficiency with carbon capture installed	-
$\eta_{without\ capture}$	power plant energy efficiency without carbon capture installed	-
ε	porosity or voidage of the particle	-
ε_D	relative dielectric constant of quartz tube	-
ε_{mf}	voidage at minimum fluidisation	-
ε_{vacuum}	dielectric constant of the vacuum	Fm^{-1}
τ^2	tortuosity factor of the particle	-
θ	surface active coverage	-
δ	oxygen vacancy in $SrFeO_{3-\delta}$	-

Reference

[1] J.-M. Jancovici, Manicore - Using coal? But what for?, (2013). http://www.manicore.com/anglais/documentation_a/oil/coal_use.html (accessed February 15, 2015).

[2] E. McLamb, Fossils Fuels vs. Renewable Energy | Ecology Global Network, Ecology Global Network. (2011).

[3] I.E.A. IEA, CO2 Emissions from Fuel Combustion 2017 - Highlights, International Energy Agency. 1 (2017) 1–162. doi:10.1787/co2_fuel-2017-en.

[4] IPCC, CLIMATE CHANGE 2014 SYNTHESIS REPORT Approved Summary for Policymakers, 2014.

[5] The Linde Group, Pre-combustion capture - Process Plants > CCS and CO2 Plants > Carbon Capture and Storage (CCS) > Pre-combustion capture | Linde Engineering, (2014). http://www.linde-engineering.com/en/process_plants/CCS/CCS/Pre-combustion/index.html (accessed February 15, 2015).

[6] M. Kanniche, R. Gros-Bonnivard, P. Jaud, J. Valle-Marcos, J.-M. Amann, C. Bouallou, Pre-combustion, post-combustion and oxy-combustion in thermal power plant for CO2 capture, Applied Thermal Engineering. 30 (2010) 53–62. doi:10.1016/j.applthermaleng.2009.05.005.

[7] IPCC, IPCC special report on Carbon Dioxide Capture and Storage, (2005). http://www.ipcc.ch/pdf/special-reports/srccs/srccs_wholereport.pdf (accessed February 15, 2015).

[8] Parliamentary Office of Science and Technology, co2 Capture, transport and storage, (2009). http://www.parliament.uk/documents/post/postpn335.pdf (accessed February 15, 2015).

[9] G.P. Hammond, S.S.O. Akwe, S. Williams, Techno-economic appraisal of fossil-fuelled power generation systems with carbon dioxide capture and storage, Energy. 36 (2011) 975–984. doi:10.1016/j.energy.2010.12.012.

[10] Carbon Capture& Storage Association, Post-combustion capture – The Carbon Capture & Storage Association (CCSA), (2015). http://www.ccsassociation.org/what-is-ccs/capture/post-combustion-capture/ (accessed February 15, 2015).

[11] G.P. Hammond, J. Spargo, The prospects for coal-fired power plants with carbon

capture and storage: A UK perspective, Energy Conversion and Management. 86 (2014) 476–489. doi:10.1016/j.enconman.2014.05.030.

[12] Carbon Capture& Storage Association, Oxy-fuel combustion systems – The Carbon Capture & Storage Association (CCSA), (2015). http://www.ccsassociation.org/what-is-ccs/capture/oxy-fuel-combustion-systems/ (accessed February 15, 2015).

[13] J. Adanez, A. Abad, F. Garcia-Labiano, P. Gayan, L.F. de Diego, Progress in Chemical-Looping Combustion and Reforming technologies, Progress in Energy and Combustion Science. 38 (2012) 215–282. doi:10.1016/j.pecs.2011.09.001.

[14] M.A. Saucedo, J.Y. Lim, J.S. Dennis, S.A. Scott, CO2-gasification of a lignite coal in the presence of an iron-based oxygen carrier for chemical-looping combustion, Fuel. 127 (2014) 186–201. doi:10.1016/j.fuel.2013.07.045.

[15] A. Lyngfelt, B. Kronberger, J. Adanez, J.-X. Morin, P. Hurst, Greenhouse Gas Control Technologies 7, Elsevier, 2005. doi:10.1016/B978-008044704-9/50013-6.

[16] C. Saha, S. Bhattacharya, Experimental investigation of fluidized bed chemical looping combustion of Victorian brown coal using hematite, Journal of Environmental Chemical Engineering. 2 (2014) 1642–1654. doi:10.1016/j.jece.2014.02.014.

[17] L.F. de Diego, F. Garcı´a-Labiano, P. Gayán, J. Celaya, J.M. Palacios, J. Adánez, Operation of a 10kWth chemical-looping combustor during 200h with a CuO–Al2O3 oxygen carrier, Fuel. 86 (2007) 1036–1045. doi:10.1016/j.fuel.2006.10.004.

[18] Q. Imtiaz, A.M. Kierzkowska, M. Broda, C.R. Müller, Synthesis of Cu-rich, Al2O3-stabilized oxygen carriers using a coprecipitation technique: redox and carbon formation characteristics., Environmental Science & Technology. 46 (2012) 3561–6. doi:10.1021/es2042788.

[19] J. Adánez, A. Cuadrat, A. Abad, P. Gayán, L.F. de Diego, F. García-Labiano, Ilmenite Activation during Consecutive Redox Cycles in Chemical-Looping Combustion, Energy & Fuels. 24 (2010) 1402–1413. doi:10.1021/ef900856d.

[20] C.D. Bohn, J.P. Cleeton, C.R. Müller, S.Y. Chuang, S.A. Scott, J.S. Dennis, Stabilizing Iron Oxide Used in Cycles of Reduction and Oxidation for Hydrogen Production, Energy & Fuels. 24 (2010) 4025–4033. doi:10.1021/ef100199f.

[21] M. Ishida, D. Zheng, T. Akehata, Evaluation of a chemical-looping-combustion power-generation system by graphic exergy analysis, Energy. 12 (1987) 147–154. doi:10.1016/0360-5442(87)90119-8.

[22] N.R. McGlashan, Chemical-looping combustion – a thermodynamic study, Proceedings of the Institution of Mechanical Engineers, Part C: Journal of Mechanical Engineering Science. 222 (2008) 1005–1019. doi:10.1243/09544062JMES790.

[23] International Environmental Agency, CO2 EMISSIONS FROM FUEL COMBUSTION HIGHLIGHTS, (2013).

[24] T. Mattisson, A. Lyngfelt, H. Leion, Chemical-looping with oxygen uncoupling for combustion of solid fuels, International Journal of Greenhouse Gas Control. 3 (2009) 11–19. doi:10.1016/j.ijggc.2008.06.002.

[25] A. Shulman, E. Cleverstam, T. Mattisson, A. Lyngfelt, Chemical – Looping with oxygen uncoupling using Mn/Mg-based oxygen carriers – Oxygen release and reactivity with methane, Fuel. 90 (2011) 941–950. doi:10.1016/j.fuel.2010.11.044.

[26] M. Luo, S. Wang, L. Wang, M. Lv, Reduction kinetics of iron-based oxygen carriers using methane for chemical-looping combustion, Journal of Power Sources. 270 (2014) 434–440. doi:10.1016/j.jpowsour.2014.07.100.

[27] A.E. Abasaeed, A.S. Al-Fatesh, M.A. Naeem, A.A. Ibrahim, A.H. Fakeeha, Catalytic performance of CeO2 and ZrO2 supported Co catalysts for hydrogen production via dry reforming of methane, International Journal of Hydrogen Energy. 40 (2015) 6818–6826. doi:10.1016/j.ijhydene.2015.03.152.

[28] D. Jing, M. Arjmand, T. Mattisson, M. Rydén, F. Snijkers, H. Leion, A. Lyngfelt, Examination of oxygen uncoupling behaviour and reactivity towards methane for manganese silicate oxygen carriers in chemical-looping combustion, International Journal of Greenhouse Gas Control. 29 (2014) 70–81. doi:10.1016/j.ijggc.2014.07.003.

[29] J.S. Dennis, S.A. Scott, In situ gasification of a lignite coal and CO2 separation using chemical looping with a Cu-based oxygen carrier, Fuel. 89 (2010) 1623–1640. doi:10.1016/j.fuel.2009.08.019.

[30] M. Rydén, A. Lyngfelt, T. Mattisson, Combined manganese/iron oxides as oxygen carrier for chemical looping combustion with oxygen uncoupling

(CLOU) in a circulating fluidized bed reactor system, Energy Procedia. 4 (2011) 341–348. doi:10.1016/j.egypro.2011.01.060.

[31] A. Lyngfelt, C. Linderholm, Chemical-looping Combustion of Solid Fuels – Technology Overview and Recent Operational Results in 100kW Unit, Energy Procedia. 63 (2014) 98–112. doi:10.1016/j.egypro.2014.11.011.

[32] H. Leion, T. Mattisson, A. Lyngfelt, The use of petroleum coke as fuel in chemical-looping combustion, Fuel. 86 (2007) 1947–1958. doi:10.1016/j.fuel.2006.11.037.

[33] C. Linderholm, A. Lyngfelt, C. Dueso, Chemical-looping combustion of solid fuels in a 10kW reactor system using natural minerals as oxygen carrier, Energy Procedia. 37 (2013) 598–607. doi:10.1016/j.egypro.2013.05.147.

[34] E. Jerndal, T. Mattisson, A. Lyngfelt, Thermal Analysis of Chemical-Looping Combustion, Chemical Engineering Research and Design. 84 (2006) 795–806. doi:10.1205/cherd05020.

[35] J.P. Cleeton, Chemical Looping Combustion with Simultaneous Power Generation and Hydrogen Production using Iron Oxides, Cambridge, 2011.

[36] W. Liu, M. Ismail, M.T. Dunstan, W. Hu, Z. Zhang, P.S. Fennell, S.A. Scott, J.S. Dennis, Inhibiting the interaction between FeO and Al 2 O 3 during chemical looping production of hydrogen, RSC Adv. 5 (2015) 1759–1771. doi:10.1039/C4RA11891J.

[37] W. Liu, J.S. Dennis, S.A. Scott, The Effect of Addition of ZrO 2 to Fe 2 O 3 for Hydrogen Production by Chemical Looping, Industrial & Engineering Chemistry Research. 51 (2012) 16597–16609. doi:10.1021/ie302626x.

[38] S. Chuang, J. Dennis, A. Hayhurst, S. Scott, Development and performance of Cu-based oxygen carriers for chemical-looping combustion, Combustion and Flame. 154 (2008) 109–121. doi:10.1016/j.combustflame.2007.10.005.

[39] I. Starkov, S. Bychkov, A. Matvienko, A. Nemudry, Oxygen release technique as a method for the determination of “δ-pO2-T” diagrams for MIEC oxides., Physical Chemistry Chemical Physics : PCCP. 16 (2014) 5527–35. doi:10.1039/c3cp52143e.

[40] E. Marek, W. Hu, M. Gaultois, C.P. Grey, S.A. Scott, The use of strontium ferrite in chemical looping systems, Applied Energy. 223 (2018) 369–382. doi:10.1016/j.apenergy.2018.04.090.

[41] J. Mizusaki, M. Okayasu, S. Yamauchi, K. Fueki, Nonstoichiometry and phase relationship of the SrFeO2.5SrFeO3 system at high temperature, Journal of Solid State Chemistry. 99 (1992) 166–172. doi:10.1016/0022-4596(92)90301-B.

[42] C.Y. Lau, M.T. Dunstan, W. Hu, C.P. Grey, S.A. Scott, Large scale in silico screening of materials for carbon capture through chemical looping, Energy Environ. Sci. 10 (2017) 818–831. doi:10.1039/C6EE02763F.

[43] H. Leion, T. Mattisson, A. Lyngfelt, Use of Ores and Industrial Products As Oxygen Carriers in Chemical-Looping Combustion, Energy & Fuels. 23 (2009) 2307–2315. doi:10.1021/ef8008629.

[44] A. Abad, J. Adánez, A. Cuadrat, F. García-Labiano, P. Gayán, L.F. de Diego, Kinetics of redox reactions of ilmenite for chemical-looping combustion, Chemical Engineering Science. 66 (2011) 689–702. doi:10.1016/j.ces.2010.11.010.

[45] M.B. C. Higman, The Kinetics of Gasification and Reactor Theory, in: Gasification, 2nd ed., Gulf Professional Publishing, 2008.

[46] T. LIU, Y. FANG, Y. WANG, An experimental investigation into the gasification reactivity of chars prepared at high temperatures, Fuel. 87 (2008) 460–466. doi:10.1016/j.fuel.2007.06.019.

[47] B.B. Beamish, K.J. Shaw, K.. Rodgers, J. Newman, Thermogravimetric determination of the carbon dioxide reactivity of char from some New Zealand coals and its association with the inorganic geochemistry of the parent coal, Fuel Processing Technology. 53 (1998) 243–253. doi:10.1016/S0378-3820(97)00073-8.

[48] A.S. Čejka, Jiří; van Bekkum, Herman; Corma, 21.6.1 Catalytic Effectiveness Factors, in: Introduction to Zeolite Science and Practice, Volume 168 (3rd Edition), 3rd ed., Elsevier, 2007. http://app.knovel.com/web/view/swf/show.v/rcid:kpIZVE0002/cid:kt00BZMQY5/viewerType:pdf/root_slug:introduction-zeolite?cid=kt00BZMQY5&page=41&q=effectiveness factor&b-q=effectiveness factor&sort_on=default&b-subscription=TRUE&b-group-by=true&b-search-type (accessed July 27, 2015).

[49] W. Thiele, Relation between Catalvtic * Activity and Size of Particle, 31 (n.d.) 916–920.

[50] E.M. Hodge, D.G. Roberts, D.J. Harris, J.F. Stubington, The Significance of Char Morphology to the Analysis of High-Temperature Char–CO_2 Reaction Rates †, Energy & Fuels. 24 (2010) 100–107. doi:10.1021/ef900503x.

[51] B. V Babu, Biomass pyrolysis: a state-of- the-art review, Biofuels, Bioproducts & Biorefining. 2 (2008) 393–414. doi:10.1002/bbb.92.

[52] M. Jahirul, M. Rasul, A. Chowdhury, N. Ashwath, Biofuels Production through Biomass Pyrolysis —A Technological Review, Energies. 5 (2012) 4952–5001. doi:10.3390/en5124952.

[53] A. Demirbas, Pyrolysis Mechanisms of Biomass Materials, Energy Sources, Part A: Recovery, Utilization, and Environmental Effects. 31 (2009) 1186–1193. doi:10.1080/15567030801952268.

[54] F. Shafizadeh, Introduction to pyrolysis of biomass, Journal of Analytical and Applied Pyrolysis. 3 (1982) 283–305. doi:10.1016/0165-2370(82)80017-X.

[55] C.A. Koufopanos, A. Lucchesi, G. Maschio, Kinetic modelling of the pyrolysis of biomass and biomass components, The Canadian Journal of Chemical Engineering. 67 (1989) 75–84. doi:10.1002/cjce.5450670111.

[56] R.S. MILLER, J. BELLAN, A Generalized Biomass Pyrolysis Model Based on Superimposed Cellulose, Hemicelluloseand Liqnin Kinetics, Combustion Science and Technology. 126 (1997) 97–137. doi:10.1080/00102209708935670.

[57] F.-X. Collard, J. Blin, A review on pyrolysis of biomass constituents: Mechanisms and composition of the products obtained from the conversion of cellulose, hemicelluloses and lignin, Renewable and Sustainable Energy Reviews. 38 (2014) 594–608. doi:10.1016/j.rser.2014.06.013.

[58] R.J. Evans, T.A. Milne, Molecular characterization of the pyrolysis of biomass, Energy & Fuels. 1 (1987) 123–137. doi:10.1021/ef00002a001.

[59] J.D. Rocha, E.O. Gómez, J.M.M. Pérez, L.A.B. Cortez, O. Seye, L.E.B. González, THE DEMONSTRATION FAST PYROLYSIS PLANT TO BIOMASS CONVERSION IN BRAZIL, Proceedings of World Renewable Energy Congress VII (WRC 2002). (2002).

[60] A.. Bridgwater, Renewable fuels and chemicals by thermal processing of biomass, Chemical Engineering Journal. 91 (2003) 87–102. doi:10.1016/S1385-8947(02)00142-0.

[61] H.B. Goyal, D. Seal, R.C. Saxena, Bio-fuels from thermochemical conversion of

renewable resources: A review, Renewable and Sustainable Energy Reviews. 12 (2008) 504–517. doi:10.1016/j.rser.2006.07.014.

[62] E. Kantarelis, A. Zabaniotou, Valorization of cotton stalks by fast pyrolysis and fixed bed air gasification for syngas production as precursor of second generation biofuels and sustainable agriculture, Bioresource Technology. 100 (2009) 942–947. doi:10.1016/j.biortech.2008.07.061.

[63] Y. Shen, J. Wang, X. Ge, M. Chen, By-products recycling for syngas cleanup in biomass pyrolysis – An overview, Renewable and Sustainable Energy Reviews. 59 (2016) 1246–1268. doi:10.1016/j.rser.2016.01.077.

[64] P. De Wild, U. Zielke, M. Suomalainen, H. Knoef, J. Good, T. Liliedahl, C. Unger, M. Whitehouse, J. Neeft, J. Kiel, Tar measurement standard for sampling and analysis of tars and particles in biomass gasification product gas, 14th European Biomass Conference & Exhibition. (2005) 17–21.

[65] L. Devi, K.J. Ptasinski, F.J.J.. Janssen, A review of the primary measures for tar elimination in biomass gasification processes, Biomass and Bioenergy. 24 (2003) 125–140. doi:10.1016/S0961-9534(02)00102-2.

[66] J.H. Byeon, J.H. Park, Y.S. Jo, K.Y. Yoon, J. Hwang, Removal of gaseous toluene and submicron aerosol particles using a dielectric barrier discharge reactor., Journal of Hazardous Materials. 175 (2010) 417–22. doi:10.1016/j.jhazmat.2009.10.022.

[67] A. Bosmans, S. Wasan, L. Helsen, WASTE TO CLEAN SYNGAS: AVOIDING TAR PROBLEMS, (2013).

[68] Q. Yu, C. Brage, G. Chen, K. Sjöström, Temperature impact on the formation of tar from biomass pyrolysis in a free-fall reactor, Journal of Analytical and Applied Pyrolysis. 40–41 (1997) 481–489. doi:10.1016/S0165-2370(97)00017-X.

[69] I. Narváez, A. Orío, M.P. Aznar, J. Corella, Biomass Gasification with Air in an Atmospheric Bubbling Fluidized Bed. Effect of Six Operational Variables on the Quality of the Produced Raw Gas, Industrial & Engineering Chemistry Research. 35 (1996) 2110–2120. doi:10.1021/ie9507540.

[70] C.M. Kinoshita, Y. Wang, J. Zhou, Tar formation under different biomass gasification conditions, Journal of Analytical and Applied Pyrolysis. 29 (1994) 169–181. doi:10.1016/0165-2370(94)00796-9.

[71] R.A. Knight, Experience with raw gas analysis from pressurized gasification of biomass, Biomass and Bioenergy. 18 (2000) 67–77. doi:10.1016/S0961-9534(99)00070-7.

[72] C. Li, K. Suzuki, Tar property, analysis, reforming mechanism and model for biomass gasification—An overview, Renewable and Sustainable Energy Reviews. 13 (2009) 594–604. doi:10.1016/j.rser.2008.01.009.

[73] A. Di Carlo, D. Borello, M. Sisinni, E. Savuto, P. Venturini, E. Bocci, K. Kuramoto, Reforming of tar contained in a raw fuel gas from biomass gasification using nickel-mayenite catalyst, International Journal of Hydrogen Energy. 40 (2015) 9088–9095. doi:10.1016/j.ijhydene.2015.05.128.

[74] T. Chen, H. Liu, P. Shi, D. Chen, L. Song, H. He, R.L. Frost, CO2 reforming of toluene as model compound of biomass tar on Ni/Palygorskite, Fuel. 107 (2013) 699–705. doi:10.1016/j.fuel.2012.12.036.

[75] J.L.R.-T. J. Corella, J. Herguido, J. Gonzalez-Saiz, F.J. Alday, Research in Thermochemical Biomass Conversion, Springer Netherlands, Dordrecht, 1988. doi:10.1007/978-94-009-2737-7.

[76] J. Corella, M.-P. Aznar, J. Gil, M.A. Caballero, Biomass Gasification in Fluidized Bed: Where To Locate the Dolomite To Improve Gasification?, Energy & Fuels. 13 (1999) 1122–1127. doi:10.1021/ef990019r.

[77] S. Rapagnà, Steam-gasification of biomass in a fluidised-bed of olivine particles, Biomass and Bioenergy. 19 (2000) 187–197. doi:10.1016/S0961-9534(00)00031-3.

[78] M.M. Yung, W.S. Jablonski, K.A. Magrini-Bair, Review of Catalytic Conditioning of Biomass-Derived Syngas, Energy & Fuels. 23 (2009) 1874–1887. doi:10.1021/ef800830n.

[79] N. Tippayawong, P. Inthasan, C. Mai, Investigation of Light Tar Cracking in a Gliding Arc Plasma System Investigation of Light Tar Cracking in a Gliding Arc Plasma System *, (n.d.). https://www.degruyter.com/downloadpdf/j/ijcre.2010.8.1/ijcre.2010.8.1.2181/ijcre.2010.8.1.2181.pdf (accessed February 28, 2018).

[80] S. Nijdam, E. van Veldhuizen, P. Bruggeman, U. Ebert, An Introduction to Nonequilibrium Plasmas at Atmospheric Pressure, Plasma Chemistry and Catalysis in Gases and Liquids. (2012) 1–44. doi:10.1002/9783527649525.ch1.

[81] P.L. Vasile I. Parvulescu, Monica Magureanu, Plasma Chemistry and Catalysis in Gases and Liquids, Wiley-VCH Verlag GmbH & Co. KGaA, Weinheim, Germany, 2012. doi:10.1002/9783527649525.

[82] S. Masuda, H. Nakao, Control of NO/sub x/ by positive and negative pulsed corona discharges, IEEE Transactions on Industry Applications. 26 (1990) 374–383. doi:10.1109/28.54266.

[83] NOx Removal From Air Streams by a Superimposed AC/DC Energized Flow Stabilized Streamer Corona, IEEJ Transactions on Fundamentals and Materials. (2008) 948.

[84] C. Liu, A. Marafee, B. Hill, G. Xu, R. Mallinson, L. Lobban, Oxidative Coupling of Methane with ac and dc Corona Discharges, Industrial & Engineering Chemistry Research. 35 (1996) 3295–3301. doi:10.1021/ie960138j.

[85] K. Okazaki, S. Hirai, T. Nozaki, K. Ogawa, K. Hijikata, Plasma chemical reactions at atmospheric pressure for high efficiency use of hydrocarbon fuels, Energy. 22 (1997) 369–374. doi:10.1016/S0360-5442(96)00129-6.

[86] G. Prieto, M. Okumoto, K. Shimano, K. Takashima, S. Katsura, A. Mizuno, Reforming of heavy oil using nonthermal plasma, IEEE Transactions on Industry Applications. 37 (2001) 1464–1467. doi:10.1109/28.952522.

[87] G. Prieto, M. Okumoto, K. Shimano, K. Takashima, S. Katsura, A. Mizuno, O. Prieto, C.R. Gay, Heavy oil conversion by plasma chemical reactors, in: Conference Record of the 1999 IEEE Industry Applications Conference. Thirty-Forth IAS Annual Meeting (Cat. No.99CH36370), IEEE, 1999: pp. 1144–1149. doi:10.1109/IAS.1999.801648.

[88] S. Sultana, A. Vandenbroucke, C. Leys, N. De Geyter, R. Morent, Abatement of VOCs with Alternate Adsorption and Plasma-Assisted Regeneration: A Review, Catalysts. 5 (2015) 718–746. doi:10.3390/catal5020718.

[89] P. Liang, W. Jiang, L. Zhang, J. Wu, J. Zhang, D. Yang, Experimental studies of removing typical VOCs by dielectric barrier discharge reactor of different sizes, Process Safety and Environmental Protection. 94 (2015) 380–384. doi:10.1016/j.psep.2014.09.003.

[90] M. Materazzi, P. Lettieri, L. Mazzei, R. Taylor, C. Chapman, Reforming of tars and organic sulphur compounds in a plasma-assisted process for waste gasification, Fuel Processing Technology. 137 (2015) 259–268.

doi:10.1016/j.fuproc.2015.03.007.

[91] S. Morrin, P. Lettieri, C. Chapman, L. Mazzei, Two stage fluid bed-plasma gasification process for solid waste valorisation: technical review and preliminary thermodynamic modelling of sulphur emissions., Waste Management (New York, N.Y.). 32 (2012) 676–84. doi:10.1016/j.wasman.2011.08.020.

[92] M. Materazzi, P. Lettieri, L. Mazzei, R. Taylor, C. Chapman, Tar evolution in a two stage fluid bed–plasma gasification process for waste valorization, Fuel Processing Technology. 128 (2014) 146–157. doi:10.1016/j.fuproc.2014.06.028.

[93] K.H. Becker, U. Kogelschatz, K.H. Schoenbach, R.J. Barker, Non-equilibrium air plasmas at atmospheric pressure, 2005. doi:10.1016/0006-291X(79)91191-4.

[94] P. Talebizadeh, M. Babaie, R. Brown, H. Rahimzadeh, Z. Ristovski, M. Arai, The role of non-thermal plasma technique in NOx treatment: A review, Renewable and Sustainable Energy Reviews. 40 (2014) 886–901. doi:10.1016/j.rser.2014.07.194.

[95] W. Zhao, F. Wang, Y. Liu, R. Zhang, H. Hou, W. Zhao, F. Wang, Y. Liu, R. Zhang, H. Hou, Effects of Electrode Structure and Electron Energy on Abatement of NO in Dielectric Barrier Discharge Reactor, Applied Sciences. 8 (2018) 618. doi:10.3390/app8040618.

[96] Y. Huang, S. Dai, F. Feng, X. Zhang, Z. Liu, K. Yan, A comparison study of toluene removal by two-stage DBD-catalyst systems loading with MnOx, CeMnOx, and CoMnOx, Environmental Science and Pollution Research. 22 (2015) 19240–19250. doi:10.1007/s11356-015-5121-3.

[97] T. Pham Huu, S. Gil, P. Da Costa, A. Giroir-Fendler, A. Khacef, Plasma-catalytic hybrid reactor: Application to methane removal, Catalysis Today. 257 (2015) 86–92. doi:10.1016/j.cattod.2015.03.001.

[98] Plasma-catalytic removal of formaldehyde using Cu-Ce Catalysts, (n.d.). http://www.ispc-conference.org/ispcproc/ispc22/P-III-9-11.pdf (accessed May 17, 2016).

[99] X. Tang, M. Wang, W. Feng, F. Feng, K. Yan, VOCs degradation with non-thermal plasma and Ag-MnOx catalysis, Ispc_20. (2011).

[100] M. Keller, H. Leion, T. Mattisson, Chemical looping tar reforming using La/Sr/Fe-containing mixed oxides supported on ZrO2, Applied Catalysis B:

Environmental. 183 (2016) 298–307. doi:10.1016/j.apcatb.2015.10.047.

[101] A. Fridman, Plasma Chemistry, Cambridge University Press, 2008. doi:http://dx.doi.org/10.1017/CBO9780511546075.

[102] Heat values of various fuels - World Nuclear Association, (2016). http://www.world-nuclear.org/information-library/facts-and-figures/heat-values-of-various-fuels.aspx (accessed February 27, 2018).

[103] I. Dincer, C. Acar, Review and evaluation of hydrogen production methods for better sustainability, International Journal of Hydrogen Energy. 40 (2014) 11094–11111. doi:10.1016/j.ijhydene.2014.12.035.

[104] P.L. Spath, M.K. Mann, Life Cycle Assessment of Hydrogen Production via Natural Gas Steam Reforming, National Renewable Energy Laboratory, DOE, U.S. (2001) NREL/TP-570-27637. doi:10.2172/764485.

[105] B. Anzelmo, J. Wilcox, S. Liguori, Natural gas steam reforming reaction at low temperature and pressure conditions for hydrogen production via Pd/PSS membrane reactor, Journal of Membrane Science. 522 (2017) 343–350. doi:10.1016/J.MEMSCI.2016.09.029.

[106] J.P. Van Hook, Methane-Steam Reforming, Catalysis Reviews. 21 (1980) 1–51. doi:10.1080/03602458008068059.

[107] A. Igarashi, T. Ohtaka, S. Motoki, Low-temperature steam reforming ofn-butane over Rh and Ru catalysts supported on ZrO2, Catalysis Letters. 13 (1992) 189–194. doi:10.1007/BF00770990.

[108] J.R. Rostrup-Nielsen, Activity of nickel catalysts for steam reforming of hydrocarbons, Journal of Catalysis. 31 (1973) 173–199. doi:10.1016/0021-9517(73)90326-6.

[109] T.L. Levalley, A.R. Richard, M. Fan, The progress in water gas shift and steam reforming hydrogen production technologies - A review, International Journal of Hydrogen Energy. 39 (2014) 16983–17000. doi:10.1016/j.ijhydene.2014.08.041.

[110] Y. Matsumura, T. Nakamori, Steam reforming of methane over nickel catalysts at low reaction temperature, Applied Catalysis A: General. 258 (2004) 107–114. doi:10.1016/j.apcata.2003.08.009.

[111] S.D. Angeli, G. Monteleone, A. Giaconia, A.A. Lemonidou, State-of-the-art catalysts for CH4steam reforming at low temperature, International Journal of Hydrogen Energy. 39 (2014) 1979–1997. doi:10.1016/j.ijhydene.2013.12.001.

[112] L. Nalbandian, A. Evdou, V. Zaspalis, La1−xSrxMyFe1−yO3−δ perovskites as oxygen-carrier materials for chemical-looping reforming, International Journal of Hydrogen Energy. 36 (2011) 6657–6670. doi:10.1016/J.IJHYDENE.2011.02.146.

[113] R.D. Solunke, G. Veser, Hydrogen Production via Chemical Looping Steam Reforming in a Periodically Operated Fixed-Bed Reactor, Industrial & Engineering Chemistry Research. 49 (2010) 11037–11044. doi:10.1021/ie100432j.

[114] M. Rydén, A. Lyngfelt, Using steam reforming to produce hydrogen with carbon dioxide capture by chemical-looping combustion, International Journal of Hydrogen Energy. 31 (2006) 1271–1283. doi:10.1016/j.ijhydene.2005.12.003.

[115] M. Tang, L. Xu, M. Fan, Progress in oxygen carrier development of methane-based chemical-looping reforming: A review, Applied Energy. 151 (2015) 143–156. doi:10.1016/j.apenergy.2015.04.017.

[116] *,† Qamar Zafar, ‡ and Tobias Mattisson, B. Gevert†, Redox Investigation of Some Oxides of Transition-State Metals Ni, Cu, Fe, and Mn Supported on SiO2 and MgAl2O4, (2005). doi:10.1021/EF0501389.

[117] M. Rydén, A. Lyngfelt, T. Mattisson, D. Chen, A. Holmen, E. Bj??rgum, Novel oxygen-carrier materials for chemical-looping combustion and chemical-looping reforming; LaxSr1−xFeyCo1−yO3−δ perovskites and mixed-metal oxides of NiO, Fe2O3 and Mn3O4, International Journal of Greenhouse Gas Control. 2 (2008) 21–36. doi:10.1016/S1750-5836(07)00107-7.

[118] J.R. Fincke, R.P. Anderson, T.A. Hyde, B.A. Detering, Plasma pyrolysis of methane to hydrogen and carbon black, Industrial and Engineering Chemistry Research. 41 (2002) 1425–1435. doi:10.1021/ie010722e.

[119] Q. Wang, H. Shi, B. Yan, Y. Jin, Y. Cheng, Steam enhanced carbon dioxide reforming of methane in DBD plasma reactor, International Journal of Hydrogen Energy. 36 (2011) 8301–8306. doi:10.1016/j.ijhydene.2011.04.084.

[120] X. Tu, J.C. Whitehead, Plasma-catalytic dry reforming of methane in an atmospheric dielectric barrier discharge: Understanding the synergistic effect at low temperature, Applied Catalysis B: Environmental. 125 (2012) 439–448. doi:10.1016/j.apcatb.2012.06.006.

[121] Y. Zeng, X. Zhu, D. Mei, B. Ashford, X. Tu, Plasma-catalytic dry reforming of

methane over γ-Al2O3 supported metal catalysts, Catalysis Today. 256 (2015) 80–87. doi:10.1016/j.cattod.2015.02.007.

[122] Y. Chao, C.T. Huang, H.M. Lee, M.B. Chang, Hydrogen production via partial oxidation of methane with plasma-assisted catalysis, International Journal of Hydrogen Energy. 33 (2008) 664–671. doi:10.1016/j.ijhydene.2007.09.024.

[123] X. Tu, H.J. Gallon, M. V Twigg, P.A. Gorry, J.C. Whitehead, Dry reforming of methane over a Ni/Al 2 O 3 catalyst in a coaxial dielectric barrier discharge reactor, Journal of Physics D: Applied Physics. 44 (2011) 274007. doi:10.1088/0022-3727/44/27/274007.

[124] Q. Wang, B.-H. Yan, Y. Jin, Y. Cheng, Dry Reforming of Methane in a Dielectric Barrier Discharge Reactor with Ni/Al $_2$ O $_3$ Catalyst: Interaction of Catalyst and Plasma, Energy & Fuels. 23 (2009) 4196–4201. doi:10.1021/ef900286j.

[125] N.Z. Muradov, T.N. Veziroğlu, From hydrocarbon to hydrogen–carbon to hydrogen economy, International Journal of Hydrogen Energy. 30 (2005) 225–237. doi:10.1016/J.IJHYDENE.2004.03.033.

[126] J. Genovese, K. Harg, M. Paster, J. Turner, Current (2009) State-of-the-Art Hydrogen Production Cost Estimate Using Water Electrolysis Independent Review, 2009. doi:NREL/BK-6A1-46676.

[127] T. Nakamura, Hydrogen production from water utilizing solar heat at high temperatures, Solar Energy. 19 (1977) 467–475. doi:10.1016/0038-092X(77)90102-5.

[128] W. Hu, F. Donat, S.A. Scott, J.S. Dennis, Kinetics of oxygen uncoupling of a copper based oxygen carrier, Applied Energy. 161 (2016) 92–100. doi:10.1016/j.apenergy.2015.10.006.

[129] Zirconium Hydroxide Nanoparticles / Nanopowder (Zr(OH)4, 99.9%, 40 nm, Amorphous), (n.d.). http://www.us-nano.com/inc/sdetail/6232 (accessed January 26, 2018).

[130] C.Y. Wen, Y.H. Yu, A generalized method for predicting the minimum fluidization velocity, AIChE Journal. 12 (1966) 610–612. doi:10.1002/aic.690120343.

[131] E.P.J. Linstrom, W.G. Mallard, eds., NIST Chemistry WebBook, NIST Standard Reference Database Number 69, 2017. doi:doi:10.18434/T4D303.

[132] S. Brunauer, P.H. Emmett, E. Teller, Adsorption of Gases in Multimolecular Layers, Journal of the American Chemical Society. 60 (1938) 309–319. doi:10.1021/ja01269a023.

[133] E.P. Barrett, L.G. Joyner, P.P. Halenda, The Determination of Pore Volume and Area Distributions in Porous Substances. I. Computations from Nitrogen Isotherms, Journal of the American Chemical Society. 73 (1951) 373–380. doi:10.1021/ja01145a126.

[134] J.S. on I. and S.B.R.J.C. on R. within B. Furnaces, Blast furnace phenomena and modelling, Elsevier Applied Science, 1987. https://books.google.co.uk/books/about/Blast_furnace_phenomena_and_modelling.html?id=YJxTAAAAMAAJ&pgis=1 (accessed June 18, 2015).

[135] W.P. R. Spitzer, F. Manniing, Mixed-control reaction kinetics in the gaseous reduction of hematite. Trans. Metall. Doc. AIME, 1966.

[136] H. Chen, Z. Zheng, W. Shi, Investigation on the Kinetics of Iron Ore Fines Reduction by CO in a Micro-fluidized Bed, Procedia Engineering. 102 (2015) 1726–1735. doi:10.1016/j.proeng.2015.01.308.

[137] C.D. Bohn, J.P. Cleeton, C.R. Müller, J.F. Davidson, A.N. Hayhurst, S.A. Scott, J.S. Dennis, The kinetics of the reduction of iron oxide by carbon monoxide mixed with carbon dioxide, AIChE Journal. (2010) NA-NA. doi:10.1002/aic.12084.

[138] R.A. GIDDINGS, R.S. GORDON, Review of Oxygen Activities and Phase Boundaries in Wustite as Determined by Electromotive-Force and Gravimetric Methods, Journal of the American Ceramic Society. 56 (1973) 111–116. doi:10.1111/j.1151-2916.1973.tb15423.x.

[139] R.H. Davies, A.T. Dinsdale, J.A. Gisby, J.A.J. Robinson, S.M. Martin, MTDATA-thermodynamic and phase equilibrium software from the national physical laboratory, Calphad. 26 (2002) 229–71. doi:10.1016/S0364-5916(02)00036-6.

[140] S.K. Bhatia, D.D. Perlmutter, A random pore model for fluid-solid reactions: I. Isothermal, kinetic control, AIChE Journal. 26 (1980) 379–386. doi:10.1002/aic.690260308.

[141] A. Hayhurst, M. Parmar, Measurement of the mass transfer coefficient and sherwood number for carbon spheres burning in a bubbling fluidized bed,

Combustion and Flame. 130 (2002) 361–375. doi:10.1016/S0010-2180(02)00387-5.

[142] A.N. Hayhurst, The mass transfer coefficient for oxygen reacting with a carbon particle in a fluidized or packed bed, Combustion and Flame. 121 (2000) 679–688. doi:10.1016/S0010-2180(99)00178-9.

[143] F. Scala, Fluidized bed gasification of lignite char with CO2 and H2O: A kinetic study, Proceedings of the Combustion Institute. 35 (2015) 2839–2846. doi:10.1016/j.proci.2014.07.009.

[144] M. Troiano, P. Ammendola, F. Scala, Attrition of lignite char under fluidized bed gasification conditions: The effect of carbon conversion, Proceedings of the Combustion Institute. 34 (2013) 2741–2747. doi:10.1016/j.proci.2012.05.105.

[145] L. Hofer, E. Sterling, J. McCartney, Structure of Carbon Deposited from Carbon Monoxide on Iron, Cobalt and Nickel, The Journal of Physical …. 176 (1955) 1953–1955. doi:10.1021/j150533a010.

[146] C. Park, N.M. Rodriguez, R.T.K. Baker, Carbon Deposition on Iron–Nickel during Interaction with Carbon Monoxide–Hydrogen Mixtures, Journal of Catalysis. 169 (1997) 212–227. doi:10.1006/jcat.1997.1691.

[147] Microwave-Specific Enhancement of Carbon-Carbon Dioxide (Boudouard) Reaction, (n.d.). http://www.chem.fsu.edu/mcwg/Resources/jp4076965.pdf (accessed August 21, 2015).

[148] A. Maitre, P. Lefort, Solid state reaction of zirconia with carbon, Solid State Ionics. 104 (1997) 109–122. doi:10.1016/S0167-2738(97)00398-6.

[149] R. Ebrahimi-Kahrizsangi, E. Amini-Kahrizsangi, Zirconia carbothermal reduction: Non-isothermal kinetics, International Journal of Refractory Metals and Hard Materials. 27 (2009) 637–641. doi:10.1016/j.ijrmhm.2008.10.011.

[150] J. Gadsby, F.J. Long, P. Sleightholm, K.W. Sykes, The Mechanism of the Carbon Dioxide-Carbon Reaction, Proceedings of the Royal Society A: Mathematical, Physical and Engineering Sciences. 193 (1948) 357–376. doi:10.1098/rspa.1948.0051.

[151] J.F. Strange, P.L. Walker, Carbon-carbon dioxide reaction: Langmuir-Hinshelwood kinetics at intermediate pressures, Carbon. 14 (1976) 345–350. doi:10.1016/0008-6223(76)90008-7.

[152] N.M. Laurendeau, Heterogeneous kinetics of coal char gasification and

combusion, Progress in Energy and Combustion Science. 4 (1978) 221–270. doi:10.1016/0360-1285(78)90008-4.

[153] P.K. Gbor, C.Q. Jia, Critical evaluation of coupling particle size distribution with the shrinking core model, Chemical Engineering Science. 59 (2004) 1979–1987. doi:10.1016/j.ces.2004.01.047.

[154] M.F. Irfan, M.R. Usman, K. Kusakabe, Coal gasification in CO2 atmosphere and its kinetics since 1948: A brief review, Energy. 36 (2011) 12–40. doi:10.1016/j.energy.2010.10.034.

[155] G.Q. Lu, D.D. Do, Comparison of structural models for high-ash char gasification, Carbon. 32 (1994) 247–263. doi:10.1016/0008-6223(94)90188-0.

[156] M. a. Saucedo, J.S. Dennis, S. a. Scott, Modelling rates of gasification of a char particle in chemical looping combustion, Proceedings of the Combustion Institute. (2014). doi:10.1016/j.proci.2014.07.005.

[157] R.C. Everson, H.W.J.P. Neomagus, H. Kasaini, D. Njapha, Reaction kinetics of pulverized coal-chars derived from inertinite-rich coal discards: Gasification with carbon dioxide and steam, Fuel. 85 (2006) 1076–1082. doi:10.1016/j.fuel.2005.10.016.

[158] P. Dai, J.S. Dennis, S.A. Scott, Using an experimentally-determined model of the evolution of pore structure for the gasification of chars by CO2, Fuel. 171 (2016) 29–43. doi:10.1016/j.fuel.2015.12.041.

[159] P.L. Walker, F. Rusinko, L.G. Austin, Gas Reactions of Carbon, Advances in Catalysis. 11 (1959) 133–221. doi:10.1016/S0360-0564(08)60418-6.

[160] J.D. Blackwood, A.J. Ingeme, the Reaction of Carbon With Carbon Dioxide At High Pressure, Australian Journal of Chemistry. 13 (1960) 194–209. doi:http://dx.doi.org/10.1071/CH9600194.

[161] S. Ergun, KINETICS OF THE REACTION OF CARBON DIOXIDE WITH CARBON, 60 (1956) 480–485.

[162] S. Dutta, C.Y. Wen, R.J. Belt, Reactivity of Coal and Char. 1. In Carbon Dioxide Atmosphere, Industrial & Engineering Chemistry Process Design and Development. 16 (1977) 20–30. doi:10.1021/i260061a004.

[163] M. Mentser, S.. Ergun, A Study of the Carbon Dioxide-Carbon Reaction by Oxygen Exchange, (1973). http://digital.library.unt.edu/ark:/67531/metadc12808/.

[164] Handbook of Alternative Fuel Technologies, Second Edition, CRC Press, 2014. https://books.google.com/books?id=nXfSBQAAQBAJ&pgis=1 (accessed January 13, 2016).

[165] J.L. Figueiredo, J.A. Moulijn, Carbon and Coal Gasification: Science and Technology, Springer Science & Business Media, 2012. https://books.google.com/books?id=27LwCAAAQBAJ&pgis=1 (accessed February 9, 2016).

[166] J.B. Young, B. Todd, Modelling of multi-component gas flows in capillaries and porous solids, International Journal of Heat and Mass Transfer. 48 (2005) 5338–5353. doi:10.1016/j.ijheatmasstransfer.2005.07.034.

[167] S. Ergun, Kinetics of the Reactions of Carbon Dioxide and Steam with Coke, (1962).

[168] E. Fuller, P. Schettler, J.C. Giddings, A new method for prediction of binary gas, Industrial and Engineering Chemistry. 58 (1966) 18–27. doi:10.1016/0042-207X(66)90400-3.

[169] S.K. Bhatia, D.D. Perlmutter, A random pore model for fluid-solid reactions: II. Diffusion and transport effects, AIChE Journal. 27 (1981) 247–254. doi:10.1002/aic.690270211.

[170] S.A. Scott, J.F. Davidson, J.S. Dennis, P.S. Fennell, A.N. Hayhurst, The rate of gasification by CO2 of chars from waste, Proceedings of the Combustion Institute. 30 (2005) 2151–2159. doi:10.1016/j.proci.2004.08.061.

[171] R.I. Masel, Principles of Adsorption and Reaction on Solid Surfaces, John Wiley & Sons, 1996. https://books.google.co.uk/books/about/Principles_of_Adsorption_and_Reaction_on.html?id=cf9bR3MqgIIC&pgis=1 (accessed January 27, 2016).

[172] G.W. Roberts, C.N. Satterfield, Effectiveness Factor for Porous Catalysts. Langmuir-Hinshelwood Kinetic Expressions, Industrial & Engineering Chemistry Fundamentals. 4 (1965) 288–293. doi:10.1021/i160015a009.

[173] T. Mendiara, J.M. Johansen, R. Utrilla, P. Geraldo, A.D. Jensen, P. Glarborg, Evaluation of different oxygen carriers for biomass tar reforming (I): Carbon deposition in experiments with toluene, Fuel. 90 (2011) 1049–1060. doi:10.1016/j.fuel.2010.11.028.

[174] M. Rydén, P. Moldenhauer, T. Mattisson, A. Lyngfelt, M. Younes, T. Niass, B.

Fadhel, J.-P. Ballaguet, Chemical-Looping Combustion with Liquid Fuels, Energy Procedia. 37 (2013) 654–661. doi:10.1016/j.egypro.2013.05.153.

[175] T. Mendiara, a. Abad, L.F. de Diego, F. García-Labiano, P. Gayán, J. Adánez, Biomass combustion in a CLC system using an iron ore as an oxygen carrier, International Journal of Greenhouse Gas Control. 19 (2013) 322–330. doi:10.1016/j.ijggc.2013.09.012.

[176] L. Shen, J. Wu, J. Xiao, Q. Song, R. Xiao, Chemical-Looping Combustion of Biomass in a 10 kW th Reactor with Iron Oxide As an Oxygen Carrier, Energy & Fuels. 23 (2009) 2498–2505. doi:10.1021/ef900033n.

[177] H. Gu, L. Shen, J. Xiao, S. Zhang, T. Song, Chemical looping combustion of biomass/coal with natural iron ore as oxygen carrier in a continuous reactor, Energy and Fuels. 25 (2011) 446–455. doi:10.1021/ef101318b.

[178] O. Karatum, M.A. Deshusses, A comparative study of dilute VOCs treatment in a non-thermal plasma reactor, Chemical Engineering Journal. 294 (2016) 308–315. doi:10.1016/j.cej.2016.03.002.

[179] A. Baylet, P. Marécot, D. Duprez, X. Jeandel, K. Lombaert, J.M. Tatibouët, Synergetic effect of plasma/catalysis hybrid system for CH4 removal, Applied Catalysis B: Environmental. 113 (2012) 31–36. doi:10.1016/j.apcatb.2011.10.026.

[180] S. Bhavsar, B. Tackett, G. Veser, Evaluation of iron- and manganese-based mono- and mixed-metallic oxygen carriers for chemical looping combustion, Fuel. 136 (2014) 268–279. doi:10.1016/j.fuel.2014.07.068.

[181] S.K. Haider, G. Azimi, L. Duan, E.J. Anthony, K. Patchigolla, J.E. Oakey, H. Leion, T. Mattisson, A. Lyngfelt, Enhancing properties of iron and manganese ores as oxygen carriers for chemical looping processes by dry impregnation, Applied Energy. 163 (2016) 41–50. doi:10.1016/j.apenergy.2015.10.142.

[182] F. Donat, W. Hu, S.A. Scott, J.S. Dennis, Characteristics of Copper-based Oxygen Carriers Supported on Calcium Aluminates for Chemical-Looping Combustion with Oxygen Uncoupling (CLOU), Industrial & Engineering Chemistry Research. 54 (2015) 6713–23. doi:10.1021/acs.iecr.5b01172.

[183] D. Yap, J.-M. Tatibouët, C. Batiot-Dupeyrat, Carbon dioxide dissociation to carbon monoxide by non-thermal plasma, Journal of CO2 Utilization. 12 (2015) 54–61. doi:10.1016/j.jcou.2015.07.002.

[184] R. Aerts, T. Martens, A. Bogaerts, Influence of Vibrational States on CO_2 Splitting by Dielectric Barrier Discharges, The Journal of Physical Chemistry C. 116 (2012) 23257–23273. doi:10.1021/jp307525t.

[185] A. Al-Abduly, P. Christensen, An in situ and downstream study of non-thermal plasma chemistry in an air fed dielectric barrier discharge (DBD)., (2016). doi:10.1088/0963-0252/24/6/065006.

[186] A.M. Starik, V.E. Kozlov, N.S. Titova, On the influence of singlet oxygen molecules on characteristics of HCCI combustion: A numerical study, Combustion Theory and Modelling. 17 (2013) 579–609. doi:10.1080/13647830.2013.783238.

[187] U. Kogelschatz, Dielectric-barrier Discharges: Their History, Discharge Physics, and Industrial Applications, Plasma Chemistry and Plasma Processing. 23 (2003).

[188] K.-P. Francke, R. Rudolph, H. Miessner, Design and Operating Characteristics of a Simple and Reliable DBD Reactor for Use with Atmospheric Air, Plasma Chemistry and Plasma Processing. 23 (2003). https://link.springer.com/content/pdf/10.1023/A:1022412718224.pdf (accessed September 23, 2017).

[189] D. Mei, X. Zhu, Y.-L. He, J.D. Yan, X. Tu, Plasma-assisted conversion of CO 2 in a dielectric barrier discharge reactor: understanding the effect of packing materials, Plasma Sources Science and Technology. 24 (2014) 015011. doi:10.1088/0963-0252/24/1/015011.

[190] A.A. Fridman, L.A. Kennedy, Plasma physics and engineering, Taylor & Francis, 2004. https://books.google.co.uk/books?id=9wqtYiy_gloC&pg=PA187&lpg=PA187&dq=mean+electron+energy+a+function+of+the+reduced+electric+field&source=bl&ots=hf5IU-r0yL&sig=_u87yii5-F2gvs6za15TbO4HtAg&hl=en&sa=X&ved=0ahUKEwjyruufs_3YAhWNLFAKHVIvC0QQ6AEIPzAD#v=onepage&q=mean electron energy a function of the reduced electric field&f=false (accessed January 29, 2018).

[191] S. Al-Amin, Electron swarm parameters in oxygen and methane, Journal of Physics D: Applied Physics. 1781 (1985) 1781–1794. doi:10.1088/0022-3727/18/9/009.

[192] K. Zhang, T. Mukhriza, X. Liu, P.P. Greco, E. Chiremba, A study on CO2 and CH4 conversion to synthesis gas and higher hydrocarbons by the combination of catalysts and dielectric-barrier discharges, Applied Catalysis A: General. 502 (2015) 138–149. doi:10.1016/j.apcata.2015.06.002.

[193] A. Jahanmiri, M.R. Rahimpour, M. Mohamadzadeh Shirazi, N. Hooshmand, H. Taghvaei, Naphtha cracking through a pulsed DBD plasma reactor: Effect of applied voltage, pulse repetition frequency and electrode material, Chemical Engineering Journal. 191 (2012) 416–425. doi:10.1016/j.cej.2012.02.031.

[194] C. De Bie, J. Van Dijk, A. Bogaerts, The Dominant Pathways for the Conversion of Methane into Oxygenates and Syngas in an Atmospheric Pressure Dielectric Barrier Discharge, Journal of Physical Chemistry C. 119 (2015). doi:10.1021/acs.jpcc.5b06515.

[195] K. Tao, N. Ohta, G. Liu, Y. Yoneyama, T. Wang, N. Tsubaki, Plasma enhanced catalytic reforming of biomass tar model compound to syngas, Fuel. 104 (2013) 53–57. doi:10.1016/j.fuel.2010.05.044.

[196] Y. Sekine, H. Koyama, M. Matsukata, E. Kikuchi, Plasma-assisted oxidation of carbon particle by lattice oxygen on/in oxide catalyst, Fuel. 103 (2013) 2–6. doi:10.1016/j.fuel.2011.03.046.

[197] H.M. Lee, L.K. Juan, F.M. Yeh, H.Y. Li, H.L. Chen, M.B. Chang, S.H. Chen, C.C. Tzeng, Plasma-pretreated catalyst for methanol synthesis from syngas, IEEE Transactions on Plasma Science. 37 (2009) 2213–2220. doi:10.1109/TPS.2009.2030726.

[198] Q. Wang, Y. Cheng, Y. Jin, Dry reforming of methane in an atmospheric pressure plasma fluidized bed with Ni/γ-Al2O3 catalyst, Catalysis Today. 148 (2009) 275–282. doi:10.1016/j.cattod.2009.08.008.

[199] P. Manimuthu, C. Venkateswaran, Evidence of ferroelectricity in SrFeO 3–δ, Journal of Physics D: Applied Physics. 45 (2012) 015303. doi:10.1088/0022-3727/45/1/015303.

[200] Y.-R. Zhang, E.C. Neyts, A. Bogaerts, Influence of the Material Dielectric Constant on Plasma Generation inside Catalyst Pores, The Journal of Physical Chemistry C. 120 (2016) 25923–25934. doi:10.1021/acs.jpcc.6b09038.

[201] B.-R.J.S. and L.-C.R. Valdivia-Barrientos R, Pacheco-Sotelo J, Pacheco-Pacheco M, Analysis and electrical modelling of a cylindrical DBD configuration at

different operating frequencies, in: Plasma Sources Science and Technology, IOP Publishing, 2006: pp. 237–245. doi:10.1088/0963-0252/15/2/008.

[202] W.H. Tay, S.S. Kausik, S.L. Yap, C.S. Wong, Study on Discharge Dynamics in an Atmospheric Pressure Dielectric Barrier Discharge, Universal Journal of Physics and Application. 11 (2017) 80–84. doi:10.13189/ujpa.2017.110302.

[203] M. Pishahang, Y. Larring, M. Sunding, M. Jacobs, F. Snijkers, Performance of Perovskite-Type Oxides as Oxygen-Carrier Materials for Chemical Looping Combustion in the Presence of H_2S, Energy Technology. 4 (2016) 1305–1316. doi:10.1002/ente.201600177.

[204] A. Kramida, Y. Ralchenko, J. Reader, NIST ASD Team, NIST Atomic Spectra Database Lines Form, NIST Atomic Spectra Database (Ver. 5.2) [Online]. (2018) Available: http://physics.nist.gov/asd. doi:2015.

[205] M. Sun, Y. Wu, J. Li, N.H. Wang, J. Wu, K.F. Shang, J.L. Zhang, Diagnosis of OH Radical by Optical Emission Spectroscopy in Atmospheric Pressure Unsaturated Humid Air Corona Discharge and its Implication to Desulphurization of Flue Gas, Plasma Chemistry and Plasma Processing. 25 (2005) 31–40. doi:10.1007/s11090-004-8833-6.

[206] P.C. Miles, B. Li, Z. Li, M. Aldén, Atmospheric Pressure Acetylene Detection by UV Photo-Fragmentation and Induced C2 Emission, Applied Spectroscopy. 67 (2013) 66–72. doi:10.1366/12-06731.

[207] E.C. Neyts, K. Ostrikov, M.K. Sunkara, A. Bogaerts, Plasma Catalysis: Synergistic Effects at the Nanoscale, (n.d.). doi:10.1021/acs.chemrev.5b00362.

[208] C. Robinson, D.B. Smith, The auto-ignition temperature of methane, Journal of Hazardous Materials. 8 (1984) 199–203. doi:10.1016/0304-3894(84)85001-3.

[209] H. Falcón, J.A. Barbero, J.A. Alonso, M.J. Martínez-Lope, J.L.G. Fierro, SrFeO3-δ perovskite oxides: Chemical features and performance for methane combustion, Chemistry of Materials. 14 (2002) 2325–2333. doi:10.1021/cm011292l.

[210] A.M. James, M.P. Lord, Macmillan's Chemical and Physical Data, Macmillan, London, 1992.

[211] J.E. Huheey, E.A.Keiter, R.L.Keiter, Inorganic Chemistry:Principles of Structure and Reactivity, 4th ed., HarperCollins, New York, 1993.

[212] M. Brünglinghaus, Mean free path, European Nuclear Society. (2011).

doi:10.1615/AtoZ.m.mean_free_path.

[213] R.C. (Richard C. Fernow, Introduction to experimental particle physics, Cambridge University Press, 1989. https://books.google.co.uk/books?id=WNhMzhm0SscC&pg=PA80&dq=Rate+and+cross+section+particle+physics&redir_esc=y#v=onepage&q=Rate and cross section particle physics&f=false (accessed October 29, 2018).

[214] H. Matsumoto, S. Tanabe, K. Okitsu, Y. Hayashi, S.L. Suib, Selective Oxidation of Methane to Methanol and Formaldehyde with Nitrous Oxide in a Dielectric-Barrier Discharge-Plasma Reactor, (n.d.). doi:10.1021/jp001099z.

[215] de Ligny D., P. Richet, High-temperature heat capacity and thermal expansion of SrTiO3 and SrZrO3 perovskites, Physical Review. B, Condensed Matter. 53 (1996) 3013–3022. doi:10.1103/PhysRevB.53.3013.

[216] I.S. Ertesvåg, Sensitivity of chemical exergy for atmospheric gases and gaseous fuels to variations in ambient conditions, Energy Conversion and Management. 48 (2007) 1983–1995. doi:10.1016/j.enconman.2007.01.005.

[217] Vehicle Technologies Program: Fact #205: February 25, 2002 Hydrogen Cost and Worldwide Production, (2009). http://www1.eere.energy.gov/vehiclesandfuels/facts/favorites/fcvt_fotw205.html.

[218] T. Nozaki, N. Muto, S. Kado, K. Okazaki, Dissociation of vibrationally excited methane on Ni catalyst: Part 1. Application to methane steam reforming, in: Catalysis Today, 2004: pp. 57–65. doi:10.1016/j.cattod.2003.11.040.

[219] Y.-G. Chen, J. Ren, Conversion of methane and carbon dioxide into synthesis gas over alumina-supported nickel catalysts. Effect of Ni-A1203 interactions, Catalysis Letters. 29 (1994) 39–48. https://link.springer.com/content/pdf/10.1007/BF00814250.pdf (accessed November 20, 2017).

[220] V. Raghavan, Fe-Ni-O (Iron-nickel-oxygen), Journal of Phase Equilibria and Diffusion. 31 (2010) 369–371. doi:10.1007/s11669-010-9714-8.

[221] C.A. Callaghan, Kinetics and Catalysis of the Water-Gas-Shift Reaction: A Microkinetic and Graph Theoretic Approach, 2006. https://web.wpi.edu/Pubs/ETD/Available/etd-050406-023806/unrestricted/ccallaghan.pdf (accessed November 27, 2017).